



HAL
open science

Surface tension effects in microrobotics.

Pierre Lambert

► **To cite this version:**

Pierre Lambert. Surface tension effects in microrobotics.. Automatic. Université de Franche-Comté, 2007. tel-00536852

HAL Id: tel-00536852

<https://theses.hal.science/tel-00536852>

Submitted on 17 Nov 2010

HAL is a multi-disciplinary open access archive for the deposit and dissemination of scientific research documents, whether they are published or not. The documents may come from teaching and research institutions in France or abroad, or from public or private research centers.

L'archive ouverte pluridisciplinaire **HAL**, est destinée au dépôt et à la diffusion de documents scientifiques de niveau recherche, publiés ou non, émanant des établissements d'enseignement et de recherche français ou étrangers, des laboratoires publics ou privés.

Habilitation à diriger des recherches
Habilitation work toward the supervision of doctoral candidates

Pierre LAMBERT

Ingénieur Civil Mécanicien et Electricien de l'Université libre de Bruxelles
Docteur en Sciences appliquées de l'Université libre de Bruxelles
Chercheur CNRS CR1
Rattaché à l'UMR 6174, FEMTO-ST/Département AS2M

SURFACE TENSION EFFECTS IN MICROROBOTICS

Université de Franche-Comté

Jury composed of

Prof. Karl F. Bohringer (Rapporteur) University of Washington
Prof. Bruno Le Pioufle (Rapporteur) ENS Cachan
Prof. Philippe Lutz (Rapporteur) Université de Franche-Comté
Prof. Dominiek Reynaerts (Rapporteur) Katholieke Universiteit Leuven
Prof. Nicolas Chaillet Université de Franche-Comté
Prof. Dominique Collard University of Tokyo
Prof. Alain Delchambre Université libre de Bruxelles
Prof. Jacques Jacot Ecole Polytechnique Fédérale de Lausanne
Prof. Stéphane Régnier Université Pierre et Marie Curie

September 6, 2010

Contents

1	Introduction	1
2	Personal record	3
2.1	Resume	3
2.2	Research management	5
2.2.1	Research contracts	5
2.2.2	Organisation of scientific events	6
2.3	Students supervision (in French)	7
2.3.1	Internships	7
2.3.2	Masters in engineering science	7
2.3.3	MD in engineering sciences (DEA)	10
2.3.4	PhD works	10
2.4	Administrative tasks, teaching and contacts with industry	12
2.4.1	Administrative tasks	12
2.4.2	Teaching activities	13
2.4.3	Industrial experience	13
2.5	Publications	13
3	Context and scientific positioning	19
3.1	Milestones and international positioning	19
3.2	Scientific positioning	22
3.3	PhD summary and related publications	24
3.4	Post doctoral research	25
3.4.1	Personal research	26
3.4.2	Supervised research	27
3.5	Collaborations	31
4	Models	33
4.1	Introduction	33
4.2	Modeling liquid bridges geometry: an overview	35
4.2.1	Energetic method: example of two parallel plates	35
4.2.2	Introduction to Surface Evolver	37
4.2.3	Exact resolution for axially symmetric problems	41

4.2.4	Geometrical models	43
4.2.5	Conclusions	44
4.3	Contributions to capillary forces modeling	45
4.3.1	Capillary force developed by a meniscus at equilibrium	45
4.3.2	Equivalence of formulations	46
4.3.3	Axial static forces	47
4.3.4	Axial dynamic forces	56
4.3.5	Conclusions	61
4.3.6	Lateral capillary forces: statics and dynamics	62
4.3.7	Discussion and perspectives	74
4.4	Additional contributions to capillary forces modeling	78
4.4.1	Validity of capillary force model at the nanoscale	78
4.4.2	Gas law and capillary forces	85
4.5	Other contribution	91
4.5.1	Influence of surface topography on electrostatic adhesion	91
4.6	Conclusions	92
5	Measurement set ups	93
5.1	Introduction	93
5.2	Axial capillary forces	95
5.2.1	Static forces	95
5.2.2	Dynamic forces	99
5.3	Lateral capillary forces	102
5.3.1	Principle	102
5.3.2	Experimental setup and protocol	104
5.3.3	Set up calibration	105
5.4	Force measurement in the nanonewton range	107
5.5	Characterization of an acoustic field	109
5.5.1	Wire technique	109
5.5.2	Example: axial acoustic radiation force as a function of the sphere position	112
5.5.3	Conclusion	113
5.6	Watch shock absorbers characterization	114
5.6.1	Introduction	114
5.6.2	Shock absorber mechanism for watches	114
5.6.3	Goals of the study	115
5.6.4	Testbed design	115
5.6.5	Test bed characterization	118
5.6.6	Results analysis	120
5.6.7	Results	122
5.7	General conclusions	123

6	Case studies	125
6.1	Introduction	125
6.2	Capillary gripper	127
6.2.1	State of the art	127
6.2.2	Presentation of the case study	128
6.2.3	Analytical force model for gripper design	129
6.2.4	Gripper characterization	134
6.2.5	Micromanipulation results	137
6.2.6	Discussion and conclusions	142
6.3	Capillary feeder	143
6.3.1	Requirements list	143
6.3.2	Design	144
6.3.3	Results	144
6.3.4	Integration with the capillary gripper	146
6.4	Non contact feeder	147
6.4.1	Gripper and ball models	147
6.4.2	Numerical results of the non contact feeder	147
6.4.3	Conclusions	149
6.5	Hybrid assembly	150
6.5.1	Presentation of the case study	150
6.5.2	Model parameters	151
6.5.3	Application of the model	152
6.5.4	Conclusions	153
6.6	Assembly machine case study	154
6.6.1	What accelerations can undergo a liquid bridge?	154
6.6.2	What is the typical cycle time?	154
6.6.3	What is the force applied on the component during picking?	155
6.6.4	What liquids are recommended not to pollute the surfaces	158
6.7	Surface tension based robotic platform	159
6.7.1	Kinematics of the microrobotic platform	159
6.7.2	Current results	159
6.7.3	Conclusions	159
6.8	Soil mechanics	161
6.8.1	Presentation of the problem	161
6.8.2	Experimental study	161
6.8.3	Simulation	162
6.8.4	Conclusion	163
6.9	Capillary rise	164
6.9.1	Introduction	164
6.9.2	Dynamic contact angles	165
6.9.3	Slip length	167
6.9.4	1D benchmark	168
6.9.5	Experimental results	170
6.9.6	Numerical results	171

6.9.7	Conclusions	171
6.10	Electrosprays	171
6.10.1	Introduction	171
6.10.2	Literature review: from monosprays to mutisprays	172
6.10.3	Current results	173
6.11	Additional contribution: Stick and slip actuator	175
6.12	General conclusions	176
7	Perspectives	177
7.1	Microfluidic assembly	177
7.1.1	Context and motivation	177
7.1.2	Research objective and methodology	178
7.1.3	Droplets feeding and component encapsulation	178
7.1.4	Components displacement	179
7.1.5	Droplet merging	180
7.1.6	Related literature review	181
7.2	Laser excimer manufacturing	183
7.2.1	Machine performances	183
7.2.2	Capillary stops	184
7.2.3	Ceramic micro-electrodes patterning	186
7.3	Other perspectives	187
7.3.1	Applications of spray technologies	187
7.3.2	Liquid encapsulation	188
8	Conclusions	189
A	Energetic method	191
A.1	Preliminary	191
A.2	Between a sphere and a plane (Israelachvili approximation)	192
A.3	Between two spheres	195
A.3.1	Preliminaries	195
A.3.2	Expression of the interfacial energy	195
B	Energetic method vs Laplace equation	199
B.1	Introduction	199
B.2	Qualitative Arguments	199
B.3	Analytical Arguments	201
B.3.1	Definition of the Case Study	201
B.3.2	Preliminary Computations	202
B.3.3	Determination of the Immersion Height h	203
B.3.4	Laplace Equation Based Formulation of the Capillary Force	205
B.3.5	Energetic Formulation of the Capillary Force	205
B.3.6	Equivalence of Both Formulations	206
B.4	Conclusions	207

C	Design rules for capillary grippers	209
C.1	Introduction	209
C.2	Picking Operations	209
C.3	Releasing Strategies	210
C.4	Design Aspects	213
D	Parabola model	217
E	Axial dynamics	221
E.1	Volume of liquid as a function of the contact angle and the gap . . .	221
E.2	Numerical validation	221
E.3	Experimental validation	226
F	Lateral dynamics	231
G	Surface tension transducer	237
G.1	Parabolic model of the meniscus	237
G.1.1	Equations	237
G.1.2	Numerical scheme	238
H	Symbols	239
	Bibliography	259

Chapter 1

Introduction

This introduction is essentially a reading suggestion, and presents the structure of this document.

Chapter 2 presents my personal record: education and work experience, research contracts, supervised students, and a list of my publications.

Chapter 3 describes the context of my research and my scientific positioning. In this chapter, the reader will find an introduction to my research work, carried by three main influences: industrial assembly, microtechnologies and adhesion science. I also explain my research strategy, based on theoretical models, their experimental validation and application to case studies.

This strategy is mapped by the structure of this document.

Chapter 4 presents the models developed in this research. It highlights our contributions, after a brief description of pre-existing work (section 4.2). Let us already indicate main topics such as capillary forces (axial vs. lateral capillary forces, statics vs. dynamics, at scales from millimeter to nanometer). This matrical structure is shown in figure 4.2.

Chapter 5 describes the experimental set ups which have been designed to experimentally validate our theoretical work: it essentially consists in force measurement set ups, from nanonewton to newton (see figure 5.2).

Case studies are described in chapter 6, including for example assembly products and studies (gripper, feeder, hybrid assembly), soil mechanics, electrosprays.

Chapter 7 draws perspectives in direction of fluidic assembly toward handling of microcomponents in droplets, excimer laser ablation for fluidic structures and electrosprays.

At the beginning of the main three chapters (4-6), an introduction summarizes its content and graphically presents the structure organizing all the related contributions (figures 4.1, 5.1, 6.1). In these three chapters, each (sub)section is ended by a frame highlighting the main contribution. In this way, we hope the reading to be a bit less tedious. Finally, for a quick overview of this document, table 1 presents a reading suggestion.

	Title	Page
Section 2.1	Personal resume	3
Tab. 2.1 & 2.2	Summary of my publications	16, 17
Chapter 3	Context and scientific positioning	19
	<i>Map of my co-authors</i>	32
Section 4.1	Presentation of the models	33
	<i>Map of the models</i>	33
	<i>Capillary forces: axial/radial vs statics/dynamics criteria</i>	34
Section 5.1	Presentation of the experimental set ups	93
	<i>Map of the set ups</i>	94
	<i>Force-scale diagram of all experiments</i>	95
Section 6.1	Presentation of the case studies	125
	<i>Map of the case studies</i>	126
Chapter 7	Perspectives	177
Chapter 8	Conclusions	189

Table 1.1: Reading suggestions

A series of appendices have been added but are not essential to the reading of this document. They just provide additional information for interested readers.

Chapter 2

Personal record

This chapter includes a personal resume (section 2.1), a summary of research management including research contracts (section 2.2), the list of supervised students (section 2.3), a description of administrative tasks and teaching activities (section 2.4) and finally a summary of my publications (section 2.5).

2.1 Resume

Education

2000–2004 : PhD in engineering sciences (doctorat en sciences appliquées), Université libre de Bruxelles, presented on December 10th 2004: *A Contribution to Microassembly: a Study of Capillary Forces as a gripping Principle*

Jury : Prof. M.-P. Delplancke, Prof. P. Gaspart, Prof. A. Delchambre (Supervisor), Prof. A. Preumont, Prof. E. Filipi, Prof. J. Jacot, Prof. N. Chaillet

2002–2003 : **MD in engineering sciences**, Université libre de Bruxelles, July 2nd 2003: Simulation dynamique d'une tâche de micromanipulation utilisant les forces de surface

1999–2000 : **Agrégation de l'enseignement secondaire supérieur (pedagogical degree)** (Physics), Université libre de Bruxelles, June 2000

1993-1998 : **MD in mechanical and electrical engineering**, Université libre de Bruxelles, June 1998

Work experience

- Since 01/10/09** : **CNRS senior scientist (CR1)** in UMR 6174 (FEMTO-ST, AS2M Department, Besançon)
: Assistant professor (20%), Université libre de Bruxelles
- 10/05–09/09** : **Assistant professor** at Université libre de Bruxelles (ULB): permanent position since 01/10/2007, supervision of microtechnique research group of the Bio-Electro-And-Mechanical Systems (BEAMS) since May 2006
- en 2009** : 4 research periods as **invited researcher** in FEMTO-ST, AS2M department: collaboration on European Hydromel project (Prof. Philippe Lutz and Prof. Nicolas Chaillet)
- 04/08–10/08** : **Hôte académique (Invited professor)** in the Laboratoire de Production Microtechnique of the Ecole Polytechnique Fédérale de Lausanne (EPFL, Prof. Jacques Jacot)
- 01/06–06/06** : **Post-Doc** in Robotics Laboratory of Paris (Pierre and Marie Curie University), Prof. Stéphane Régnier
- 02/05–11/05** : **Post-Doc** in the Laboratoire de Production Microtechnique of l’Ecole Polytechnique Fédérale de Lausanne (EPFL, Prof. Jacques Jacot)
- 08/00–01/05** : **Research assistant**, Université libre de Bruxelles, PhD preparation (dir. Prof. Alain Delchambre)
- 09/99–06/00** : **Physics teacher** in the Ville de Bruxelles, and teaching assistant in mechanics (ULB, BA1)
- 05/99–08/99** : **Engineer** in Aricie company (logistics)
- 09/98–04/99** : **Engineer** in Trasys-France company: SAP software (logistic modules)

2.2 Research management

2.2.1 Research contracts

1. Assembly Net, 2000-2004, in collaboration with academic and industrial leaders in the field of micro-assembly (European Thematic Network)
Thanks to this thematic action, I took part to two summer schools and wrote a proposal toward a Research Thematic Network Marie Curie in collaboration with Fraunhofer IPA (Germany), CLFA, FEMTO-ST and LVR (France), CSEM, EPFL, FSRM and Leica (Switzerland), TU Delft (NL), the University of Nottingham (UK) and UL-Lasim (Slovenia). Unfortunately, this project was not funded
2. Méthodes et Moyens de la Miniaturisation des Machines (4M), 2000-2004, in collaboration with the Université catholique de Louvain and the Université de Liège (Funded by the Région wallonne)
This project allowed me to study flexible structures modeling [24, 186] and precision actuation [111].
3. Miniaturisation de Micromanipulateurs par la caractérisation et la modélisation de nanomatériaux, 2004-2009, in collaboration with partners of ULB (Funded by a so-called Action de Recherche Concertée ARC)
I contributed to define this project and supervised Marion Sausse-Lhernould's PhD. This project led many publications [105, 126, 125, 127, 123, 124, 122].
4. Modèles et outils pour le micro-assemblage (MOMIE), 2006-2008, in collaboration with University Paris VI (Pierre et Marie Curie) (joint funding CNRS-FNRS)
Thanks to this project, I could start a close collaboration with Prof. S. Régnier, which was later on funded by two so-called Tournesol calls: CNRS/CGRI and Egide/CGRI. This project was the origin of the joint supervision of Sausse-Lhernould's PhD.
5. Contribution à la plate-forme wallonne pour l'administration de médicaments (Neofor), 2007-2010 (Funded by the Région wallonne, Biowin project)
I contributed to write the proposal and supervised the researcher on this project, Michel Pierobon.
6. Micro Nozzle Arrays (MuNA), 2009-2010, Région Wallonne, First Post Doc Project
I proposed the subject and wrote down the proposal. This project started on

January 1st 2009.

7. Micro-assemblage, 2009, joint funding CNRS-CGRI, Tournesol Project
This new collaboration with Michaël Gauthier (FEMTO-ST) allows us to organize the joint supervision of Lenders's PhD
8. Participation to the European Hydromel project on hybrid assembly, 2009
Development of new models and experimental set ups [106]

Except the first two projects, I contributed to the definition of the scientific program of these projects.

2.2.2 Organisation of scientific events

1. International workshop on hybrid assembly, ULB, March 12th 2009
2. Workshop on Grand Challenges on Microrobotics and Microassembly, in the conference Robotics : Science and Systems, Zurich, 25-27 June 2008, ETHZ
3. Special session " Microassembly " (in collaboration with Prof. M. Tichem, TU Delft), IEEE International Symposium on Assembly Manufacturing (ISAM'07), Ann Arbor, Michigan, 22-25 July 2007
4. Special session " Microassembly " (in collaboration with Prof. M. Tichem, TU Delft), IEEE International Symposium on Assembly and Task Planning (ISATP'05), Montréal, 19-21 July 2005
5. Workshop on micro-assembly: scaling laws, similitude and dimensional analysis (with Sandra Koelemeijer),EPFL, June 15th 2005
6. Seminar on micro-assembly with TU Delft, ULB, June 3rd 2004

2.3 Students supervision (in French)

2.3.1 Internships

1. Raphaël HAMELRIJCKX, Conception assistée par ordinateurs: création d'une bibliothèque de composants pour engins de levage, société SAERENS (2007-2008)
2. Laurence GEBHART, société VOLCANO (2006-2007)
3. Sven DE ROECK, ENDOSTENT: a novel Drug Eluting Stent Design, société MEDPOLE (2006-2007)

2.3.2 Masters in engineering science

1. Année académique 2009-2010
 - Xavier GIRAUD, Conception et réalisation d'un dispositif pour l'application de patches de micro-aiguilles pour l'injection transdermique sans douleur de médicaments
2. Année académique 2008-2009
 - Jeanne BOUTE, Conception et réalisation de la structure mécanique d'un robot de chirurgie téléopérée, en collaboration avec le Prof. M. Kinnaert
 - Quang CAO, Miniaturisation de muscles artificiels (Assistant : Aline De Greef)
 - Dorian STEVENS, Etude de systèmes d'alimentation microfluidique: application et influence sur l'électrospray (Assistant : Michel Pierobon)
 - Jean-Arnaud CHERVILLE, Manipulation de composants SMD par tension de surface. Etude et conception d'un préhenseur (en collaboration avec la société ISMECA)
 - Frédéric DENDAL, Conception et réalisation d'un contrôle de vision pour une station de micro-assemblage pour roulements à billes
 - Carsten ENGEL, Conception d'un capteur un axe pour un retour de force en endoscopie flexible, en collaboration avec le Prof. A. Delchambre et Nicolas Cauche
3. Année académique 2007-2008
 - Amaury DAMBOUR, Development and control of the rotational and linear motion of the highly versatile mechatronic support system for minimally invasive surgery, travail réalisé sous la supervision du Prof. Can (TU München)

- Nicolas GIELIS, Conception d'un robot de téléopération avec retour de force applicable à la chirurgie mini-invasive, en collaboration avec le Prof. M. Kinnaert
- Raphaël HAMELRIJCKX, Conception d'un robot de téléopération avec retour de force applicable à la chirurgie mini-invasive, en collaboration avec le Prof. M. Kinnaert
- Thomas HAINE, Développement et réalisation d'une transmission magnétique de faible puissance, en collaboration avec le Prof. J. Gijssels
- Christophe DIAKODIMITRIS, Développement et réalisation d'une transmission magnétique de faible puissance, en collaboration avec le Prof. J. Gijssels

4. Année académique 2006-2007

- Nadia TANOUTI, Outil d'évaluation d'options par différences finies via Matlab, en collaboration avec Alex Van Tuykom et Thierry Becker, Dexia
- Michel PIEROBON, Etude expérimentale d'un électrospray, en collaboration avec Pierre Mathys
- Nicolas BASTIN, Réalisation d'un système de mesure de déflexion de poutre AFM à l'aide d'un laser réfléchi sur une photodiode (Assistant : Alexandre Chau), en collaboration avec Stéphane Régner, Paris 6-ISIS
- Sven DE ROECK, Feasibility study of a reservoir drug eluting stent concept, en collaboration avec Sophie Henry, Medpole
- Tarek OUAJIR GUELAI, Simulation et validation expérimentale du remplissage d'un tube par capillarité (Assistant : Jean-Baptiste Valsamis)
- Maxime DESAEDELEER, Etude et réalisation d'un dispositif d'alimentation en composants microtechniques (Assistant : Cyrille Lenders)
- Pham Quynh Lan Emilie NGUYEN, Instrumentation d'un banc de micromanipulation basée sur la préhension capillaire (Assistant : Jean-Baptiste Valsamis)

5. Année académique 2005-2006

- Jonathan GUTT, Etude de l'électromouillage en micromanipulation.

6. Année académique 2004-2005

- Bart DESLOVERE, Reconception d'un cadre de stéréotaxie utilisé chez le rat, en collaboration avec le Docteur Mario Manto, Hôpital Erasme.

7. Année académique 2003-2004

- Antoine GOLDSCHMIDT, Optimisation d'un cadre de stéréotaxie utilisé chez le rat, en collaboration avec le Docteur Mario Manto, Hôpital Erasme.
- Maxime FRENNET, Conception et réalisation d'un axe de translation commandable en accélération, vitesse et position : application à la manipulation par capillarité de petits composants.

8. Année académique 2002-2003

- Alexandre CHAU, Conception et réalisation d'un système de guidage flexible en rotation de type col circulaire (en collaboration avec le Prof. Ph. Bouillard)
- Vincent VANDAELE, Conception et réalisation d'un système de guidage flexible en translation de type spider (en collaboration avec le Prof. Ph. Bouillard)
- Tanguy MERTENS, Conception d'une pince d'endoscopie digestive (en collaboration avec le Prof. Ph. Bouillard)
- Olivier DIEU, Conception et réalisation d'une station de micromanipulation (en collaboration avec le Prof. P. Mathys)
- Mahé BURY, Conception et réalisation d'un mécanisme de blocage d'un système de positionnement de grande précision

9. Année académique 2001-2002

- Kevin ROBINSON, Etude, miniaturisation et contrôle d'un translateur piézoélectrique (en collaboration avec le Prof. P. Mathys)
- Olivier LEURQUIN, Conception et réalisation d'une table de micropositionnement à deux degrés de liberté
- Jonathan LEMBERGER, Conception et réalisation d'une table de micropositionnement à trois degrés de liberté (I) (en collaboration avec le Prof. P. Mathys)
- Jean-David THIEBAUT, Conception et réalisation d'une table de micropositionnement à trois degrés de liberté (II) (en collaboration avec le Prof. P. Mathys)
- Pierre LETIER, Etude des forces dues aux liquides et modélisation dynamique de microsystèmes
- Cyrille LENDERS, Etude des forces électrostatiques et modélisation dynamique de microsystèmes

10. Année académique 2000-2001

- Christine PAYEN, Conception et réalisation d'une micromachine rampante à l'aide d'alliage à mémoire de forme

- Ariana VALENTINI, Conception et réalisation d'un micro-actuateur piézo-électrique
- Vincent CROQUET, Etude théorique et réalisation d'une micromachine de préhension

2.3.3 MD in engineering sciences (DEA)

1. Michel PIEROBON, Etude de l'électrospray (2008-2009)
2. Nicolas BASTIN, Outils électrostatiques pour la micromanipulation (2007-2008)
3. Cyrille LENDERS, Etude de dispositifs anti-retour utilisés en microfluidique (2005-2006)
4. Aline DEGREEF, Etude d'un actionneur à structure flexible et gonflable (2005-2006)
5. Marion SAUSSE-LHERNOULD, Modélisation des forces électrostatiques pour le micro-assemblage (2004-2005)
6. Vincent VANDAELE, Contactless handling for microassembly (2003-2004)
7. Alexandre CHAU, Modelling of capillary condensation applied to microassembly (2003-2004)

2.3.4 PhD works

1. Alexandre CHAU, Theoretical and experimental study of capillary condensation and its possible application in micro-assembly, 11/12/2007, co-supervision with Prof. A. Delchambre (supervision: 90%)
2. Vincent VANDAELE, Contactless handling for micro-assembly : acoustic levitation, 21/02/2008, co-supervision with Prof. A. Delchambre (supervision: 90%)
3. Marion SAUSSE-LHERNOULD, Theoretical and experimental study of electrostatic forces applied to micromanipulation : influence of surface topography, 28/11/2008, co-supervision with Prof. A. Delchambre and Prof. S. Régnier (supervision: 50%)
4. Jean-Baptiste VALSAMIS, Liquid bridge dynamics, 31/05/2010 (supervision: 90%)
5. (**Ongoing**) Cyrille LENDERS, Fluid/Solid interaction in micromechanics: Use of Surface Tension in Immersed Microsystems, co-supervision with Prof Nicolas CHAILLET and Michaël GAUTHIER (FEMTO-ST), foressen in 2010 (supervision: 50%)

6. (**Ongoing**) Aline DE GREEF, Flexible fluidic actuators, foreseen in 2010 (supervision: 70%)

2.4 Administrative tasks, teaching and contacts with industry

2.4.1 Administrative tasks

Popularization activities

- Fêtes de la science, Lille, October 2007: demonstration of a stick-slip nano-actuator and an acoustical levitator;
- Exhibition 'La physique dans la bande dessinée', Parentville, January 2008: acoustical levitation;

Scientific and administrative responsibilities

- Student member of the direction board of ULB (1995-1997);
- Scientific member of the direction board of ULB (2001-2003);
- Member of several Faculty committees;
- Member of the research committee of ULB;
- Scientific review for *Langmuir*, *Nanotechnology*, *IEEE Transactions on Robotics*, *IEEE/ASME Journal of Microelectromechanical Systems*, *Journal of Fluid Engineering*, *Journal of Micromechanics and Microengineering*, *Micro-Nano-Letters*;
- Scientific review for the conferences IROS, ICRA, IEEE ISAM, International Precision Assembly Seminar (IPAS)
- Scientific review for research calls ANR (2006 and 2007, France) and Microned (NL)
- Member of the technical committee on Micro/NanoRobotics and Automation IEEE, of the international advisory committee of IPAS conference, of the program committee of IEEE International Symposium on Assembly and Manufacturing
- Associate editor T-ASE (Transaction on Automation Science and Engineering)
- PhD juries:
 1. 2007
 - (a) Alexandre Chau, December 11th, Université libre de Bruxelles
 2. 2008
 - (a) Vincent Vandaele, February, Université libre de Bruxelles

- (b) Julien Vitard, July, Université Pierre et Marie Curie (Prof. Stéphane Régnier)
 - (c) Carlo Bagnera, March 28th, Université libre de Bruxelles (Prof. Gérard Degrez)
 - (d) Marion Sausse-Lhernould, November 28th, Université libre de Bruxelles
 - (e) Peter Berke, December 18th, Université libre de Bruxelles (Prof. Thierry Massart)
3. 2009
- (a) Frank Seigneur, February, Ecole Polytechnique Fédérale de Lausanne (Prof; J. Jacot)
 - (b) Enrico Tam, December 3rd, Université libre de Bruxelles (Prof. M.-P. Delplancke)
4. 2010
- (a) Emir Vela, May 28st, Université Pierre et Marie Curie (Prof. Stéphane Régnier)
 - (b) Jean-Baptiste Valsamis, May 31st, Université libre de Bruxelles
 - (c) Massimo Mastrangeli, Katholieke Universiteit Leuven (Prof. J.-P. Celis)

2.4.2 Teaching activities

As a research assistant between 2000 and 2004, I used to teach exercises during 300 h/year (Mechanics and Technologies)

As assistant professor (since 2005), I used to teach a lecture on microtechniques components (24h), micromanufacturing techniques (24h), machines-tools (12h), concurrent engineering (12h), kinematics and dynamics of machines (24h), applied mechanics (36h). I gave a lecture on machine elements in the university of Lubumbashi (RD Congo).

I supervised 2 BA2 projects, 18 MA1 projects, 36+6 master thesis and 4 PhDs (2 other ones are under preparation).

2.4.3 Industrial experience

I worked between September 2nd 1998 and September 10th 1999 for two French IT companies, Trasys-France (Paris) and Aricie (Lyon).

2.5 Publications

An overview of my publications¹ is given in tables 2.1 (page 16) and 2.2 (page 17). More particularly, here is the detail of the publications related to my own

¹<http://beams.ulb.ac.be/beams/staff/all/view/plambert.html>

PhD work: 3 journals in international peer-reviewed journals [111, 101, 100] and 6 publications in proceedings of international conference (2 of which selected on entire paper [104, 99], 3 of which accepted on abstract [103, 97, 113] and 1 without selection [98]).

The list of oral communications is presented in table 2.2. Scientific seminars are listed here below.

1. Scaling Effects in Microfluidics and Its Application to Micro-Assembly, séminaire présenté à l'université Ritsumeikan (Kyoto, 17 avril 2009)
2. Surface Tension in Microsystems - The Case Study of Micro-Assembly, séminaire présenté au LIMMS (Tokyo, 9 avril 2009)
3. Fluidic Assembly and Capillary Forces - Modeling, Experiments and Case Studies, séminaire présenté au sein de la conférence Smart Systems Integration à Bruxelles, le 11 mars 2009
4. Utilisation de la tension de surface dans les microsystemes, séminaire présenté au CSEM (septembre 2008)
5. Utilisation de la tension de surface dans les microsystemes, séminaire présenté à l'EPFL (mai 2008)
6. Utilisation de la tension de surface dans les microsystemes, séminaire présenté à l'université de Pise (mars 2008)
7. Utilisation de la tension de surface dans les microsystemes, séminaire présenté au laboratoire FEMTO-ST (juin 2007)
8. Utilisation de la tension de surface dans les microsystemes, séminaire présenté à l'Institut des Systemes Intelligents et Robotique-Paris VI (décembre 2007)
9. Préhension à tension de surface, Laboratoire de robotique de Paris (S. Régnier) en janvier 2006
10. Préhension à tension de surface, TU Delft (Prof. Marcel Tichem), février 2007;
11. Préhenseur à tension de surface, Séminaire " Microfactory ", Institut de Robotique et de Production, EPFL, le 7 novembre 2005;
12. Introduction à l'analyse dimensionnelle, Séminaire de micro-assemblage portant sur les effets d'échelles, les lois de similitude et l'analyse dimensionnelle, EPFL, 15 juin 2005 [102] et [26, 126] ;
13. Capillary forces : fluidic manipulation of mesoscale components, Workshop on " Fluidic manipulation and self-assembly of mesoscale components ", organisé par le Prof. J.-M. Breguet et A. Rida, Laboratoire des Systemes Robotiques, EPFL, 11 et 12 mai 2005;

14. Etude des forces de capillarité pour le micro-assemblage, séminaire interne, Laboratoire de Production Microtechnique, EPFL (Prof. J. Jacot), 22 février 2005
15. A Contribution to Microassembly: a Study of Capillary Forces as a gripping Principle, communication effectuée au sein du Service de Chimie-Physique, ULB (P. Colinet), 31 janvier 2005
16. Simulation of an Handling Task Based on Capillary Forces, Poster présenté à la 2nd European Postgraduate Summer School in Precision Assembly, Eindhoven, June 30 - July 3
17. Forces Acting in Micro-Assembly, Communication lors du séminaire d'assemblage de précision organisé à l'EPFL, 3 février 2003.

Publication types	Number	Names
Internat. journals	16	RCIM [111], Precision Engineering [185, 67], Assembly Automation [101], Langmuir [100, 96], $J\mu M$ [107], JMM [108, 134], MSMSE [28], Appl. Surf.Sc. [125, 176], JAST [122, 29, 3], Microfluidics and Nanofluidics [106]
Nat. journals	None	
Miscellaneous		
- didactics	2	Cours de mécanique appliquée BA1, 136p [90] Recueil d'exercices (mécanique rationnelle) [160]
- scientific reports	2	Analyse dimensionnelle, EPFL (49p) Etude des antichocs, Association suisse de recherche horlogère (44p)
Books chapters		
Monography	22	Capillary forces in microassembly, Springer [92] (22 chapters)
Other books	3	La microrobotique: applications à la micromanipulation, Hermès, 3 chapters, [2]
	(2)	Microrobotic Microassembly, John Wiley and Sons, 2 chapters (to be published in 2010)
	(3)	Microrobotics: applications to micromanipulation, translation of eponymous book in French, 3 chapters (to be published in 2010)
Proc. of internat. conf.		
- full paper acceptance	10	IEEE ISATP [104, 99, 179], IEEE MechRob [61], IEEE/ASME Int. Conf. on Adv.Int. Manufact. [124], IEEE ISAM [189, 27, 66], IEEE EMBS [65], IROS [117]
- abstract acceptance	12	FAIM[103], MINIT [24, 186], IPAS [97, 113, 109, 118], SSI [93], μ Mech. Europe [25], CIRP ISAS [112], Euspén [123], EAC [128]
- no selection	1	Int. Conf. Int. Manipulation and Grasping [98]
Proc. of nat. conf.		
- abstract acceptance	1	Nat. Cong. on Th. and Appl. Mech [110]

Table 2.1: List of publications

Publications type	Number	Publication names
Invited speaker	2	RSS [94], IARP [105]
Conferences without proceedings (abstract acceptance)		
- international	8	IWMF [23, 127, 168, 182, 188], IROS [7], Congrès de l'Association Int. de Pédagogie Universitaire AIPU [162], Smart Systems Integration [93]
- national	None	
Other talks	17	See the list in the text

Table 2.2: List of talks

Chapter 3

Context and scientific positioning

This chapter presents the milestones of my research and its international positioning (section 3.1), my scientific strategy (section 3.2), my PhD work (section 3.3) and my postdoctoral research (either personal or supervised research) in section 3.4. Collaborations are presented in section 3.5.

3.1 Milestones and international positioning

At the very beginning of my PhD under the supervision of Prof. Alain Delchambre (Université libre de Bruxelles), we decided to address downscaling issues in micro-assembly from the point of view of modeling and understanding the dominant forces at the submillimetric scale (electrostatic, surface tension and adhesion effects were candidates).

The question of micro-assembly at that time was at the intersection between three disciplines: industrial assembly, microtechnologies and adhesion science.

Industrial assembly is indeed the natural perspective for micro-assembly developments. Thanks to the network of Prof. Alain Delchambre, I could quickly access to the European Thematic Network Assembly Net, including academic (Svetan Ratchev in Nottingham, Mauro Onori in Stockholm, Marcel Tichem in Delft, Jacques Jacot in Lausanne, Nicolas Chaillet in Besançon...) and industrial (Philips, Zanussi...) leaders in the field.

Research in micro-assembly had already started and used to focus on miniaturized technological developments, mainly led in Europe by German (Fraunhofer Institute IPA in Stuttgart¹, University of Oldenburg) and Swiss teams (EPFL in Lausanne, ETHZ in Zürich, CSEM in Neuchâtel). Microrobotics was focused on micro-actuation using the properties of so-called smart materials (shape memory alloys, piezo-electric transducers...) or adequate principles to combine high resolution (nm) and large range (cm) such as the accumulation principle of stick-slip actuators developed by Breguet [17]. There was also a worldwide trend toward microfactories (MEL laboratory and Olympus in Japan, Fraunhofer IPA and IPT in

¹This team was at the source of a German norm for microproducts

Germany, the Laboratoire d'Automatique de Besançon in France, LSRO in EPFL, Microdynamic Systems Laboratory in Carnegie Melon).

The third foundation of this work was adhesion science, as scientific background which quickly turned out to be of the utmost importance in the development of research and industrial demonstrators. Indeed, adhesion science and more generally scaling laws are the key to the physics governing microsystems, as early mentioned by Fearing [58]. Main contributors to this field are undoubtedly J.N. Israelachvili [74] and B. Bhushan [8].

The first milestone of my research was therefore to observe the dominance of surface tension effects at scales smaller than a few millimeters. This limit is known as the capillary length L_C , which makes the trade off between gravity and surface tension effects:

$$L_C = \sqrt{\frac{\gamma}{\rho g}} (\approx 2.7 \text{ mm for water}) \quad (3.1)$$

where γ is the surface tension of the liquid (Nm^{-1}), ρ is its density and $g = 9.81 \text{ ms}^{-2}$. Moreover, as it can be observed from dimensions, capillary forces linearly depend on length scale ($F \div \gamma\ell$), leading to the dominance of surface tension effects over other physical effects at small scale. Consequently, studying capillary forces was a good starting point to enter microworld since it was a dominant effect which could be studied just below the millimeter, i.e. at a scale sufficiently large to be addressed without dedicated experimental material.

The second milestone is more related to the strategies found in literature to tackle adhesive problems in pick and place or manipulation of small components:

1. adhesion can be reduced: working in ionized environment to decrease electrostatic effects, in dry or liquid environment to avoid capillary forces ...
2. adhesion can be overcome: gluing a microcomponent on its final location may overcome adhesion between the component and the picking head (this is done when placing SMD² components on a pad filled with solder paste);
3. adhesion can be avoided by handling components without contact, as the wafers displaced by traveling ultrasonic waves;
4. adhesion can be used as a gripping principle: this latter approach requires to master the chosen adhesive principle.

It was decided to investigate the fourth strategy in my PhD, focusing on apparently dominant surface tension effects³. Focus was then put on 'capillary forces as a gripping principle', leading to capillary forces modeling and measurements in my PhD (2000-2004) and gripper development within the framework of my post doctorate research under the supervision of Prof. Jacques Jacot (EPFL, 2005). This

²Surface Mounted Device: flat electronic component

³In supervised research started afterwards, other aspects were considered such as the electrostatic adhesion (Marion Sausse-Lhernould, [121]) or acoustic levitation (Vincent Vandaele, [184])

initial work was actually focused on axial capillary forces at equilibrium, at the submillimetric scale.

A third milestone was to broaden this initial focus by extending it in three other directions:

1. capillary condensation, i.e. capillary forces down to the nanoscale (Chau'PhD, 2003-2007);
2. lateral capillary forces, which are of interest in hybrid and self-assembly (EU Hydromel project, 2009);
3. dynamics of capillary forces, both for axial (Valsamis's PhD, 2006-2010) and lateral forces ([106] recently published);

These developments can be considered as building boxes to the concept of fluidic joint, i.e. to the mechanical description of a liquid bridge linking two solids as a mechanical joint with 6 degrees-of-freedom (figure 3.1). The static study outputs the stiffness and the dynamic study lead to the damping coefficients.

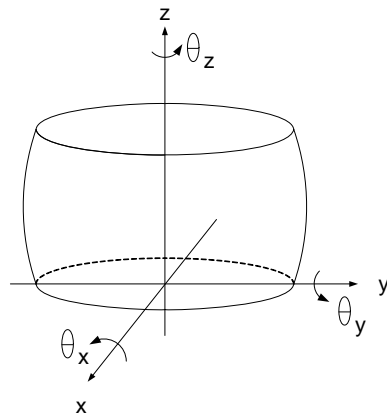


Figure 3.1: Liquid joint with 6 degrees-of-freedom

A fourth step was the introduction of an additional physics in these models: combining gas compressibility and surface tension effects introduces compliance in microsystems (Lenders's PhD, 2005-2010). As recalled in section 4.4.2, this allows to address (1) the understanding of the effects of microbubbles in microfluidic systems, (2) to compensate the lack of compliance due to the use of brittle materials instead of ductile ones and (3) to open miniaturization perspectives to flexible fluidic actuators. Within this perspective, we are working with Cyrille Lenders on the modeling, characterization and development of a kind of miniaturized Stewart platform, or at least to a submillimetric robotic platform with fluidic actuators introducing 6 passive degrees of freedom and 3 active ones, tuning the attitude of the platform along z , θ_x and θ_y .

As it can be seen, we started with the most theoretical aspects somehow related to adhesion: modeling of capillary forces. This choice was done because the research equipment could not allow to compete in terms of research demonstrators. Nowadays, we try to address these aspects.

3.2 Scientific positioning

As briefly introduced, my research focuses on modeling, characterizing and applying surface tension effects in microsystems. These three research levels are represented in figure 3.2. Applicative domains are manifold: microsystems and microtechniques, microrobotics and micro-assembly, drug delivery and microfluidics...

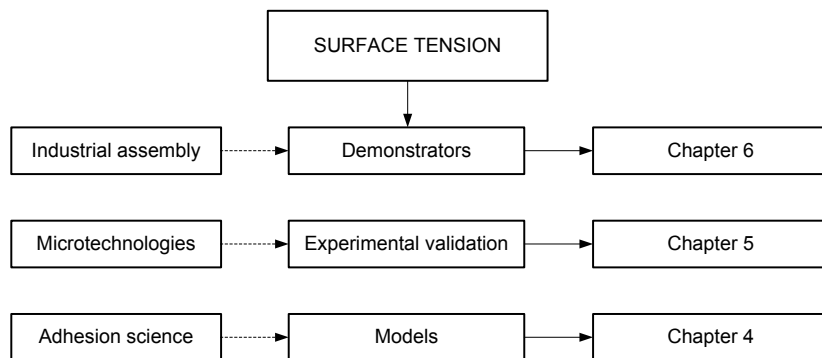


Figure 3.2: Three levels of research: applications, demonstrators and validation, fundamental background. These levels which are inspired by industrial assembly, microtechnologies and adhesion science respectively feed chapters 4, 5 and 6 of this work.

These levels can be read from this document, falling into related chapters: chapter 4 presents my contributions to capillary forces modeling, chapter 5 describes the design of several experimental testbeds and related results, and chapter 6 describes the applications and demonstrators which have been addressed and developed in my research.

The source feeding these chapters are the results obtained by my PhD students (capillary condensation, dynamics of capillary forces, capillary forces acting on mechanical structures) and by my own publications (see for example the monograph published by Springer on "Capillary forces in micro-assembly" [92]).

The models presented in this work find their far origin in the theory of capillary effects⁴ which has existed for two centuries (Pierre-Simon Laplace, 1805 [45]): it used to focus essentially on the description of capillary filling of small gaps with liquids.

⁴Théorie des actions capillaires

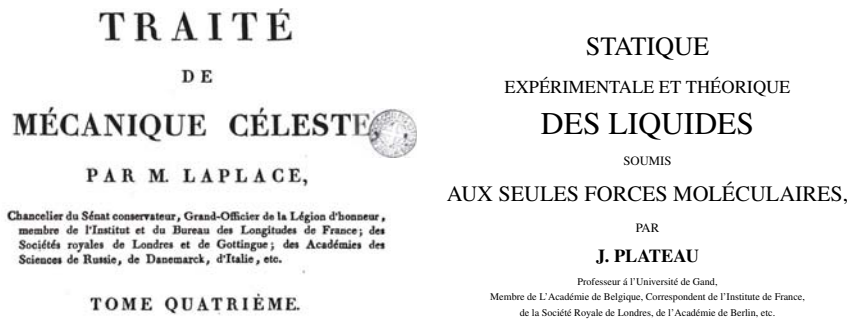


Figure 3.3: Pierre-Simon Laplace in 1805 [45] and Joseph Plateau in 1873 [153] set the basis for the study of capillary phenomena. A third famous precursor is Jurin in 1718 [80]

Nevertheless, Laplace went beyond phenomenological description and already wrote down the famous Laplace equation (see equation 4.24) introducing the concept of surface tension from geometry (i.e. curvature) and mechanics (i.e. pressure). A few decades later, in 1873, Joseph Plateau (Professor at the University of Ghent, Belgium) described the equilibrium shape of droplets immersed in a bath with identical density [153]. These precursor works were restricted to equilibrium, such as the famous Jurin’s law [80] giving the rising height of a liquid in a thin capillary. Today, these effects can be simulated with powerful finite elements software such as Surface Evolver (section 4.2.2). As soon as 1921, Washburn [192] introduced an equation to model the dynamics of capillary rise. In 1936, Wenzel [194] described the effect of roughness of wettability but dynamic contact angles were not studied before the end of XXth century by Voinov [190], Tanner [178] and Jiang [77]. Dynamic contact angles have been under study these last years [15, 41, 191].

With the introduction of numerical simulation and high speed cameras, dynamics has been more studied but still focusing on the shape of liquid bridges: Orr presented in 1975 a numerical simulation to compute the shape of liquid bridges at equilibrium [144], Edgerton published in 1937 the first results on the dynamics of drop formation [51]. Experimental results on liquid bridges dynamics was only published at the end of XXth century [146]. Beside the shape of the liquid bridges, another question is to study how these bridges acts on solids, i.e. provide forces which can be used in mechanical systems. Most famous model is probably Israelachvili’s equation (ref) describing the capillary force linking a flat plane and a sphere. Based on this background, we clarified some aspects of capillary forces calculation, extended the modeling from static to dynamic behaviors, and from axial to radial forces. We led a study on capillary condensation to study these capillary forces at the nanoscale, and we have recently introduced the combination of surface tension and gas compliances.

More generally, we contributed to studying adhesion within the framework

of micro-assembly and packaging⁵. Traditionally, the microrobotic community - which applies pick-and-place know-how to downscaled applications - makes use of surface science adhesion and mechanical contact models, because downscaling laws require an adequate understanding of the physical background. This improves design, simulation, haptic feedback and automation of developed products. Since engineers are usually not familiar to the scale effects, good models are mandatory to ensure reliability, *sine qua non* condition for industrial perspectives of our research developments. To this aim, we could show the importance of roughness on electrostatic adhesion (Marion Sausse-Lhernould's PhD) and get extend the capillary forces models developed during my PhD to the nanoscale, addressing the well-known capillary condensation problem, acknowledged as a major source of stiction in MEMS (Alexandre Chau's PhD).

From the experimental point of view, we developed a series of force measurement set ups well adapted to the characterization of industrial microcomponents or to the experimental validation of forces models. For example, we recently published results on lateral dynamics of liquid bridges, which can serve as a basis toward design of flip-chip applications [106].

As it will be detailed in the perspectives of this work (see chapter 7), future work will address slightly different (and however related) questions such as open microfluidics (i.e. fluidics on surfaces vs fluidics in microchannels), and drug delivery.

3.3 PhD summary and related publications

I defended my PhD entitled: "A Contribution to Microassembly: a Study of Capillary Forces as a gripping Principle" on December 10th 2004. The general background of this work is the trend to the miniaturization of product and of their production tools (including assembly). Due to scaling laws, assembly of small components is perturbed by so-called surface forces such as capillary forces. The latter forces are generated by the liquid bridge linking the gripper and the component (see figure 3.4). They are usually neglected in usual macroscale assembly, which is ruled by gravity.

The original approach followed in my PhD consists in taking advantage of these forces, by using them as a gripping principle for the handling of microcomponents, i.e. components with a size ranging from a few tens of microns up to a few millimeters. This dissertation proposes to address design problems arising from this choice: what are the advantages of using these forces? How do they 'work'? Are they large enough to pick up small components? How can they be overcome in order to achieve the releasing task? What is the role of surface tension? Is the choice of materials relevant? How can the gripper be optimized? Throughout this work, the reader will find a review of the existing gripping principles, elements to

⁵ which includes a large variety of topics such as designing, manufacturing, feeding, positioning, joining, testing

model capillary forces and the description of the simulation and the experimental test bench built by the author to study the design parameters. The results presented in this dissertation mainly cover two aspects: what are the design rules in order to maximize the capillary forces (picking task issue) and how to choose a handling strategy allowing to release the component (releasing task issue)?

Since the laboratory started this activity with my PhD, I decided to focus on theoretical aspects, postponing applicative developments to my post doc in EPFL (2005). Nevertheless, my participation to the meetings of the European Thematic Network Assembly-Net pushed me to think these development toward the applicative framework of microassembly and micromanipulation. I entered the domain of microrobotics thanks to a participation to the AMOS project⁶ (Analyse, MODélisation at Simulation du micromonde), led by Prof. S. Régnier.

Beside the main focus on capillary forces, this period was also the opportunity to study flexible guiding (notch hinges [24], flat springs [186]), actuation (stick-slip [103, 111], shape memory alloys), and miniaturized mechanisms (insulin micropump, stereotaxy frame). These projects have been achieved with master students and funding from the Région wallonne, from April 2001 to March 2004.

My PhD work led to 2 publications in journals [100, 101] and 6 contributions to international conferences [61, 97, 104, 113, 98, 99].

3.4 Post doctoral research

Post doctoral research was achieved within the framework of two post docs (EPFL in 2005, University Pierre and Marie Curie in 2006), an invitation as Hosted Profes-

⁶Action spécifique

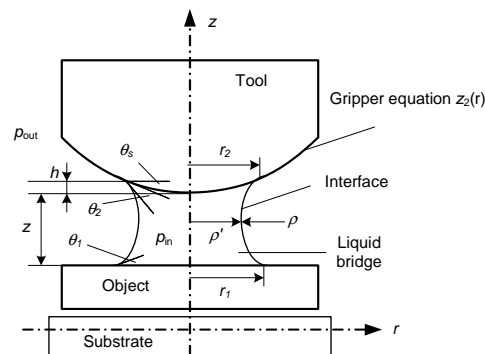


Figure 3.4: Example of liquid bridge (also called meniscus) linking a gripper and a component: capillary forces developed by this meniscus depend on the gap between both solids (z), surface tension γ , contact angles θ_1 et θ_2 , volume of liquid and geometries ($z_2(r)$). These forces originate from pressure difference $p_{in} - p_{out}$ across the liquid-gas interface, due to curvature radii ρ et ρ' of this meniscus.

sor⁷ (EPFL, 2008) and a participation to the European Hydromel project on hybrid assembly (FEMTO-ST, 2009). Parallely, I have developed supervised research, which led to 4 PhD thesis (2 additional students are finishing).

3.4.1 Personal research

Post docs (EPFL 2005 and UPMC 2006)

1. I worked at EPFL under the supervision of Prof. Jacques Jacot (Laboratoire de production microtechnique) from 01/02/05 to 30/11/05, following three objectives: (1) design and test a gripper prototype using surface tension as a gripping principle; (2) apply dimensional analysis to modeling in micro-assembly; (3) learn about micromanufacturing.

Grippers have been produced to pick and place the balls of watch ball bearings: this validated my capillary forces models and proofed the feasibility of surface tension based pick and place. An example of pick and place sequence can be seen in figure 3.5 [108]. This principle was also applied to the manipulation of small light sensors ($100\mu\text{m} \times 100\mu\text{m} \times 50\mu\text{m}$) [168].

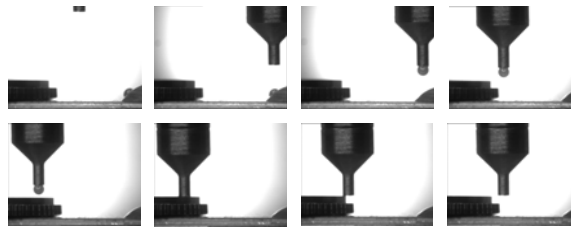


Figure 3.5: Placement of $\text{Ø}500 \mu\text{m}$ balls in a watch ball bearing using capillary forces: the one-finger gripper is first positioned on top of the ball, before picking, displacing and positioning it inside the right location in the cage of the bearing. Release is achieved by radial translation of the gripper.

The work on dimensional analysis led to the organization of a workshop on scaling laws, similitude and dimensional analysis (Lausanne, June 15th 2005), [102, 26, 126].

This first postdoc led to 1 publication in *Journal of Micromechanics and Microengineering* [108], 2 communications in international conferences [109, 112] and 1 communication in the National Congress on Theoretical and Applied Mechanics [110].

2. I worked at Université Pierre et Marie Curie from January 2006 to July 2006, under the supervision of Prof. S. Régnier. I developed new models to describe the adhesion of carbon nanotubes due to capillary forces, which served as a first building block toward a nanomanipulation platform with haptic feedback. I acquired expertise in design of nanoforces measurement.

⁷Hôte académique

This second post doc led to 2 publications in journals [107, 96] and 4 communications in international conferences [105, 94, 188, 189].

Invited professor (EPFL, 2008)

From April to October 2008 I was invited by Prof. Jacques Jacot to work on a new test bed devoted to the experimental characterization of watch components. This case study is described in section 5.6.

European project Hydromel (FEMTO-ST, 2009)

In 2009, I was asked by FEMTO-ST to contribute to the European Hydromel project on hybrid assembly. I developed lateral capillary forces models, to describe the dynamics of self-centering of small components. This led to 1 publication in *Microfluidics and Nanofluidics* [106]

3.4.2 Supervised research

Since May 2006 I have managed the research group in microtechnologies of the Bio-Electro- And Mechanical Systems (BEAMS) of Université libre de Bruxelles. We have studied several problems at the intersection between microrobotics, micro-assembly, surface science and surface microfluidics. The connecting thread is surface tension, from the points of view of modeling and measuring. These researches have been led targeting two domains: micro-assembly and biomedical application. A list of finished and ongoing PhDs is given here below (see also figure 3.6). The last project started in 2009 with a post doctoral researcher.

1. Alexandre Chau (PhD defended on December 11th 2007, supervision: 90%) – **Theoretical and experimental study on capillary condensation and its possible application in micromanipulation** : numerical and experimental study of parameters ruling capillary condensation: materials, geometries, environment. Main results are an experimental validation of the so-called Kelvin equation 'équation dite de Kelvin at nanoscale (see figure 3.7), an exhaustive parametric study achieved with the developed numerical model and proposals toward capillary force controlling for micromanipulation of components. This work is of interest for atomic force microscopy and clean room micromanufacturing (stiction problems). This work was funded by the financement FRIA⁸;
2. Vincent Vandaele (PhD defended in February 2008, supervision: 90%) – **Contactless handling for microassembly : acoustic levitation** : numerical and experimental study of parameters ruling acoustic levitation: geometrical and mechanical parameters influence standing waves between two parallel

⁸FNRS: Fonds pour la formation à la Recherche dans l'Agriculture et l'Industrie (Belgian research funds)

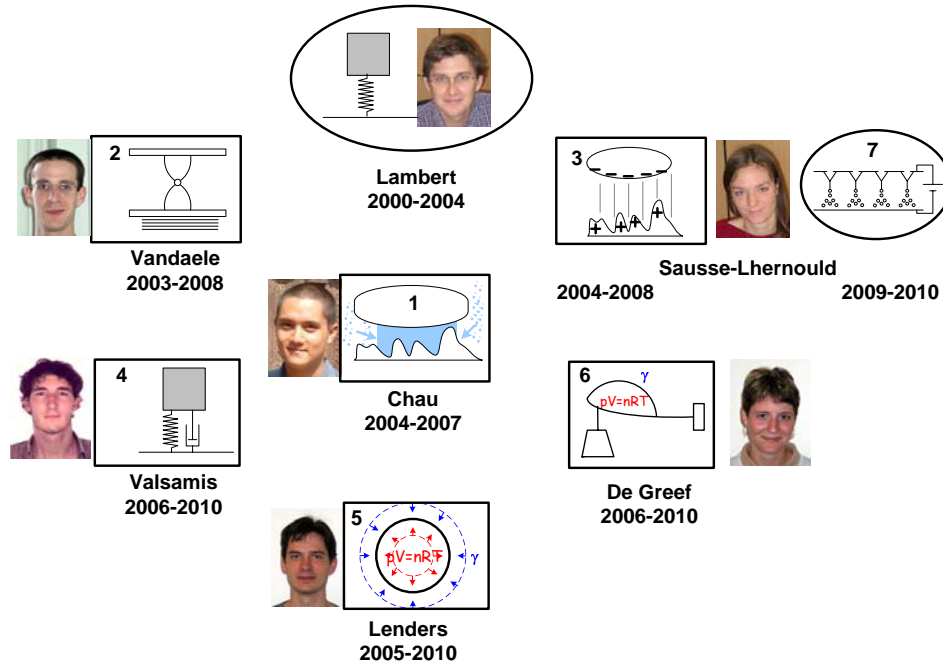


Figure 3.6: Overview of my team in Université libre de Bruxelles

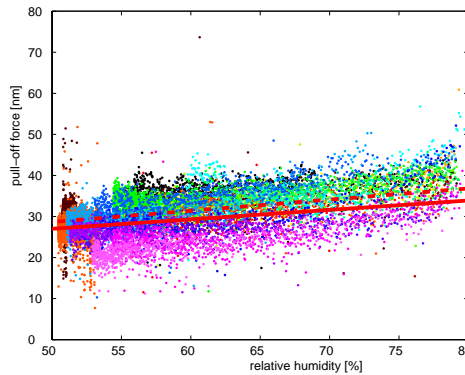


Figure 3.7: Comparison between experimental points and simulation results (solid red line). The dashed red line indicates the least square regression of the experimental cloud.

plates. Levitation is a way to avoid adhesion between microcomponents (see figure 3.8). This tool allows to study crystals growth or liquid droplets in levitation, i.e. without the influence of walls. This work was funded by the financement FRIA;

3. Marion Sausse-Lhernould (PhD defended on November 28th 2008, supervision: 50%, joint supervision with Prof. Stéphane Régnier de l'Université



Figure 3.8: Millimetric part hold in the central node of a 40kHz acoustic wave (13mm between plates, i.e. 3 nodes)

Pierre et Marie Curie) – **Theoretical and experimental study of electrostatic forces applied to micromanipulation : influence of surface topography** : this work studied the influence of geometry (scale 10 – 100 μm) and surface roughness (scale 10 – 100nm) on electrostatic forces in order to better control picking (avoid repulsive effects) and releasing (avoid adhesion) of microcomponents. Figure 3.9 presents the force measurement test bed developed for this PhD and that of Alexandre Chau. This work was funded by an ARC ⁹ (Belgian funding);

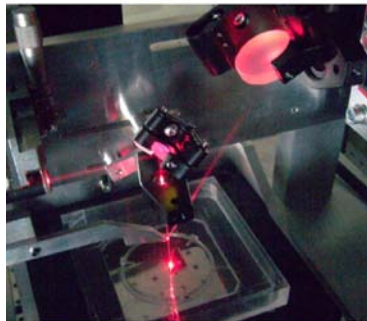


Figure 3.9: Nanoforce measurement set up developed for capillary condensation and electrostatic adhesion studies

4. Jean-Baptiste Valsamis (PhD defended on May 10th 2010, supervision: 90%)
 - **A study of liquid bridges dynamics: an application to micro-assembly:** theoretical and experimental study of parameters ruling the efficiency of a pick and place using capillary forces. More particularly, the study of cycle times is of interest to industrial partners targeting the future assembly of

⁹action de recherche concertée

miniaturized SMD¹⁰ components. This work was funded by the financement FRIA;

5. Cyrille Lenders (PhD to defend in 2010, supervision 50%, joint supervision with Prof. Nicolas Chaillet and Dr Michaël Gauthier, FEMTO-ST)– **Fluid/Solid interaction in micromechanics: Use of Surface Tension in Immersed Microsystems:** this work study the introduction of compliance in microsystems, using surface tension and gas compressibility. This can be applied to develop forces sensors or actuators of interest to microrobotics (see for example a miniaturized robotic platform in figure 3.10). This work has been funded by the Université libre de Bruxelles (research assistant);



Figure 3.10: Picture of a millimetric platform actuated by three fluid legs, i.e. gas bubbles in an immersed environment.

6. Aline De Greef (PhD to defend in 2010, supervision 50%, joint supervision with Prof. Alain Delchambre, Université libre de Bruxelles)– this work has studied a flexible fluidic actuator to be applied in minimal invasive surgery. According to the work of Prof. Konishi [87], this study targets the modeling and characterization of this kind of actuators, aiming at designing and controlling such actuators. This work has been funded by the FNRS (National Belgian Research Funds);

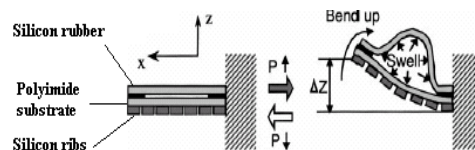


Figure 3.11: Example of flexible fluidic actuator (Konishi)

7. Marion Sausse-Lhernould has started a post doctoral project under my supervision aiming at developing multi-nozzle arrays for electrospray generation. This work has been funded as a First Postdoc project (Belgian funds)

¹⁰Surface Mounted Devices

3.5 Collaborations

A lot of collaborations are ongoing, leading to joint publications (see the map of my co-authors in figure 3.12, page 32), joint supervision of PhD students, organization of international scientific workshops (special sessions on micro-assembly in conferences IEEE ISAM et Robotics: Science and Systems, international workshop at the Université libre de Bruxelles on March 12th 2009).

Among all collaborations, let us cite FEMTO-ST (Prof. Nicolas Chaillet et Philippe Lutz, Dr Michaël Gauthier), ISIR (Institut des Systèmes Intelligents et Robotique de Paris, Prof. Stéphane Régnier), university of Pisa (Prof. Marco Santochi), Technische Universiteit Delft (Dr. Marcel Tichem), the Helsinki University of Technology (Quan Zhou).

A very strong collaboration has been led with EPFL (Prof. Jacques Jacot): (1) manufacturing of microgrippers in Lausanne; (2) lecture on design of experiments given at Université libre de Bruxelles by Prof. J.-M. Fürbringer; (3) invitation to work on the characterization of watch components.

Let us indicate that Marion Sausse-Lhernould's experiments have been successfully replicated in Lawrence Berkeley National Laboratory.

Finally, the PhD of J.-B. Valsamis has been supported by Assembléon, Dutch leader in manufacturing of assembly machines. Another industrial collaboration is also going on with a Swiss company in the field of microcomponents packaging. We also have strong contact with Belgian pharmaceutical industry.

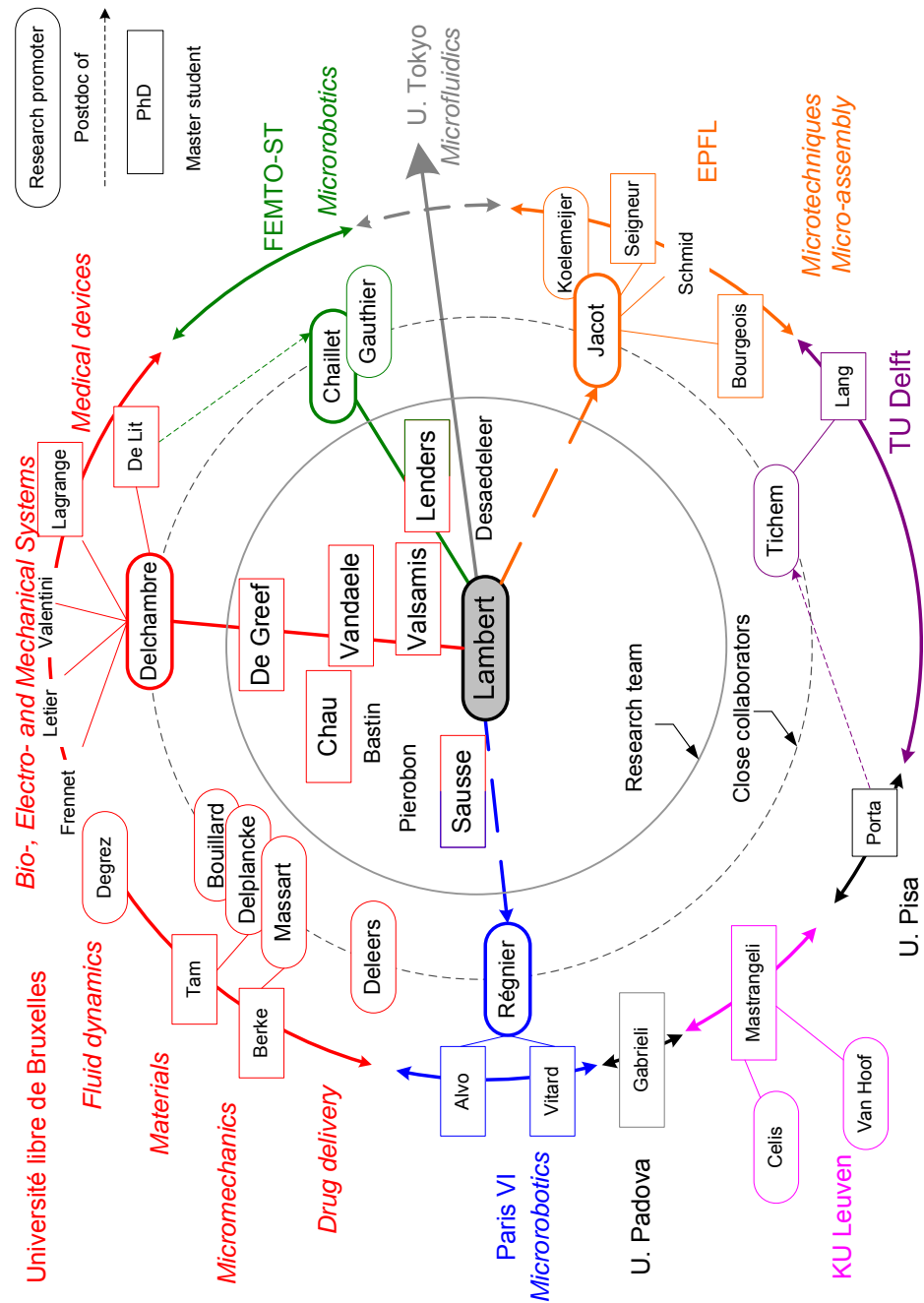


Figure 3.12: Map of my co-authors: researchers and students positioned close to my label have worked under my supervision, people located on the first dashed circle include my PhD and post doctoral supervisors or colleagues I work with in important research projects. People located on the external circle are other co-authors.

Chapter 4

Models

4.1 Introduction

The contributions of this chapter are illustrated in figure 4.1. The main developments concern the modeling of surface tension effects, in order to understand and predict the force exerted on solids by capillary bridges. As already mentioned in

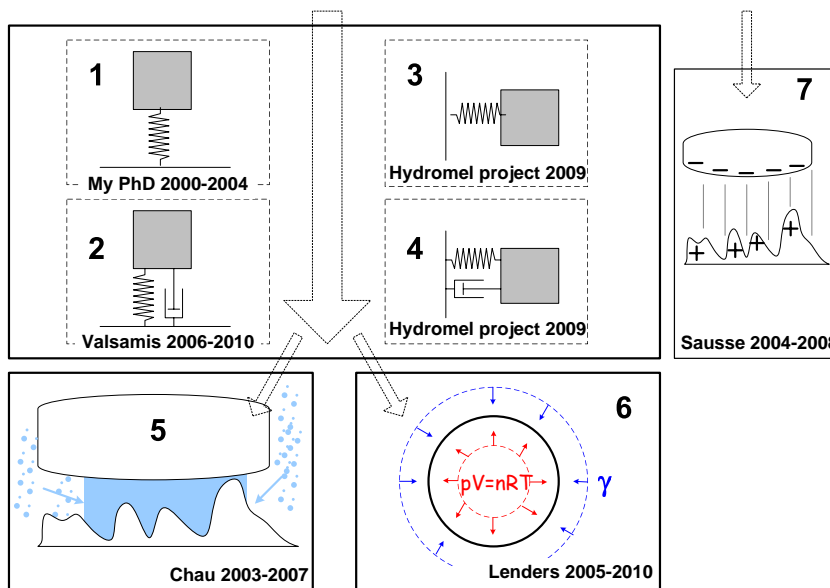


Figure 4.1: Models overview: the main track focuses on capillary forces (1-4), leading to additional work at nanoscale (capillary condensation in 5) and combining surface tension and gas compressibility (detail 6). Electrostatic adhesion of rough surfaces was also studied (7)

the introduction, these liquid bridges can be seen as mechanical joints with 6 degrees of freedom. This chapter focuses on axial and radial degrees of freedom,

i.e. on the forces developed along and perpendicular to the symmetry axis of the liquid bridges. Forces at equilibrium were studied first, but effort was also put on modeling their dynamics. Combining both criteria led to the study of static axial forces (see figure 4.2), dynamic axial forces, static lateral forces and dynamic lateral forces. Beside this main track, developments were extended toward nanoscale (capillary condensation in sketch 5 of figure 4.1), coupling with gas compressibility (6) and electrostatic adhesion of rough surfaces (7).

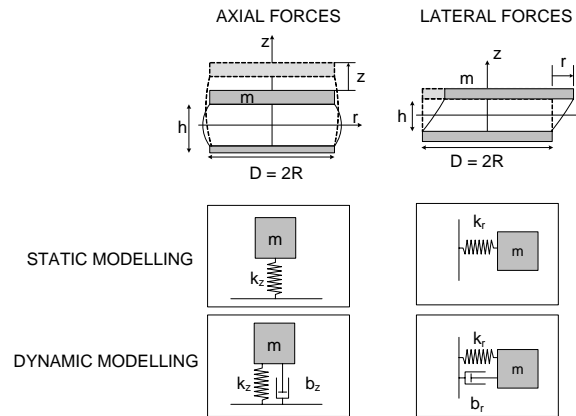


Figure 4.2: Capillary force models, combining two criteria: axial vs radial configurations and static vs. dynamic behaviors

As experimentally confirmed in chapter 5 (as shown in figure 5.2), the very first model of a phenomenon usually relies on its scaling law, acknowledging the linear dependence of capillary forces to the size of the set up, and more generally, the importance of dimensional analysis and scaling laws.

Nevertheless, targeting the design of devices using surface tension effects, it was useful to get a more detailed insight on the parameters ruling capillary forces. This was the starting point of models development. The axial capillary forces are of interest in all micromanipulation case studies, to know for example the amount of picking force in a microassembly application. At the nanoscale, the capillary force is an important contribution to adhesion, such as for example adhesion in atomic force microscopy or stiction in RF MEMS. The lateral capillary forces models are more dedicated to self-assembly problems or to the dynamics of components floating on solder paste menisci, such as in flip-chip assembly. The dynamics of a chip submitted to a meniscus has been studied as a classical second order system, including inertial, viscous and stiffness effects. Only the stiffness term depends on capillary forces, while the viscous term depends on the shear stress on the component, i.e. on the liquid viscosity and the liquid flow inside the meniscus.

In order to make our results useful to readership we tried to propose analytical models or to present numerical results in the form of maps and graphs.

Next section will focus on classical approaches to capillary forces modeling, while details on own contributions will be given in sections 4.3, 4.4 and 4.5 .

4.2 Modeling liquid bridges geometry: an overview

Literature highlights two different ways to compute capillary forces. The first one consists in computing first the surface energy of the liquid bridge and deriving it with respect to the degree-of-freedom of interest¹ (section 4.2.1). The second approach directly gives the force from the liquid bridge geometry (section 4.2.3). Note well that in both cases finding the right liquid bridge geometry is the key point, leading to some useful approximations (section 4.2.4). Computing the force from surface energy is quite straightforward and will be done in the following. At the contrary, beside this approach based on energy, a second approach based on forces directly was highlighted in literature: basically, it consists in computing separately the effect of surface tension and the effect of pressure gap induced by the curvature of the liquid bridge. We contributed to that point by giving formal and experimental evidences of the equivalence of both approaches [100]. This will be detailed later on in section 4.3.2. Consequently, in the current section, we don't focus on force computation but rather on liquid bridge geometry. The link between geometry and force will be introduced in section 4.3.1.

Additional details can be found in our related publications [100, 92, 106], or in the lecture given for the FSRM².

4.2.1 Energetic method: example of two parallel plates

As an introduction, we propose the case of a meniscus between two parallel plates, with a contact angle $\theta = \pi/2$. This method consists in:

- writing the interfacial energy W of the system as a function of the parameters defining the geometry of the system;
- deriving this energy with respect to one of the parameters (the separation distance z is often used) in order to calculate the capillary force as a function of this parameter;
- estimating the derivative of the other parameters with respect to the chosen parameter by assuming a mathematical relationship (for example the conservation of the liquid volume).

This approach can be illustrated by the case of two parallel plates linked by a meniscus, such as represented in figure 4.3:

The system has three phases (S: solid, L: liquid, V: vapor) and three interfaces (LV:liquid-vapor, SL: solid-liquid, SV: solid-vapor) leading to a total energy equal to:

$$W = W_{SL} + W_{SV} + W_{LV} = \gamma_{SL}S_{SL} + \gamma_{SV}S_{SV} + \gamma\Sigma \quad (4.1)$$

¹e.g. the force along the z -direction is the derivative with respect to z

²Fondation Suisse pour la Recherche en Microtechnique, www.fsr.ch, Micro Assembly using Surface Tension

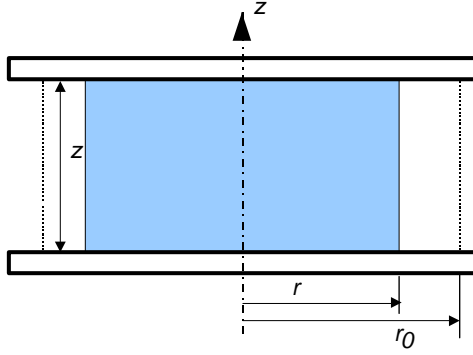


Figure 4.3: Example of the energetic method: case of two parallel plates. z is the gap between plates, r the wetting radius i.e. the radius of the wetting circle, and r_0 an arbitrary radius for area computation (see the related explanation in the text)

where:

$$W_{SL} = 2\gamma_{SL}\pi r^2 \quad (4.2)$$

$$W_{SV} = 2\gamma_{SV}(\pi r_0^2 - \pi r^2) \quad (4.3)$$

$$W_{LV} = \gamma\Sigma = \gamma 2\pi r z \quad (4.4)$$

In these equations, r_0 is an arbitrary constant radius, larger than r and γ_{SL} (γ_{SV}) state for the interfacial energy between solid and the liquid (vapor). Σ states for the area of the liquid-vapor interface (the lateral area of the meniscus).

$$\begin{aligned} W &= 2\gamma_{SL}\pi r^2 + 2\gamma_{SV}(\pi r_0^2 - \pi r^2) + \gamma 2\pi r z \\ &= \underbrace{2\gamma_{SV}\pi r_0^2}_{\text{constant}} - 2\pi r^2 \underbrace{(\gamma_{SV} - \gamma_{SL})}_{\gamma \cos \theta = 0} + \gamma 2\pi r z \end{aligned}$$

As we try to get the expression of the force F acting on one of the plates along the vertical z as a function of the separation distance z , the latter equation must be derived with respect to z :

$$\begin{aligned} F &= -\frac{dW}{dz} \\ &= -2\pi r \gamma - \underbrace{2\pi z \gamma \frac{dr}{dz}}_{\text{requires an additional assumption}} \end{aligned} \quad (4.5)$$

In order to calculate all the derivatives involved in this expression, additional assumptions must be stated. The assumption is that the volume $V = \pi r^2 z$ of the

meniscus remains constant (we consequently do not consider the evaporation of the liquid), and its conservation leads to:

$$\frac{dV}{dz} = 2\pi r \frac{dr}{dz} + \pi r^2 = 0 \quad (4.6)$$

Finally, the force can be written as:

$$F = -\pi r \gamma \quad (4.7)$$

Of course, this methods only gives exact analytical results in the very restrictive case of two parallel plates and a contact angle equal to $\pi/2$. When the liquid-vapor interface cannot be estimated analytically, it is necessary to turn oneself toward a software such as Surface Evolver (see next section).

Israelachvili [74] applied this method to calculate the capillary force between a sphere and a flat surface³:

$$F = -4\pi R \gamma \cos \theta \quad (4.8)$$

where R is the sphere radius, γ is the surface tension, and $\cos \theta$ the mean cosine of contact angles θ_1 and θ_2 on sphere and plate.

Let us add a recently published model [158] giving an analytical expression for the capillary force between two spheres with radii R_1 and R_2 , as a function of the separation distance z :

$$F_{\text{sphere/sphere}} = -\frac{2R \cos \theta}{1 + z/(2h)} \quad (4.9)$$

where R is the equivalent radius given by $R = \frac{2R_1R_2}{R_1+R_2}$, $2 \cos \theta = \cos \theta_1 + \cos \theta_2$, z is the separation distance or gap and h is the immersion height, approximately given by [158]:

$$h = \frac{z}{2} \left(-1 + \sqrt{1 + 2V/(Rz^2)} \right) \quad (4.10)$$

where V is the volume of the liquid bridge.

4.2.2 Introduction to Surface Evolver

Surface Evolver is a simulation software which computes minimal energy surfaces⁴. Therefore, constraints on contact angles, pinning lines, volume of liquid must be defined in a text file which is processed to evolve the vapor-liquid interface toward an energy minimum (figure 4.4).

In general, the energy can be written as (see previous section):

$$W = \text{constant} - A_{\text{SL}} \underbrace{(\gamma_{\text{SV}} - \gamma_{\text{SL}})}_{\gamma \cos \theta} + \gamma \Sigma \quad (4.11)$$

I

³As it can be seen this expression does not depend on the volume of liquid. This approximation is only valid for small volumes. More rigorous expressions, valid for large volumes are given by [144].

⁴<http://www.susqu.edu/brakke/evolver/evolver.html>

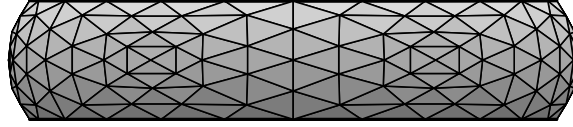


Figure 4.4: Example of a meniscus meshed in Surface Evolver

The surface energy $\gamma\Sigma$ is easy to compute as soon as the liquid-vapor is meshed. But usually in Surface Evolver, it is tried to mesh **only** this surface and **not** the solid-liquid interface.

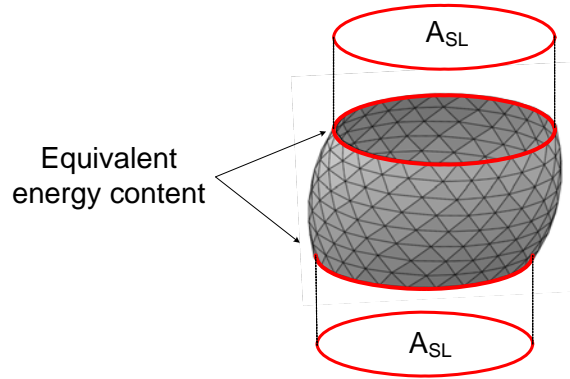


Figure 4.5: The surface energy of the meniscus must be computed from the meshed elements, i.e. from the triple line.

Therefore, the energetic content of this interface $-A_{SL}\gamma\cos\theta$ has to be computed from the single elements of this interface to be meshed, which in this case is its boundary, i.e. the triple line. This is achieved using the Stokes theorem:

$$\iint \text{rot}\bar{w} \cdot d\bar{S} = \oint \bar{w} \cdot d\bar{l} \quad (4.12)$$

where $\text{rot}\bar{w}$ is equal to $\bar{\nabla} \times \bar{w}$:

$$\begin{aligned} \bar{\nabla} \times \bar{w} &= (\partial_y w_z - \partial_z w_y)\bar{I}_x + (\partial_x w_z - \partial_z w_x)\bar{I}_y \dots \\ &\dots + (\partial_x w_y - \partial_y w_x)\bar{I}_z \end{aligned} \quad (4.13)$$

$$\begin{aligned} &= \left(\frac{1}{r}\partial_\theta w_z - \partial_z w_\theta\right)\bar{I}_r + (\partial_z w_r - \partial_r w_z)\bar{I}_\theta \dots \\ &\dots + \frac{1}{r}(\partial_r(rw_\theta) - \partial_\theta w_r)\bar{I}_z \end{aligned} \quad (4.14)$$

The integral I defined in equation 4.11 can be developed using $\bar{\nabla} \times \bar{w} = \bar{I}_z$:

$$I = -2\gamma\cos\theta \underbrace{\iint \bar{I}_z \cdot d\bar{S}}_{A_{SL}} = -2\gamma\cos\theta \oint \bar{w} \cdot d\bar{l} \quad (4.15)$$

with:

$$\bar{w} = x\bar{1}_y = r \sin \theta \cos \theta \bar{1}_r + r \cos^2 \theta \bar{1}_\theta \quad (4.16)$$

and:

$$d\bar{l} = rd\theta \bar{1}_\theta \quad (4.17)$$

The vector \bar{w} must be defined in the input file of Surface Evolver, so that the software can compute the energetical content of the non-meshed interface.

Similarly, we saw in the previous section that the condition of constant volume was imposed to achieve the computation. Here again, Surface Evolver needs information to compute a volume V whose a part only of its boundary is meshed. We

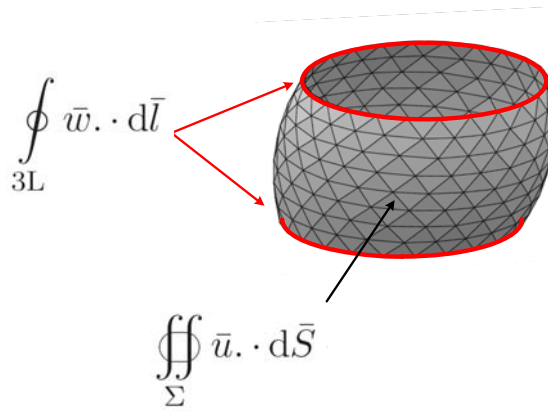


Figure 4.6: The volume of the meniscus must be computed from the meshed elements, i.e. by summing a contribution from the lateral area and a contribution from the triple line

refer now to the divergence theorem:

$$\iiint_V \text{div} \bar{u} dV = \iint_{\partial V} \bar{u} \cdot d\bar{S} \quad (4.18)$$

Choosing a vector \bar{u} whose divergence is equal to 1, the volume can be written as:

$$\begin{aligned} V &= \iiint_V dV \\ &= \iint_{\Sigma} \bar{u} \cdot d\bar{S} + \iint_{\text{SL}} \underbrace{\bar{u}}_{\text{rot} \bar{w}} \cdot d\bar{S} \\ &= \iint_{\Sigma} \bar{u} \cdot d\bar{S} + \oint_{3L} \bar{w} \cdot d\bar{l} \end{aligned} \quad (4.19)$$

where Σ denotes the meshed liquid-vapor interface, SL the solid-vapor interface (not meshed) and 3L the triple line contours (on top and bottom of the meniscus). The vector \bar{w} is defined by $\text{rot} \bar{w} = z(x,y)\bar{1}_z$ where $z(x,y)$ is the equation of the solid-liquid interface.

Example: truncated cone

Let us take the case of a truncated cone limited by the planes $z = 0$ and $z = z_H$ (such as depicted in figure 4.7). The cone equation is:

$$r(z) = r_H + (z_H - z) \tan a \quad (4.20)$$

and the normal vector is given by:

$$\bar{n} = \cos a \bar{1}_r + \sin a \bar{1}_z \quad (4.21)$$

With the surface element $dS = \frac{r}{\cos a} dz d\theta$, the volume is computed as follows:

$$\begin{aligned} V &= \iint_{\Sigma} z \bar{1}_z \cdot d\bar{S} + \oint_{3L} \bar{w} \cdot d\bar{l} \\ &= \iint_{\Sigma} z \bar{1}_z \cdot d\bar{S} + \oint_{3L} z_H r_H \cos \theta (\sin \theta \bar{1}_r + \cos \theta \bar{1}_\theta) \cdot r_H d\theta \bar{1}_\theta \\ &= \int_0^{2\pi} d\theta \int_0^{z_H} \tan a r(z) z dz + z_H r_H^2 \int_0^{2\pi} \cos^2 \theta d\theta \\ &= \pi r_H z_H^2 \tan a + \frac{\pi}{3} z_H^3 \tan^2 a + \pi r_H^2 z_H \end{aligned} \quad (4.22)$$

which is obviously equal to the difference of two cone volumes ($r_0 = r(z = 0)$):

$$V = \frac{\pi}{3} r_0^2 H - \frac{\pi}{3} r_H^2 (H - z_H) \quad (4.23)$$

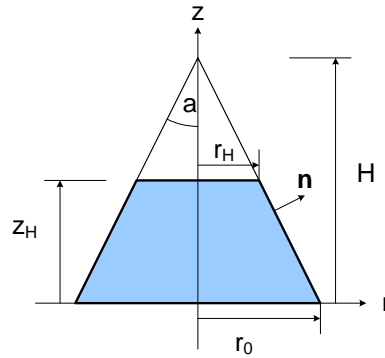


Figure 4.7: Truncated cone illustrating the computation of volume is Surface Evolver

Surface Evolver has been used to deduce lateral capillary forces (section 4.3.6) and capillary forces due to capillary condensation (section 4.4.1).

4.2.3 Exact resolution for axially symmetric problems

For axially symmetric menisci of equation $r = r(z)$, the curvature $2H$ can be written as follows (see [92] for details):

$$2H = -\frac{r''}{(1+r'^2)^{\frac{3}{2}}} + \frac{1}{(1+r'^2)^{\frac{1}{2}}} = \frac{p_{\text{in}} - p_{\text{out}}}{\gamma} \equiv \frac{\Delta p}{\gamma} \quad (4.24)$$

where p_{in} and p_{out} are the pressures inside and outside the liquid bridge, and γ is the surface tension of the considered liquid. Δp is the pressure gap across the liquid-gas interface: as it will be seen later on, it is one of the drivers of capillary forces. This equation was written by Pierre-Simon Laplace in 1805 [45].

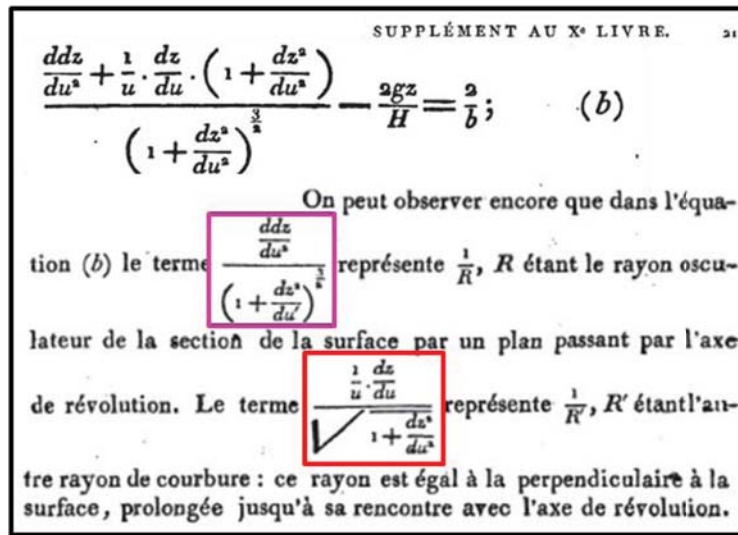


Figure 4.8: Laplace's original equation [45]

As illustrated in figure 4.9, it can be seen that the first term of equation (4.24) is the curvature of the planar curve defined by the meniscus profile, known to be $\frac{d\theta}{ds}$ where θ is the angle between the meniscus tangent and a fixed direction, for example the horizontal direction. ds is the infinitesimal intrinsic length along the meniscus. Consequently, the first curvature radius is $\frac{ds}{d\theta}$. The second curvature radius is the distance between the surface and the symmetry axis along the normal vector, given by $r/\sin \theta$.

Let us now put (4.24) as a system of two first-order differential equations:

$$\begin{cases} u = \frac{dr}{dz} \\ \frac{du}{dz} = \frac{1+u^2}{r} - \frac{\Delta p}{\gamma}(1+u^2)^{\frac{3}{2}} \end{cases} \quad (4.25)$$

To solve these equations, Δp must be known and boundary conditions have to be set (figure 4.10): let us assume that we know the point P of the meniscus

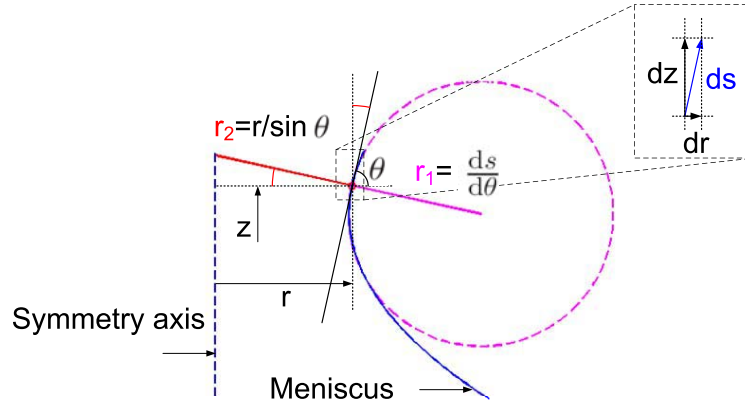


Figure 4.9: Curvature radii of an axially symmetric surface: r_1 is the azimuthal curvature radius (in a plane containing the symmetry axis) and r_2 is the radial curvature radius (distance between the curve and the symmetry axis, measured along the normal)

in contact with the gripper. Therefore z_P and $r_P = r(z_P)$ are given by the initial coordinates of P and the slope of the meniscus in P is given by:

$$u_P = \left. \frac{dr}{dz} \right|_{z_P} = \begin{cases} \frac{1}{\tan(\phi_P + \theta_2)}, & \text{if } (\theta_2 + \phi_P) \neq \frac{\pi}{2} \\ 0, & \text{if } (\theta_2 + \phi_P) = \frac{\pi}{2} \end{cases} \quad (4.26)$$

where the contact angle θ_2 and ϕ_P depends on the gripper geometry.

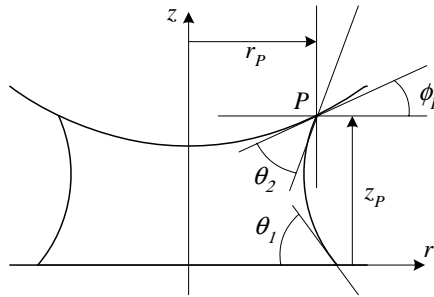


Figure 4.10: Boundary conditions depend on the geometry and materials: the upper line states for the gripper, while the lower straight line states for the component

In our problem (how to determine the meniscus for given contact angles θ_1 and θ_2 and liquid volume V), only θ_2 is known. Indeed, Δp and the position of P are a priori unknown. [46] already suggested to iterate on Δp in order to adjust θ_1 to the prescribed value. Indeed, increasing pressure difference (i.e. more negative Δp) leads to a more curved meniscus, and, consequently, to smaller θ_1 . P is still unknown and the condition on V has not yet been used. Therefore, a second

iteration loop is used [104] to determine P : an initial position of P is guessed in order to solve the first iteration loop (i.e. determine a meniscus that would be correct as far as contact angles are concerned), leading to a candidate whose volume is computed. If this volume is smaller (larger) than the prescribed one, P is moved away (closer) from the symmetry axis (this is achieved by dichotomous search). This double iterative scheme is actually an application of the so-called shooting method. It is graphically illustrated in figure 4.11.

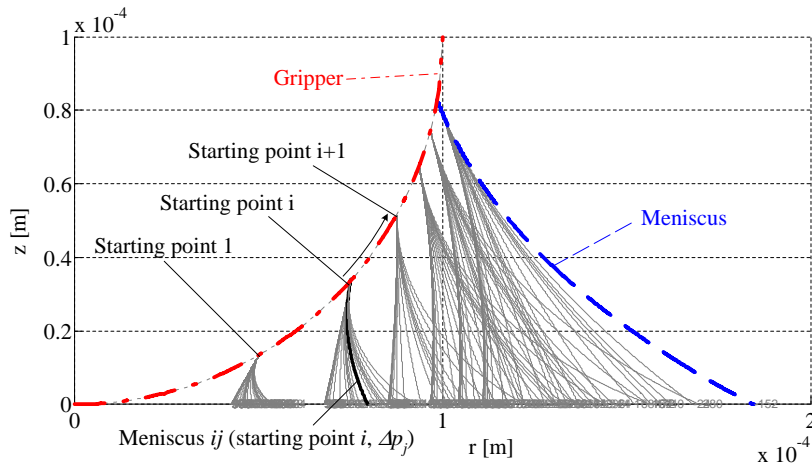


Figure 4.11: Graphical illustration of the double iterative scheme for a sphere of $100\mu\text{m}$ radius, contact angles equal to 3° , a volume of liquid equal to 45nL and a gap equal to zero. Meniscus ij is obtained with the i th starting point and the j th pressure difference

This method was developed during my PhD, but this problem can also be solved with the `bvp4c` routine of MATLAB for boundary values problems.

4.2.4 Geometrical models

It has been seen in the previous section that solving equation (4.24) requires the knowledge of two initial values (position and slope of the meniscus) and the pressure difference parameter. Therefore, three conditions of the problem were used: the volume of liquid, the initial slope and the final slopes. These three conditions can alternatively be used to find the three parameters of a circle (two center coordinates and the radius) or the three coefficients of the parabola $r(z) = a_0 + a_1z + a_2z^2$.

These models are physically incorrect, but they provide a good estimate of the

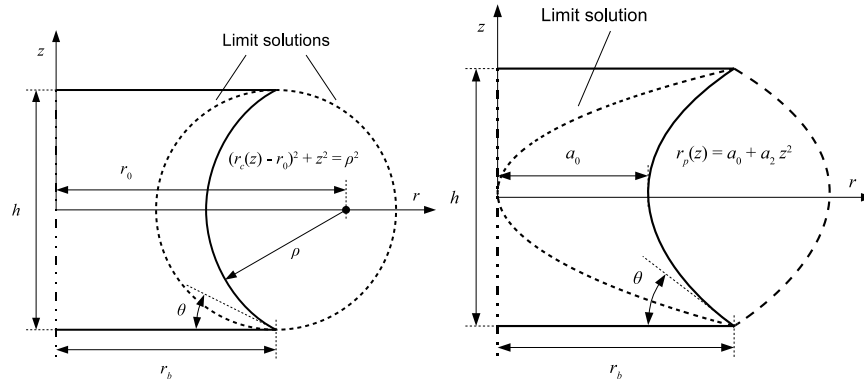


Figure 4.12: Circular and parabolic models (Courtesy of J.-B. Valsamis [181])

meniscus geometry from which the force is computed. Moreover, the parabolic model provides a full analytical resolution, as shown by Jean-Baptiste Valsamis in his PhD. He also provided in his PhD two maps (see section 4.3.3) giving the relative error of these models with respect with the exact numerical resolution of equation 4.24.

As a conclusion, the meniscus shape may be assumed circular, which is valid when the radius r of the triple line is much larger than the meniscus height, or it may be assumed parabolic, which is valid for contact angles near $\pi/2$. The parabolic model has been used to get analytical estimates of the axial stiffness (section 4.3.3) and in combination with gas law (section 4.4.2).

4.2.5 Conclusions

We have seen different methods to compute the geometry of a liquid bridge at equilibrium. When using surface energy minimization, the surface energy is known and the link to capillary force is obvious (the force is found by derivation). For both other methods, the link between geometry on the one hand and capillary force on the other hand has to be explained: this is the focus of next section.

4.3 Contributions to capillary forces modeling

This section highlights our contribution to capillary forces modeling. Equivalence between the force derivation from the surface energy and the exact resolution in axially symmetric configurations is presented in section 4.3.2. It is therefore necessary to explain how to compute capillary forces from geometries (section 4.3.1). Axial static forces⁵ are treated in section 4.3.3 and dynamic axial forces⁶ are presented in section 4.3.4. Lateral forces developments⁷ are described in section 4.3.6. Finally, the general modeling of a liquid bridge as a mechanical joint with 6 degrees of freedom is discussed in section 4.3.7.

Let us note that to make the reading easier, main results of this section are embedded in boxes.

4.3.1 Capillary force developed by a meniscus at equilibrium

Let us consider the meniscus depicted in figure 4.13. At equilibrium, the sum of forces acting on any slice of the meniscus must be equal to zero. On each face, capillary forces can be split into two contributions: the so-called tension force \bar{F}_T , due to the action of surface tension along the tangent to liquid-gas interface, and the Laplace or (also called) capillary force F_L originating from the pressure acting on the face.

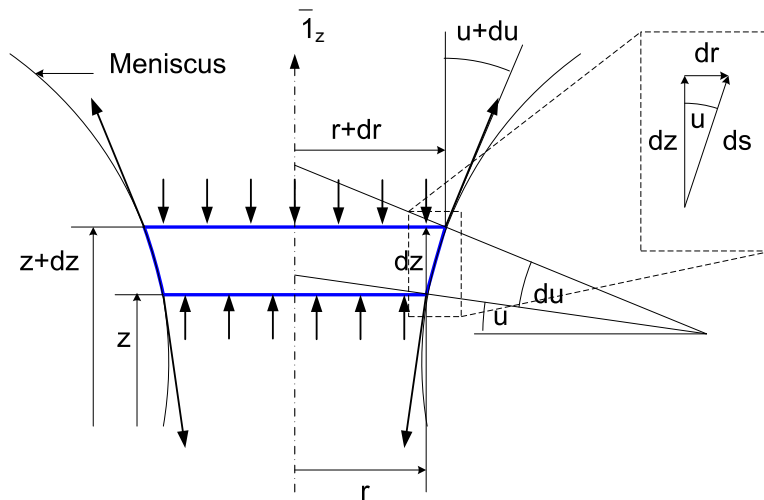


Figure 4.13: Equilibrium of a meniscus slice comprised between z and $z + dz$. It can be shown that the capillary force computed at height z exactly balance the the capillary force computed at height $z + dz$.

The force exerted on the bottom face of the slice is equal to:

⁵Results of my own PhD (2000-2004)

⁶Jean-Baptiste Valsamis's PhD (2006-2010)

⁷My contribution to the EU Hydromel project (2009-2010)

$$\bar{F}(z) = \left(\underbrace{\pi r^2 \Delta p}_{F_L} - \underbrace{2\pi r \gamma \cos u}_{F_T} \right) \bar{I}_z \quad (4.27)$$

while the force acting on the top face of the slice is given by:

$$\begin{aligned} \bar{F}(z+dz) &= (-\pi(r+dr)^2 \Delta p + 2\pi(r+dr)\gamma \cos(u+du)) \bar{I}_z \\ &= \left[-\pi r^2 \Delta p + 2\pi r \gamma \cos u + 2\pi \underbrace{(-rdr \Delta p + r\gamma \sin u du + \gamma \cos u dr)}_I \right] \bar{I}_z \end{aligned} \quad (4.28)$$

The underbraced expression I can be shown to be equal to zero by expressing the Laplace law (equation (4.24)):

$$\begin{aligned} \Delta p &= 2H\gamma \\ &= \left(-\frac{r''}{(1+r'^2)^{3/2}} + \frac{1}{r(1+r'^2)^{1/2}} \right) \gamma \end{aligned} \quad (4.29)$$

$$= \left(\frac{du}{ds} + \frac{\cos u}{r} \right) \gamma \quad (4.30)$$

$$= \left(\frac{du}{dr} \sin u + \frac{\cos u}{r} \right) \gamma \quad (4.31)$$

leading to:

$$I = -rdu \sin u \gamma - dr \cos u \gamma + r\gamma \sin u du + \gamma \cos u dr = 0 \quad (4.32)$$

Consequently, the forces $\bar{F}(z) + \bar{F}(z+dz)$ balance, and the capillary force given by $F(z)$ can be computed at any value of z . This means that in the case of two solids linked by a liquid meniscus, the force can be computed on the top component or on the bottom component. For the sake of convenience, it can also be computed at the neck in case the latter exists (it may not exist if the extremum radius of the meniscus corresponds to one of both wetting radii).

4.3.2 Equivalence of formulations

A lot of work has been reported on capillary forces modeling (see for example [74, 46, 100, 144, 174, 157, 158, 149]), based on the energetic method (i.e. derivation of the total interface energy) or a direct force computation from the meniscus geometry, the latter being either determined exactly through the numerical solving of the so-called Laplace equation or approximated by a predefined geometrical profile such as a circle (i.e. toroidal approximation) or a parabola. The energetic approach is usually quite clear on its approximations: the liquid-vapor interface energy is sometimes neglected in order not to compute the exact shape of the meniscus, but an exact solution can be found if the lateral is computed for example by

mean of a finite element solver such as Surface Evolver. At the contrary, literature results are not so clear as far as the other method is concerned. For example, some authors neglect the so-called tension term with respect to the Laplace term. This sometimes pertinent assumption has led many author authors to add the tension term to the result obtained by deriving the interface energy, i.e. to mix both methods. A paper published in Langmuir [96] contributed to clarify this situation by showing that the capillary force obtained by deriving the interface energy is exactly equal to the sum of the Laplace and tension terms. The equivalence is considered with three qualitative arguments, and an analytical argument is developed in the case of the interaction between a prism and a plate. Experimental results also contributed to show this equivalence.

Mathematically, the developments led in appendix B give evidence of the equivalence between the energetic approach and the direct formulation based on the Laplace and the tension term:

$$F = F_L + F_T = -\frac{dW}{dz} \quad (4.33)$$

where F_L and F_T are given by equation (4.27), W by equation (4.1). z is the separation distance between both solids.

As it is shown that both approaches are equivalent, it means that the energetic approach already involves the tension term and the Laplace term on an implicit way. Consequently, the energetic approach as proposed by Israelachvili (see equation (4.8)) includes both terms, even if, for zero separation distance, the pressure term usually dominates the tension one. For axially symmetric configurations, the method based on the Laplace equation will be preferred because it can be easily numerically solved.

4.3.3 Axial static forces

Introduction

The results concerning axial forces have been obtained during my PhD and the EU Hydromel project. They include a parametric study achieved thanks to the numerical scheme explained in section 4.2.3 (page 41) and the development of a geometrical meniscus model (parabolic model). The parametric study is valid for liquid bridges with a constant contact angle but an unknown triple line radius while the parabolic model is more suited to menisci with imposed wetting radius and unknown contact angle. The pinning of the triple line is made possible at the intersection between two surfaces with different surface energies or on sharp edges.

Non pinned menisci: parametric study

The double iterative scheme briefly presented in figure 4.11 allowed us to study the influence of the pertinent parameters on the capillary forces between two solids:

surface tension γ , contact angle θ , volume of liquid V , separation distance between both solids z . All these numerical experiments were performed with axial symmetry, solving equation 4.24.

Preliminarily, in order to validate the developed simulation code, we have studied the case of two parallel plates separated by a distance b and for a difference of pressure equal to zero, leading to the analytical equation of a catenary curve [92] (figure 4.14a). For $z = 0$, the relative error between the numerical radius and the analytical one is about 1.5%.

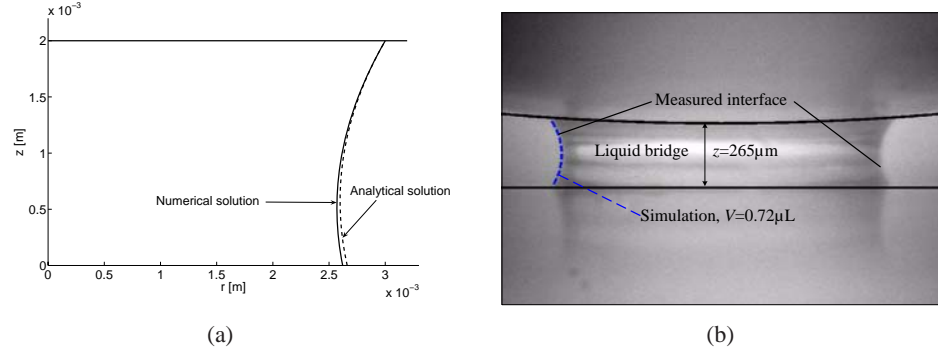


Figure 4.14: Study of the meniscus shape **(a)** Comparison between the numerical and analytical meniscus shape, with $\Delta p = 0$, $a = 3$ mm, $b = 2$ mm and $\theta_2 = 60^\circ$; **(b)** Comparison between the simulation and the experimental meniscus shape (water, steel component, spherical steel gripper ($R = 6.35$ mm))

A second case has been tested, namely the case of a meniscus between two parallel plates, with contact angles equal to 90° , leading to a cylindrical meniscus (with radius R) whose principal curvature radii are $R_1 = \infty$ and $R_2 = R$.

The last verification operated on the meniscus shape is the comparison between the output profile and the picture of the meniscus, as presented in figure 4.14b. This picture corresponds to a 12.7 mm diameter spherical steel gripper catching a steel component (blade St-004-2) with $0.72 \mu\text{L}$ water. The gap in this case is $265 \mu\text{m}$. The dashed line states for the meniscus output by the simulation tool.

The numerical computation of the force has also been compared with the analytical approximation of the capillary force between a plane and a sphere (radius R), for a gap equal to zero and an equivalent contact angle θ (if $\theta \neq \theta_2$, $\cos \theta \equiv \frac{\cos \theta_1 + \cos \theta_2}{2}$).

$$F = 4\pi R\gamma \cos \theta \quad (4.34)$$

figure 4.15 plots the force as a function of the equivalent contact angle θ for a $\Phi 26$ mm spherical gripper and for two liquids: the upper curve shows the force for water and the lower one that for silicone oil (R47V50). It can be seen on this picture that the results of the simulations tend to the analytical approximations (solid and dashed lines).

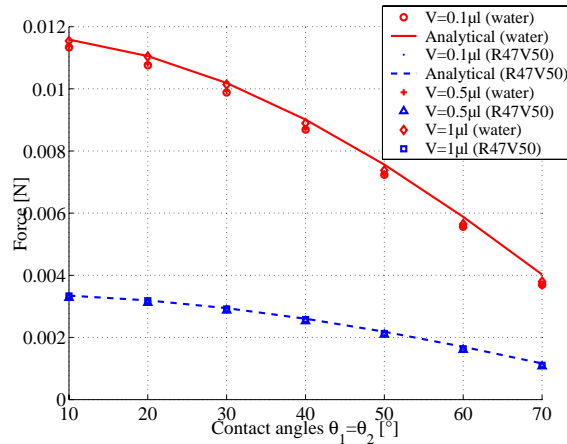


Figure 4.15: Comparison between the simulation results and the analytical approximation $F = 4\pi\gamma R \cos \theta$ for a spherical gripper with diameter 13.0 mm, $\gamma = 72 \cdot 10^{-3} \text{ N m}^{-1}$ (water) and $\gamma = 20.8 \cdot 10^{-3} \text{ N m}^{-1}$ (R47V50). The results are presented for different volumes (0.1, 0.5 and 1 μL) and different contact angles simulating different materials; the simulation points tend to the analytical approximations for water (*solid line*) and silicone oil (*dashed line*) (Reprinted with permission from [100]. Copyright 2005 American Chemical Society)

After these preliminary validations, the influence of the following parameters was studied:

1. **Separation distance:** The curve of figure 4.16 plots the capillary force exerted by a 7.9 mm Φ spherical gripper (steel, GS-St-7.9, see [91] for details) on a silicon component (Si-004-01). The force is exerted by a 0.5 μL silicone oil droplet (R47V50). This curve has been measured with an almost zero velocity (equilibrium curve). As far as the simulation is concerned, receding contact angles have been input since the meniscus is stretched by moving the gripper upwards. The correspondence between simulation and experiment can be seen on this picture although the rupture distance predicted by the simulation is a little smaller than the measured one.

This result indicates that the simulation tool can predict the capillary force with separation distances different from zero: this comes as a complement to the previous validations made by comparing the simulation with the analytical approximations, that was valid only at contact. From the point of view of a capillary gripper design, this curves means that the sticking effect due to the capillary force can be reduced or suppressed by increasing the distance between the gripper and the component. This separation could be achieved either by dynamical effects or by pushing the component away from the gripper with a less adhesive auxiliary tool or tip. The curve plotted in figure 4.16 helps to design the gripper by indicating the required range to

separate the component from the gripper and/or the residual force.

2. **Pressure term vs. tension term:** The simulation results of figure 4.16 also allow to calculate and compare the importance of the interfacial tension force and the Laplace term of the capillary force (see figure 4.17). The results presented in this figure justify some approximations found in the literature, neglecting the ‘tension’ term for small gaps. Nevertheless, this assumption is no longer valid for larger gaps and the tension term even becomes dominant.
3. **Surface tension:** Additionally, the force has been shown to be proportional to surface tension γ which ranges from 20mNm^{-1} to 72mNm^{-1} for usual

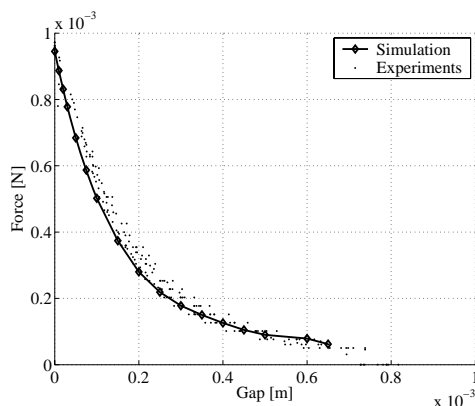


Figure 4.16: Force-Distance curve for $V = 0.5 \mu\text{L}$ R47V50, Si-component and GS-St-7.9 (Both reprinted with permission from [100]. Copyright 2005 American Chemical Society)

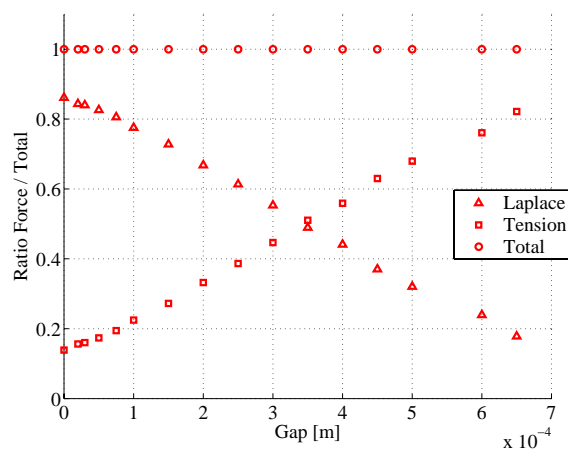


Figure 4.17: Respective contribution of the ‘tension’ and ‘Laplace’ terms in the total amount of the force - Ratios without dimensions (Both reprinted with permission from [100]. Copyright 2005 American Chemical Society)

liquids such as alcohols, silicone oils or water. Solder pastes can exhibit surface tensions as high as a few hundreds of mNm^{-1} , leading to an important surface tension effect in solder paste assembly processes. An increase of surface tension nevertheless increases the contact angle (i.e. reduces the wettability), leading to a decrease of the force: the cut-off between both effects cannot be decided without numerical quantification.

4. **Volume of liquid:** The influence of the volume of liquid depends on the geometry of the objects. It can be surprising indeed in equation 4.8 to observe that the force does not depend on the volume of liquid. Hence this formula is widely used in capillary adhesion studies, since the exact volume of liquid got by capillary condensation is usually unknown. This formula is nevertheless only valid for small volumes of liquid (the so-called immersion height must be small, see appendix A for details). Other geometries lead to different dependences on the volume of liquid: for conical tips, the force increases with increasing volume of liquid, while in the case of the concave concavity of the gripper presented in section 6.2, the force decreases with increasing volume of liquid (the underlying mechanism will be explained later on).

As a conclusion of this part of the work, we set up a numerical tool ready to compute the force in whatever axially symmetric geometry. It was used to set design rules for capillary grippers, which are summarized in appendix C. Three main limitations arise: (1) finding an optimum with a numerical tool is very tedious, and an analytical estimate will be proposed in the next point; (2) non axially symmetric geometries cannot be studied with this tool: the case of lateral capillary forces will be considered in section 4.3.6; (3) finally, the dynamical aspects will be studied at points 4.3.4 and 4.3.6.

Analytical contribution for pinned menisci: the parabolic model for axial forces

As briefly exposed in the introduction in page 47, we must distinguish between non-pinned menisci with imposed contact angle and pinned menisci with imposed wetting radius. In the latter case, such as depicted in figure 4.18, analytical approximations can be set, which is of the utmost interest to serve as benchmarks or to be exploited in design. According to section 4.2.4 on geometrical approximations, it must be chosen between the circle or the parabola models. In this case, since the separation distance h may vary such that the meniscus switches from concave to convex shapes, it is preferable to use a parabola model to manage the curvature change in the plane r, z . Indeed, when curvature is equal to zero, the circle model diverges since the radius tends to ∞ .

This assumption of parabolic profile does not rely on any physical consideration but corresponds to the meniscus shape observed experimentally. The equation

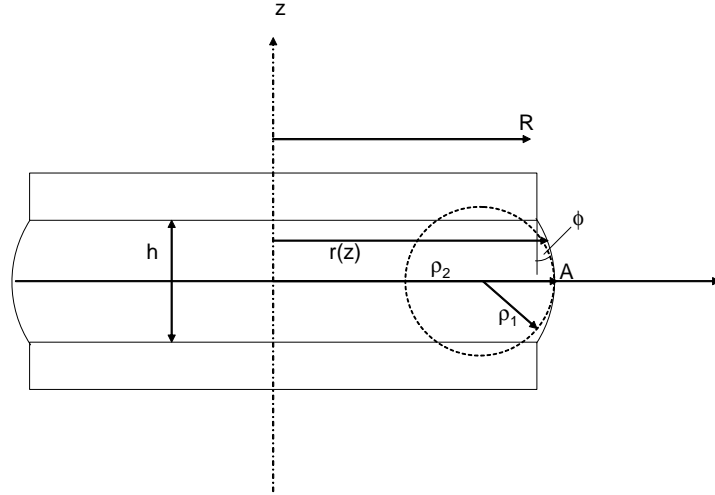


Figure 4.18: Parabola model: as usual, three information (volume of liquid, pad radius and gap) are used to determine the three coefficients of a parabola.

of this parabola is given by:

$$r(z) = a_0 + a_1 z + a_2 z^2 \quad (4.35)$$

where r and z are the axis shown in figure 4.18. Since the parabola passes through the edges of the pad and for symmetry reasons, we have two conditions to find a_0 and a_1 as a function of a_2 :

$$a_0 = R - \frac{a_2 h^2}{4} \quad (4.36)$$

$$a_1 = 0 \quad (4.37)$$

The parameter a_2 is to be determined to respect the volume of liquid condition (V and R are known and h is an input parameter, see details in appendix D):

$$V = \pi \left(hR^2 + \frac{a_2^2 h^5}{30} - \frac{a_2 R h^3}{3} \right) \quad (4.38)$$

From this volume equation, we can determine a_2 and its derivative with respect to h (V is assumed to be constant), consequently, the force F_z can be determined from its both components (see details in appendix D):

$$\begin{aligned} F_z &= F_L + F_T \\ &= \pi R \gamma \left(-2a_2 R + \frac{4R}{4R - a_2 h^2} \right) - \frac{2\pi R \gamma}{\sqrt{1 + a_2^2 h^2}} \end{aligned} \quad (4.39)$$

In the particular case of $a_2 = 0$ (corresponding to a cylindrical meniscus), the force is equal to the well-known value $-\pi R\gamma$ (equation 4.7).

The axial stiffness k_z can be computed by derivation ($d_2 = \frac{da_2}{dh}$):

$$k_z = \frac{dF_z}{dz} \quad (4.40)$$

$$= -2\pi R^2 \gamma a_2' + \frac{4\pi R^2 \gamma (a_2' h^2 + 2a_2 h)}{(4R - a_2 h^2)^2} + 2\pi R \gamma \frac{a_2 a_2' h^2 + a_2^2 h}{(1 + a_2^2 h^2)^{3/2}} \quad (4.41)$$

For a cylindrical meniscus, $a_2 = 0$, and we have $a_2' = 3R/h^3$, which leads to:

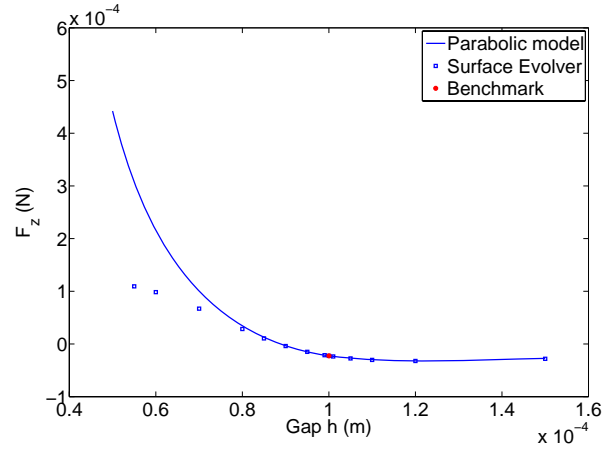
$$k_{z0} = -\pi \gamma \left[6 \left(\frac{R}{h} \right)^3 - \frac{3}{4} \left(\frac{R}{h} \right) \right] \quad (4.42)$$

We see that the stiffness increases when h decrease (i.e. when the volume of liquid V decreases) and when the radius of the pad decreases. It is interesting to note that if the system is downscaled homothetically, i.e. the ratio R/h remains unchanged (in the case of cylindrical menisci), the stiffness is independent on the size of the system.

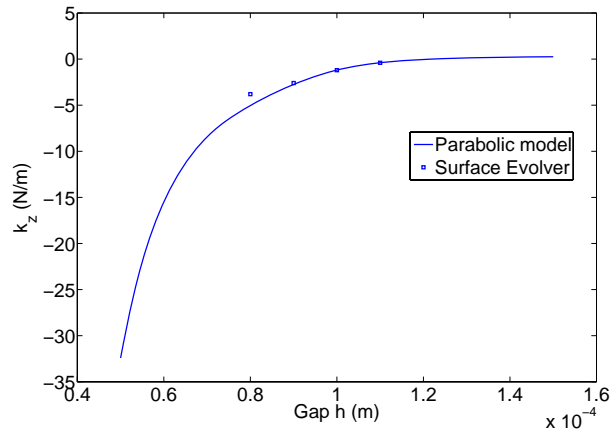
The model validation has been led by comparing the parabolical model output with the force benchmark $F = -\pi R\gamma$ for a cylindrical meniscus and by comparing it with numerical results obtained with Surface Evolver. This has been led for a pad of radius $R = 100 \mu\text{m}$, a surface tension $\gamma = 72 \text{ mNm}^{-1}$ and a volume of liquid $V = \pi 10^{-12} \text{ m}^{-3} = \pi \text{ nL}$, which corresponds to a separation distance between the pad and the component equal to $h_0 = 100 \mu\text{m}$ for a cylindrical cylinder.

We see in figure 4.19a the good correspondence between the parabolic model and the software results, for a large range of separation distances, between 80% and 150% of the separation distance h_0 . The stiffness is also compared in figure 4.19b. No analytical benchmark exist for the stiffness, even for cylindrical menisci, so that the proposed equation 4.41 is very original.

As a conclusion, we proposed a new analytical model to compute the axial force and the axial stiffness of a liquid meniscus between two circular pads. The validity domain of this model - deduced from the comparison with numerical results output by Surface Evolver - ranges from 80% to 150% of the separation distance h_0 for which the meniscus is a cylindre. Let us well note that the lower limit of the physics seems to be about 55% of h_0 . Below this level, the Surface Evolver does not converge anymore, which is related to the non physical existence of such a meniscus. Experimental results should and will be searched in literature.



(a) Axial shift



(b) Radial shift

Figure 4.19: Benchmarking of our parabola model with equation 4.7 and numerical simulation (Surface Evolver). (a) Force ; (b) Stiffness (no analytical benchmark exists for this stiffness).

Error maps for the circular and the parabolic models

Beside the parabola model developed in the previous section, the circular or so-called toroidal approximation can also be used. The advantages of the parabola model are twofold: switching from negative to positive curvatures is smoothly done when $a_2 = 0$, while the circular approximation is not continuous: the center of the circle abruptly switches from $-\infty$ to $+\infty$. Secondly, the volume of liquid can be analytically expressed as indicated by equation 4.38. The complete comparison between both geometrical models with the numerical resolution of the Laplace equation has been done by Jean-Baptiste Valsamis in his PhD: figures 4.20 and 4.21 present the relative errors of the circular and parabolic models.

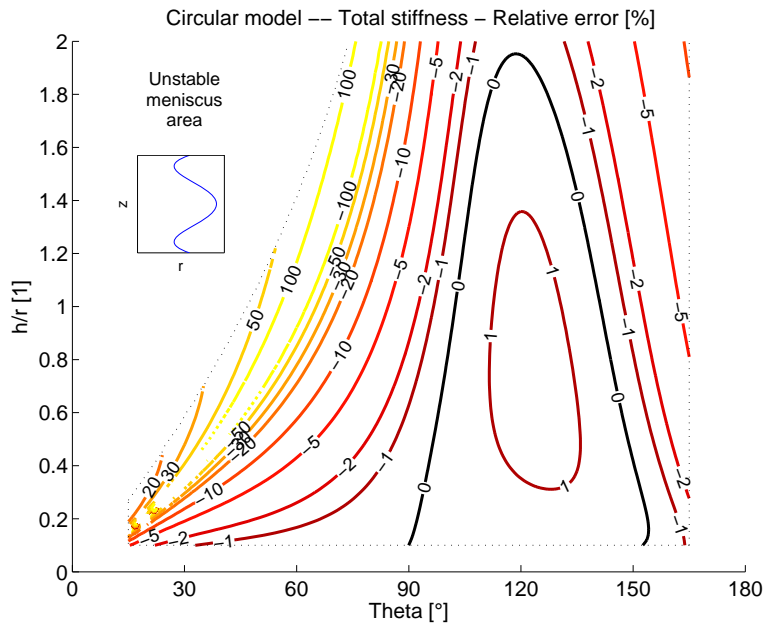


Figure 4.20: Relative error on the axial meniscus stiffness computed with the circular model. The black line is the zero error line (Courtesy of J.-B. Valsamis [181])

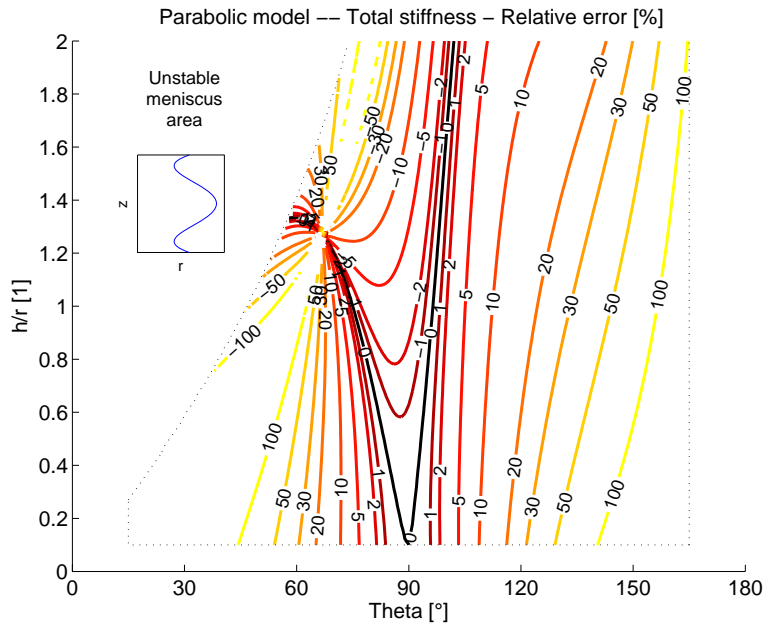


Figure 4.21: Relative error on the axial meniscus stiffness computed with the parabolic model. The black line is the zero error line (Courtesy of J.-B. Valsamis [181])

4.3.4 Axial dynamic forces

Up to now, we have only considered liquid bridges at equilibrium. Therefore, the forces applied by these menisci on solids they connect are only due to surface tension effects. If the meniscus is stretched or compressed with an important velocity or an important acceleration, viscous or inertial effects have to be added to capillary forces. Viscous effects will be governed by the viscosity of the liquid while inertial effects will be governed by density. Normally at small scales, density can be neglected, but attention must be paid in case of high accelerations, such those used in inertial micromanipulation [69]. From a mechanical point of view, these three terms form the well known Kelvin-Voigt model. After a brief state of the art, this section explains how to estimate the coefficients of this Kelvin-Voigt model and compares the related results with numerical simulation and experiments.

Literature review

The review of the literature on vertical dynamics highlights the works of van Veen et Al. [183], Cheneler et Al. [33] and Pitois et Al [152].

In [183] van Veen has developed an analytical study of the motion of the flip chip soldered components. The model is based on the computation of the free surface energy for axisymmetric geometries delimited by two parallel and circular interfaces. The free interface is developed as a fourth order polynomial and its derivative is the origin of the motion equation. A second order equation governs the time evolution of the height of the bump. Cheneler et al [33] propose a quite close analysis of liquid bridge with a totally different goal: they developed a micro-rheometer intended to determine the viscosity of liquids. However the device is not defined in the paper, the underlying idea is that the liquid added between two solids generates a dashpot in series with a calibrated spring/mass system. By measuring the phase shift between the position of the solids and the force exerted, the friction can be deduced. The method used is based on an estimation of the stiffness and the friction. This stiffness is deduced from an analytical approximation of the free interface, that is in this case a revolution of a part of a sphere (a piece of tore). However, the stiffness was calculated with a corrective multiplicative term of the capillary force, instead of the calculus of the derivative. The friction force is estimated from shear stresses inside the liquid. The complete analytical development are done in Valsamis 's PhD [181]. This friction and the stiffness have been linearized and added in the Newton equation governing the motion of the component wetted by the meniscus. Its validation is done thanks an numerical analysis. However, the numerical analysis does not solve the Navier-Stokes equation inside the meniscus. Finally, the authors do not support their study with any experimental data. In [152], Pitois et al have studied the evolution of the force between two spheres moving aside at a given constant velocity. The analytical model involves also estimation of stiffness and friction. The stiffness is computed from the deriva-

tive of the capillary force, itself calculated with geometrical approximation of the different order of magnitude. The friction force is based on similar assumption but a corrective term is added. Contrarily to Cheneler, the liquid bridge is not pinned and the contact surface varies in time. The study is based on an analytical approach of the problem together with an experimental setup. As the main result, they highlighted different behaviors of the capillary forces (negative and positive, according to the separating distance z), the influence of the velocity illustrating the effect of viscosity. Nevertheless, the authors do not expose some important aspects, such as the way to control the volume (volumes are small and the viscosity high, making the use of pipette very difficult), the variation of the contact angles during the separation and, as a corollary, the motion of the triple line, making the interpretation of their results difficult.

Kelvin-Voigt model of the meniscus

The work of Jean-Baptiste Valsamis recently led to the complete modeling of the vertical dynamics of a meniscus through an adapted Kelvin-Voigt model depicted in figure 4.22. The force $\vec{f}(t) = f(t)\vec{1}_x$ applied by a meniscus (opposed to the force

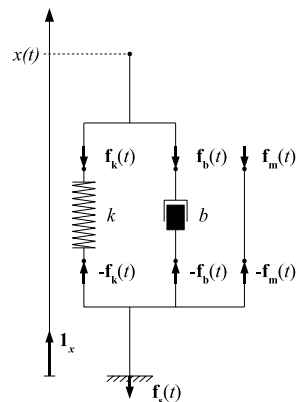


Figure 4.22: Equivalent mechanical model of a meniscus as far as its vertical dynamics is concerned: $\vec{f}_k(t)$, $\vec{f}_b(t)$ and $\vec{f}_m(t)$ respectively represent the forces of the spring, the dashpot and the inertia of the equivalent mass. $\vec{f}_s(t)$ represents the force exerted on the meniscus by the bottom solid wetted by the meniscus (Adapted from J.-B. Valsamis [181])

\vec{f}_s applied on the meniscus) is therefore given by:

$$f(t) = kx(t) + b\dot{x}(t) + m\ddot{x}(t) \quad (4.43)$$

where k is the meniscus stiffness defined as the derivative of the capillary force with respect to the meniscus height, b is a damping coefficient and m an equivalent inertia. More explicitly, using the parameters presented in figure 4.23, k is defined

by:

$$k = 2\pi r_b \cos \theta \frac{d\theta}{dh} - \pi r_b^2 \frac{d(2H)}{dh} \quad (4.44)$$

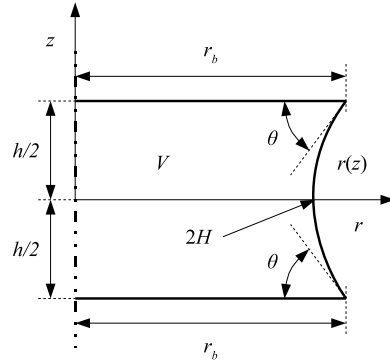


Figure 4.23: Geometry and parameters for the model of meniscus stiffness of equation 4.44

The computation of the derivatives in the later equation can be achieved on 3 ways:

1. estimate them by finite difference, using the numerical scheme presented in section 4.2.3: the results obtained by J.-B. Valsamis are presented in figure 4.24;
2. use the parabolic model and especially equation (4.41);
3. apply the circular model

Based on a geometrical meniscus (i.e. $\theta = 90^\circ$ in figure 4.23) with a small aspect ratio $r_b \gg h$, and assuming that the surface tension does not affect the velocity field inside the meniscus, the damping coefficient was shown to be [181]:

$$b = \frac{3\pi}{2} \frac{\mu r_b^4}{h^3} \quad (4.45)$$

Similarly, assuming the conservation of kinetic energy and a small aspect ratio $r_b \gg h$, the equivalent mass was shown to be:

$$m = M \frac{r_b^2 b}{8h^2} \quad (4.46)$$

where M is the mass of the meniscus, i.e. its volume times its density.

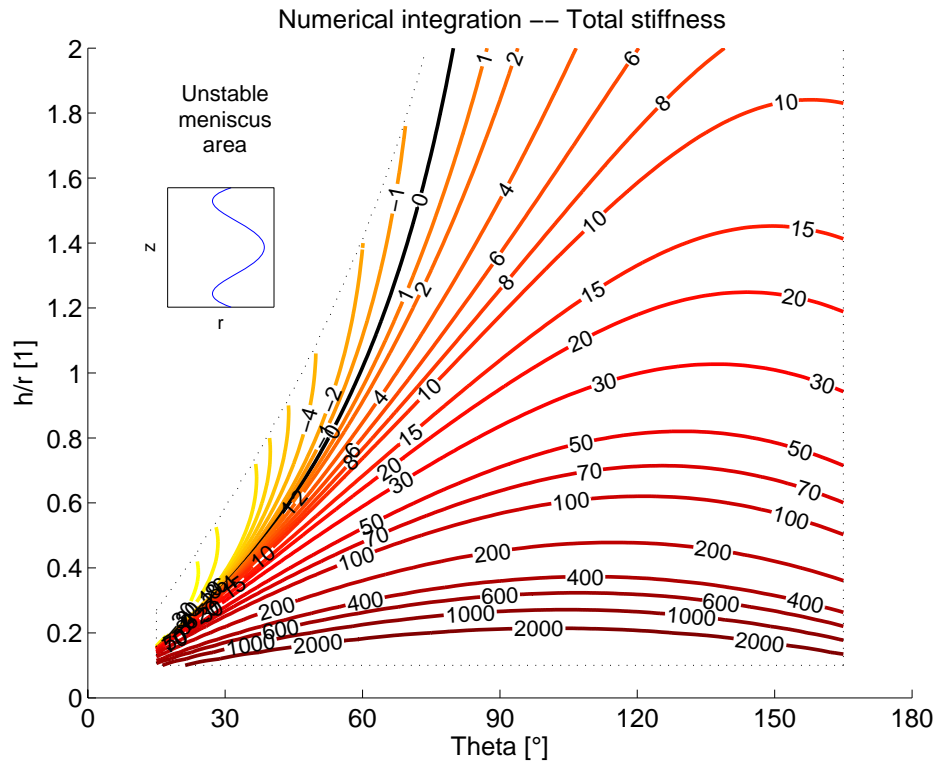


Figure 4.24: Total non dimensional stiffness computed by numerical integration (physical stiffness may be obtained by multiplying the values of this figure by the surface tension). The black line is the zero stiffness. The results are presented as a function of the reduced gap (r is the pad radius also defined as r_b) and the contact angle θ . Obviously, there is a relation between the gap, the contact angle and the volume of liquid, which is given in appendix E

Comparison between the Kelvin-Voigt model and numerical simulations

These approximations have been compared both with numerical simulation (Navier-Stokes equations, moving mesh technique, Comsol) and with experiments.

Firstly, let us note that equation (4.43) lead to a gain $G(\omega)$ depending on the pulsation ω :

$$G(\omega) = \sqrt{(k - \omega^2 m)^2 + \omega^2 b^2} \quad (4.47)$$

This gain defines three different regimes:

1. the k -regime for low frequency: $\lim_{\omega \rightarrow 0} G(\omega) = k$;
2. the b -regime for frequency near the resonance frequency: $\lim_{\omega \rightarrow \sqrt{k/m}} G(\omega) = \omega b$;

3. the m -regime for high frequency: $\lim_{\omega \rightarrow \infty} G(\omega) = \omega^2 m$;

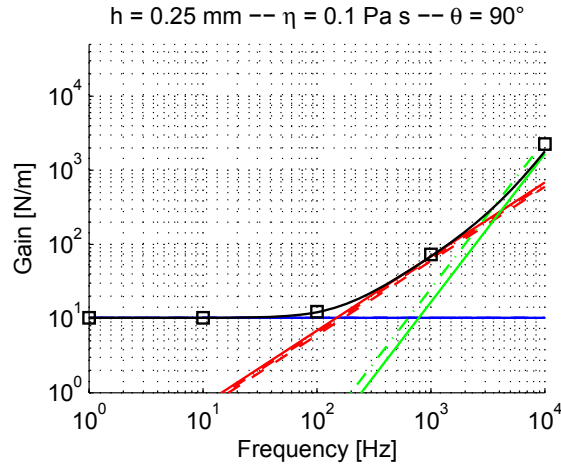


Figure 4.25: Example of comparison between the Kelvin-Voigt model and the numerical simulation (the value of the parameters is indicated on top of the figure). In blue, the stiffness gain $\log k$, in red the damping gain $\log \omega + \log b$, in green, the inertial gain $2 \log \omega + \log m$. The differences between solid and dashed lines come from slightly different assumptions, briefly mentioned in appendix E and detailed in [181]. Note that for menisci with small aspect ratio $r_b \gg h$, the results does not depend on these assumptions.

An example of comparison between these asymptotic behaviors with the numerical simulation is given in figure 4.25. More extensive comparisons have been led by Jean-Baptiste Valsamis: results are presented in appendix E for the parameters indicated in table 4.1.

Parameter	Symbol	Value
Radius	r_b	0.75mm
Gap	h	0.15mm, 0.25mm
Contact angle	θ	45°, 90°, 135°
Viscosity	μ	0.001Pas, 0.01Pas, 0.1Pas, 1Pas
Frequency	f	1Hz, 10Hz, 100Hz, 1kHz, 10kHz

Table 4.1: Parameters of the numerical simulations

Comparison between experiments and numerical simulations

Experiments have been led whose parameters are summarized in table 4.2.

All the results are reported in appendix E. As an illustration, we propose the results of figure 4.26, obtained in experiment 1 with oil7 (i.e. $\rho = 971 \text{kgm}^{-3}$, $\mu = 0.485 \text{Pas}$ and $\gamma = 21.2 \text{mNm}^{-1}$).

Exp	Liquid	Bot. radius (mm)	Top radius (mm)	Bot. angle (°)	Top angle (°)	Gap (mm)
1	Oil7	0.726	0.713	15.9	20.6	0.282
2	Oil7	0.750	0.736	29.5	35.7	0.231
3	Oil1	0.756	0.747	26.7	29.5	0.320
4	Oil1	0.754	0.746	26.5	37.9	0.279
5	Oil1	0.757	0.751	43.9	46.3	0.249
7	Oil6	0.749	0.747	33.9	35.0	0.159
8	Oil2	0.750	0.746	40.1	40.8	0.565
9	Oil2	0.752	0.749	58.5	59.5	0.483
10	Oil2	0.751	0.752	27.4	27.0	0.266
11	Oil8	0.743	0.750	29.4	27.1	0.296
12	Oil8	0.747	0.760	15.2	11.5	0.339

Table 4.2: Parameters of the different experiments (properties of liquids are given page 134 in table 6.1)

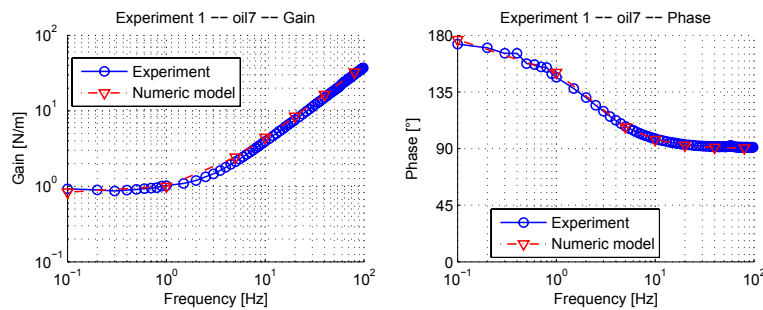


Figure 4.26: Gain and phase curves for numerical simulations and experimental results, for experiment 1 with oil7

4.3.5 Conclusions

Dynamic forces exerted by a liquid bridges have been described thanks to a well known Kelvin Voigt model. The contribution of Jean-Baptiste Valsamis is here to provide powerful estimates for the stiffness, damping and inertial coefficients required in this model. The goal is to provide results which could be used independently from numerical or experimental tools. A fair concordance with numerical (based on the resolution of Navier-Stokes equations) and experimental results has been shown.

4.3.6 Lateral capillary forces: statics and dynamics

This section presents a study on the dynamics of lateral motion of a liquid meniscus confined by a circular pad and a circular chip moving parallelly to the pad. This problem is a typical flip-chip case study, whose use is wide-spread in industrial assembly. The proposed model describing this dynamics is made of two coupled physics: the Navier-Stokes equation governing the liquid flow between the pad and the chip, and the Newton's law describing the motion of the chip. This coupled problem is solved with a spectral method based on Chebyshev polynomials, by assuming an analytical expression of the lateral stiffness of the meniscus in the cases of circular and square pads. The theoretical results are benchmarked with literature results and thoroughly experimentally validated. From these results, we propose a map giving the characteristic time of the chip dynamics according to only two non-dimensional parameters, constructed with the physical (density, surface tension, viscosity), geometrical (pad area, gap) or dynamical (chip mass) parameters of the problem.

State of the art and definition of the problem

Most modeling works are quasi-static, i.e. based on surface energy minimization to find the equilibrium positions of the system, and on energy gradient to compute restoring forces [130][171]. For small displacements, an analytical model to estimate the lateral restoring force developed by a meniscus between two square pads is sketched in [180]. Nevertheless, most of these studies does not address dynamical aspects such as characteristic damping time and resonance frequencies.

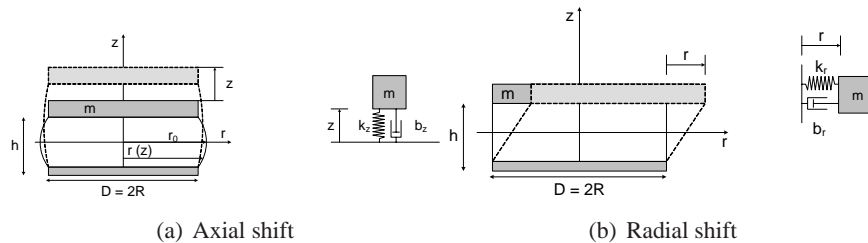


Figure 4.27: Axial and radial models used by van Veen [183].

In this direction, van Veen [183] derived analytical relations to model both the axial compressive motion and the lateral motion (figure 4.27). Kim et al. [83] proposed a study on dynamic modeling for resin self-alignment mechanism. Because the authors used a material with a low surface tension such as liquid resin, they claimed the alignment motion to be different from the oscillatory motion of the solder described by van Veen [183]. Recently, Lin et al compared 2D numerical results with experiments [129]. To solve these motion equations, these authors used the CFD-ACE+ package making use of an iterative algorithm alternating one time step resolution of Navier-Stokes equations (and the continuity equation) with

one time step resolution of the structural mechanics equations [129]. The authors observed a good match of their 2D simulation to experimental data in case of fluid meniscus aspect ratios larger than 3.

Lastly, Lu and Bailey [132] predicted the dynamical behavior of a chip in flip-chip alignment, whose dynamics is governed by the following Newton's law:

$$m\ddot{x} = -k(x)x - c\dot{x} \quad (4.48)$$

where $k(x)$ is the lateral stiffness of a meniscus linking a circular pad and a circular substrate, and the viscous force $-c\dot{x}$ is applied by the viscous stress on the chip. The lateral stiffness was computed with Surface Evolver and found to be almost constant, while the viscous force $c\dot{x} = \mu S \frac{\partial u}{\partial y}|_{y=h}$ was computed from the liquid flow between the chip and the pad, governed by the Navier-Stokes equation (μ is the dynamic viscosity of the liquid, S is the area of the chip in contact with liquid, u is the velocity along x -axis, y is the coordinate perpendicular to the chip):

$$\rho \frac{\partial u}{\partial t} - \mu \frac{\partial^2 u}{\partial y^2} = 0 \quad (4.49)$$

The coupled problem defined by equations (4.48) and (4.49) is thus described by two unknowns: firstly the position of the chip $x(t)$, and secondly the velocity profile inside the meniscus $u(y,t)$.

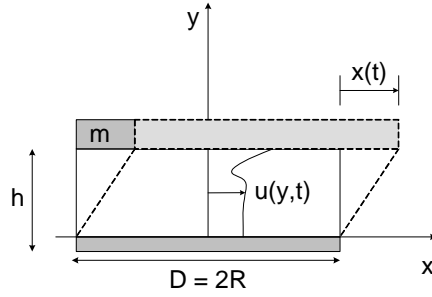


Figure 4.28: Problem modeled in this work: a moving top pad is linked to a fixed bottom pad through a liquid meniscus whose velocity profile is assumed to be described by the horizontal velocity component u only.

The first equation (4.48) is associated with the following initial conditions (δ is the initial elongation):

$$x(t=0) = \delta \quad (4.50)$$

$$\dot{x}(t=0) = 0 \quad (4.51)$$

while the initial and boundary conditions for the second equation (4.49) are:

$$u(y=0,t) = 0 \quad (\text{no slip condition}) \quad (4.52)$$

$$u(y=h,t) = \dot{x}(t) \quad (\text{coupling term}) \quad (4.53)$$

$$u(y,t=0) = 0 \quad (\text{zero initial velocity}) \quad (4.54)$$

To decouple the equations of this problem, Lu and Bailey solved this problem by assuming a linear velocity profile $u(y,t) = (y/h)\dot{x}$. They also considered the application of a constant force along the top surface of the meniscus to compute the velocity profile. Their developments led to several response times: they showed that considering the chip dynamics only, the pseudo-period of the oscillating motion was of the order of 3.77ms (using the underlying assumption of a linear velocity profile). On the other hand, they also showed that the characteristic time required for the velocity profile to become linear was of the same order of magnitude (5.3ms). Therefore, they concluded that both physics (chip dynamics and fluid dynamics inside the meniscus) were strongly coupled and should be solved accordingly. They consequently proposed an iterative scheme including the alternate use of Surface Evolver to compute the meniscus stiffness and of a CFD package to compute the liquid flow.

To solve the same problem more efficiently, we hereby propose to use an analytical model for the lateral stiffness and a resolution based on Chebyshev polynomials, which transform the coupled problem of equations (4.48-4.49) into the form of a system of constant-coefficients ordinary differential equations (ODEs).

We finally mention the need to study the other degrees-of-freedom (dof): beside the lateral motion, it is necessary to study the axial and tilt motions dynamically. Concerning the first one and additionally to the study of van Veen, partial information can be found in [53] (Stefan equation to estimate the axial viscous force), [137] and [148] (the latter one studied the compression flow modeling). As far as the tilt motion is concerned, we refer to the work of [82], where use is made of water and also glycerin ($\gamma = 0.0635 \text{ Nm}^{-1}$ and $\mu = 0.900 \text{ Pas}$) to study the oscillation of a tilted circular pad on a droplet for the self-alignment process. With their model, these authors estimated the damping ratio and the oscillating frequencies.

Lateral stiffness of liquid meniscus

General approach

The equilibrium shape of a meniscus is ruled by the so-called Laplace equation [92] which in the axially symmetric case is written as a non-linear second-order differential equation. Except in the case of a cylindrical meniscus or in the case of the catenoid, this problem does not have analytical solutions. Nevertheless, analytical approximations can be found in the case of circular and square pads. These approximations can be benchmarked using numerical solutions obtained with Surface Evolver [16]. It will be interesting to note that in both cases, the stiffness is proportional to half-perimeter of the wetted chip and to the surface tension, and inversely proportional to the gap. Another way to interpret this result is to note that the lateral stiffness is proportional to the ratio of the component size over the gap of the meniscus.

Circular pads

To estimate analytically the lateral stiffness of a meniscus confined between two

circular pads, we compute firstly the lateral area of a tilted cylinder of height h , radius R and shift s (also called elongation x in figure 4.28): this means that the cylinder axis is not perpendicular to both circles but inclined with an angle ϕ given by $\tan \phi = s/h$.

The vectorial equation of a point P of this cylinder is given by:

$$\begin{aligned}\bar{OP} &= z\bar{I}_z + s(z)\bar{I}_x + R\bar{I}_r \\ &= \left(\frac{z}{h}s + R\cos\theta\right)\bar{I}_x + (R\sin\theta)\bar{I}_y + z\bar{I}_z\end{aligned}\quad (4.55)$$

The lateral area is consequently equal to:

$$S = R \int_0^h dz \int_0^{2\pi} \sqrt{1 + \cos^2\theta \frac{s^2}{h^2}} d\theta \quad (4.56)$$

and the total surface energy of the system is here equal to:

$$E = \gamma S = \gamma R h \int_0^{2\pi} \sqrt{1 + \cos^2\theta \frac{s^2}{h^2}} d\theta \quad (4.57)$$

where γ is the surface tension.

The lateral restoring force is consequently equal to:

$$F = -\frac{\partial E}{\partial s} = -\frac{\gamma R s}{h} \underbrace{\int_0^{2\pi} \frac{\cos^2\theta}{\sqrt{1 + \cos^2\theta \frac{s^2}{h^2}}} d\theta}_I \quad (4.58)$$

The integral I in the latter equation can be numerically computed (see the result in Figure 4.29) or expressed in terms of elliptic integrals of the first (EllipticK) and second (EllipticE) kinds:

$$I = 4\frac{h^2}{s^2} \left[\text{EllipticE} \left(\sqrt{-\frac{s^2}{h^2}} \right) - \text{EllipticK} \left(\sqrt{-\frac{s^2}{h^2}} \right) \right] \quad (4.59)$$

Nevertheless, it is interesting to calculate it in our domain of interest (i.e. for small s/h ratio, $\sqrt{1 + \cos^2\theta \frac{s^2}{h^2}} \approx 1$ in equation (4.58)), which gives the following analytical relationship:

$$F = -\frac{\partial E}{\partial s} = -\pi R \gamma \frac{s}{h} \quad (4.60)$$

which corresponds to a constant stiffness k_c given by:

$$k_c = \frac{\pi R \gamma}{h} \quad (4.61)$$

The existence of an analytical expression of the stiffness allows the numerical simulation presented in section 4.3.6, where the advantages of such a resolution will be discussed.

This formulation has been benchmarked using Surface Evolver, in the case of $r = 50\mu\text{m}$, $h = 70\mu\text{m}$, $\gamma = 0.325\text{Nm}^{-1}$ and a volume of liquid given by $V = \pi r^2 h$. The comparison is plotted in figure 4.29. The discrepancy between the numerical and Surface Evolver results comes from the fact that the cylindrical geometry of equation (4.55) is not physically exact, since such a shape does not have a constant curvature.

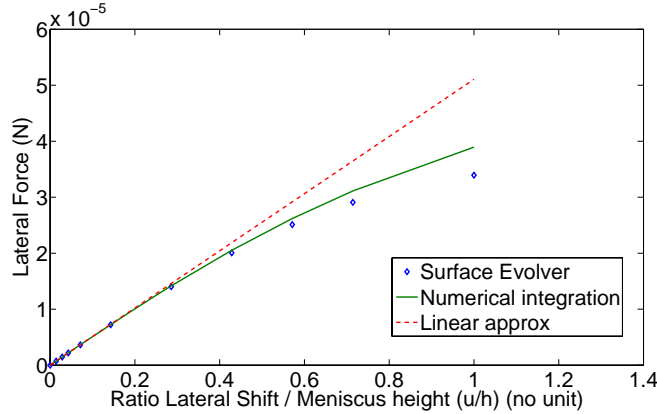


Figure 4.29: Lateral restoring force and related stiffness of a cylindrical meniscus: comparison between the Surface Evolver benchmark, the analytical approximation of equation 4.60 and the numerical evaluation of equation (4.58) ($R = 50\mu\text{m}$, $h = 70\mu\text{m}$ and $\gamma = 0.325\text{Nm}^{-1}$). Note that the '-' sign of the force has been omitted here.

Square pads

Tsai [180] already presented a model to compute the lateral stiffness of a square pad shifted by a distance s along one of its edges. This model is based on the assumption of a prismatic meniscus whose volume is equal to the area of the square pad multiplied by the gap. In this case, a shift of the component keeps the volume constant at constant gap, but the lateral area Σ of the liquid-vapor interface is increasing, given by:

$$\Sigma = 2ch + 2c\sqrt{h^2 + s^2} \quad (4.62)$$

Consequently, the surface energy E in this problem is given by:

$$E = \gamma\Sigma + C \quad (4.63)$$

where C is an arbitrary constant. The derivation with respect to the shift s leads to the restoring force:

$$F = -\frac{2\gamma cs}{\sqrt{s^2 + h^2}} \approx -\frac{2cs\gamma}{h} \quad (4.64)$$

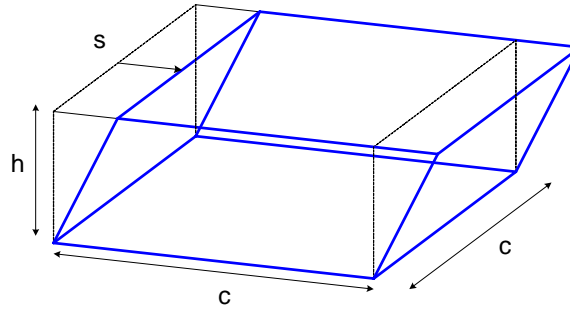


Figure 4.30: Geometrical model used to compute the lateral stiffness of a square pad

The approximation is consistent with the assumption that $s < h$ and consequently $s^2 \ll h^2$. To fix the ideas, let us consider $s < h/10$. Note that the force direction is opposite to the shift. The force derivative leads to the stiffness:

$$k_s = \frac{2ch^2\gamma}{(s^2 + h^2)^{\frac{3}{2}}} \approx \frac{2c\gamma}{h} \tag{4.65}$$

Note well that $2c$ in this formula is half perimeter of the pad, which was also the case in the circular pad ($\pi R\gamma/h$). The comparison between equation (4.65) and Surface Evolver is shown in figure 4.31, where again there is a small difference between the model and Surface Evolver because the shape of figure 4.30 does not have a constant curvature.

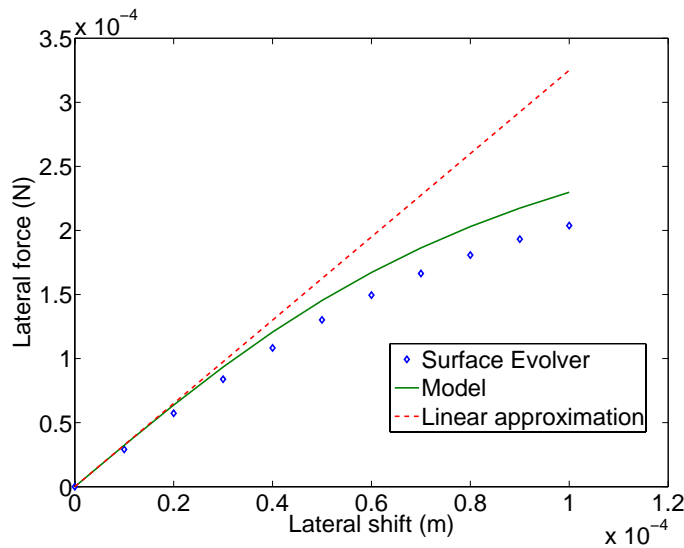


Figure 4.31: Lateral capillary force in case of a square pad with edge $c = 500 \mu\text{m}$, a gap $h = 100 \mu\text{m}$, a surface tension 325 mNm^{-1}

Coupled problem resolution with a pseudo-spectral method based on Chebyshev polynomials

The problem described by equations (4.48-4.49) is firstly normalized using characteristic length δ and time τ :

$$x = \delta \tilde{x} \quad (4.66)$$

$$t = \tau \tilde{t} \quad (4.67)$$

$$u = \frac{\delta}{\tau} \tilde{u} \quad (4.68)$$

where δ is the initial position of the chip and $\tau = \sqrt{\frac{m}{k}}$ is a characteristic time of the chip dynamics. The y coordinate ranging from 0 to h is replaced by \tilde{y} ranging from -1 to 1 ($y = (1 + \tilde{y})\frac{h}{2}$). This leads to two non dimensional equations:

$$\ddot{\tilde{x}} = -\tilde{x} - \underbrace{\frac{\rho Sh}{2m}}_{\tilde{m}^{-1}} \underbrace{\frac{4v\tau}{h^2}}_{\alpha} \frac{\partial \tilde{u}}{\partial \tilde{y}} \Big|_{\tilde{y}=+1} \quad (4.69)$$

$$\frac{\partial \tilde{u}}{\partial \tilde{t}} = \frac{4v\tau}{h^2} \frac{\partial^2 \tilde{u}}{\partial \tilde{y}^2} \quad (4.70)$$

with the following boundary and initial conditions:

$$\tilde{u}(\tilde{y} = -1, \tilde{t}) = 0 \quad (4.71)$$

$$\tilde{u}(\tilde{y} = +1, \tilde{t}) = \dot{\tilde{x}} \quad (4.72)$$

$$\tilde{u}(\tilde{y}, \tilde{t} = 0) = 0 \quad (4.73)$$

$$\tilde{x}(\tilde{t} = 0) = 1 \quad (4.74)$$

$$\dot{\tilde{x}}(\tilde{t} = 0) = 0 \quad (4.75)$$

It can be seen from both non dimensional equations that the problem only depends on two non dimensional parameters: (i) $\alpha = 4v\tau/h^2$ the diffusion coefficient and (ii) $\tilde{m} = 2m/(\rho Sh)$ the mass ratio.

In the following the symbol \sim has been dropped everywhere and the superscript (i) indicates the i th derivative with respect to y . With these conventions, the unknown velocity field u can be written as a series of Chebyshev polynomials $T_k(y)$:

$$u(y, t) = \sum_{k=0}^N a_k(t) T_k(y) \quad (4.76)$$

After some developments indicated in appendix F, a new (linear) system of equations can be written as:

$$M\dot{X} = AX \quad (4.77)$$

where the unknown vector X with $N + 2$ unknowns contains the unknown Chebyshev coefficients a_i and the chip position x :

$$X = (a_0 \ a_1 \ .. \ a_i \ .. \ a_N \ x)^T \quad (4.78)$$

The corresponding initial condition are:

$$X(t=0) = X_0 = (\underbrace{0 \dots 0}_{1 \times N+1} \ 1)^T \quad (4.79)$$

M and A matrices are detailed in Tables F.1 and F.2.

This constant coefficient system of ODEs (4.77) is easily solved analytically:

$$X_i = \sum_{j=1}^{N+2} r_{ij} w_j e^{\lambda_j t} \quad (4.80)$$

where λ_j is the j th eigen value, r_{ij} the i th component of the j th eigenvector associated with λ_j and w_j the j th component of the vector \mathbf{w} given by $\mathbf{w} = V^{-1}X_0$, and V is the matrix whose columns are the eigenvectors r_j .

Results and discussion

Benchmark

We have benchmarked our method with the theoretical results of Lu and Bailey [132], as indicated in figure 4.32 by superimposing the results of our work on the results of Lu and Bailey (figure 9 of their paper). The difference is about 4%.

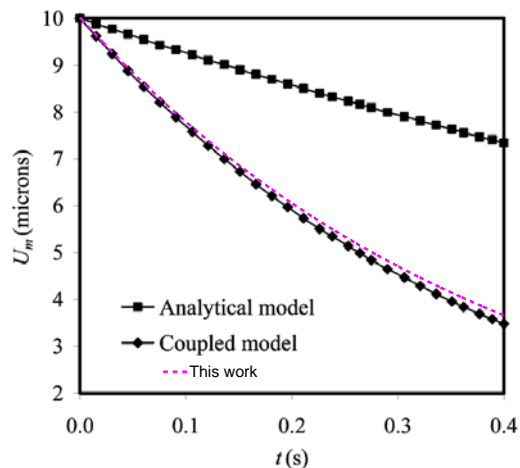


Figure 4.32: Benchmark of our solution by comparison with figure 9 from Lu and Bailey. For $\alpha = 0.18$, $\tilde{m} = 99$, $\delta = 10 \mu\text{m}$, $N = 11$, we found a non dimensional damping time $\tau_d = 0.3958$ where Lu and Bailey found $\tau_d = 0.3784$ (4% difference).

The main advantage of the proposed resolution method is to reduce the computing time drastically while still keeping the physics coupled (224 couples (\tilde{m}, α) can be

computed in 5-10 minutes), by comparison with the method of Lu and Bailey using Surface Evolver and a CFD package for the flow problem. This advantage permits the parametric study presented in the next subsection.

Numerical results

For any couple of parameters (α, \tilde{m}) , equation (4.80) gives $x(t) = X_{W+2}(t)$ the position of the plate as a combination of different modes whose amplitude decreases with time (real parts of λ_j are negative). Consequently, the decrease of x with time is governed by the slowest mode, i.e. by the mode with the eigen value λ whose (negative) real part has the smallest absolute value. τ is then equal to $-1/\lambda$. The combinatory space defined by $\alpha = 40 - 4000$ (logspace with 16 points) and $\tilde{m} = 400 - 1000$ (logspace with 14 points) has been explored, outputting a grid of 16×14 points. The τ_c at these points have been divided by their respective characteristic time $\tau = \sqrt{m/k}$ and interpolated with Matlab using the contour function in order to display the iso-lines of figure 4.33.

Experimental results

Thanks to a set up described in section 5.3, a large set of experiments has been performed, as indicated in Table 4.3, whose column "liquid ID" points to the liquid properties given in Table 4.4. The good signal-to-noise ratio given by the ratio of the average over the standard deviation of characteristic time τ is reported. Missing numbers in the table are experiments that were discarded because of smaller signal-to-noise ratio, that would have led to a large scattering of results ; they correspond to less viscous liquids, i.e. water ($\mu = 1$ mPas) and Dow Corning DC200FLUID10 oil ($\mu = 9.3$ mPas), leading to longer damping times up to 32 s: since $u(t)$ has not been registered on a sufficiently large period of time, the amplitude decrease was not large enough to ensure reliable fit, hence a larger standard deviation. For the other experiments, we can see in figure 4.33 the fair concordance between simulation and experimental results. Thanks to both non dimensional parameters α and \tilde{m} , the map of figure 4.33 contains all information concerning the dynamical lateral behavior of a liquid meniscus.

Analytical expression of the damping time

Additionally, it is worth noting that in figure 4.33, τ_d contour lines are essentially straight lines of the form:

$$\log_{10} \alpha - \log_{10} \alpha_0 = \beta (\log_{10} \tilde{m} - \log_{10} \tilde{m}_0(\tau_d)) \quad (4.81)$$

with $\beta = 1.0241$, $\log_{10} \alpha_0 = 4$ and the relationship between \tilde{m}_0 and τ_d being expressed as :

$$\log_{10} \tau_d = a + b \log_{10} \tilde{m}_0 \quad (4.82)$$

where $(a, b) = (3.7, -1)$ if $\log_{10}(\alpha - 4) > \beta (\log_{10} \tilde{m} - 3.55)$ else $(a, b) = (-3.4, 1)$ (figure 4.34). Consequently, the non-dimensional characteristic time τ_d of figure

Exp. nr	Liquid ID	α (no unit)	\tilde{m} (no unit)	Times				
				τ_{c-mean} (s)	τ_{c-std} (s)	$\frac{\tau_{c-mean}}{\tau_{c-std}}$ (no unit)	τ (s)	$\tau_d = \frac{\tau_{c-mean}}{\tau}$ (no unit)
34	Dymax	72.6	770	1.749	0.081	21.6	0.097	18.0
16	6	43.2	445	4.396	0.094	46.9	0.108	40.6
17	6	57.8	522	3.523	0.110	32.1	0.105	33.5
18	6	90.8	661	2.306	0.138	16.7	0.103	22.4
19	6	119	777	2.147	0.153	14.0	0.098	21.9
10	1	395	597	0.686	0.070	9.8	0.107	6.3
8	7	761	593	0.272	0.012	23.1	0.104	2.6
9	7	2390	1030	0.101	0.013	7.7	0.110	0.9
26	7	451	440	0.475	0.010	48.0	0.113	4.2
27	7	669	552	0.366	0.007	50.9	0.106	3.4
28	7	1580	855	0.236	0.009	26.8	0.104	2.2
3	2	1700	386	0.254	0.029	8.6	0.110	2.3
29	2	2190	439	0.193	0.010	20.2	0.109	1.7
30	2	2610	484	0.249	0.008	29.8	0.107	2.3
31	2	4030	609	0.305	0.024	12.6	0.104	2.9

Table 4.3: In this table, experiments are stacked by liquid ID (see also table 6.1). We indicate for each experiment the gap. The characteristic time τ is the characteristic time obtained from the dynamic response of the shuttle $u(t)$. As indicated in the text, these data have been averaged and the standard deviation has been used to compute a signal-to-noise ratio, which is shown to be always larger than 7.7. The characteristic time $\tau = \sqrt{m/k_d}$ is recalled – where m is the equivalent mass of the shuttle and k_d is the sum of the shuttle stiffness $k = 1 \text{ Nm}^{-1}$ and the meniscus stiffness measured in that experiment (not shown here). The last column gives τ_d , the non dimensional ratio of τ_c over τ , which is plotted in figure 4.33.

Liquid ID	ρ (kgm^{-3})	μ (Pas)	γ (Nm^{-1})	Supplier
1	970	0.485	0.0211	Rhodorsil R47V500
7	971	0.971	0.0212	Dow Corning DC200FLUID1000
2	973	4.865	0.0211	Rhodorsil R47V5000
Dymax	1050	0.055	0.025	ρ and μ : Dymax 628-VLV data γ : own measurement

Table 4.4: Liquid properties

4.33 can be estimated by the following expression in case $\alpha > 10$:

$$\log_{10} \tau_d = b \log_{10} \tilde{m} - \frac{b}{\beta} \log_{10} \alpha + a + \frac{4b}{\beta} \quad (4.83)$$

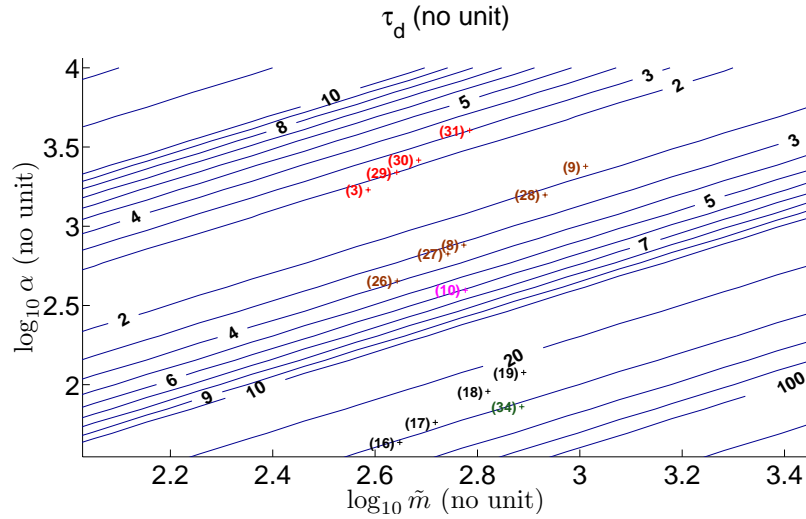


Figure 4.33: Non-dimensional map of damping times, for experiments 3,29-31 (Oil 2); 10 (Oil 1); 16-19 (Oil 6); 8-9,26-28 (Oil 7); 34 (Dymax 628 VLV). The family set of parallel lines represents the iso-values of $\tau_{d(sim)}$ obtained by simulation. Each experiment number is indicated between brackets, the '+' mark to its right showing the exact location of the experimental couple (\tilde{m}, α) . The numerical comparison between simulation and experiment can be found in Table 4.3, this map of iso-values of τ_d can be used to estimate the damping time. For example, experiment 30 ($\alpha = 2610$, $\tilde{m} = 484$) lies between the iso-line 2 and the iso-line 3 (the measured value is 2.3).

Over- and underdamping

Theoretically, a mechanical system governed by equation (4.48) is underdamped if $c^2 - 4km < 0$. Since c is related to the dimensional characteristic time τ_c by the relation $c = 2m/\tau_c$, the former condition for overdamping becomes $\tau_c > \sqrt{\frac{m}{k}}$ which can also be expressed using the non-dimensional damping time τ_d as $\tau_d > 1$. Experimentally, the last column of Table 4.3 indicates a border between both behaviors between 2 and 3 instead of 1.

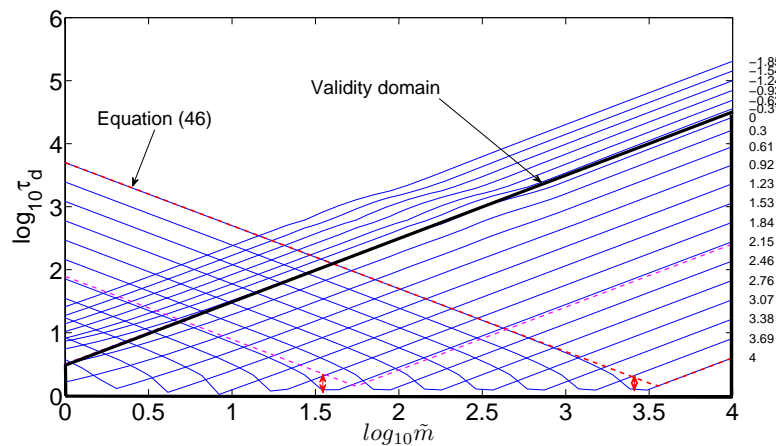


Figure 4.34: This figure graphically illustrates the evolution of the characteristic damping time τ_d of figure 4.33 as a function of \tilde{m} for different values of α (the small figures to the right of this plot indicate the values $\log_{10} \alpha$). It can be seen that these values can reasonably be estimated by straight lines (the red dashed line is given for $\alpha = 10000$, whose equation is given by equation (4.82)). The coefficients a and b associated to equation (4.82) are valid for $\log_{10} \alpha$ larger than 0. This simplified model suffers from a small lack of fit indicated by red double arrows. It is however shown with the magenta solid-dashed line the fair concordance, at least within the validity domain indicated by the bold black contour.

Summary

We showed that the coupled problem of liquid and chip dynamics could be efficiently solved with a pseudo-spectral method based on Chebyshev polynomials. The theoretical results were benchmarked using literature results, and a thorough experimental validation was pursued. Some discrepancies were however observed for low viscosity configurations (i.e. low values of the non dimensional parameter α). These discrepancies are thought to be caused by a too-short acquisition time of the position $u(t)$ of the chip, leading to a non-robust fitting and a characteristic time with large scattering. Therefore, for various experiments covering the experimental space $\alpha = 40 - 4000$ and $\tilde{m} = 400 - 1000$, the numerical proposed resolution and the subsequent modeling have been proven reliable. From the linear relation between α and \tilde{m} , we could propose a mathematical formulation of the damping time.

Future experiments will try to fix the scattering problem for low α experiments. Future work will consist in developing a full resolution of the liquid flow between the pad and the chip, in order to determine the limits of the spectral resolution. Finally, it could be interesting to develop two new experimental set-ups: the first one would include a heat source in order to work with actual solder pastes, and the second one would be downsized in order to tackle the $10 - 100 \mu\text{m}$ scale.

4.3.7 Discussion and perspectives

The study of capillary forces led in this section is manifold:

1. the condition of imposed contact angle versus the condition of pinned triple line have been studied. We showed a double iterative scheme to address the problem of moving triple lines with given contact angle. At the contrary, section 4.3.3 highlighted some useful analytical relationships to estimate capillary forces in the case of fixed triple line, i.e. when the triple line is blocked by chemical surface treatments or by structured roughness of the substrate;
2. the study has been led within the frameworks of statics and dynamics, for fixed triple lines;
3. the cases of axial and lateral forces have been considered.

These models can be used to study adhesion, self-centering effects of liquid bridges, capillary forces between components... More conceptually, a liquid bridge between two solids can also be seen as a mechanical joint with 6 degrees-of-freedom, and consequently defined by 6 stiffnesses and 6 damping coefficients.

If z is assumed to be the symmetry axis of such a liquid bridge, translations x and y are identical. Similarly, θ_x and θ_y also present the same behaviors. In this

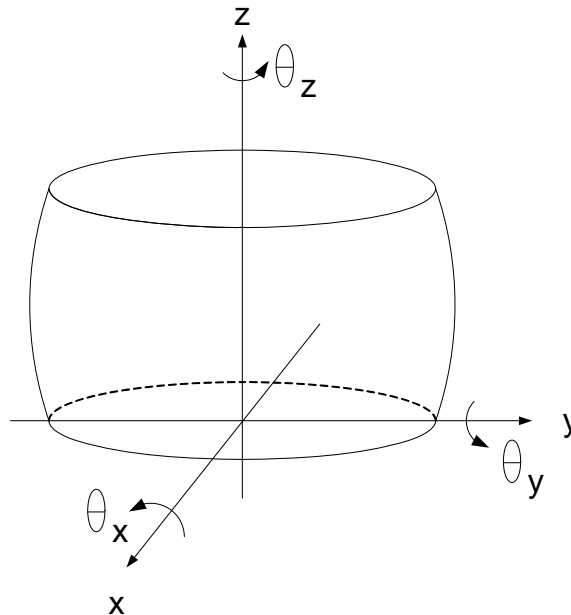


Figure 4.35: Liquid joint with 6 degrees-of-freedom

section, we developed the stiffnesses k_r (radial stiffness computed as the second derivative of the surface energy) and k_z (axial stiffness computed with the numerical tool or the parabolic and circular models), and the damping coefficients b along the z axis (equation 4.45) and through map concerning the radial motion (figure 4.33). The tilt $\theta_x = \theta_y$ has been studied by Kaneda et Al. [82], as schematically illustrated in figure 4.36.

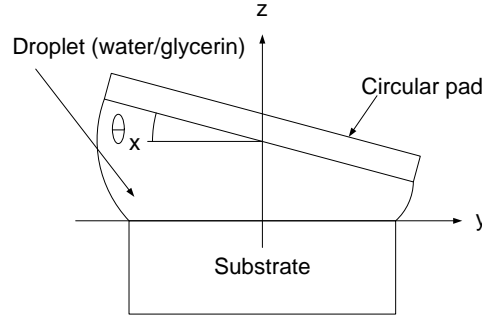


Figure 4.36: Kaneda

Actually, since a mechanical structure is likely to be supported by several liquid joints such as shown in 2D in figure 4.37, the restoring couples are mainly generated by the restoring forces multiplied by the typical distance L between the joints. In other words, we assume the capillary torque to be much smaller than the torque of capillary forces. To validate this assumption, we started from the motion equation of the oscillating pad given by [82]:

$$I\ddot{\theta}_x = T \quad (4.84)$$

where I is the inertia momentum of the circular pad of figure 4.36, θ_x the tilt angle of this pad and T the capillary torque. In the results presented by Takeda for a disk with a radius $r = 1.9$ mm, the the oscillating frequency is 6.5 Hz, which corresponds to a pulsation $\omega = 40.8$ rad \cdot s $^{-1}$. Consequently, if we assume:

$$\theta_x = \theta_{x0} \cos(\omega t) \quad (4.85)$$

this gives (with $\theta_{x0} \approx 7^\circ$) $\ddot{\theta}_x \approx 207$ rad \cdot s $^{-2}$. Using the value of I given by Takeda ($I = 1.15 \cdot 10^{-11}$ kg \cdot m 2) we find that:

$$T \approx 2 \cdot 10^{-9} \text{ Nm} \quad (4.86)$$

Now, let us find the order of magnitude of the torque generated by the capillary forces, in the configuration of figure 4.37 where the liquid joints are separated by a distance $2L$ (the order of magnitude of L will be chosen compatible with the dimensions of the liquid bridge of Takeda, let us say 2 mm).

1. the stiffness of both liquid bridges is estimated using the map of figure 4.24. Based on the images given by Takeda, we found the contact angle to be about

100° and the gap about 1.25 mm, leading to a aspect ratio $h/r = 0.66$. For these values, the map indicates a stiffness of about 100 Nm^{-1} ;

- the distance L and the tilt angle θ_{x_0} lead to the order of magnitude of the elongation of each liquid bridge (the left one is compressed, the second one is stretched):

$$e = L \tan \theta_{x_0} = 0.25 \text{ mm} \quad (4.87)$$

- each capillary force is consequently about:

$$F = k \cdot e = 25 \text{ mN} \quad (4.88)$$

- the torque exerted by this couple of forces is:

$$\Gamma = 2LF = 10^{-4} \quad (4.89)$$

We see that the torque exerted by the capillary forces Γ is 5 orders of magnitude larger than the capillary torque T . This conclusion has been obtained for millimetric liquid bridges. Nevertheless, the conclusion should remain valid for smaller liquid joints since the capillary torque T scales down as $T = \gamma \ell^2$ (since surface tension is expressed in Nm^{-1}), while the torque of capillary forces Γ scales down as $\Gamma = 2Lke = 2\theta_{x_0} k \ell^2$ (assuming an identical tilt angle and a constant aspect ratio for the liquid bridge, leading to a constant stiffness over scales). We can see that the scaling laws for both torques are identical.

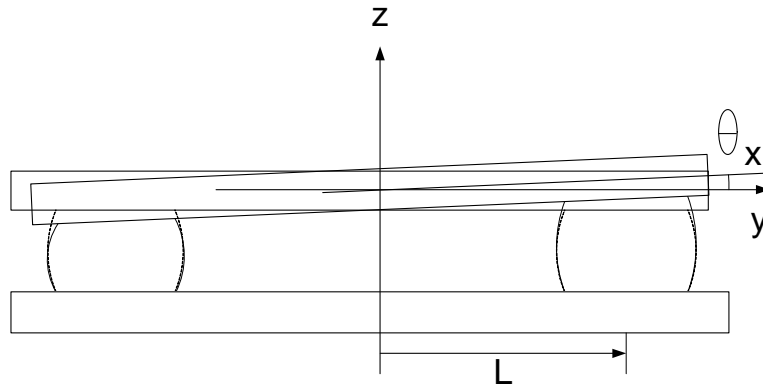


Figure 4.37: 2D representation of a solid linked to a substrate by two liquid joints

Concerning the last degree-of-freedom to discuss (rotation about the symmetry axis), the elastic capillary torque about the z axis is null in case of perfect axial symmetry - however the damping torque is not. For non axially symmetric shape, Takei et Al. [175] proposed an elegant method to compute the capillary torque with a perturbation method due to De Gennes [42]. An example of studied geometry is proposed in figure 4.38. Once again, the restoring torque is of the order of 10^{-10} Nm .

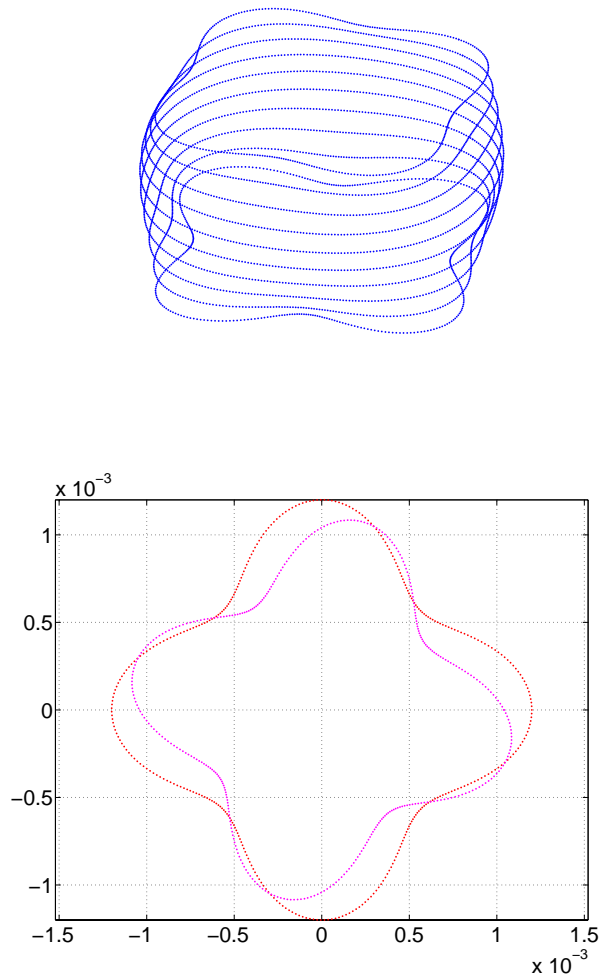


Figure 4.38: The bottom geometry (in red) is a circle of radius 1mm with a perturbation of radial amplitude equal to 0.2mm and a frequency of 4. The top geometry (in magenta) is a circle of radius 0.9mm with a perturbation of radial amplitude equal to 0.2mm and a frequency equal to 4. The angular deviation between both geometry about the z axis is here 45° . (Based on the work of [175])

4.4 Additional contributions to capillary forces modeling

Since the criteria statics vs. dynamics and lateral vs. axial led to the concept of liquid joint, we grouped all the related aspects in the previous section. This new section gives details on two additional contributions:

1. the capillary force model has been applied to the capillary condensation problem, and subsequently experimentally validated at the nanoscale. Details are given in section 4.4.1 and [27, 29]. This work has been done by Alexandre Chau during his PhD (2003-2007).
2. the surface tension physics has been coupled with gas law, in order to combine compliance coming from gas compressibility and compliance due to surface tension. This framework can also be applied to the comprehension of the effects of residual gas bubbles in liquid environments (problem of micropumps priming or problem of microvalves with movable part). Details are provided in section 4.4.2 and in [117]. A patent is currently pending. This work constitutes the ongoing but finishing PhD of Cyrille Lenders (2005-2010).

4.4.1 Validity of capillary force model at the nanoscale

Adhesion issues are present in many disciplines such as, for examples, surface science, microrobotics or MEMS design. Within this framework, we investigated the role of capillary forces due to capillary condensation. A simulation tool had been developed using Surface Evolver and Matlab to compute the shape of a meniscus in good agreement with the Kelvin equation and contact angles [28]. The numerical results of this simulation are well complying with literature results. One very important result is the ability to compute the evolution of the capillary force depending on the tilt angle of the gripper with respect to the object.

The main contribution of this work is however the experimental validation of these numerical results, illustrating the role of humidity and tilt angle in capillary forces at the nanoscale. This extends the validity domain of the model from the nanoscale (in this section, 100 nm) to the milliscale (see previous sections, up to a few mm).

Positioning of the capillary condensation framework

When considering applications at small scale, adhesion cannot be ignored. For example, capillary adhesion is important in micromanufacturing [195] or in assembly of small components [135]. Contrary to macro world ruled by gravity, small scale applications are governed by surface forces. Indeed, when size diminishes and the objects are scaled down, surface forces become more important and the major opposing force to picking up and releasing micro- and nanocomponents becomes the

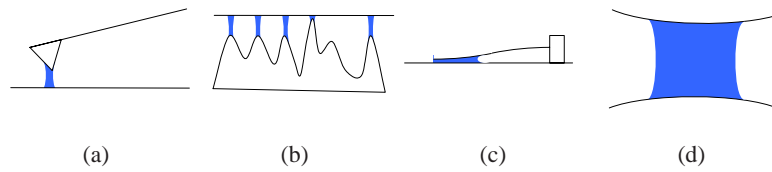


Figure 4.39: Some case studies in which capillary condensation can occur: (a) adhesion between an AFM tip and a substrate; (b) capillary bridges between roughness asperities and a – rough or not – substrate; (c) stiction of a cantilevered beam, and (d) scheme of the problem tackled in this work (two solids S_1 and S_2 are linked by a capillary bridge. Besides geometry, the main parameters of this problem are the contact angles made by the liquid on S_1 and S_2 , surface tension γ of the liquid and the surrounding humidity).

force of adhesion [74]. The force needed to separate two objects is also known as pull-off force. Adhesion can also prevent structures like RF-MEMS or any high aspect ratio structures from normal functioning [86].

The adhesion force is actually composed of different components : electrostatic force, van der Waals force, chemical forces, and capillary force. Electrostatic force can be avoided by choosing materials properly (conductive materials to avoid charge accumulation and similar junction potentials to avoid a capacitive effect between two objects brought close to one another). Van der Waals force arises from the intrinsic constitution of matter : it is due to the presence of instantaneous dipoles. It becomes non-negligible at the nanometer scale. Chemical forces are due to the bondings between objects. It is active when objects are in contact (*i.e.* the distance between them is about an intermolecular distance).

Capillary force between two objects is due to the presence of liquid between them (see figure 4.39). It has already been shown [100, 108] that it can be used to manipulate submillimetric objects (with 300 – 500 μm characteristic dimension) by manually placing a liquid droplet on the object (a fraction of μL). At nanoscale liquid comes from capillary condensation of ambient moisture.

This nanomanipulation will require force modulation, in order to pick up and release components: the picking force should be larger than the other forces while the force applied on the component during release should be lower than its weight or any other adhesion force. It is proposed here to control the force by tilting the tip (an application could be an AFM tip) with respect to the object. Models which assume objects and meniscus to be axially symmetrical [174, 144], therefore, become inapplicable. A more general model thus has been developed to compute the capillary force without this constraint of axisymmetry.

Kelvin equation

In any method used to compute the capillary force, the meniscus shape appears explicitly or implicitly. In the Kelvin equation approach, the meniscus geometry is involved through the total mean curvature H of the meniscus, or its inverse r , the mean curvature radius

$$H = \frac{1}{r} = \frac{1}{2r_K} = \frac{1}{2} \left(\frac{1}{r_1} + \frac{1}{r_2} \right) \quad (4.90)$$

where r_K is, in the case of capillary condensation, the so-called Kelvin radius, and r_1 and r_2 are the two principal curvature radii. The Kelvin radius is governed by the Kelvin equation [1, 74] which is the fundamental equation for capillary condensation. It links the curvature of the meniscus with environmental and materials properties:

$$r_K = \frac{\gamma V_m}{RT \log_e(p/p_0)} \quad (4.91)$$

where V_m is the molar volume of the liquid, R is the gas constant (8.31 J/mol K), T the temperature (in Kelvin) and p/p_0 is the relative humidity (RH), between 0 and 1. Typically, for water, this gives $r_K = 0.54 \text{ nm}/\log_e(RH)$, which gives for RH=90%, a Kelvin radius of about 5 nm at 20°C.

Validity of the equations

Both methods presented here are based on macroscopic assumption on the nature of the liquid and solids : matter is continuous and so are their properties such as surface tension. It has been shown experimentally that the Kelvin equation is valid down to menisci of radii in the range 4-20 nm for cyclohexane condensed between mica surfaces [60] and in the range 5-65 nm for water [85]. For smaller radii, the discrete nature of matter should be taken into account, via molecular dynamics or Monte-Carlo calculations [76]. The results will thus have to be interpreted keeping in mind that their validity is not proven for very small sizes of meniscus (*i.e.* for menisci with radii < 4nm).

Another question raised by the literature is the parameter which is kept constant during the derivative : should the latter be computed keeping the volume or the curvature constant [172] ? Different mechanisms play a role here, mainly the condensation/ evaporation rate. It seems that the condensation takes place on the millisecond (< 5 ms [172]) scale while the evaporation needs more time. It has been measured that meniscus stretching at tip-object distance is much larger than r_K . Capillary condensation also has a long term (up to tens of days) component, which will not be considered here [161].

If experimental investigation could provide an estimation of the characteristic times involved in the processes, it would seem natural to compute the volume condensed -fulfilling the Kelvin equation- at the smallest tip-object distance and then compute the evolution of the force with constant volume when retracting the tip.

Simulation tool

The numerical model presented in [27] is able to cope with non-axisymmetrical menisci, based on the energetical approach described previously. The solver makes use of the software Surface Evolver (SE) [16] to compute the meniscus shape and henceforth to compute the surface energy and the capillary forces.

To develop complex shapes without having to define each point of the tip (or the object), analytical shapes have been used. In the xz plane (see figure 4.40), usual profiles can be chosen : circular, conical or parabolical, while in the (x,y) plane, the section of the tip can be described as a polar function.

Elementary sections are

- circle : $r(\theta) = R$
- triangle : $r(\theta) = c/(2\sqrt{3}\cos\theta)$ for $-\pi/3 < \theta \leq \pi/3$
- square : $r(\theta) = c/(2\cos\theta)$ for $-\pi/4 < \theta \leq \pi/4$

In a similar way, any regular polygon of side length c can be very easily implemented. Actually, virtually any section can be represented as it is developed in Fourier series (in polar coordinates) in order to obtain an analytical shape in the domain $\theta = [0; 2\pi]$.

The profile and section are then coupled to obtain the complete tip that has to be used in the equations. An example of a tip with parabolic profile and triangular section is shown in figure 4.40. Such a geometrical description can also be applied to the object.

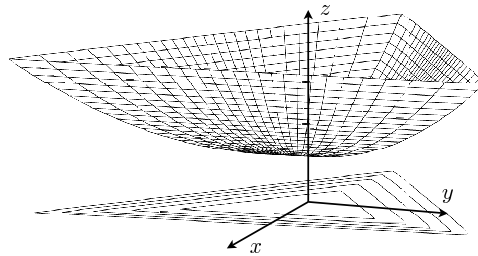


Figure 4.40: Example of a tip and its projection on the (x,y) plane. Here, the section is a triangle and the profile is a parabola (Reproduced with permission from [27] © 2007 IEEE)

Experimental results

The model presented here above computes only the capillary component of the adhesion force, while experimental results include all other effects (van der Waals and electrostatic forces). In order to compare model results with experimental ones, we chose to vary a parameter that had an effect only on capillary force (see section 5.4 for a detailed description of the testbed).

The most relevant parameter meeting this criterion is relative humidity. Indeed, the assumption that relative humidity has minor impact on other forces than capillary force is acceptable. The variation of the capillary force with respect to relative humidity can thus be computed and experimentally measured.

In figure 4.41, different batches of pull-off measurements have been made with varying RH. A least squares fit is then made on the points. It is shown as a dashed line. For the same geometry, computations have been made, and the results are given by the solid line (as already said, only the slope of these curves is to be observed, *i.e.* the dependence on humidity). The simulation gives a slope of $0.23nN/\%$ while the best fit leads to a slope equal to $0.27nN/\%$ with a standard deviation equal to $0.035nN/\%$. In these simulations the contact angles have been assumed close to zero since they cannot be measured at this scale.

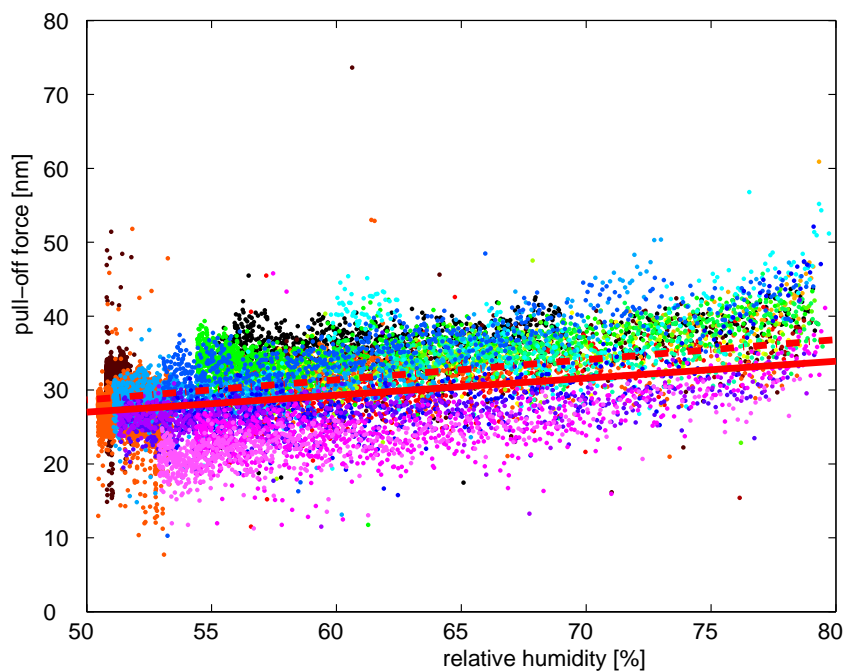


Figure 4.41: Force measurements : for different humidities, the pull-off force has been measured. The dashed line is the linear regression of the measurement points. The solid line is the result of the model.

Similarly, the measurements and computations of figure 4.41 have been done for different tip to substrate tilt angles. The results are shown in figure 4.42. Results qualitatively fit but a significant deviation can be observed. One assumption is that there is an error in the angle u between the tangent to the mica substrate placed on the bottom of the environmental box (figure 5.18, detail 9) and the cantilever which is glued on the holding part (figure 5.18, detail 10). This error can come from different sources: gluing of the cantilever on the holding part, manufacturing and assembly errors in the chain linking the holding part to the environmental box,

alignment error between the bottom of the box and the mica substrate. This error cannot be measured easily in our setup, consequently we decided to study the sensitivity of the capillary force to this angle parameter u . To do so, the environmental box was tilted with respect to the reference horizontal orientation. The capillary force as a function of this tilt angle (i.e. variation of u) is plotted in figure 4.42.

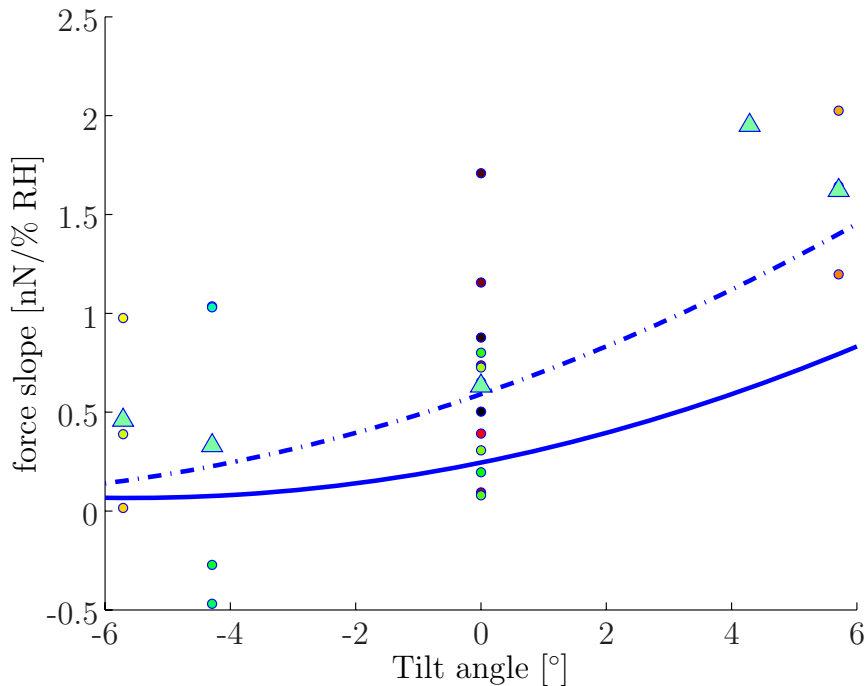


Figure 4.42: Slope of the pull-off force vs humidity with respect to the tilt angle. For each tilt angle, the mean is given by the triangles. The 4th triangle must be treated with care as it is based on a single batch. The solid line is the result of the model; the dot-dashed line is the result of the model for a 4 degree tilt bias because this 4 degree tilt deviation is assumed to be a measure for the uncertainty in the initial value of the angle u (it is shown for sensitivity demonstration purpose).

Discussion

In the previous paragraphs, it was shown that our model could be used to compute the capillary force between two objects for usual shapes : spheres, cones, planes,... and reproduce existing results. In addition, the three-dimensional capabilities of the model allow the user to compute capillary force for complex configurations with simple shapes or even with complex shapes (e.g. pyramids, rounded pyramids that can model the Berkovich AFM tips).

Results presented in figures 4.41 and 4.42 show fair agreement between experimental and theoretical measurements. Different sources of measurement noise

were identified out of which the main one was the surface modification. To overcome the scatter, we repeated the measurements to be able to have statistical results. Another method to limit the scatter could be to work with atmospheres of controlled composition, not just humidity control.

A very interesting result presented is that the force can be varied using tip tilting. This should allow the user to pick up and release a part by controlling the tilt angle of the tip with respect to the object.

To give the order of magnitude, a force of about 50 nN is sufficient to lift a cube of about 280 μm for a density of 2300 kg/m^3 (approximately the density of silicon). For objects with such masses, a tip should be able to pick up, manipulate, and then release them.

The manipulable part weights can also be extended using different tip shapes or using multiple tips

To conclude this section, let us recall the development of a three-dimensional model for the computation of the capillary force, allowing to compute the effects of capillary condensation, with configurations that are not mandatorily axisymmetrical. The model has been validated by comparing it with existing theoretical results. The model was also compared to experimental results using a dedicated test bench. The comparison has shown fair correspondence even if the quantitative correlation is arguable. Experiments under controlled atmosphere could improve measurements.

It was shown here that the tilt angle of a tip with respect to a flat substrate is an important parameter to vary the capillary force between them. This result is promising for a new application in micromanipulation of components. Nevertheless, experiments are going on to determine how to make use of this effect with better repeatability.

4.4.2 Gas law and capillary forces

This work done by Cyrille Lenders⁸ has three distinct origins:

1. the breakdown of microvalve made of a small free ball applied to or expelled out of its seat by the driving pressure: except by filling a microfluidics circuit under vacuum, residual air bubbles in liquid are a source of liquid-gas interfaces and therefore of surface tension effects. These effects are likely to prevent the closing of the valve, because air bubbles present a relatively strong stiffness at small scales (this was shown for liquid menisci in section 4.3). Additionally, the volumic effects vanish with decreasing dimensions, preventing the buoyancy from pushing the bubbles upward. A detailed analysis is reported in Lenders's master thesis [115];
2. the increasing need in microtechniques for new sources of compliances: this analysis relies on the switch from ductile materials such as steel and aluminum to brittle materials such as glass⁹ and silicon. While ductile materials accommodate manufacturing and positioning errors, brittle materials cannot. Therefore, joining at the 100 μm is unlikely to be achieved with a downscaled screw in silicon: it will rather be done using press-fit (see for example the study by Bourgeois [12]), which relies on the Lamé-Clapeyron relationship (the joining force is proportional to the interference). Bourgeois explains how the introduction of compliance in the substrate reduces the scattering on the joining force for a given diameter scattering. Therefore, microtechniques is not only focused on "increasing stiffness" but can also require new sources of compliances. The purpose of this study was therefore to quantify the compliance introduced by a "gaseous joint" (by analogy with the liquid joint of section 4.3.7).
3. the miniaturization of flexible fluidic actuators, which is a hot topic in actuators research for biomedical applications [67]. These actuators are made of flexible membranes inflated with a fluid (pressure and volume are the inputs) in order to apply a force and a displacement. At scales smaller than the millimeter, the membrane can simply be replaced by the interface between a liquid (surrounding medium) and an actuation gas.

Presentation of the problem

The proposed transducer is based on a gas bubble confined between a top movable plate (called the platform) and a bottom plate (called the substrate). Laterally, the gas bubble is confined by the gas-liquid interface which exists thanks to the surface tension between both media. The gas inside the meniscus can be compressed thanks to a control variable u which commands a piston moving in an inlet

⁸Ongoing PhD (2005-2010)

⁹even if the behavior of glass may be discussed

tube drilled into the substrate. By adequate manufacturing, the contact line of the meniscus with the platform and the substrate is fixed. The total volume of gas is

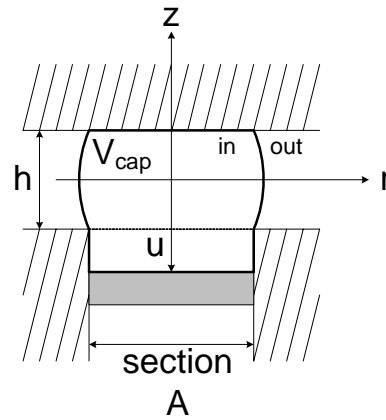


Figure 4.43: Sketch of the surface tension transducer (also called fluidic leg)

the sum of the volume confined by the meniscus V_{cap} and the volume of the inlet pipe uA , where A is the section of the inlet pipe. The position of the platform is indicated by the gap parameter h . The pressure outside the meniscus is p_0 and the pressure in the meniscus is p , different from p_0 (see the next section).

Physics

The underlying physics is twofold:

1. the surface tension effects, mainly characterized by two aspects: (1) there is a pressure gap dp between both sides of the meniscus interface, which is ruled by the so-called Laplace law:

$$dp = 2H\gamma \quad (4.92)$$

where $2H$ is the curvature of the meniscus (1/m) and γ the surface tension (N/m)

2. the compressibility of gas, described by the well-known gas law:

$$\underbrace{(p_0 + dp)}_{\text{Pressure inside the meniscus}} \underbrace{(V_{\text{cap}} + uA)}_{\text{Total volume}} = nRT \quad (4.93)$$

Both effects contribute to the compliance of the device and allows to use it as a sensor (based on the pressure measurement) or an actuator (use of the control variable u).

Stable generation of gas bubbles

A preliminary requirement to the projected device is the stable generation of gas bubbles in liquid, each bubble corresponding to a fluidic leg bearing the platform.

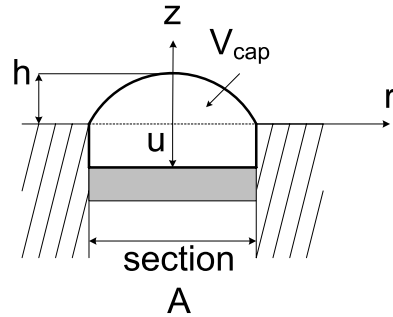


Figure 4.44: A gas bubble can be generated by pushing the piston of section A, i.e; by decreasing u

After various trials described in [116], we came to the principle described in figure 4.44: the piston pushes the gas out of the pipe of section A, leading to the formation of a spherical cap of height h and volume V_{cap} . Lenders showed that the height of the bubble h was governed by a fifth degree polynomial, whose a solution

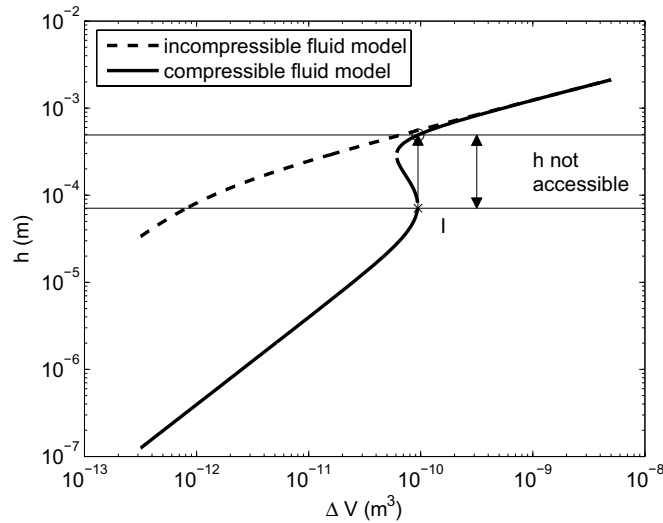


Figure 4.45: Evolution of bubble height with volume variation (second set of parameters), i.e. with the volume swept by the piston in the syringe. In this configuration, the model gives three solutions for a range of ΔV . Physically, the bubble will grow all the way to point I, then its height will jump suddenly to the upper curve. This growing instability means there is a whole range of height that cannot be reached (see the text for the definition of ΔV).

can be numerically found, as illustrated in figure 4.45 (ΔV is the volume displaced by the piston during a translation Δu , and is counted positive when the volume in the cylinder decreases, i.e. when u decreases). We see in this figure an instability avoiding to reach all the values of the cap height h .

The conditions for stable bubbles generation were studied numerically and analytically. But preliminary, the governing equation was normalized, leading to:

$$\frac{\pi\tilde{P}}{384}\tilde{h}^5 + \frac{\pi}{48}\tilde{h}^4 + \frac{\pi\tilde{P}}{96}\tilde{h}^3 + \left(\frac{\pi}{16} - \frac{\pi\tilde{E}}{8} + \frac{\tilde{P}}{8}\tilde{v}\right)\tilde{h}^2 + \left(\frac{\pi\tilde{P}}{128} + \tilde{v}\right)\tilde{h} + \frac{\tilde{P}}{8}\tilde{v} - \frac{\tilde{E}}{8} = 0 \quad (4.94)$$

where \tilde{v} is the normalized volume of gas and \tilde{h} the normalized droplet height (ratio of the physical height over the s corresponding to section A, $\tilde{h} = 1$ states for a hemispherical bubble). \tilde{E} is a reduced energy parameter and \tilde{P} is a reduced pressure, both respectively given by:

$$\tilde{E} = \frac{nRT}{\gamma s^2} \quad (4.95)$$

$$\tilde{P} = \frac{p_0}{\gamma/s} \quad (4.96)$$

where n is the number of gas molecule in the pipe and the cap, $R = 8.32 \text{ Jmol}^{-1} \text{ K}^{-1}$ is the gas constant, T the absolute temperature of the gas, p_0 the pressure in the liquid (i.e. the atmospheric pressure since the liquid height is small enough to neglect hydrostatic pressure) and s is the diameter corresponding to section A.

It is remarkable in equation (4.94) that the normalized height only depends on \tilde{E} , \tilde{P} and \tilde{v} . Moreover, \tilde{v} is an actuation parameter, related to the volume displaced by the piston translation during the bubble generation. The existence of an instability is consequently only governed by \tilde{E} and \tilde{P} . Based on this observation, a map could be built indicating the (un)stability for each couple (\tilde{E}, \tilde{P}) , as illustrated in figure 4.46. We can therefore deduce that stability is ensured by the condition:

$$\sigma \equiv \frac{p_0^2 s^4}{\gamma n R T} > 1 \quad (4.97)$$

Tedious developments given in [116] also lead to an analytical estimation of this criterion:

$$\sigma \equiv \frac{p_0^2 s^4}{\gamma n R T} > \frac{128}{27\pi} \approx 1.5 \quad (4.98)$$

The difference between both criteria is very small, as shown in figure 4.46.

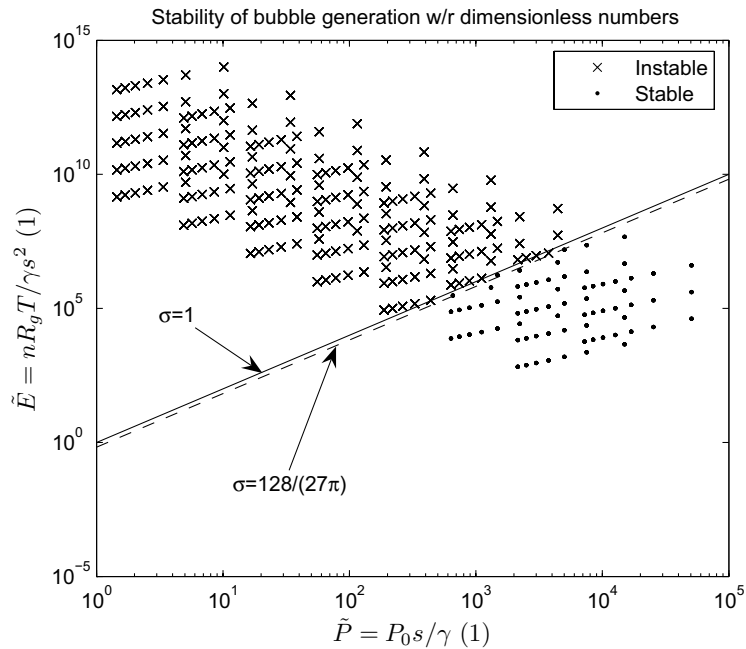


Figure 4.46: We have run several simulations varying the input parameters. The crosses represent the configurations that led to an instability during bubble growing. The dots represent the configurations for which the growing was continuous. There is a clear border between both situations that can be approximated by a solid line corresponding to the numerical limit $\sigma = 1$ given by equation (4.97) and a dashed line corresponding to the analytical limit $\sigma = \frac{128}{27\pi}$ of equation (4.98).

Models of the actuator

The actuator model to set up must be able to output the position or gap h as a function of the control variable u and the external force f the actuator works against. Additionally, due to our physics, a second output can be predicted, namely the pressure inside the meniscus $p + dp$.

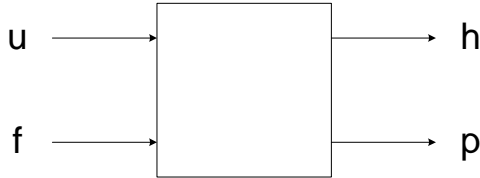


Figure 4.47: Diagram of a generic actuator with two inputs (the control variable u and the exerted force f) and two outputs (the position or gap h and the pressure inside the meniscus $p = p_0 + dp$)

A parabolic model has been developed (see appendix G) for this kind of actuator, while Lenders developed a numerical resolution of equations (4.92)-(4.93). An example of results obtained by Lenders is given in figure 4.48, showing that the force developed by the actuator is a trade-off between the tension effect which pulls the platform downwards (the force is negative) and the pressure force which pushes the platform upwards (the force is positive). The actuator can therefore acts in both directions.

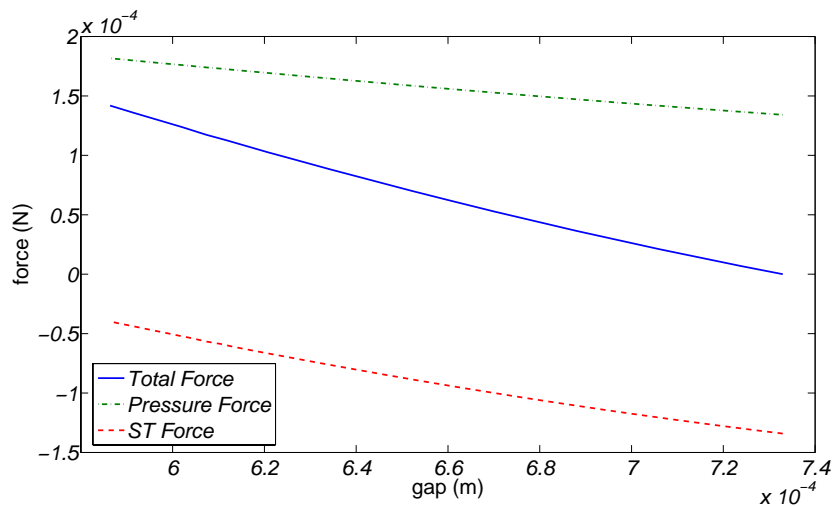


Figure 4.48: Simulation of the force-displacement behavior of a fluidic leg (Parameters: $V_0 = \frac{nRT}{p_0} = 98.17 \cdot 10^{-9} \text{ m}^3$, $T =$, $\gamma = 72 \text{ mNm}^{-1}$, s , $p_0 =$.)

4.5 Other contribution

4.5.1 Influence of surface topography on electrostatic adhesion

Marion Sausse-Lhernould studied¹⁰ the influence of surface roughness on electrostatic adhesion. She showed [125, 121, 122, 176] the decrease of electrostatic forces with increasing roughness, even for very small roughness (R_q of the order of a few nm). The points developed in her work are manifold:

1. preparation of samples by mechanical and electrochemical polishing;
2. scanning of the surface and modeling the roughness through two fractal parameters: the dimension D and the amplitude G ;
3. simulation with the Comsol Multiphysics Software the effect of roughness on electrostatic adhesion;
4. experimental validations thanks to the adaptation of the experimental testbed (see section 5.4)¹¹

To illustrate the results of this PhD thesis, we give the comparison between simulation and experiments for the interaction between a $10\mu\text{m}$ diameter sphere and a plane (figure 4.49).

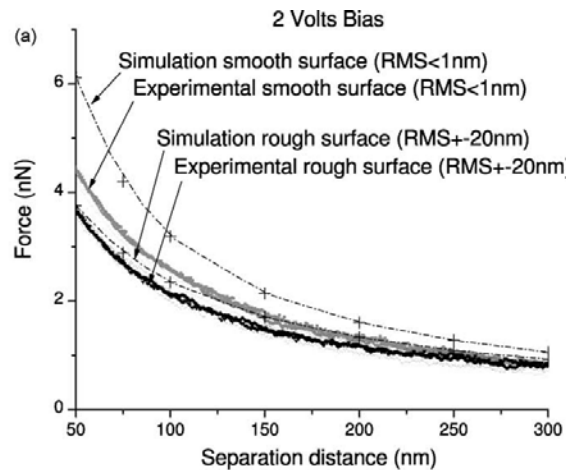


Figure 4.49: Comparison between experimental measures and numerical simulations in the case of a $10\mu\text{m}$ diameter sphere and a plane. The plot shows the result for a 2V bias (from [176])

As it can be seen, the effects of roughness is to reduce the electrostatic adhesion force drastically, even for small roughness (RMS in the order of a few nm).

¹⁰PhD thesis (2004-2008)

¹¹These experiments were successfully replicated in Lawrence Berkeley National Lab

4.6 Conclusions

This chapter clearly highlighted our contribution to capillary forces modeling in many directions: lateral forces, dynamics, nanoscale, multiphysics enhancement. Additionally, a contribution was achieved in describing the role of surface topography on electrostatic adhesion. These contributions constitute the scientific foundations of any reliable application submitted to adhesion or surface tension drivers, as for example the demonstrators presented in chapter 6. Next chapter will describe the tools developed for experimental validation of these models.

Chapter 5

Measurement set ups

5.1 Introduction

This chapter is devoted to the experimental set ups which have been designed and developed to validate the models proposed in our research. These set ups are sketched in figure 5.1. We can see again the main track exploring the capillary forces from static vs. dynamic and axial vs. radial points of view (details 1-3). These first three set ups were developed with the related models among the same research projects: tes bed (1) for static axial forces measurement was developed by myself during my PhD (2000-2004), (2) was developed by Jean-Bastiste Valsamis during his PhD (2006-2010) and (3) was my contribution to the Hydromel project in 2009. The fourth set up targeting force measurement in the nanonewton range was much more complex to build and is the result of a collective work done under my supervision¹. It was used by Chau in 2007 and Sausse in 2008 for the results presented in their PhD's. Lenders is still working on it. Beside these four set ups mainly dedicated to capillary forces measurements, other set ups have been designed. Vandaele applied the so-called "wire technique" (5) to the measurement of acoustic forces presented in his PhD in 2008. At the same time, I developed a 2 axis measurement set up during my research at EPFL in 2008 (6). I owe Professor Clavel a debt of gratitude for indicating me the other design sketched in (7), which is currently under achievement in the PhD work of Angelo Buttafuoco² at Université libre de Bruxelles.

The large variety of efforts measured with these test beds is represented in figure 5.2, in which each case study is positioned in a force-scale map. The scale here is the typical length of the considered case study. For example, forces generated by capillary condensation (1) were measured to be about tens of nanonewtons with

¹design: Lambert, Chau and Bastin (who worked with me as a master student during the year 2006-2007 and as a researcher paid by the ARC project from the summer 2007 to the end of 2008), CAD: Bastin, software developments: Sacré (Xavier helped us A LOT in these developments) and Chau

²Angelo Buttafuoco is a PhD student of Prof. Michel Kinnaert but I'm a member of his PhD committee

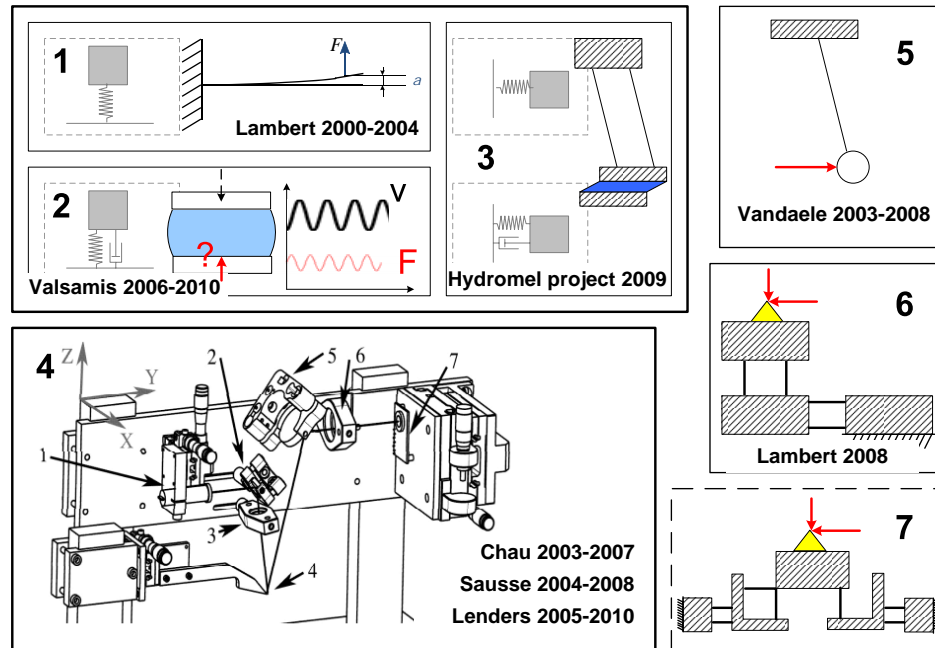


Figure 5.1: Overview of the developed test beds: (1) axial (static) capillary forces measurement set up (Lambert 2000-2004), (2) axial (dynamic) capillary forces measurement set up (Valsamis 2006-2010), (3) test bed for lateral forces (Lambert 2009), (4) AFM-like set up for nanonewton measurement (collective work 2007), (5) acoustic force measurement based on the wire technique (Vandaele 2003-2008) and (6) 2 axis force sensor for the characterization of shock absorbers (Lambert 2008). (7) is still under development.

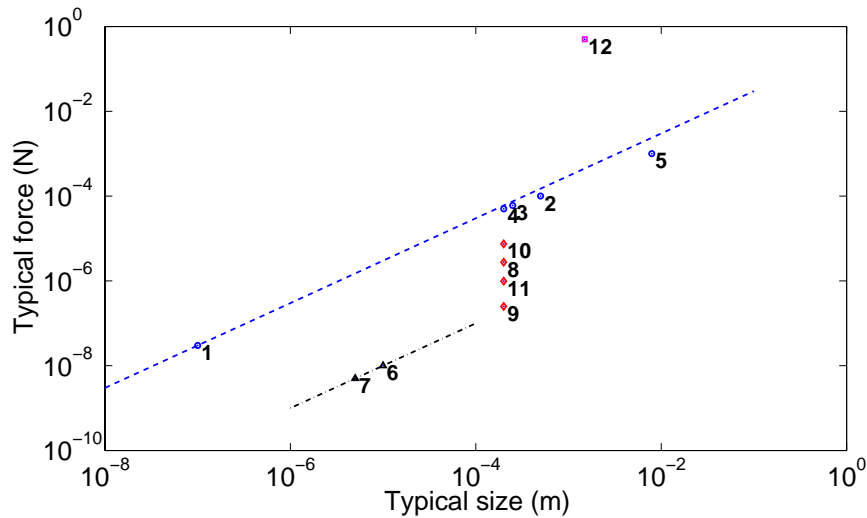


Figure 5.2: Map of our case studies: (1) capillary condensation, (2) capillary gripper, (3) Static lateral restoring force, (4) Dynamic axial force, (5) Static axial force, (6-7) Electrostatic forces, (8) Axial acoustic force (planar reflector), (9) Radial acoustic force (planar reflector), (10) Axial acoustic force (spherical concave reflector), (11) Radial acoustic force (spherical concave reflector), (12) watch component characterization.

AFM-tips of 100 nm typical length scale. It is interesting to note that all capillary force case studies (1-5) are aligned on a straight line, whose slope is about 1, which confirms the linear dependence of the force on the length scale. Without any surprise, the case study (12) related to the characterization of a mechanical spring indicates a larger force, while electrostatic adhesion is clearly lower than capillary adhesion (6-7). We can also see at a glance that acoustic forces are very sensitive to geometry (case studies 8-11).

This chapter presents these test beds as follows: axial and lateral capillary forces measurements set ups are respectively described in sections 5.2 and 5.3. The AFM-like force sensor developed for the nanonewton range is presented in section 5.4. The wire technique for acoustic force measurement is presented in section 5.5. Finally, the design and use of the two-axis force sensor is described in section 5.6. The set up developed by Angelo Buttafuoco is still under development and will not be presented here.

5.2 Axial capillary forces

5.2.1 Static forces

The results of this section have been published in my PhD [91] and Langmuir [100].

The model of static axial capillary forces described in section 4.3.3 was experimentally validated with the set up described in this section. The outputs were the meniscus geometry and the capillary force exerted on the component, while the inputs must be understood as the contact angles θ_1 and θ_2 , surface tension, volume of liquid and gap. Characterized liquids (i.e. milli-Q water and silicone oil) have been used so that the surface tension γ was well known. Thanks to a dispensing device (Eppendorf Pipette Research 0.1-2.5 μ L with a corresponding accuracy guaranteed to be within the range of 1.4%- 12%), the amount of liquid was tuned from 0.1 μ L to 1 μ L. The imaging has been done with a conventional CCD camera (zoom $\times 40$, 480×512 pixels, calibration by imaging a 1 mm thick ceramic slip gage, leading to an accuracy of about 2 μ m/pixel) while the force measurement was based on the deflection measurement of a cantilevered beam, as depicted in figure 5.3. The



Figure 5.3: Force sensing principle

typical stiffness of the set up is about 5Nm^{-1} : this value has been determined by calibration, i.e. by measuring the deflection due to the weight of a known mass (the beam is made of steel, its length is about 5cm, its width about 12mm and its thickness about 0.1mm). The very good linearity of the force sensor is represented in figure 5.4. The deflection is measured with a non-contact displacement sensor with a resolution of about 0.2 μ m, allowing a force measurement with a resolution of about 1 μ N. The maximum measuring range was about 1mm, leading to a full-scale force of about 5mN. For larger forces, the stiffness has been increased by shortening the cantilevered length of the beam.

The complete set up can be seen in figures 5.5 and 5.6. The following elements can be seen: the beam (along the Y axis) is located just below the spherical tip stating for the gripper. Its extremity is located in the view field of the camera and its cantilevered length can be changed to tune flexibility. The camera is mounted on a plate that can be moved along the X axis and in the plane YZ with two manual stages. The gripper tip (here it is a spherical tip) can be changed easily thanks to the gripper interface. This one is mounted on a manual stage allowing a relative motion along the Z axis with respect to the upper displacement sensor. Both can be moved together in the XY plane thanks to a manual stage mounted on the top of a gantry. The role of the latter is to carry a back light used to sharpen the image.

This simple and robust set up is consequently able to measure capillary forces (with a resolution of about 1 μ N) and the related inputs such as volume of liquid, contact angles and gap. Examples of results have already been given: figures 4.14 and 4.16. Additional results will be given in the section devoted to the capillary gripper case study, in section 6.2.

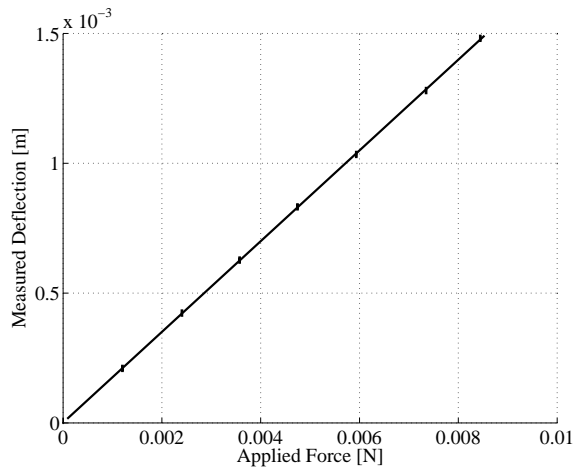


Figure 5.4: Linearity of the force measurement set up

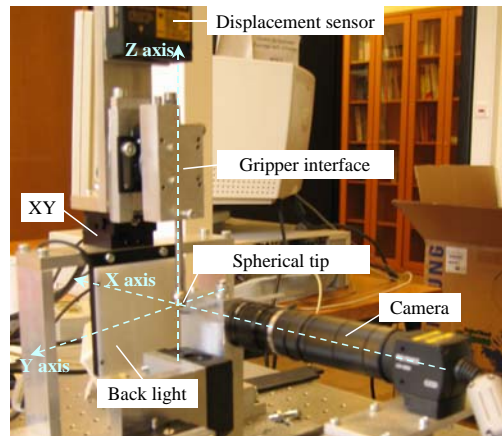


Figure 5.5: Picture of the testbed

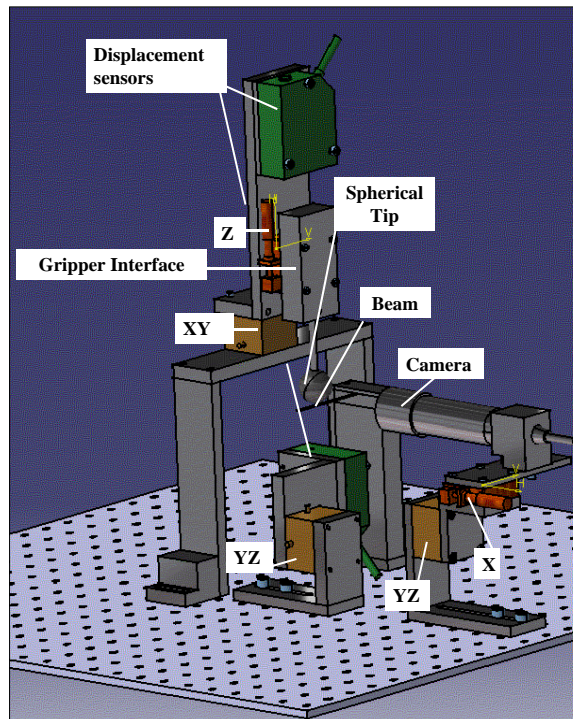


Figure 5.6: CAD drawing of the test bed

5.2.2 Dynamic forces

In Valsamis's PhD, dynamic characterization of a liquid bridge is done by tracking its harmonic response. As indicated in figure 5.7, this requires an actuator driven by an harmonic signal (to move the top of the liquid bridge), an imaging system to characterize the liquid meniscus, a force sensor on bottom of the liquid bridge and two circular pads able to confine the liquid bridge by pinning the triple lines.

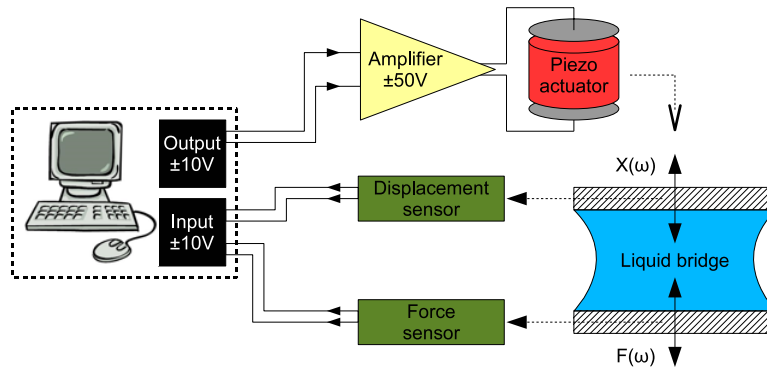


Figure 5.7: General view

The displacement was imposed thanks to a piezo-electric actuator whose frequency-stroke characteristics is illustrated in figure 5.8. Details can be found in [181].

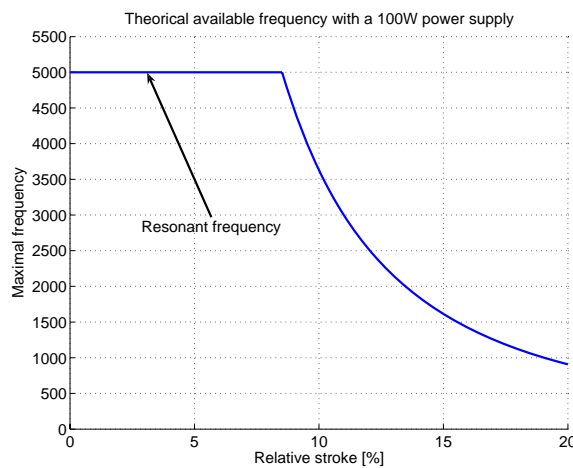


Figure 5.8: Maximal theoretical frequency of the piezo actuator, depending on the relative stroke

As far as the force sensor is concerned, two different approaches have been followed. The first solution consisted in a double cantilevered beam whose deformation under the action of the liquid bridge is a measure of the applied force (this deflection would have been measured with a non contact displacement sensor LK-G10 by Keyence, with a resolution of 10 nm, a millimetric range and a maximal

acquisition frequency of 50 kHz). The principle is sketched in figure 5.9. Mathematical relationships corresponding to the model of figure 5.9b are given in [181]. The advantage of this system was its robustness (by comparison with the second solution which will be described in the following), but the frequency band was limited by its own resonance frequency (a few Hertz due to the low frequency which is required in terms of force measurement resolution). Therefore, a commercial FEMTO-TOOLS force sensor was used instead (figure 5.10a).

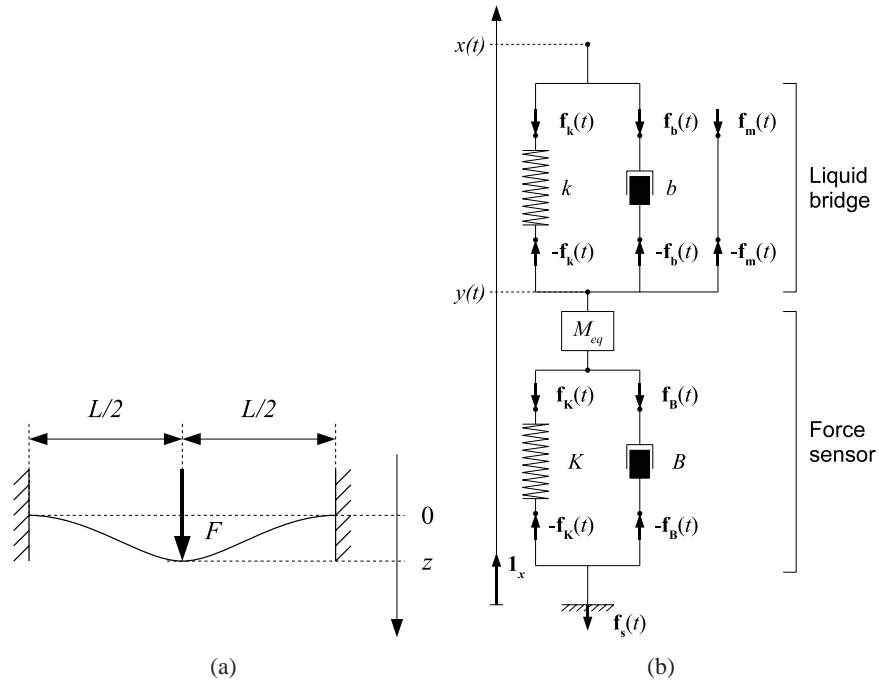


Figure 5.9: Example

The principle of this sensor is a change of capacitance. This technique has two advantages: the sensor is very dynamic due to the absence of mechanical part and the stiffness is high (the value is not given by the constructor). The tip and the capacitor is mounted on a circuit board that integrates chips converting the change of capacitance into an output voltage. Each sensor is provided with its own unique characteristic (the sensitivity may vary from 9 to 1.1 mV/ μ N). A major inconvenience is the reduced range of measurable force. These sensors are quite cheap (190 €) but the tips are extremely fragile. The maximum load of this sensor is 2 mN, with a resolution equal to 0.4 μ N at 30 Hz and 2 μ N at 1 kHz. Its stiffness is large enough to neglect the sensor deformation with respect to the gap amplitude imposed on the liquid bridge. The resonance frequency is about 6400 Hz, which is much more larger than with the first design. It will however limit our bandwidth.

This sensor was embedded in a design, whose principle is shown in figure 5.10b: (1) the non contact displacement sensor LK-G10 points towards the top surface of a mechanical connector, linking the actuator imposing the harmonic dis-

placement (2) to the top pad glued on the bottom of the connector. This harmonic displacement is measured by the signal u of the displacement sensor. The displacement of the top pad is therefore known with a constant offset $u + \text{constant}$. The bottom pad (3) is fixed to the tip of the force sensor (4). Since the force sensor is assumed to be stiff enough, the position of the bottom pad is assumed to be a reference. Note well that the gap between both pads is actually not known with a precision better than $25 \mu\text{m}$ ($\pm 2 \times 8$ pixel, 900 pixels for 1.5 mm). Figure 5.11 shows pictures of the manufactured test bed.

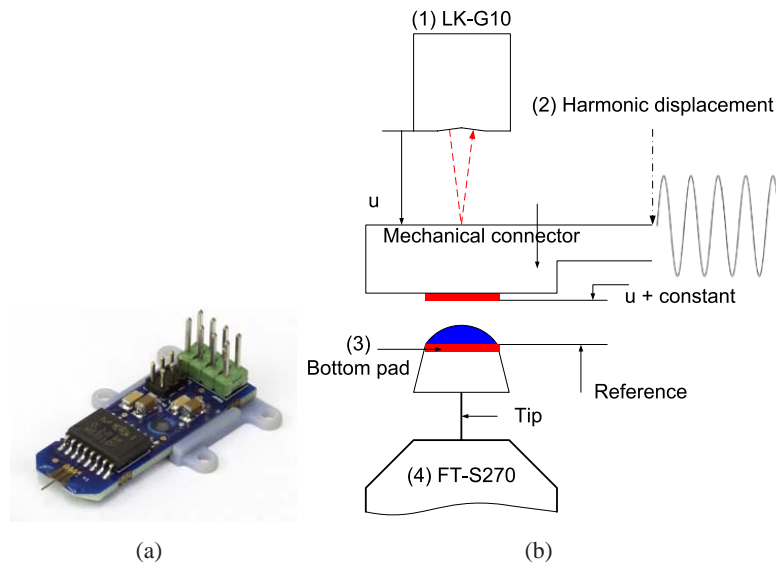


Figure 5.10: (a) force sensor FT-S270 (b) Measurement principle (see text for description)

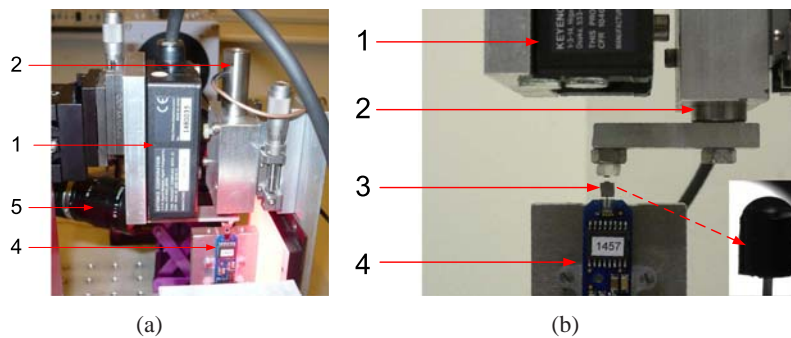


Figure 5.11: Pictures of the test bed: (1) is the displacement sensor LK-G10, (2) is the piezo actuator imposing the harmonic displacement to the top pad, (3) is the bottom pad, (4) is the FT-S270 sensor and (5) is a lateral camera with optical axis perpendicular to the liquid bridge symmetry axis (vertical on these pictures).

5.3 Lateral capillary forces

The need for measuring lateral capillary forces in the Hydromel project (Lambert, 2009) led to the design of a new test bed. As the other ones, it is based on converting the mechanical displacement of a mechanical structure in a force. Among all requirements for this set up which are recalled here below, let us just mention the need for a stiffness as small as possible (lateral capillary forces are even smaller than axial ones). It therefore became necessary to design the set up with vertical flexible structures, so that gravity does not interfere with the force to measure which will be exerted horizontally.

One more time, this open design allows us to ensure all functions beside force measurement, for which commercial sensors can of course be found. We think for example about imposing the lateral distorsion of the liquid bridge, imaging, dispensing...

Both static and dynamic forces have been measured, these results being submitted to JMM or accepted to Microfluidics and Nanofluidics [106].

5.3.1 Principle

The experimental set up is made of two circular pads of diameter D whose separation distance h can be accurately adjusted (see figure 5.12). The bottom pad is glued on a translation stage which can be displaced on a distance e by a micrometric screw. The upper pad which is glued on the so-called shuttle can move according to the deformation of two parallel elastic beams of length L , width b and thickness t . When both pads are linked by a liquid meniscus, the upper pad undergoes an elongation x from the rest position, allowing the balance of the restoring elastic force (directed to the left on the figure) and the lateral capillary force (directed to the right of the figure) occurring from the shift $e - x$ between both pads.

The bottom pad is carried by a 6 degrees of freedom (dof) translation stage allowing accurate alignment, tilt and orientation. The z dof tunes the gap h while the x dof tunes the shift. The cantilevered side of both elastic beams supporting the shuttle can be precisely moved along the x -axis and the y -axis.

Once the stiffness k_{sh} of the elastic suspension of the shuttle is known, the lateral capillary force $k_{sh} \times e$ can be plotted as a function of the shift $e - x$ to determine the slope which is equal to the meniscus stiffness k_c from equation (4.61). The order of magnitude of the stiffness k_{sh} of the shuttle is 1 Nm^{-1} and the accuracy on the micrometric screws is about $1 \text{ }\mu\text{m}$ leading to a force resolution of about $1 \text{ }\mu\text{N}$. This stiffness has been characterized on the one hand by measuring the resonance frequency and the mass of the shuttle and on the other hand by applying a calibrated horizontal force to the shuttle and measuring its elongation x . From these experiments, k_{sh} is estimated about 0.94 Nm^{-1} by the first method and 1.06 Nm^{-1} by the second one, leading therefore to the range $k_{sh} = 1 \text{ Nm}^{-1} \pm 0.06$.

Additionally to the measurement of the static elongation from which we deduce the lateral stiffness of the meniscus, damping properties are deduced from the

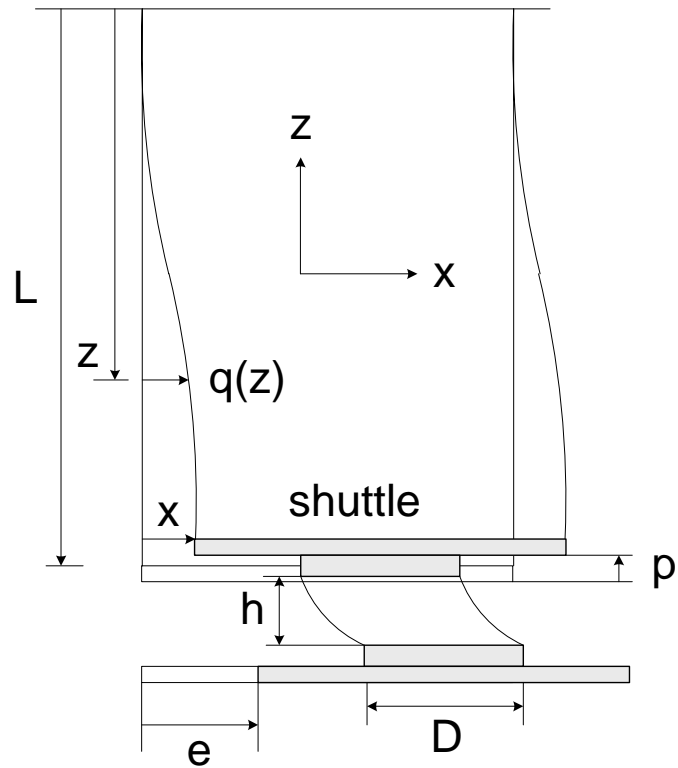


Figure 5.12: Sketch of the experimental platform: a bottom pad of diameter D is fixed on a translation stage which imposes to it a displacement e . The top pad, with the same diameter, is pulled in the direction of x by the lateral capillary force to be measured and in the opposite direction by the elastic restoring force of the spring. Since there must be a balance between the restoring force kx and the capillary force, we can explore the characteristic force-shift. The gap h can be tuned by moving the bottom pad vertically, p is a vertical parasitic motion. $q(z)$ is the deformed shape of the beam at a distance z from the cantilevered side.

dynamic response $x(t)$ (in this case, $e = 0$). $x(t)$ either shows an underdamped or an overdamped behavior, as illustrated in figure 5.13. We fit the response with either $x = A \exp(-t/\tau_c) \cos(\omega t + \phi) + B$ or with $x(t) = A \exp(-t/\tau_c) + B$ respectively and hence deduce the characteristic time τ_c . Each experiment has been repeated three times, and each set of experimental data has been fitted three times, too. A signal-to-noise ratio is then built from the ratio of the average τ_{c-mean} over the standard deviation τ_{c-std} (values are reported in Table 4.3).

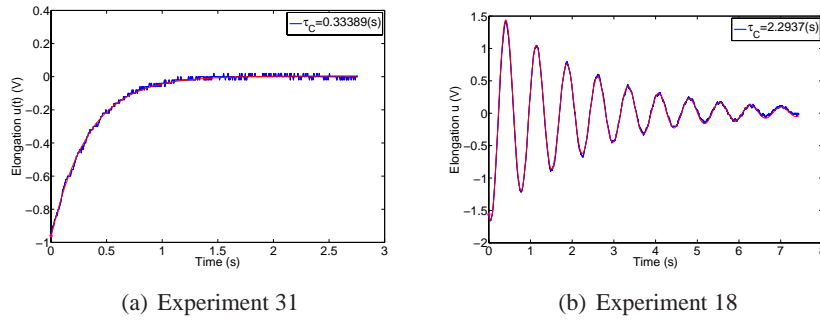


Figure 5.13: Example of dynamic responses. The elongation $x(t)$ is directly given in V (the voltage output is linearly proportional to the elongation x in m). Details of experiments 18 and 31 are given in Table 4.3.

τ_c is then divided by the characteristic time $\tau = \sqrt{m/k}$ of equation (4.67), to produce τ_d which is plotted in figure 4.33. Note that m is here the equivalent mass of the shuttle ($m = 14.8$ g) and k the sum of the experimentally deduced value of the meniscus stiffness and the stiffness of the shuttle $k_{sh} = 1 \text{ Nm}^{-1}$.

5.3.2 Experimental setup and protocol

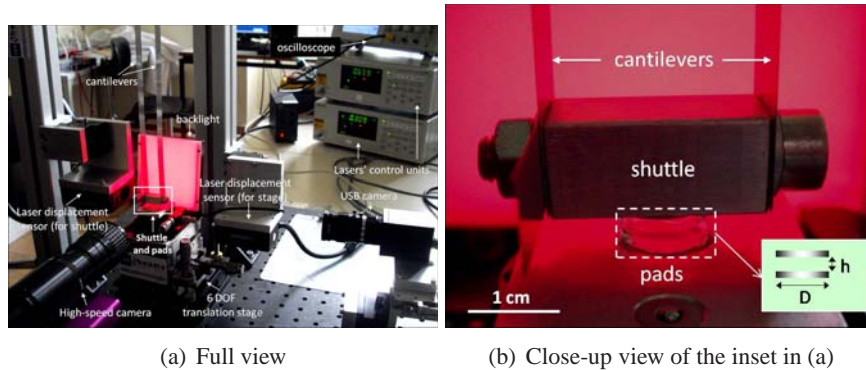


Figure 5.14: The experimental setup for lateral capillary force measurements

The actual experimental setup is shown in figure 5.14. The protocol includes the alignment and orientation of both pads, the synchronization of lasers for the

measure of e and x , the calibration of images, the determination of gaps and volumes.

The image calibration is done on pictures as depicted in figure 5.15a. Theoretically, the pad diameter should not vary from image to image (there is such an image for each experiment, i.e. for each set of parameters).

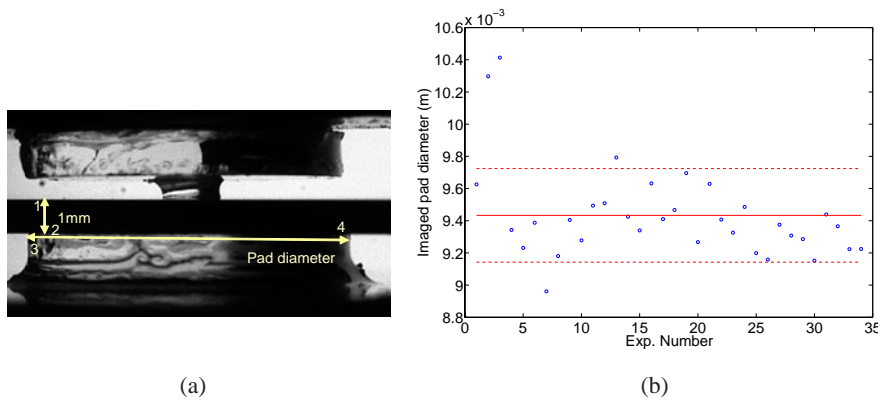


Figure 5.15: (a) Calibration image: by clicking manually on points 1 and 2, we determine the scale since the thickness of the ceramic slip gage is 1mm. Then, we can click on points 3 and 4 to determine the pad diameter. (b) The variation of diameter D - which is unchanged from experiment to experiment - is a measure of the precision of our method. We deduce from this picture a pad diameter equal to 9.4 mm.

However it does vary, and the standard deviation is a measure on the accuracy of our procedure, as indicated in figure 5.15b.

The determination of the gap and the volume is done on pictures such as depicted in figure 5.16. The gap is computed as the difference between the top and bottom line, while the volume is computed by numerical integration of the volume limited by the right meniscus on one hand and by the left meniscus on the other hand (left and right results are averaged).

We remark that, though we used only circular pads in our experiments, fluid menisci shaped by pads of *arbitrary* geometries can be investigated with our setup - though the exact knowledge of the dispensed fluid volume may be harder to obtain for non-axisymmetric menisci.

5.3.3 Set up calibration

Due to manufacturing and assembly errors, this set up needs a lot of manual micrometric adjustment screws (fine tuning) or mechanical sliding parts in grooves (rough dof):

- 6 fine dof on the bottom pad;

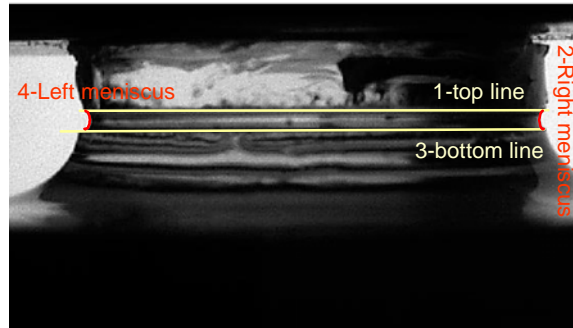


Figure 5.16: Typical meniscus image

- 2 fine dof (x and y) and 2 rough dof (x and z) on the cantilevered side of the beams;
- ideally 3 dof on the laser measuring x and 3 dof on the laser measuring u ;
- 1 dof to tune the focus of the camera imaging the meniscus (typically the optical axis is along the y -axis) and 2 dof perpendicular to the optical axis to center the image.

Each degree of freedom has a resolution (mechanical sensitivity) of the order of $1\ \mu\text{m}$. Only x and u are tracked with a corresponding $0.2\ \mu\text{m}$ sensing resolution, providing a precision of $1\ \mu\text{m}$ on them. The other degrees of freedom are not measured, excepted the alignment done with camera. The 1024 pixels images a field of view of about 20 mm, providing a resolution (and consequently a positioning resolution) of about $20\ \mu\text{m}$. The exact calibration of the images has been done by imaging a 1 mm thick ceramic slip gage leading to $14.2\ \mu\text{m}/\text{pixel}$.

Since we used silicone oils and glue, the manual pipetting device calibrated for water dispensing cannot provide accurate information on the volume of liquid. Consequently, the volume of liquid has been measured 3 times on each picture and then averaged. The ratio of the average volume over the standard deviation (i.e. the error) is expected to be larger than 10 for the experiment to be considered as valid. Similarly, the signal-to-noise ratio for gaps is larger than 10. To give an order of magnitude, the gap error is typically 2 pixels, i.e. $28\ \mu\text{m}$. This means that we tried to keep gaps larger than $280\ \mu\text{m}$, which was not a critical issue since the pad diameter D is about 9.4 mm.

5.4 Force measurement in the nanonewton range

Two PhDs have led to force measurement in the nanonewton range: Chau's PhD on capillary condensation [22] and Sausse's PhD on electrostatic adhesion [121]. In this domain, related literature used to mention the famous surface force apparatus by Israelachvili [75]. In 2007, this kind of development was beyond our possibilities. Based on the expertise acquired during my postdoc in ISIR³ (previously LRP⁴), we turned ourselves toward the atomic force principle widely described (see for example Capella in 1999 [21]). The development of this set up took one year, thanks to the help of Nicolas Bastin (Master student), Xavier Sacré (IT) and, of course, the concerned PhD students Alexandre Chau and Marion Sausse-Lhernould. The results they obtained with this set up were published in [29, 176]. The set up based on an AFM type design is shown in figure 5.17: a Thorlabs

³Institut des Systèmes Intelligents et Robotiques, Université pierre et Marie Curie, Prof. Stéphane Régnier, 2006

⁴Laboratoire de Robotique de Paris

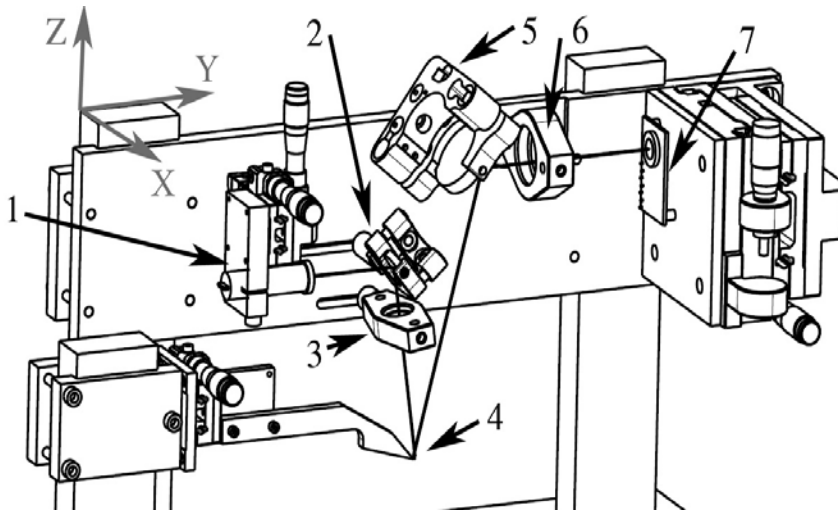


Figure 5.17: Test bed developed: the solid line indicates the optical path of the laser beam emitted from (1), reflected by a mirror (2) and passing through a lens (3) before being reflected by a cantilever (4). The reflected beam is sent towards a second mirror (5) before passing through a second lens (6) and illuminating a photodiode (7) whose voltage output is a measure of the beam deflection. Knowing the stiffness of the cantilever, this voltage output can be converted into a force with a resolution of the order of 10 nN.

CPS198 laser (detail 1) is reflected by an AFM tip (detail 4) onto a Pacific Silicon Sensor QP50-6SD2 photodiode (detail 7), using lenses (details 3-6) and mirrors (details 2-5). When a force is applied on the AFM tip, the tip is deflected, changing the direction of the reflected beam. This modification can be measured using the photodiode. The laser spot displacement on the photodiode can then be converted to a force since the tip has a known stiffness (about 0.8 N/m). Currently, the force can be measured between an AFM tip and a substrate placed in an environmental box (figure 5.18, detail 9). The substrate can be moved vertically over a 25 mm range with a 200 nm resolution (with a PI M-126 translation stage), and over a further 200 μm range with a 1 nm resolution (with a PI P-528 nanopositioning system, detail 8).

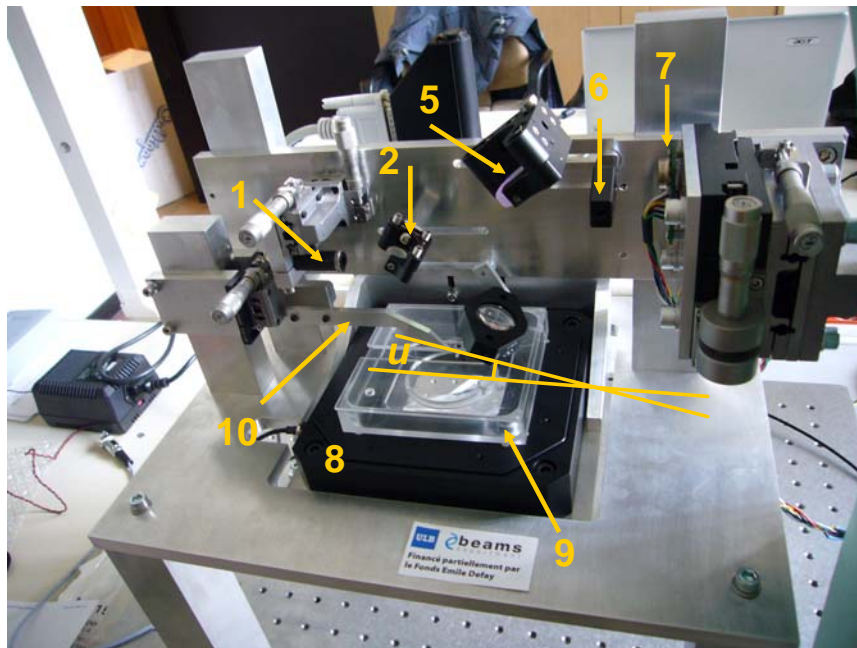


Figure 5.18: In addition to figure 5.17, we can see in this figure the nanopositioning stage (8), the environmental box (9) and the part on which the cantilever is glued (10). The angle u is the angle between the substrate to be placed on the bottom of the environmental box and the cantilever (4, not shown here).

The tip⁵ and substrate (mica, used 30 minutes after cleavage, is assumed to be atomically flat) are approached until contact, then the pull-off force is measured when retracting the substrate. As the tip and the substrate can be enclosed in a small environmental box, humidity can be controlled and the variations of the force with respect to humidity can be measured. A typical pull-off measurement has already been presented in [27].

⁵Silicon tips were supplied by Nanoandmore. They have a nominal stiffness $k_m = 0.8$ N/m, and two different curvature radii of 90 nm and 150 nm: they have been modeled as elliptical tips

The sources of error are the quality of substrate and tip surfaces, the stiffness uncertainty (estimated from the cantilever thickness 10% uncertainty to the range $(0.75 - 1.40) \times k_m$), electrical noise, positioning stages precision, and contact detection variability. The temperature variation effects can be ignored since only a variation of 0.03° has been registered during a 30-minute experiment. All these errors contribute to the experimental scatter depicted in figure 4.41.

The set up presented in this section measures forces with a resolution of a few nanometers, in mastered environment (humidity can be changed between 50% and 85%). The open architecture makes it quite versatile, including the possibility to apply an electrical voltage between the tip and the substrate or to improve it with an inverted microscope to image the substrate.

5.5 Characterization of an acoustic field

As briefly mentioned in the general introduction of this work, an alternative to avoid adhesion between a small component and a gripper is to handle it without contact. Even if this track was not the main one, we could study this opportunity during the PhD of Vincent Vandaele (2003-2008). Among different levitation principles, acoustic forces were promising, as it was pointed out in our literature review finally published in 2005 [185]. Acoustic levitation exists under two forms: standing waves levitation and squeeze film levitation. Standing wave levitation is based on acoustic forces generated by standing waves between an actuator and a reflector: as shown in figure 5.20 stable equilibrium positions exist near the pressure nodes of the wave. Squeeze film levitation relies on the same physics, but the component must be quite flat and plays the role of the reflector. The latter technique had for example be used in the TU München to transport wafers without contact [72].

During his PhD, Vincent Vandaele developed with Comsol and Matlab a numerical simulation of the standing wave levitation, and designed a demonstrator, which will be discussed later on as a microcomponents feeder in page 147. In this section, we would like to highlight the force measurement set up which was used to measure the acoustic force and henceforth validate the developed simulation. These developments are detailed in Vandaele's manuscript [184].

5.5.1 Wire technique

With the "wire technique", the acoustic force is measured on a component suspended by a thin wire. This method is widely used in acoustic radiation force measurements [32, 52, 70, 120, 163].

The experimental configuration is represented in 5.19. The levitator is in such a position that the axis is horizontal and the acoustic chamber is vertically accessible. The sphere is suspended by a thin wire. A CCD camera is pointed at the levitator chamber, so that the component position can be monitored. A precision positioning

system is used to move the wire base and thus the suspended component. The axial position of the wire base is monitored by a precision laser displacement sensor.

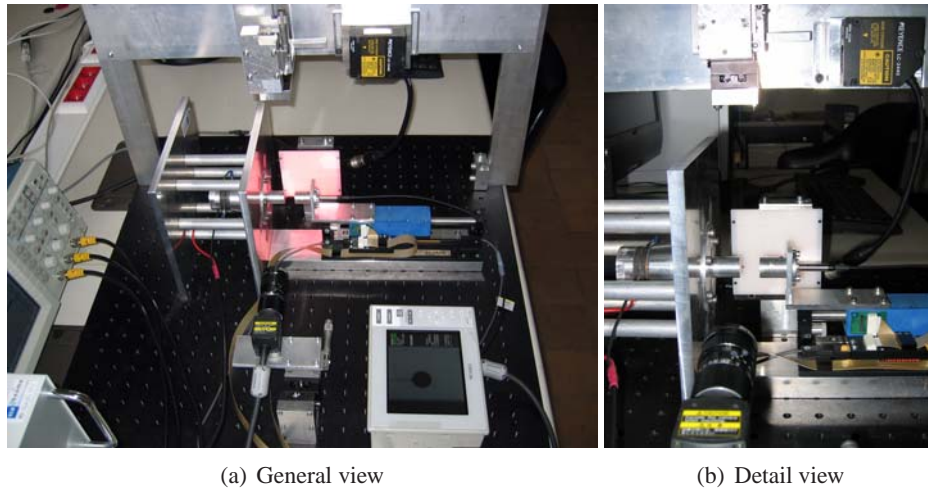


Figure 5.19: Experimental configuration of the levitator and accessories to perform force measurements on a suspended component

The wire base can be moved with the help of a Newport M-DS40 translation table with two degrees of freedom for the horizontal movements and a M-SDS-40 with one degree of freedom for the vertical translation. The component is positioned on the levitator axis in order to measure the axial force component.

A Keyence LC2440 laser displacement sensor is used to monitor the axial displacement of the wire base. This sensor has a range of 6 mm with a precision of $0.2 \mu\text{m}$.

The CCD camera is a Keyence CV-551 with the corresponding controller. After calibration, it allows to monitor the sphere position. The camera is mounted on a Newport M-DS40 translation table with two degrees of freedom for tuning the camera visual field and a M-SDS-40 with one degree of freedom for adjusting the depth of focus.

The wire is tied up to the component with the help of Loctite cyanoacrylate glue. The suspending filament is a nylon wire of diameter $74 \mu\text{m}$. The effect of the wire on the acoustic force is negligible.

From the source to the reflector surface, the acoustic chamber is schematically represented in 5.20, where the various axial coordinates of the camera z_{cam} , the laser sensor z_{las} and the levitator z are defined. The acoustic force F_{ac} and the opposite of the restoring force due to the wire $-F_{wire}$ are also represented. The sphere is stably positioned where both axial forces cancel.

The main assumption is that the component weight is much higher than the wire weight, so that the wire is supposed to be tight. The restoring force is proportional to the displacement δ and the sphere weight P_{sphere} , and inversely proportional to

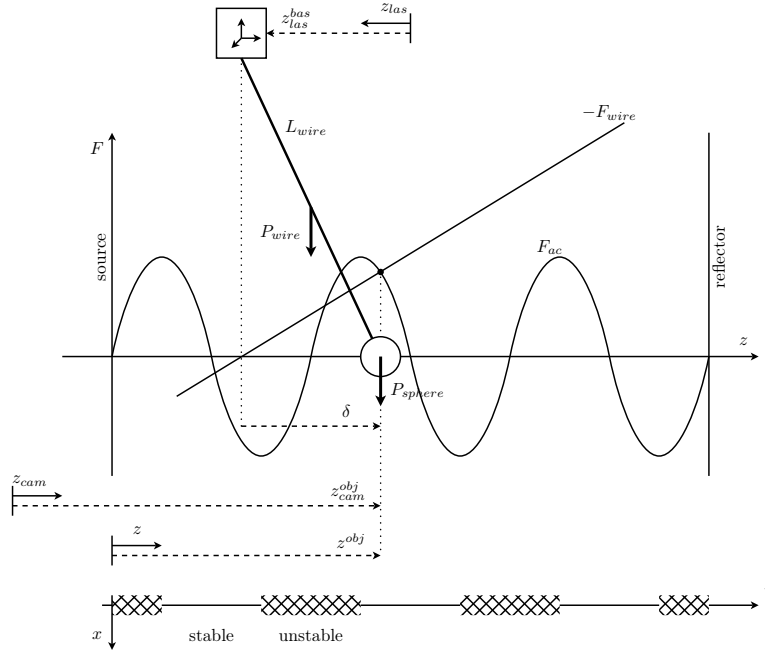


Figure 5.20: Schematic view of the levitator to perform force measurements on a suspended component — definition of coordinate systems, forces, stable positions

the wire length L_{wire} :

$$F_{wire} = -P_{sphere} \frac{\delta}{L_{wire}}. \quad (5.1)$$

The wire force is limited by the maximum deflection δ , through the positioning system stroke and the camera view. In order to get high precision force measurements over a wide position range, the maximum wire force must be of the same order of magnitude as the acoustic force. The wire restoring force can be written in the form $F_{wire} = -k_{wire} \delta$ where the stiffness constant is $k_{wire} = \frac{P_{sphere}}{L_{wire}}$. The latter can be modified by acting on the weight of the sphere or the wire length. Theoretically, the easiest parameter to modify independently is the wire length. In practice, it is easier to make the opposite, and modify the pressure p to scale the acoustic force. A compromise on the acoustic force amplitude must be found. For a strong acoustic force, the component positioning range is very narrow, whereas a low acoustic force leads to a bad precision due to small wire deflections.

Hatched positions of figure 5.20 correspond to unstable positions where no equilibrium can be found.

The component weight is advantageously supported by the wire and does not need to be compensated by the acoustic force exclusively. The component must be large enough so that the wire is tight and the wire weight can be neglected. Nevertheless, the wire scales the force down, so that the measurements are very precise. In addition, the wire has a stabilizing effect and the component vibrations

are damped. Static measurements of the force are performed, so that reproducible values are obtained.

In the wire force of equation (5.1), a correction due to the wire weight P_{wire} can be introduced. The total weight at the wire end is $P = P_{wire}/2 + P_{sphere}$ and the restoring force writes:

$$F_{wire} = -P \frac{\delta}{L_{wire}}. \quad (5.2)$$

The correction due to the wire weight $P_{wire} = \pi R_{wire}^2 L_{wire} (\rho_{wire} - \rho_s)g$, relative to the sphere weight $P_{sphere} = \frac{4}{3}\pi a^3 (\rho_o - \rho_s)g$, represents 1.4 %. When the sphere weight is reduced, this error becomes important. Moreover, the wire is no longer tight and the method is not applicable. To reduce the sphere size or density, a thinner filament should be used.

In formulas (5.1) or (5.2), the rocking motion of the component suspended to the wire has been linearized. This is valid for small tilt angles only. Therefore, the maximum deflection is limited approximately to $\delta = 6$ mm by the strokes of the instruments.

In the configuration of Vandaele, this limited deflection δ leads to a maximum restoring wire force of about $F_{wire} = 10.8$ μ N, whereas the maximum axial acoustic force is about $F_{ac} = 7.5$ μ N. The distribution is suitable for sensing the acoustic force in the whole range. When the sphere weight is reduced, the sensing range is reduced.

5.5.2 Example: axial acoustic radiation force as a function of the sphere position

The axial acoustic radiation force F_z is plotted as a function of the sphere position z_o in figure 5.21, for a steel sphere of radius $a = 1.0$ mm in the levitator with a plane reflector, working in the third mode $L_r = 13.7$ mm. The frequency is fixed to $f = 39.6$ kHz. The pressure is set to a moderate value $p = 852$ Pa. Due to the homing procedure, the sphere is close to the source surface. Experimental points are obtained in the ranges $z_o = 1.7$ – 2.9 mm and 5.9 – 6.6 mm. The central zone cannot be experimentally investigated as the positions are unstable. Experimental points are plotted in blue with circle \circ markers. The axial acoustic radiation force computed with the numerical model is superposed on the figure as a green curve with point \cdot markers.

As seen in figure 5.21, the obtained accuracy between the measured and the computed values is very good: any difference lies within the precision boundaries.

The experimental curve has been measured several times with the same sphere to study the repeatability of the results. Moreover, the reproducibility has also been investigated. Three equivalent steel spheres have been tested, along with the effect of the wire gluing point. The microphone has been dismantled and reassembled with no further calibration. Good repeatability and reproducibility are observed. The experimental precision, obtained by averaging several successive measurements, is much higher than the theoretically computed precision.

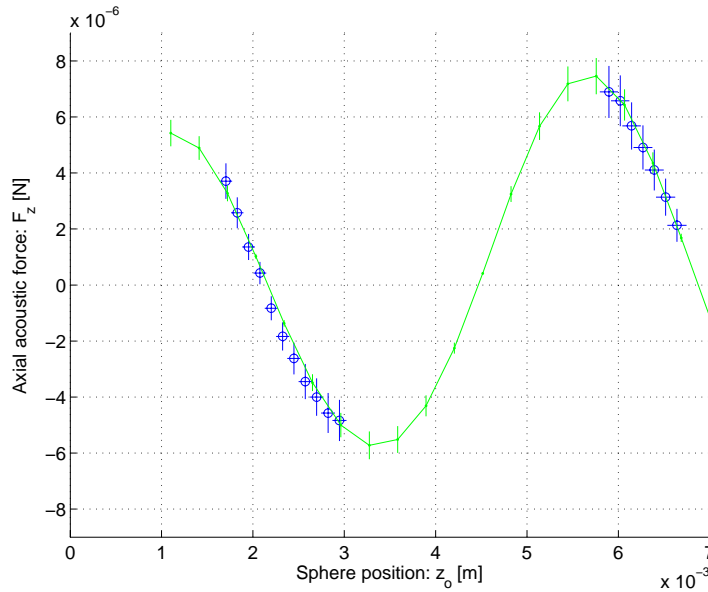


Figure 5.21: Axial acoustic radiation force F_z on a steel sphere of radius $a = 1$ mm as a function of the sphere position z_0 — levitator with a plane reflector; third mode $L_r = 13.7$ mm; steel sphere $a = 1.0$ mm, $\rho_o = 7870$ kg/m³, $c_o = 5055.3$ m/s; in air at $f = 39.6$ kHz, $p = 852$ Pa

The first stable position, where the axial force vanishes, is $z_0 = 2.2$ mm. The second stable position can be extrapolated at 6.9 mm. The force evolves approximately as the usual sinusoid $\|F_z\| \sin(2k_s z_0)$ as a function of the axial position z_0 .

5.5.3 Conclusion

This section presented a useful force sensing technique which can be applied to characterize force fields of small amplitude (μN). Moreover, the mentioned levitator can be used as a microcomponents feeder, as discussed in the next chapter. Finally, let us mention that this device could be used in crystal germination (to avoid contamination from the wall) or to study the properties of liquids: the device cannot cancel the gravity, but can hold a droplet far away from the walls, as shown in figure 5.22.



Figure 5.22: Picture of a millimetric water droplet levitated in a standing wave acoustic forces field. The wave propagates vertically.

5.6 Watch shock absorbers characterization

5.6.1 Introduction

Jacques Jacot (Ecole Polytechnique fédérale de Lausanne) – who supervised my postdoc in 2005 – proposed me a research project in collaboration with the microtechnology industry. During a few months in 2008, I consequently studied a shock absorber mechanism for mechanical watches (see for example the websites of two shock absorbers manufacturers, Kif (Vallée de Joux) and Incabloc (La Chaux-de-Fonds)). The experimental characterization of these components turned out to be mandatory. This section reports the design of a two-axis force sensor developed for this purpose. Since the topic itself is a bit out of the main track presented in this work, we decided to write this section here, after the developments related to surface forces measurements. Nevertheless, this reading order does not match the chronology. The two-parallelgram force sensor presented here after has inspired the lateral force sensor already presented in section 5.3. It also leads to the ongoing development of Angelo Buttafuoco⁶ toward a two axis force sensor for a master-slave teleoperation system.

5.6.2 Shock absorber mechanism for watches

A shock-absorber⁷ is made of a mobile jewel-setting adjusting itself to the interior of the block (fixed part of the device). The jewel-setting is pressed against the block by a spring. When the watch undergoes any shock, the energy is transferred by the pivot shank to the block, preventing the pivot from excessive mechanical stress.

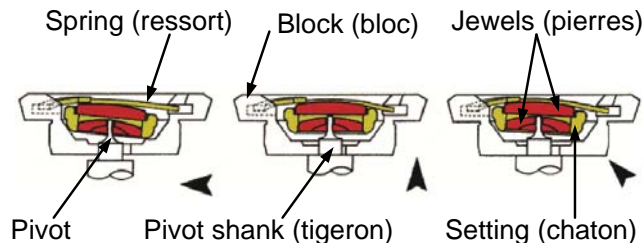


Figure 5.23: Shock-absorber Kif (Adapted from <http://www.kif-parechoc.ch>)

The first function of such a shock-absorber is to minimize the friction between the pivot and the jewel in normal working conditions. Especially, this is achieved by using very thin pivot, with diameter as small as tenths of millimeter. The second function is to transfer the energy directly from the pivot shank to the block in case

⁶Angelo Buttafuoco is a PhD student of Prof. Michel Kinnaert, in Université libre de Bruxelles. I'm a member of his PhD committee

⁷The original French words are: antichoc (shock-absorber), pierre (jewel), chaton (jewel-setting), bloc (block), ressort (spring), tigeon (pivot shank), pivot (pivot)

of shock: this prevents excessive stress on the pivot. Thirdly, the moving jewel-setting must be recentered automatically by the spring after the shock.

5.6.3 Goals of the study

To avoid non desired motions of the jewel-setting, the spring is preloaded: consequently, the mechanism can be characterized by two shock thresholds (one along the axial direction, the second one in the radial direction). These thresholds depend on the block and setting geometries, the coating materials (governing the friction), the spring stiffness and spring preload and any initial deviation from the targeted rest position. All these parameters may be affected by manufacturing errors.

The goal of this study was to develop an experimental testbed for shock-absorbers characterization:

1. characterize axial and radial thresholds by measuring the minimal axial and radial forces leading to a jewel-setting motion;
2. characterize the spring stiffness in the axial and radial directions;
3. quantify the hysteresis of the shock-absorber;
4. quantify the re-centering error after a shock.

5.6.4 Testbed design

Since it was not possible to characterize shock absorber under actual shock conditions, we led a quasi-static characterization by measuring force-displacement characteristics along axial (Z) and radial (X) directions in static mode .

During the study [95, 119], we concluded on a force measurement set up based on flexible structures. Two designs were studied, with or without axis coupling. The first design relies on two pairs of cantilevered beams put in series, as shown in figure 5.24. The second design relies on the coupling of X and Z axis, as indicated in figure 5.25.

An important advantage of the latter design is that the deformation measurement axis are parallel and could be achieved with "low-cost" LVDT sensors. Nevertheless, the X and Z stiffnesses of such a sensor are fixed during the design phase: indeed, the flexible structures cannot be adjusted after manufacturing. At the contrary, the first design is much more indicated in a prospective research, since the stiffness can be adjusted by changing the length of the cantilevered beams (or even by changing the beams). Additionally, this first set up is simpler to manufacture. It requires however non contact displacement sensors but such equipment are usually available in research labs (laser Keyence LC-2440).

The principle of the chosen design is illustrated in figure 5.26. The CAD design, dimensioning and drawing were achieved by David Lengacher during his Master Thesis⁸ at Ecole Polytechnique Fédérale de Lausanne.

⁸FR: Travail de diplôme

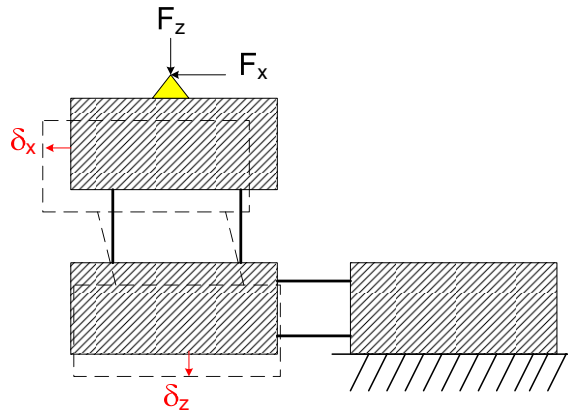


Figure 5.24: Uncoupled compliant structure for 2 axis force measurement

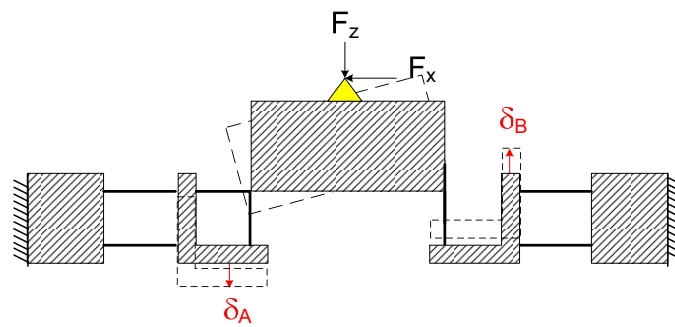


Figure 5.25: Coupled compliant structure for force measurement

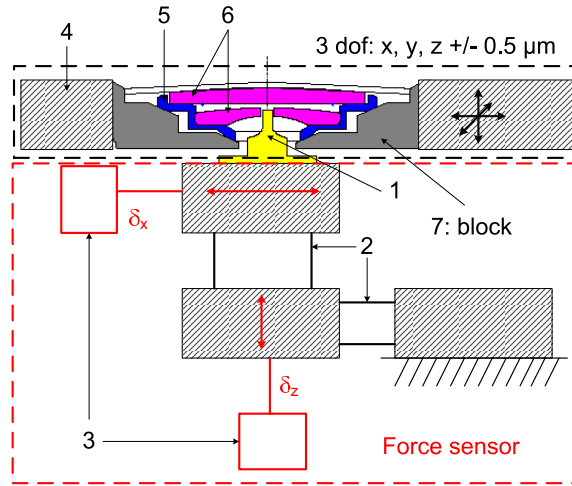


Figure 5.26: Measurement principle. The bottom elements (in the red box) represent the fixed sensing part: the pivot (1) is fixed on two serial pairs of parallel flexible beams (2), whose deformation is measured along respectively X and Z axis with two non contact displacement sensors (3). The performances of the sensor can be changed by modifying the stiffness of the beams. The top part (in the black box) holds the shock absorber and can be moved by a Sysmelec robot (4): it is therefore possible to accurately position the pivot (1) relative to the shock absorber, impose a displacement of the jewel-setting (5: setting, in blue; 6: jewels, in magenta) inside the block (7) of the shock absorber and to measure the related effort.

An overview of the set up is proposed in figure 5.27.

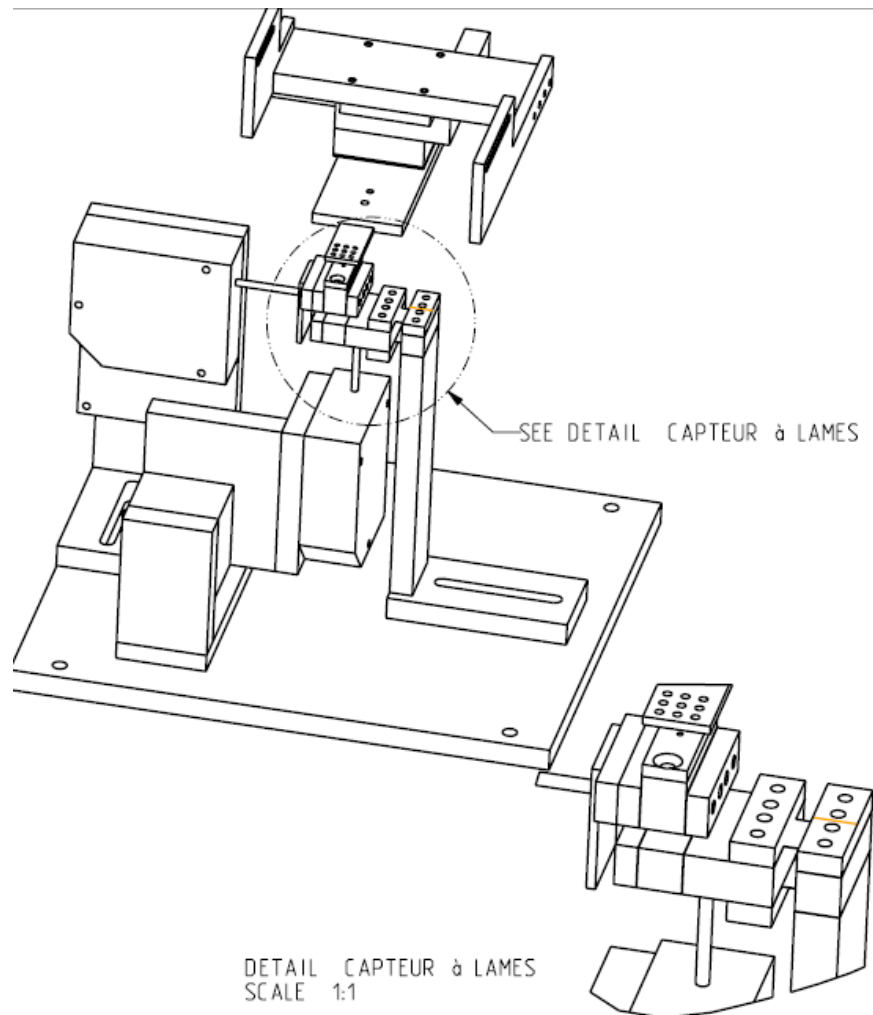


Figure 5.27: CAD view of the measurement set up (from [95])

5.6.5 Test bed characterization

Each axis has been separately characterized. To calibrate the sensor along the z axis, masses known with a tenth of milligram accuracy were used to apply known forces on the sensor. The top subfigure of figure 5.28 gives the measure of the non contact displacement sensor which tracks the displacement of the extremity of the cantilev. On the bottom diagram of figure 5.28, we can observe the parasitic signal on the x axis: if both axis were totally decoupled, the x displacement signal should be zero. To investigate the influence of the roughness of the reflection surface (i.e. the surface which reflects the laser beam of the laser displacement),

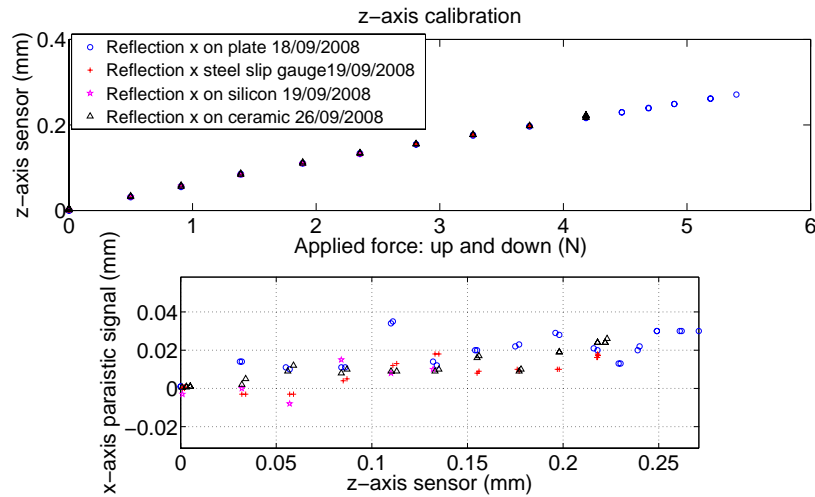


Figure 5.28: z axis calibration: hysteresis is limited to about $2\ \mu\text{m}$ and cross-talk between x and z axis is limited when using steel slip gauge as reflecting surface (bottom subfigure, + marks)

we tried different materials: a machined steel plate, a steel slip gauge, a ceramic and a silicon chip. According to our experiments, this parasitic signal is due to a parasitic motion of the flexible beams and to the roughness of the reflecting surface. As described by Henein [71], the so-called parasitic motion of the beam means is an undesired motion of the beam extremity in a direction perpendicular to the main one, and proportional to the main displacement. On the other hand, since the cantilevered side of the beams translates downwards under the action of the applied weights, the reflecting surface of the laser beam emitted by the x displacement sensor is translating downward too: actually, the x laser beam scans the roughness profile of the reflecting surface. To reduce this roughness, we tried to use a very smooth profile, but the measuring head LC-2440 is unfortunately designed to work with diffuse reflection. Looking at the mentioned figure, we conclude however that results are better using a steel slip gauge reflecting surface than using machined steel: indeed, the largest parasitic signal falls from 35 down to $20\ \mu\text{m}$.

To characterize the x axis of the set up, the test bed is rotated by 90° and the same procedure is applied. Here, we clearly see a linear coupling, probably due to the parasitic motion. Even if it is of the same order of magnitude ($20\ \mu\text{m}$ max), it can be more easily predicted and corrected. There is here no stochastic coupling due to roughness because the reflecting surface of laser z is fixed in this case.

Based on the top subfigures of figures 5.29-5.29, we could deduce the stiffnesses k_x and k_z of the force sensor.

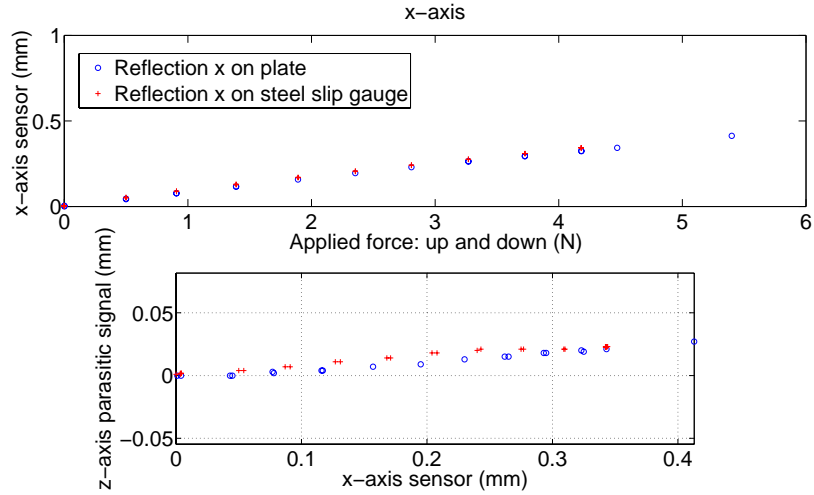


Figure 5.29: Calibration suivant l'axe x

Stiffness	Value(kNm^{-1})
k_z	16.6
k_x	12.1

Table 5.1: Experimental stiffnesses of the set up

5.6.6 Results analysis

The theoretical axial characteristic of a shock absorber is illustrated in figure 5.30. The vertical segment between point 1 and point 2 is due to the preload of the spring. Indeed, the force against the setting can be raised up to point 2 without any displacement. The shift of the characteristic to the left hand side gives the initial deformation of the spring, hereby called "preload" (armage in French).

We can apply a force to the jewel-setting thanks to a flexible beam of known stiffness k_z : a robot can impose a displacement z of the cantilevered side of this beam relatively to the block of the shock absorber. The force-displacement characteristic of this beam can consequently be drawn from point A, with a slope equal to its stiffness k_z . Since the displacement coordinate of point 3 is the difference between z and the beam deformation d measured by the non contact displacement sensor, point 3 can be drawn, at the crossing between the known sensor characteristics and the unknown shock absorber characteristics.

The measuring process can also be represented by figure 5.31. It is essential to determine the displacement of the jewel-setting inside the block of the shock absorber. Since this displacement is the difference between the robot displacement z and the force sensor deformation d , the problem becomes to know the reference level of both systems. Theoretically, the zero is reached when the pivot contacts

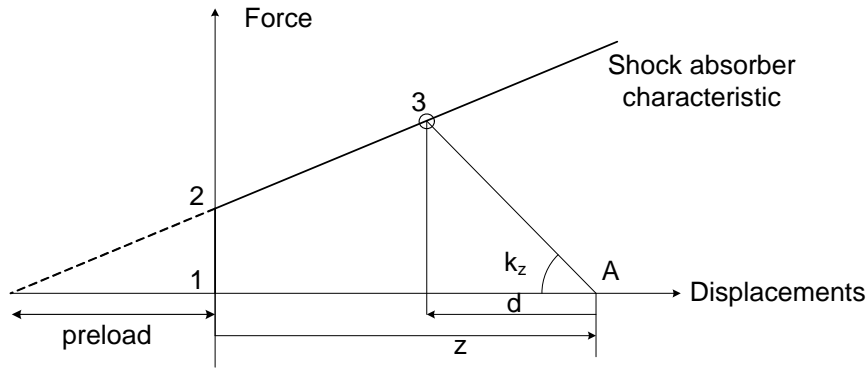


Figure 5.30: Characteristics of the sensor and the shock absorber

the jewel-setting with zero contact force⁹. Actually this initial contact is detected when the force sensor measures a very small deviation d_0 from zero ($d_0 \approx 3 \mu\text{m}$), i.e. when the shock absorber is displaced by a small distance a , whose effect is also illustrated in figure 5.32. The last picture of figure 5.31 illustrates an imposed displacement z , leading to a beam deflection d : z and d are used to build the shock absorber characteristic, as explained previously. Figure 5.32 shows that

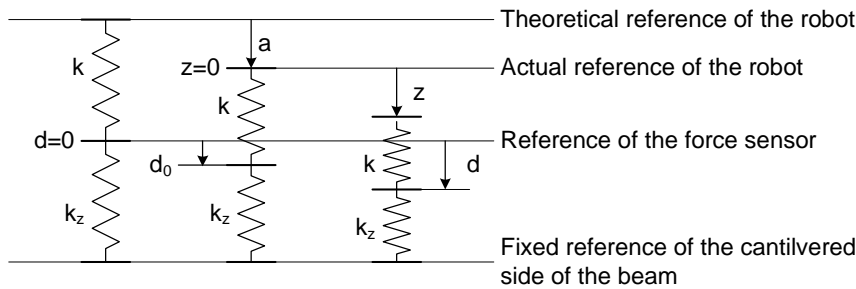


Figure 5.31: Equivalent model: spring of the shock absorber (stiffness k_z) and stiffness k of the force sensor

the characteristics cannot be explored to the left of point 2, which corresponds to a displacement $z = 0$ and an deflection d_0 . By increasing z , the characteristics can be built to the right of point 2, but if further decreased, z becomes negative, which means that the shock absorber is moved away from the initial contact position. Since the precision of the displacement sensor is in the order of $1 \mu\text{m}$, the force error is about 17 mN. The slope of a linear characteristic is a measure of the the stiffness of the spring. In case the resolution of the force sensor allows to measure the vertical part of the characteristic (dashed red line to the left of point 2), this set up also gives the force threshold activating the shock absorber mechanism.

⁹FR: accostage

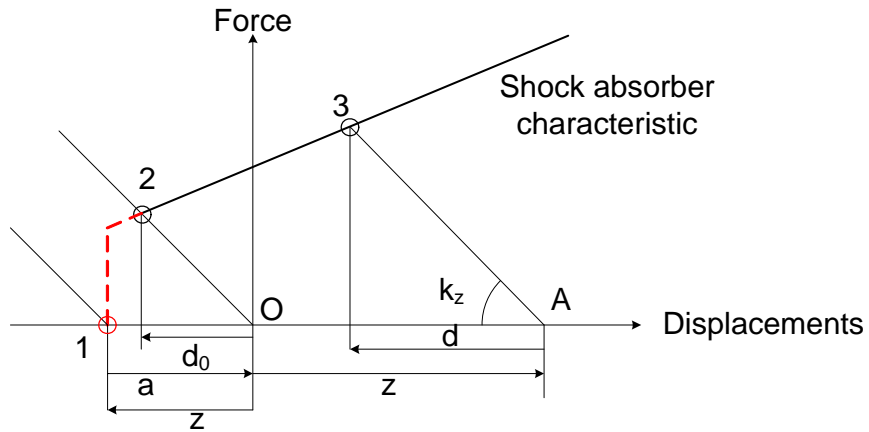


Figure 5.32: Effect of the unknown offset a

5.6.7 Results

All the results are presented in [95]. An example is given in figure 5.33. Due to confidentiality, the exact values of force and displacement are not given here.

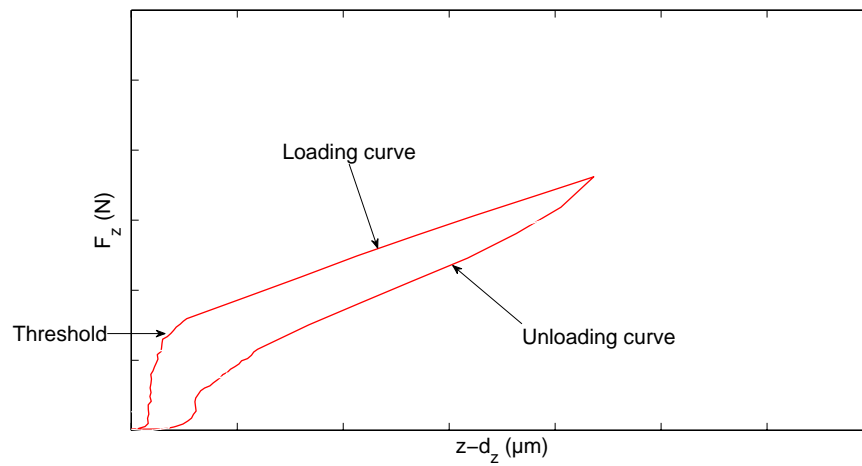


Figure 5.33: Typical shock absorber characteristic, illustrating the presence of a threshold and a linear spring (shock absorber 1, Ni coatings on block and setting)

5.7 General conclusions

Before applying the developed models to the case studies which will be described in the next chapter, it was necessary to experimentally validate our theoretical developments. A series of force measurement set ups have been built, often based the deflection of a mechanical structure. It is interesting to note that stiffnesses of a few Nm^{-1} can be reached as well with macroscopic structures, as shown for example in section 5.3.

Chapter 6

Case studies

6.1 Introduction

This chapter summarizes our applicative case studies, which are schematically shown in figure 6.1. As usual, the main track focuses on surface tension applications, including the development of a surface tension gripper and the related feeder (number 1 in figure 6.1, detailed in sections 6.2 and 6.3), the numerical quantification of cycle times and forces applied on handled components by a liquid bridge (number 2, detailed in sections 6.5 and 6.6) and the design of a flip-chip application using the results of the study of lateral capillary forces (number 3). This track has led to a current PhD work by Cyrille Lenders on the study of a microrobotic platform actuated by "fluidic legs" relying on surface tension and gas compression (number 4). Closely related to our capillary forces models, a recent collaboration with Fabio Gabrieli (University of Padova) gave me the opportunity to apply my models to soil mechanics (number 5, details in section 6.8)

This main flow led to additional work feeding strategies based on acoustic levitation (number 6, detailed in section 6.4).

Beside these developments, we also developed in early research a stick-slip actuator (number 7), inspired from the works of Zesch [200] and Breguet [18]. Finally, the PhD of Jean-Baptiste Valsamis recently highlighted some interesting points related to capillary rise (number 8) and more generally to capillary feeding of fluidic circuits. Finally, recent developments focused on electrosprays (9).

Through these case studies, we tried to apply our developments to applicative contexts or even to industrial case studies. It was also the opportunity to develop collaborations, achieved directly (with University of Padova) or within research projects (EU Hydromel project). The efforts made to diffuse and transfer our results are also attested by various dissemination events (tutorial hold during the

2009 SSI conference¹, FSRM lecture²). Finally, let us mention a patent which is currently pending on the microrobotic platform, indicating on another way to transfer the knowledge developed by our research works.

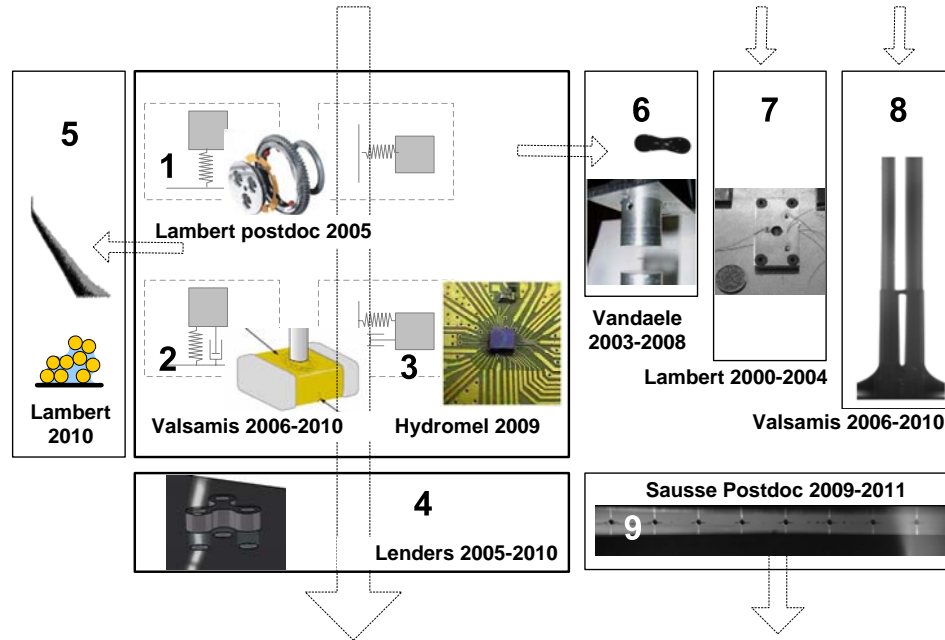


Figure 6.1: Overview of the case studies presented in this chapter. The main flow on surface tension applications includes applications related to static axial capillary forces (1: surface tension gripper for ball bearing), dynamic axial capillary forces (2: cycle times and forces exerted on components) and lateral capillary forces (3: flip chip and hybrid assembly). Current developments on surface tension focus on the development of a microrobotic platform (4). Beside this main flow, additional case studies were studied such as the application of our capillary forces models to soil mechanics (5), non contact feeding using acoustic levitation (6), stick-skip piezo-electric actuation (7) and capillary rise (8). Recent works have been done at Université libre de Bruxelles on electrospaying (9).

¹Smart Systems Integration conference, hold in Brussels on 10-11 March 2009, tutorial given on Fluidic Assembly and Capillary Forces: modeling, experiments and case studies, in collaboration with Quan Zhou case studies

²Fondation Suisse de Recherche en microtechnique, lecture on Micro Assembly using Surface Tension, given in Lausanne on March 29th 2010

6.2 Capillary gripper

During my post doc at EPFL, Jacques Jacot gave me the opportunity to apply the promising results of my PhD to the industrial case study made of a watch ball bearing. At that time, the bearing was manually assembled, and I both designed a new gripping tool and set the preliminary foundations for its automation. These results were published in *Journal of Micromechanics and Microengineering* [108]. Despite interesting reliability in terms of placing the components, the picking step was a bit disappointing due to a not well mastered feeding of the components. From the economical point of view, it also turned out that the cost of manual assembly was not really a problem for watch ball bearings, which are only embedded in (quite) large price mechanical watches. Nevertheless, the feeding problem was studied afterwards, as detailed in sections 6.2 and 6.3.

6.2.1 State of the art

The capillary or surface tension based gripper relies on surface tension forces to get parts stuck to the gripper [5, 6, 9, 68, 100, 101, 108, 147, 165]. Already in 1999, Bark [6] used a low viscosity liquid such as ethanol that evaporates without leaving particles on the part's surface. A second example [68] of capillary gripper was used by Grutzeck in 2002 to manipulate small Si plates of $2 \times 2 \text{ mm}^2$. In 2005 during the IEEE ISATP conference, Biganzoli [9] suggested to vary the gripper curvature in order to vary the capillary force, according to the well-known Israelachvili approximation. Therefore, as illustrated in figure 6.2a, the extremity of the gripper is made of a deformable membrane whose curvature increases under the action of a liquid (i.e. this liquid is inside the gripper, and only used to drive the shape of the membrane. It can be totally different from the liquid constituting the meniscus between the gripper and the component). Nowadays, the main limitation of the method is its difficulty to be miniaturized. Recently, [147] has proposed a new design (figure 6.2b) where the deformation of the membrane is obtained using an electronic EAP³ between two electrodes which can squeeze it to provoke a change of the curvature of the gripper tip. This principle is still to be implemented. [165] has proposed to use a gripper with an hemispherical concavity in order to increase the contact conformity between the gripper and a spherical component, allowing to pick it up from a flat plane. To achieve the release, the authors propose to increase the volume of liquid, which leads to a force decrease. This principle has still to be implemented.

We applied this capillary picking principle to $100\mu\text{m} \times 100\mu\text{m} \times 20\mu\text{m}$ components [168] and to $300\mu\text{m}$ and $500\mu\text{m}$ diameter balls of watch ball bearings [108]. This latter case study is developed in the following sections.

³EAP = Electro Active Polymer

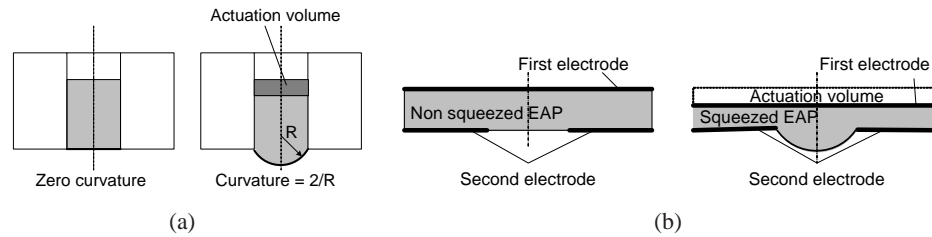


Figure 6.2: Some examples of surface tension based gripper designs (a) variable curvature driven by a liquid; (b) variable curvature driven by an actuated EAP [147] (Copyrights CIRP)

6.2.2 Presentation of the case study

The chosen case study deals with the design of a gripper to be used in the insertion of $300\mu\text{m}$ and $500\mu\text{m}$ diameter balls in the cage compartments of a watch bearing (see detail number 1 in figure 6.1). This task can be schematized by the insertion of a ball in a hole, such as displayed in the figure 6.3. One of the requirements is to avoid the conventional tweezers and vacuum grippers, because of the scratches they provoke on the balls. Due to the very small weight of the balls (about $3.8\mu\text{N}$), the surface tension based gripper is largely strong enough since it generates forces up to $150\mu\text{N}$. The handling scheme is illustrated in figure 6.3: the picking force is provided by the capillary force and the releasing task is ensured by laterally moving the gripper once the ball is in the hole.

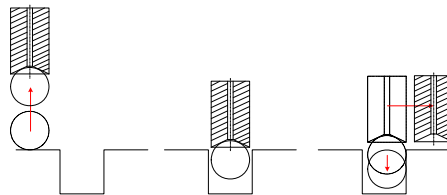


Figure 6.3: Handling scheme of the capillary gripping for the insertion of a ball in a hole.

Since the gripper uses capillary forces, a liquid has to be dispensed before each manipulation, but there is no need to eject this liquid (such as for example in ink jet printing): it is sufficient to bring a bit of liquid in contact with the ball to pick up. Beside this dispensing functionality, the other functions of the developed gripper tip can be summarized as follows: (1) to develop a picking force larger than the weight of the object ($W \approx 3.8\mu\text{N}$); (2) to develop a picking force large enough to handle the component with reasonable accelerations (manual handling); (3) to center the ball with respect to the gripper in order to ensure its positioning; (4) to release the ball once it is inserted in the hole. The proposed gripper is shown in figures 6.4 & 6.5. Prototypes have been machined in stainless steel and some of them have been coated with a hydrophobic silane-based coating.

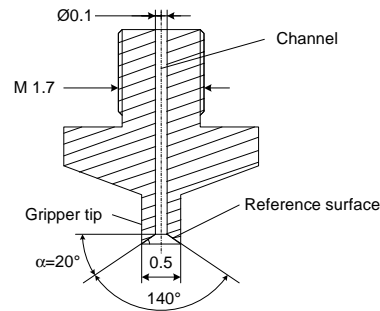


Figure 6.4: Schematic view of the designed gripper: the so-called reference surface is the surface which contacts the ball during the handling.

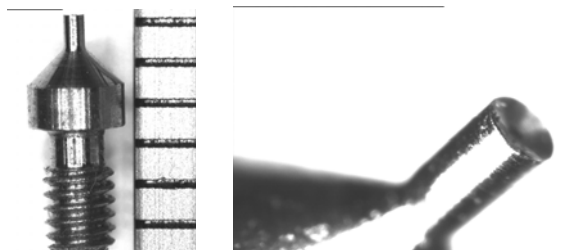


Figure 6.5: Prototype (the distance between the graduations is 1mm) and detail of the conical tip.

Two solutions have been tried to supply the gripping liquid: (1) to drive the pressure through the gripper channel; (2) to dip the tip in the liquid. Finally, the first solution has been discarded because of the instabilities of the generated droplet when its height approaches a half diameter of the gripper. It has been taken advantage of the good repeatability of the volume transferred to the gripper by dipping it to the liquid (see section 6.2.4).

6.2.3 Analytical force model for gripper design

We already proposed an analytical model describing the force exerted between the ball and the gripper in [109], which is based on the so-called circle approximation of the meniscus geometry (the detailed problem is shown in figure 6.6): this model is only valid at equilibrium (excluding for example the effect of the viscosity). The situation depicted in figure 6.6b shows that the meniscus wets the ball along the circle containing B (the position of this circle, whose radius is equal to R_B , is determined by the filling angle β).

The contact angle θ_1 is the angle between the tangent to the meniscus on the one hand and the tangent to the ball on the other hand: it is determined by the wetting properties of the materials, i.e. it is determined by the triple {handling liquid, material of the ball, surrounding environment}. On the gripper side (point

difference given by the Laplace equation ($\Delta p = 2H\gamma$) leads to infinity, as shown in figure 6.7a.

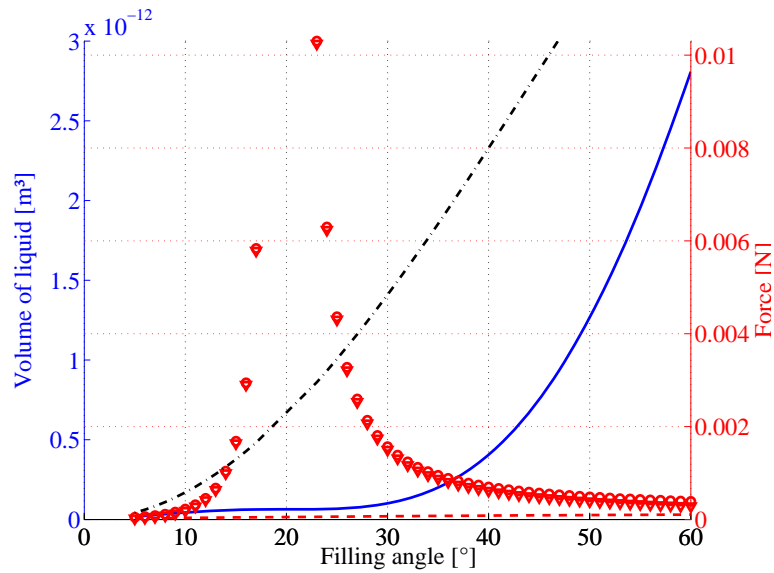
In this figure, the force (o marks) is maximum for $\beta = \alpha = 20^\circ$ (by the way, let us note the contributions of the tension term (— marks) and laplace term (triangular marks, which are superposed here with the o marks)). Nevertheless, the pressure difference cannot be unlimited, since the external pressure is assumed to be the atmospheric pressure. Consequently, the pressure difference used in the force calculation cannot be larger than 101400Pa, or even less if the cavitation of the liquid is assumed to occur at the vapor pressure. For example, in the case of water at 20°C , the vapor pressure is equal to 2839Pa. For isopropanol, the vapor pressure at 20°C is equal to 44029Pa. Therefore, the laplace force cannot exceed a value $F_M = \text{Area} \times (\text{Ambient pressure} - \text{vapor pressure})$. This limiting value is plotted in figure 6.7a (.-.- marks). This leads to a shift of the maximal force, as illustrated in figure 6.7b.

Thanks to the model of equation (6.1), we can observe that the force is proportional to the size of the gripper and to the surface tension of the used liquid. Since the gripper diameter is equal to the ball diameter, and since the weight of the ball is proportional to the third power of its diameter, it can be concluded that the smaller the ball to handle, the larger the ratio force/weight.

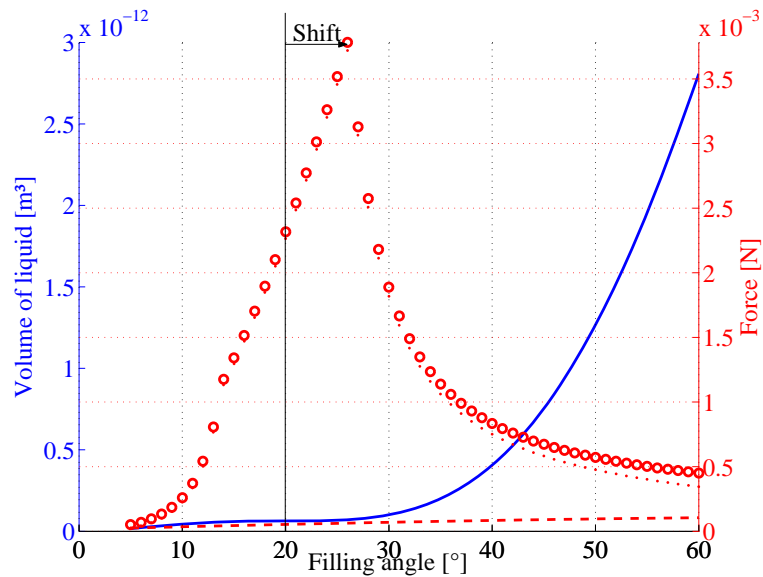
The linear influence of the surface tension must be carefully considered, because the contact angles θ_1 and θ_2 depend on this surface tension on a non-linear way. Unfortunately, there is no model giving the contact angles as a function of the surface tension only. Consequently, both must be carefully measured when the liquid is changed. Let us just emphasize the fact that the choice of the liquid must be performed according to several criteria: surface tension and related contact angles, but also evaporation time, viscosity, contact angle hysteresis and contact angle variability.

The influence of the filling angle β on the force has already been plotted in figure 6.7, so that we now only present the influence of θ_1 (figure 6.8a), θ_2 (figure 6.8b) and α (figure 6.9).

It can be concluded from figure 6.8 that the smaller the contact angles the larger the force. The choice $\alpha = 20^\circ$ leads to the right force order of magnitude.

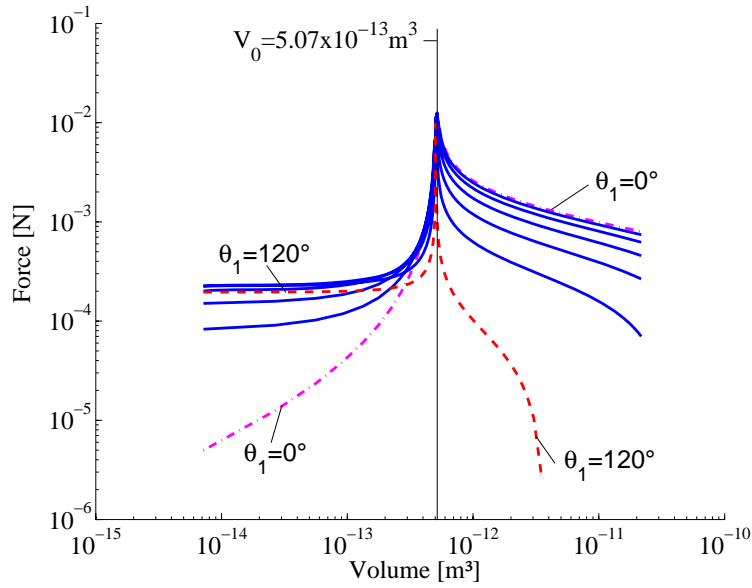


(a)

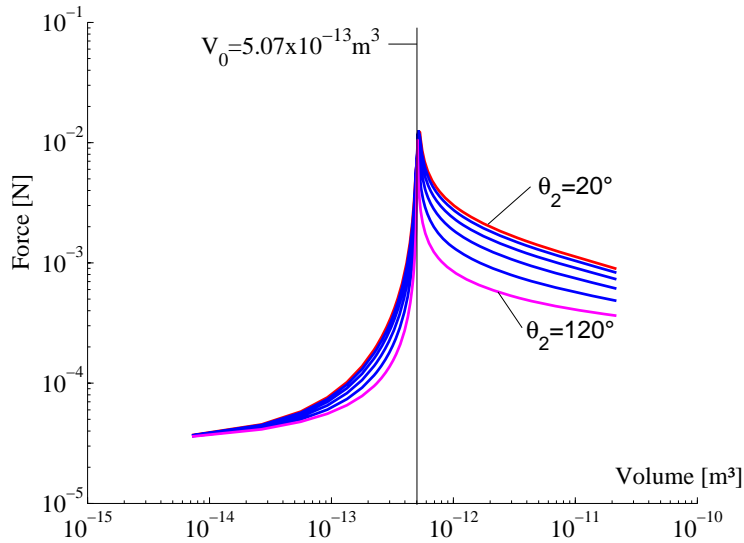


(b)

Figure 6.7: Force as a function of the filling angle β ($D = 0.5\text{mm}$, $\alpha = 20^\circ$, $\theta_1 = 8^\circ$, $\theta_2 = 50^\circ$, $\gamma = 72\text{mNm}^{-1}$). Solid line: volume of liquid, --- marks: tension term, triangles: Laplace term, circles: total capillary force. (a) .-. marks: limiting value due to cavitation. (b) Shift of the maximal force due to the pressure difference saturation.



(a)



(b)

Figure 6.8: Influence of contact angles θ_1 and θ_2 , for $D = 0.5\text{mm}$, $\alpha = 20^\circ$ and $\gamma = 72\text{mNm}^{-1}$. (a) influence of θ_1 and the volume of liquid on the force, for $\theta_1 = 0, 20, 40, 60, 80, 100, 120^\circ$ and $\theta_2 = 50^\circ$. The cut-off volume $V_0 = 5.07 \times 10^{-13}\text{m}^3$ corresponds to a filling angle $\beta = \alpha$ (where α is the gripper angle defined in figure 6.4). For $\beta > \alpha$ (i.e. $V > 5.07 \times 10^{-13}\text{m}^3$), the smaller θ_1 , the larger the force. (b) Influence of θ_2 and the volume of liquid on the force, for $\theta_2 = 20, 40, 60, 80, 100, 120^\circ$: the smaller θ_2 , the larger the force ($\theta_1 = 8^\circ$)

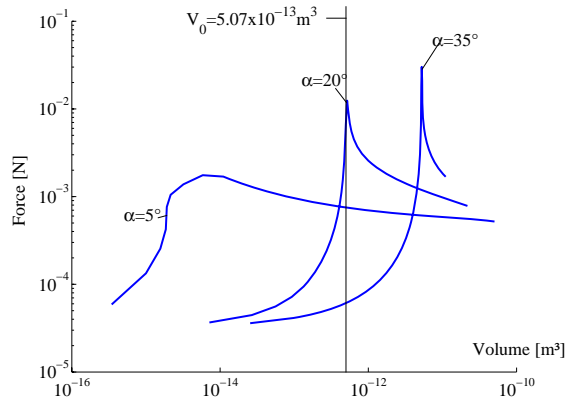


Figure 6.9: Influence of α and the volume of liquid on the force, for $\alpha = 5, 20, 35^\circ$ ($D = 0.5\text{mm}$, $\theta_1 = 8^\circ$, $\theta_2 = 50^\circ$, $\gamma = 72\text{mNm}^{-1}$).

6.2.4 Gripper characterization

Materials and contact angles

The balls of the bearing are in zirconium, and the grippers are made with stainless steel, coated or not with a silane-based layer. Three liquids have been used: demineralized water, isopropanol and L23 oil (Lube L-245X of Anderson Oil and Chemical Co.). Their properties are summarized in table 6.1. To measure the con-

	Isopropanol	Water	L23
Surface tension (Nm^{-1})	23.2×10^{-3}	73×10^{-3}	33.5×10^{-3}
Density (kgm^{-3})	768	1000	906
Dynamic viscosity at 20°C (Pas)	2.27×10^{-3}	1×10^{-3}	21.7×10^{-3}

Table 6.1: Liquid properties

tact angle hysteresis (see [91], page 76), the gripper was moved downwards (figure 6.10a) to measure the advancing contact angle and upwards (figure 6.10b) to measure the receding contact angle. Both angles were measured by moving the gripper very slowly (a few microns per second, in a quasi static configuration). All liquids have been used in combination with 6 coated stainless steel grippers and 6 non coated stainless steel grippers. The coating was a perfluorosilanization treatment (deposition of a monomolecular silane film by evaporation), supposed to have the best efficiency with water on silicon dioxide.

Each combination solid/liquid has been imaged 5 times, and on each picture, the contact angle has been measured twice (once on the left side, one on the right side). The average and the standard deviations of each of these 3×12 configurations are plotted in figures 6.11a&b and 6.12a&b. In these figures, grippers *A, B, C, D, I, J* are coated and grippers *E, F, G, H, K, L* are not.

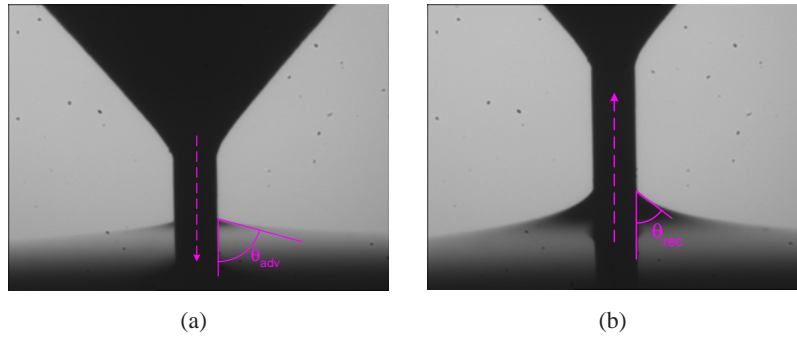


Figure 6.10: Illustration of the contact angle hysteresis (case of a stainless steel $\Phi 0.5\text{mm}$ gripper and water).

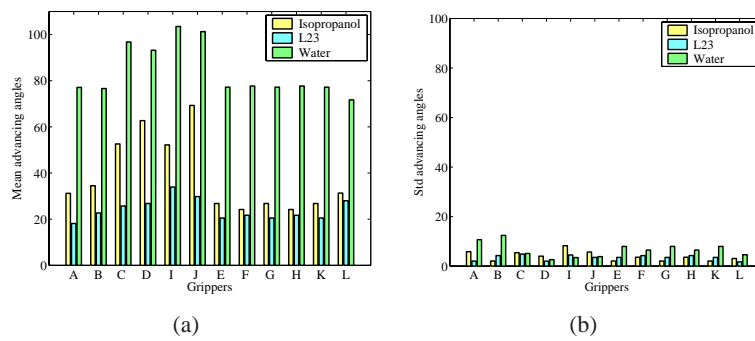


Figure 6.11: Advancing contact angles at latest 4 days after coating. (a) average values; (b) standard deviations of each ten of trials - Coated grippers: *A,B,C,D,I,J*; non coated grippers: *E,F,G,H,K,L*.

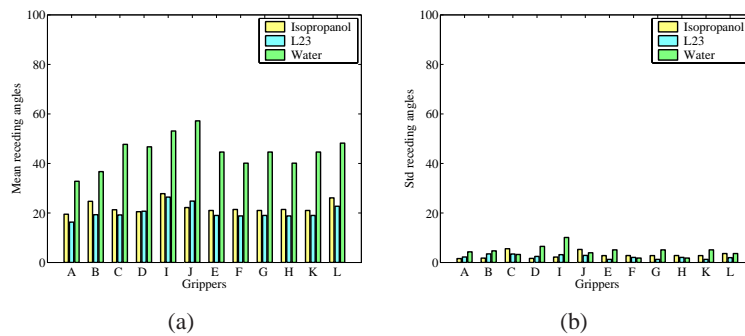


Figure 6.12: Receding contact angles at latest 4 days after coating. (a) average values; (b) standard deviations of each ten of trials - Coated grippers: *A,B,C,D,I,J*; non coated grippers: *E,F,G,H,K,L*.

In order to quantify the effect of the coating on the contact angles, an ANOVA [13] has been performed on these $360 = 3 \times 12 \times 10$ values (details in [108]).

This data analysis leads to the conclusion that the coating of the grippers is not useful in our application since the main effect of the coating is clearly negligible in comparison with the main effect of the liquid. More physically, this coating has been optimized to be vaporized on a silicon substrate. This coating is just a mono layer, which can be damaged or pulled off at some locations, leading to a quite heterogeneous surface. This physical suggestion is reinforced by the comparison of the standard deviations of the contact angles, between the coated surfaces and the non coated ones.

The conclusion of this analysis is that the currently applied coating (perfluorosilanisation) is not efficient.

Liquid feeding

In the chosen principle of liquid feeding, the gripper is dipped to a liquid tank (the immersion height is at least two times the gripper diameter d and the immersion speed is about a few tens of μms^{-1}), so that a small liquid droplet hangs at the bottom of the gripper, as illustrated in figure 6.13. One can expect the droplet

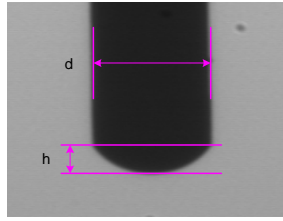


Figure 6.13: By dipping the gripper tip to a liquid, a small spherical shaped droplet hangs at the gripper tip (h is the droplet height and d is the gripper diameter).

height h to depend on the following parameters: the liquid surface tension γ , the gravity g , the liquid density ρ , the gripper diameter d , the contact angle θ . Non-dimensional formulated, it means that the ratio height/diameter can be expressed as follows:

$$\frac{h}{d} = f\left(\theta, \frac{\rho g d^2}{\gamma}\right) = f(\theta, B_o) \quad (6.2)$$

Therefore, the problem is much easier to represent: there are two non dimensional input parameters θ and B_0 and one non dimensional output parameter $H = h/d$.

We tested the following linear model without interaction:

$$H = \bar{H} + A_1\theta + A_2B_o + \varepsilon \quad (6.3)$$

and found the results of table 6.2. Accordingly the hanging height h/d is almost equal to the average value $\bar{H} = 0.315 \pm 0.001$. It is therefore a very repeatable way to feed the gripper with handling liquid. These results are based on 360 measurements (12 grippers \times 3 liquids \times 10 repetitions). The parameters θ and B_0 have been normalized, i.e. they vary between -1 and +1. This conclusion is of

	Value	Std
Average \bar{H}	0.31501	0.00126
A_1	0.00191	0.00227
A_2	-0.01298	0.00195

Table 6.2: Anova of the hanging height model

course only valid within the tested experimental space, i.e. $16.3^\circ \leq \theta \leq 57.2^\circ$ and $0.0121 \leq B_0 \leq 0.0785$.

6.2.5 Micromanipulation results

Pick and place cycle

Figure 6.14 illustrates a typical assembly cycle. On the first image, the ball to handle can be seen on the right side, 'floating' on a droplet of liquid (it 'floats' thanks to the surface tension effect, like the water strider, and not due to the Archimedes principle). On the left side of the first image there is the bearing in which the ball has to be placed. On the second image, the gripper is aligned above the ball. The third image illustrates the picking of the ball, which is then moved (images 4, 5 and 6) to its final location inside the bearing. The seventh image illustrates the radial shift of the gripper required to perform the release task. Finally, the gripper is moved away from the bearing.

Picking

The picking task cannot be separated from the feeding solution. Nevertheless, feeding was not the primary point of this study. Therefore, we have considered that in the worst case, the position of the balls could be determined by vision. We have consequently studied the possibility to pick up a ball resting on a flat substrate or at a liquid interface such as illustrated in the previous pick and place sequences.

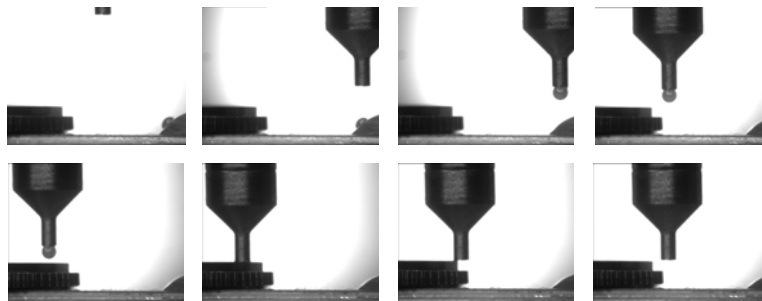


Figure 6.14: Assembly sequence: the diameter of the handled ball is 0.5mm.

We present here some picking errors observed during the experiments and propose some strategies to correct them.

The figure 6.15 illustrates some typical picking errors. In case of a centering

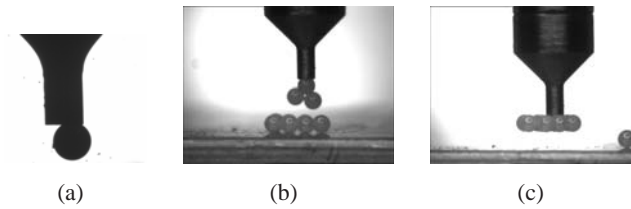


Figure 6.15: Picking errors: (a) centering error; (b-c) balls get stuck after water evaporation; ($\Phi 0.5\text{mm } ZrO_2$ balls, conical grippers).

error (i.e. the gripper is not perfectly aligned with respect to the ball) the ball can either be not picked or be badly aligned (such as depicted in figure 6.15a). The first defect can be corrected by adding a bit of liquid and by positioning the gripper properly, but in the case depicted in figure 6.15a, the ball must be released and the picking operation must be tried again. To release the ball, it is sufficient to dip it to a liquid tank: since there is no more liquid-gas interface between the ball and the gripper, there is no more capillary force and the weight of the ball pulls it downwards.

When working with water, other complications can occur: figure 6.15b&c illustrate the case of several balls sticking with each other, probably because of the capillary forces due to the residual traces of liquid. In some cases, these sticking balls form a regular hexagonal shaped alignment, depicted in figure 6.16.

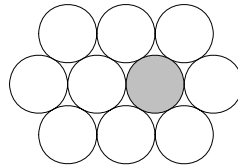


Figure 6.16: Top view of the hexagonal network of the 10 balls (the gray ball is picked by the gripper)

Different solutions can be applied to these problems. The first category of solutions aims at guaranteeing the picking of only one ball at a time. This can be best performed by posing the balls at the interface of a liquid, such as depicted in figure 6.17. These pictures illustrate the ability to pick one ball at a time from an initial alignment of four balls (figure 6.17a). The coated concave conical gripper is positioned above the second ball from left (figure 6.17b), moved downwards in contact with this ball (figure 6.17c). Figure 6.17d shows the pick operation of this ball. The pick operation is then improved with what can be called a kind of "liquid feeding". The efficiency of this strategy clearly depends on the volume of liquid (which, for water, means dependent on time because of the evaporation), on

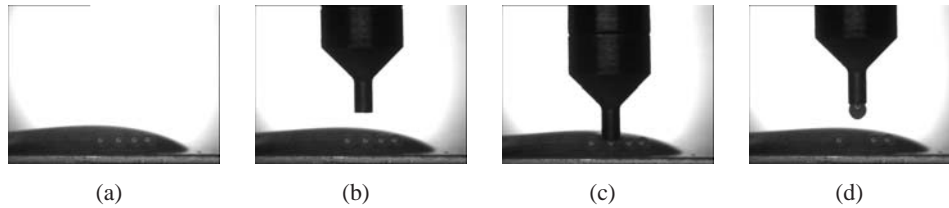


Figure 6.17: Coated conical tip (B): pick from wet bulk (balls are ordered)

the kind of liquid and on the number of balls in the neighborhood of the picked ball. Indeed, in the case of a regular balls network with the L23 oil, the picking efficiency was not clearly improved by the presence of a liquid film. The reason for this probably lies in the fact that the contact angle between the ball (in zirconium) and the oil is much smaller than the one got with water. Therefore, the capillary force between balls can be stronger, the sum of the forces between the balls being larger than the force between the gripper and the picked ball.

The pictures shown in figure 6.18 illustrate the "pick from wet bulk" strategy: a series of 10 balls float by surface tension on a spherical cap shaped water droplet put on a steel substrate. In figure 6.18, the gripper is dipped to the balls, and picks up only one ball (figures 6.18b&c).

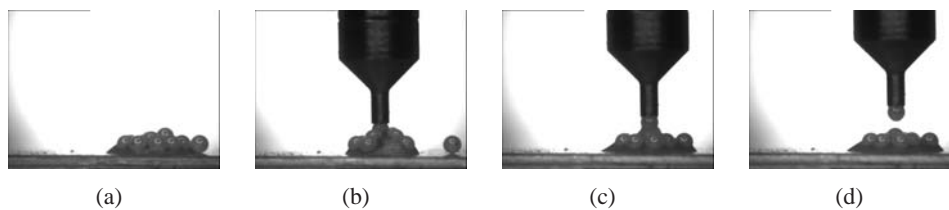


Figure 6.18: Coated conical tip (B): pick from wet bulk (balls are not ordered)

The second category of solutions consists in releasing all the picked balls, either when there is a centering error or when more than one ball has been picked. A way to release all the balls is to dip the gripper to a liquid tank: since there is no capillary force in the liquid, the weight of the balls pull them downwards.

Placing

Several release strategies have been studied in the literature (a state of the art can be found in [101]). The chosen strategy described here below is inspired by the so-called scraping release. Figure 6.19 illustrates several placement errors.

The placement reliability has been studied as a function of the ratio between the height h between the gripper and the bearing on the one hand and the gripper diameter d on the other hand. The use of this non dimensional ratio allows the comparison between the $\Phi 0.3\text{mm}$ and the $\Phi 0.5\text{mm}$ grippers. In figure 6.20, the reliability is calculated as the number of successes divided by 10 (each placement

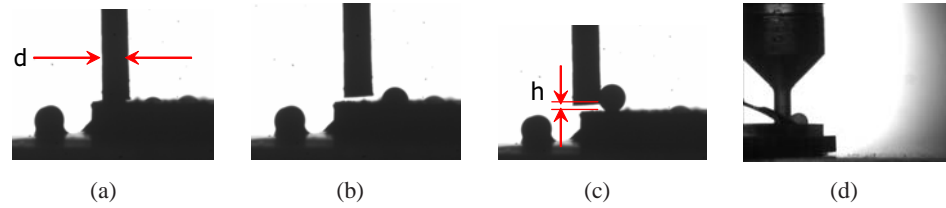


Figure 6.19: (a) Successful placement: the ball remains in position; (b) Placement error: the ball is released, but its equilibrium position is higher than the gripper; (c) Placement error: the ball is not released and sticks to the gripper; (d) Placement error: the gripper touches the cage.

has been replicated 10 times). It is represented as a function of the ratio h/d . For

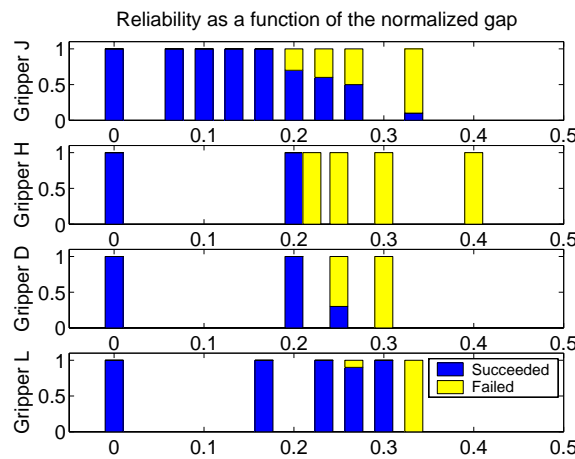


Figure 6.20: Reliability of the placement as a function of the non-dimensional gap between the gripper and the bearing - Gripper *J*: 0.3mm, coated; gripper *H*: 0.5mm, non coated; gripper *D*: 0.5mm, coated; gripper *L*: 0.3mm, non coated.

gaps smaller than 0.2 times the ball diameter, the placement is always successful.

Force measurement

The experimental set up used in this study has already been described in [91]: the force sensing is achieved by measuring the deflection (Keyence LC2440 non contact sensor) of a steel cantilevered beam whose stiffness ($\approx 1\text{Nm}^{-1}$) is known thanks to a calibration with known proof masses. The capillary force can be measured with a resolution of the order of $1\mu\text{N}$. The scene can be observed through a CCD camera (Keyence CV500 with a CV050 lens), which allows to measure the advancing and receding contact angles. Four grippers have been tested whose properties are summarized in table 6.3 (the liquid which was used for the force measurements was the L23 oil. Note that oil has been used because it does not

Table 6.3: Properties of the tested grippers: d is the gripper diameter, 'channel' denotes the presence of an internal channel, 'coated' denotes the presence of a silane-based coating, θ_A is the advancing contact angle, θ_R is the receding contact angle and h/d is the ratio between the height h of the hanging droplet after the gripper has been dipped in liquid.

Gripper	d (mm)	Channel	Coated	θ_A ($^\circ$)	σ_{θ_A} ($^\circ$)	θ_R ($^\circ$)	σ_{θ_R} ($^\circ$)	$\frac{h}{d}$
B	0.5	Yes	Yes	22.7	4.2	19.3	3.5	0.287
F	0.5	Yes	No	21.7	4.2	18.8	2.0	0.293
H	0.5	No	No	21.0	2.6	16.8	2.5	0.305
J	0.3	No	Yes	29.8	3.5	24.8	2.9	0.329

evaporate during the experiments. Moreover, since it can be the lubrication oil of the assembled device, it is not a drawback to have residual traces of liquid on the component after the manipulation). The balls are made in ZrO_2 .

Direct force measurements are shown in figure 6.21, for 4 different grippers (B, F, H, J). In each case, the gripper has been dipped to liquid and put in contact with the ball to handle (the ball diameter is equal to the one of the gripper). This

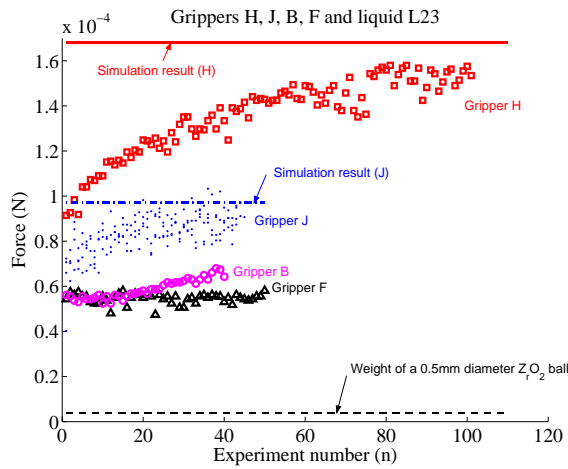


Figure 6.21: Force measurements: the behavior of grippers J and H is to be compared with simulation in the case of maximal filling angle β . These simulation results only provide a comparison of the order of magnitude since the volume of liquid is not accurately known (gripper H : 0.5mm without channel, non coated; gripper J : 0.3mm without channel, coated; gripper B : 0.5mm with channel, coated; gripper F : 0.5mm with channel, non coated).

first contact discards the main part of liquid so that the volume of liquid becomes smaller than the conical cavity of the grippers (henceforth, it cannot be seen with

the camera). Then, the gripper is applied onto the ball n times without refilling it and the capillary force between the gripper and the ball is measured. After each rupture of the meniscus (i.e. after each contact), a bit of liquid is left on the ball, so that the volume of liquid involved in the manipulation is decreasing (however it cannot be measured). Therefore, according to the models (see figure 6.7), the force should increase, which can be observed in figure 6.21 for grippers H and J. For grippers B and F, the simulation cannot be run because the effects of the channel have not been modelled. Nevertheless, the effect of this channel is to decrease the force (the force generated by larger grippers B and F is even smaller than the one generated by the smaller gripper J).

6.2.6 Discussion and conclusions

This section presented the study of a gripper using the effects of the surface tension to handle submillimetric balls. Its originality lies in the developed design and in the adaptation of existing force models to this case study. The characterization work which has been led indicates that the chosen perfluorosilanisation coating is not efficient probably due to its weak thickness. An alternative could be the dip coating, which lead to more thick layers. Nevertheless, since the simulation results indicate the capability to develop a picking force for all contact angles, we will not care about these aspects in the future. Moreover, the release task does not seem to suffer from this lack of hydrophobic coating. A test bed has been used to experimentally validate the handling principle, showing a successful cycle of pick and place. The comparison with experimental results validates the force models in terms of trend and order of magnitude. A further validation should require measuring the volume of the liquid inside the conical cavity of the gripper. The proposed gripper design is well adapted for 0.3mm and 0.5mm diameter balls. The liquid supply has been achieved by dipping the gripper tip to the handling liquid. At this step, the presence of an internal channel is not necessary to supply the liquid. Moreover, the channel decreases the force.

Criterion	Performance	
Force	100 μ N \gg weight 4 μ N	V
Picking errors	Image analysis: compacity	X
Placing errors	Mastered	V
Compliance to error positioning	Self centering effect	V
Response times	in the order of a few millisecond	V

Table 6.4: Capillary gripper: performances overview

Nevertheless, a reliable components feeding strategy is required: this will be developed in next sections.

6.3 Capillary feeder

The conclusions of my postdoctoral research on surface tension gripping presented in previous section show a weakness of this handling principle in terms of picking, due to unsatisfactory feeding device. At this period, the research context used to point out the advantages of working in liquid environments (see for example the Pronomia project⁴). According to this paradigm - which will be detailed in the following -, we developed with Cyrille Lenders and Jean-Baptiste Valsamis a feeding device working able to separate the balls in a liquid environment and position them at known locations. The results of this work were presented at the IPAS conference [118].

6.3.1 Requirements list

It turns out from previous section that a dedicated feeder would be of the utmost interest. Let us summary its requirements:

1. components are supplied in bulk, i.e. without any ordering;
2. Components are supposed to be spherical, with a diameter of 500 μm ;
3. Final location of components must be known;
4. Capillary gripper should be able to catch (only) one component.

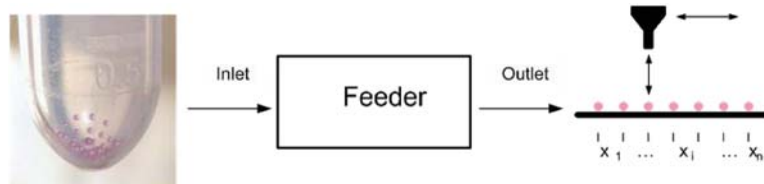


Figure 6.22: Feeder

Previous work already highlighted the reduction of disturbance effects in liquid environment:

1. there is no free surface;
2. electrostatic effects are reduced since the permittivity of water is 80 times the air permittivity;

It however requires to get the components out of the liquid before gripping.

⁴http://www.lab.cnrs.fr/pronomia/accueil_vf.php

6.3.2 Design

The principle is to sort immersed balls by using a liquid flow inside the device to lead each ball in a dedicated cavity. Once one cavity is filled with a ball, the liquid flow lines are deviated to empty cavities. When all cavities of the grid have been filled, the latter can be pulled out of water. The issue is then to know whether the capillary gripper is able to pick the balls, despite the presence of residual liquid between the walls of the cavities and the balls. This problem is related to what we call a "conformity" issue. As shown in figure 6.23, geometrical conformity between two surfaces is the major driver of the capillary force. Therefore, if we want the gripper to pick a ball from a cavity, the conformity between the gripper and the ball must be larger than the conformity between the cavity and the ball. The gripper was already designed to this aim (see previous section), and the design of cavities was chosen to minimize the conformity with the balls.

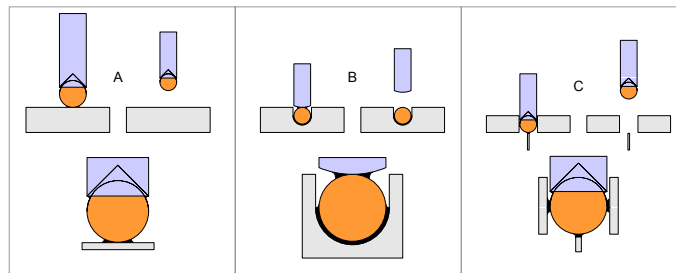


Figure 6.23: Conformity issue: (a) a concave gripper can pick up a sphere from a flat plane, but (b) a flat gripper cannot pick up a ball contained in a matching concave cavity. Therefore (c) the design of the feeder relies on a cavity limited by a cylindrical hole partially closed at the bottom side by a thin vertical blade: this allows the liquid to flow through the cavity while ensuring a larger conformity of the ball to the gripper.

The manufactured device has 20 cavities (named locations in figure 6.24). Liquid can be supplied either manually (as indicated in this figure) or automatically with a pump connected to the feeder by the green tube on the right of the figure.

6.3.3 Results

Statistical results indicated an averaged success rate of 75% in cavity filling. Nevertheless, as shown in figure 6.25 this success rate depends on the location of the cavity with respect to the liquid flow leading the balls. Especially, it can be seen that the success rates of holes 9 and 13 were 100%. This indicates a deterministic perspective in separating and feeding submillimetric components in liquid environments.

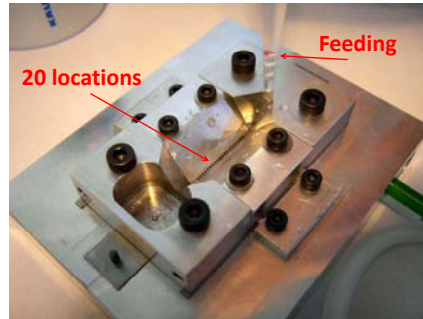


Figure 6.24: Liquid feeder containing a grid with 20 locations. The liquid flow induced either by manual pipetting or by a pump - connected to the green tube on the right of the picture - allows to separate the balls and position them in the 20 cavities. Balls in excess are evacuated in the container on the left of the device.

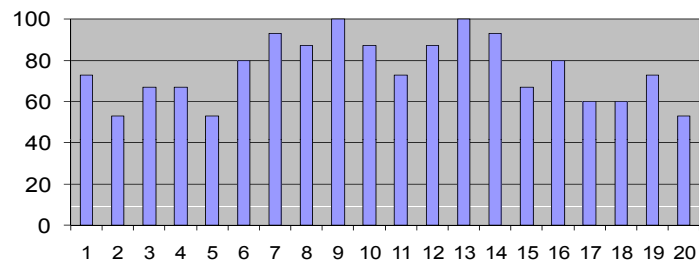


Figure 6.25: Success rate of the 20 holes, over 10 repetitions: locations number 9 and 13 are always fed with a single ball.



Figure 6.26: Integration of (a) the liquid feeder of this section and (b) the capillary gripper of section 6.2

6.3.4 Integration with the capillary gripper

Naturally, we integrated the capillary gripper and this feeder, as illustrated in figure 6.26. With this system, we could achieve a (reliable) automated pick and place of $7\ 500\ \mu\text{m}$ diameter balls inside a watch ball bearing. The cycle time is not relevant here, since it is driven by the kinematics of our platform (the order of 1s), which can of course be accelerated. The scientific question related to cycle time is to know which are the limitations induced by the capillary action. It was already shown in my PhD that the high accelerations of industrial assembly machines (up to a few tens of G) does not modify the shape of the liquid bridge drastically (the argument will be developed later on in section 6.6). Nevertheless, the assembly cycle time will obviously be limited by the characteristic time of the meniscus. This was studied by Jean-Baptiste Valsamis under my supervision: exploitation of his results to this aim are also presented in section 6.6). Before addressing this question of cycle times, let us present in the next section an original use of acoustic levitation as a components feeder.

6.4 Non contact feeder

As already mentioned in section 6.2, our capillary gripper suffers from the lack of efficient feeding. Indeed, balls tend to stick to each other, leading to multiple picking. This drawback has been corrected by the development of a dedicated liquid feeder presented in previous section. Current section takes advantage of an interesting property of acoustic fields: the field modification induced by the insertion of the gripper spontaneously leads the ball from its equilibrium position to the gripper. This phenomenon was first observed in simulation before being tested experimentally, during the PhD work of Vincent Vandaele under my supervision [184].

6.4.1 Gripper and ball models

The capillary gripper was first modeled to be inserted as a geometry in the numerical simulation environment used to compute the acoustic field. Its geometrical parameters are recalled in table 6.5.

Description	Parameter	Value
Tip diameter	d_1	0.5 mm
Tool body diameter	d_3	2.3 mm
Support diameter	d_4	1.25 mm
Thread mean diameter	d_6	1.525 mm
Tip length	l_1	1.0 mm
Tip to tool body length	l_2	0.9 mm
Tool body length	l_3	1.0 mm
Support length	l_4	1.0 mm
Support to thread length	l_5	0.3 mm
Thread length	l_6	1.8 mm
Cone opening angle	α	20°
Tip centre position	$\{x_o, y_o, z_o\}$	{2.0 mm, 0, 6.0 mm}

Table 6.5: List of the capillary gripper geometrical parameters — length and radius of the successive sections, starting from the tip side; tool axis x

Accordingly, it has a conical tip with a diameter $d_1 = 0.5$ mm. The tool axis is directed along the x axis. The gripper is inserted in the xz plane, with the tip center located at $x_o = 2$ mm and $z_o = 6.0$ mm, which corresponds to a position slightly below the central pressure node.

The levitated component is a small aluminum sphere of radius $a = 0.2$ mm.

6.4.2 Numerical results of the non contact feeder

The model has to be three-dimensional, since the inserted tool introduces an asymmetry in the problem. The force field is obtained by solving only one three-

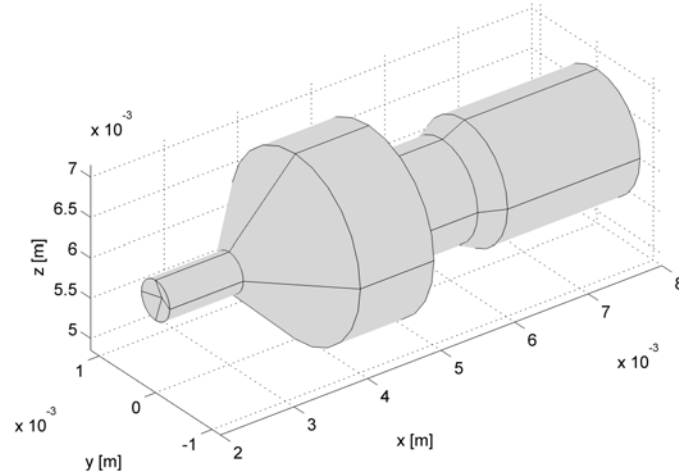
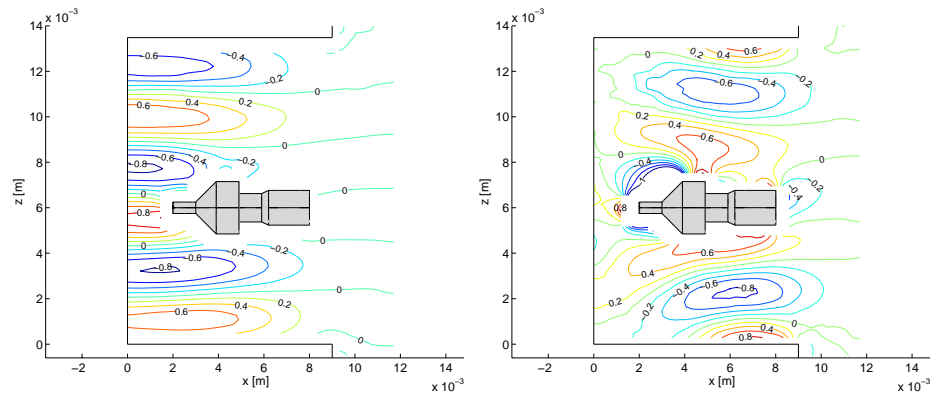


Figure 6.27: Capillary gripper geometry — conical tip; diameter $d_1 = 0.5$ mm

dimensional finite element analysis. The acoustic radiation force field is evaluated in the plane xz , going through the capillary gripper axis, for sphere positions in the whole acoustic chamber. The axial and radial force components are represented in figure 6.28 as contour plots.



(a) Axial component F_z : scaling value $3.24 \mu\text{N}$ (b) Radial component F_x : scaling value $0.45 \mu\text{N}$

Figure 6.28: Acoustic radiation force \vec{F}_{ac} as a function of the sphere positions x_o, z_o for the levitator with a plane reflector after insertion of the capillary gripper: contour plot of the force components computed with the Gor'kov62 model — $r_r = 9$ mm, $h_r = 10$ mm, $r_s = 9$ mm, $h_s = 10$ mm; reflector distance $L_r = 13.5$ mm; aluminum sphere $a = 0.2$ mm, levitated in air at $f = 40.0$ kHz, $p = 5000$ Pa; capillary gripper with conical tip of diameter $d_1 = 0.5$ mm

The maximum axial and radial force amplitudes are about $3.24 \mu\text{N}$ and $0.45 \mu\text{N}$ respectively. The maximum radial amplitude represents 13.9 % of the maximum axial amplitude. The tangential forces out of the xz plane have not been computed.

The most important feature, when inserting the capillary gripper, is the inversion of the radial force in front of the tool tip. By inversion we mean that in absence of the gripper, the radial component of the force field is negative, i.e. directed toward the symmetry axis and henceforth providing a stable self-centering effect of the component. After the tool insertion, the radial forces become positive in front of the tip. The previously stably levitated object is attracted towards the capillary gripper. Moreover, the axial force remains strong, so that the component is still levitated against gravity.

These observations can be used to remove a component from the levitator, if the adhesion force to the gripper is sufficient.

6.4.3 Conclusions

The simulated attraction effect has been tested in practical experiments (figure 6.29). The levitator could be used as a microcomponent feeding system for the capillary gripper. This device could feed as many components as its number of stable equilibrium positions, i.e. depending on number of half wave lengths between the sonotrode and the reflector generating the stationary acoustic field. Moreover, when inserting a component in the levitator with a pair of tweezers, a similar effect is experienced. The dynamical behaviour of the retraction of the tool is important to leave the component in a stable position.

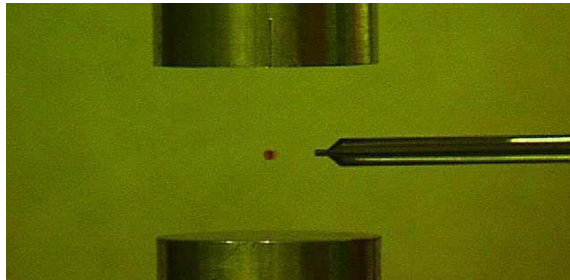


Figure 6.29: In the absence of external body, the radial component of the acoustic force field in the vicinity of equilibrium positions is directed toward the symmetry axis, leading to stable levitation of the small sphere shown in the picture. The introduction of an external rigid body such as a gripper or a tweezer modifies this radial component, inducing a push from the symmetry axis toward the inserted gripper. Consequently, the levitator could be used as a microcomponent feeding system for the capillary gripper

6.5 Hybrid assembly

Hybrid assembly is an assembly paradigm combining the advantages of high throughput pick and place mastered by industry⁵ and the emerging self-assembly developed in academic research (see for example the recent literature review by Massimo Mastrangeli on this topic [133] or the experimental work done by Quand Zhou [167]). The integration of both techniques would allow rough components positioning with the serial robot, the fine positioning being ensured by a self-centering effect, e.g. capillary forces. The related scientific problems are closely related to the modeling presented in section 4.3.6. Consequently, the underlying literature on flip-chip modeling can also be of interested to hybrid assembly (see for example [183] or [132]).

Among the framework of the EU Hydromel research project, we have collaborated with Jens Tapprogge from CSEM and applied the models presented in section 4.3.6 to the characterization of solder bumps related to his application.

6.5.1 Presentation of the case study

A substrate must be connected to a component through a series of 7 solder paste bonds. A sketch of this substrate and its pads is illustrated in figure 6.30. The solder paste to be used is Indalloy #42. Currently, there are 7 square pads ($380\mu\text{m} \times 380\mu\text{m}$) and the component beared by the 7 pads has a mass equal to 50 mg.

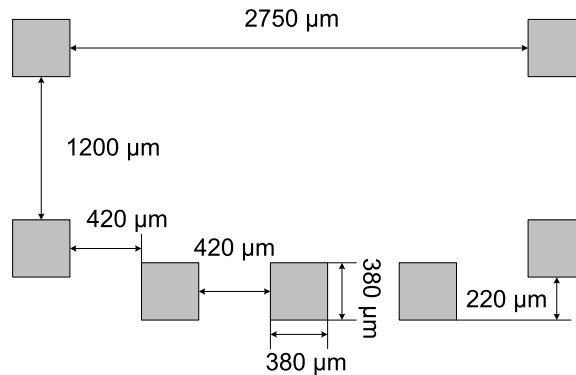


Figure 6.30: Distribution of pads in the case study of the EU Hydromel project

The lateral stiffness of the assembly during the reflow phase⁶ will depend on the volume of paste on each pad. Since this volume can be freely chosen, the question addressed here is to model the dependence of the lateral stiffness and characteristic damping time of the system on the volume of solder paste on each

⁵up to 13 components by second

⁶The paste is firstly deposited on the pads of the substrate through a stencil. After aligning the component and the substrate, a heating process is started - called reflow - during which the solder paste becomes liquid and can therefore be modeled according to the developments of section 4.3.6 on lateral capillary forces

pad. It was proposed to achieve this with our developed models on lateral capillary forces.

6.5.2 Model parameters

The model requires 3 physical properties of the liquid: density, surface tension and dynamic viscosity.

According to the supplier, density of Indalloy #42 is 8990 kgm^{-3} . Based on its composition (46Bi 34Sn 20Pb) and its phase transition temperatures (liquidus: 96°C , solidus: 96°C), we could find in [156] a surface tension of about 425 mNm^{-1} at a temperature of 250°C , close to the reflow temperature. Concerning the viscosity, [155] indicates a viscosity of 3 mPas at a temperature of 127°C , for the alloy 38Pb 62SN (i.e. without Bismuth). In [154] we found a viscosity of 3.5 mPas at a temperature of 127°C for the alloy 44Pb 56Bi (figure 8). Moreover, these authors give the following Arrhenius law to take the influence of temperature into account:

$$\mu(T) = \mu_0 \exp(E/(RT)) \quad (6.4)$$

with $\mu_0 = 0.5886 \text{ mPas}$ and $E = 5.845 \text{ kJmol}^{-1}$.

Consequently, we will take the values of $\gamma = 425 \text{ mNm}^{-1}$ and $\mu = 2.25 \text{ mPas}$ (at 250°).

Beside density, surface tension and dynamic viscosity, we have considered a component of mass $m=50\text{e-6 kg}$, put on a solder paste meniscus developing a lateral stiffness $k = 7 \times k_s$ and having an area of contact with the liquid equal to $S = 7 \times c^2$ where $c = 380 \text{ }\mu\text{m}$ is the length of an edge.

Symbol	Description	Value	Units	Source
γ	Surface tension	0.425	Nm^{-1}	[156]
η	Dynamic viscosity	2.25	mPas	[155]
ρ	Density	8990	km^{-3}	J. Taprogge
h	Gap	unknown		
V	Volume	c^2h		
c	Edge length of square pad	380	μm	J. Taprogge
m	Component mass	50e-6	kg	J. Taprogge

Table 6.6: Properties of the case study Femto-Tools

According to equation 4.65, the stiffness k_s is given by:

$$k_s = \frac{2ch^2\gamma}{(s^2 + h^2)^{\frac{3}{2}}} \approx \frac{2c\gamma}{h} \quad (6.5)$$

All these parameters are summarized in table 6.6.

6.5.3 Application of the model

According to section 4.3.6, the dynamics of the component is governed by only two dimensionless parameters α and \tilde{m} . The reduced mass \tilde{m} is given by:

$$\tilde{m} = \frac{2m}{7\rho c^2 h} \quad (6.6)$$

and the reduced viscosity α is given by:

$$\alpha = \frac{4\mu\tau}{\rho h^2} = \frac{\mu}{\rho} \sqrt{\frac{8m}{7c\gamma h^3}} \quad (6.7)$$

where τ is a characteristic time estimated as $\tau = \sqrt{\frac{m}{7k_s}}$

It is interesting to observe that if we assume the gap h to be a fraction β of the edge c ($h = \beta c$ where $0 < \beta < 1$ is also the aspect ratio of the meniscus), the terms \tilde{m} , τ and α can be rewritten into:

$$\tilde{m} = \frac{2m}{7\rho} \frac{1}{\beta} \frac{1}{c^3} \quad (6.8)$$

$$\tau = \sqrt{\frac{m}{14\gamma}} \beta^{0.5} \quad (6.9)$$

$$\alpha = \frac{4\mu}{\rho} \sqrt{\frac{m}{14\gamma}} \frac{1}{c^2} \frac{1}{\beta^{1.5}} \quad (6.10)$$

Beyond this case study in which the edge c is known, the latter equations allow to eliminate the edge c and find a relationship between α and \tilde{m} , with β as a non-dimensional parameter. This relationship is plotted in figure 6.31 for $\beta = 0.1$ (upper dashed line) and $\beta = 0.5$ (lower dashed line).

In our case ($c = 380 \mu\text{m}$), we can combine equations (6.8 and 6.10) with $\beta = 0.1$, leading to $\tilde{m} = 290$ and $\alpha = 0.97$. This couple of values is marked on the figure by the magenta disk, and corresponds to $\tau_d = 900$. This means that the corresponding damping time is estimated to $900\tau = 900 \times 1 \text{ ms} = 0.9 \text{ s}$.

We see from the iso-lines of the figure (which correspond to constant non-dimensional damping time) that reducing the damping time can be obtained on two ways: decrease β (i.e. move upwards in the figure, toward smaller damping time values) or reduce \tilde{m} (moving leftwards). Moreover, reducing β also reduces the characteristic time τ , which leads to even smaller damping time (equation 6.9). Note that if an increase of the number of pads will decrease \tilde{m} , which is favorable to a decrease of the damping time.

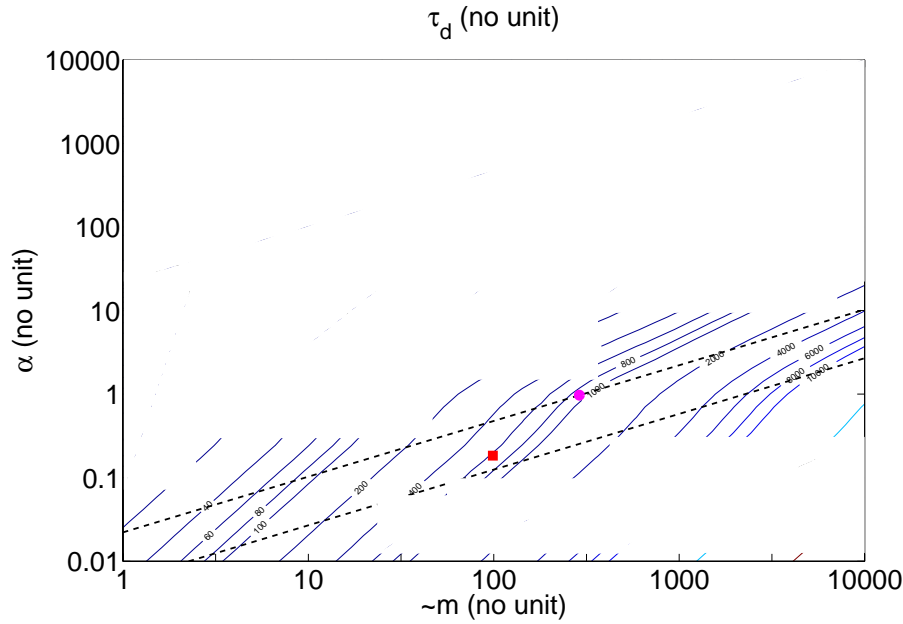


Figure 6.31: Non dimensional map giving the damping time τ_d as a function of the reduced viscosity α and the reduced mass \tilde{m} . This map has been validated in the area of interest on a benchmark published by Lu and Bailey [132]. The domain of interest for the Femto-Tools case study is limited by the upper dashed line ($\beta = 0.1$) and the lower dashed line ($\beta = 0.5$). The value of the damping time τ_c shown in this plot is the damping time normalized by the characteristic time τ defined here above which is independent on the value of the square edge c . The red square indicates the benchmark of Lu and Bailey [132], for which $\tilde{m} = 98.9$, $\alpha = 0.18$ and $\tau_d = 660$. The magenta star indicates the case of $c = 380 \mu\text{m}$ and $\beta = 0.1$, leading to $\tilde{m} = 289.6$, $\alpha = 0.97$ and τ_d about 900.

6.5.4 Conclusions

The map of figure 6.31 can be used together with equations (6.8-6.10) to estimate the damping time. The stiffness of the pads can be estimated using equation (4.65) (to multiply by the number of pads). Finally, the component is a mass-spring system whose resonance frequency is given as $f = \frac{1}{2\pi\tau}$, with τ given by equation (6.9), which turns out to be independent of the edge length c .

6.6 Assembly machine case study

Contacts from assembly machine industry usually ask about the performances of capillary gripping, through a series of questions: what is the accuracy? the success rate (or yield)? is the meniscus stiff enough to undergo the large accelerations of the picking heads (up to 10G when we focused on these aspects, maybe even more today)? what could be the cycle time of such a technique? Even if models cannot replace experimental trials on actual assembly machines (contacts have been made in this direction), they can provide partial information.

6.6.1 What accelerations can undergo a liquid bridge?

The answer to this question is based on the concept of capillary length, making the trade-off between capillary effects and gravity effects. This leads to a length L below which the effects of gravity can be neglected:

$$L = \sqrt{\frac{\gamma}{\rho g}} \quad (6.11)$$

Similarly, we defined a modified capillary length L^* below which the effects of the machine acceleration a can be neglected:

$$L = \sqrt{\frac{\gamma}{\rho(g+a)}} \quad (6.12)$$

We therefore see that for $a = 10g$, the modified capillary length is about 0.8 mm instead of 2.7 mm. This means that for meniscus heights smaller than the (modified) capillary length, the effects of acceleration may be neglected. This will always be the case in micro-assembly.

6.6.2 What is the typical cycle time?

The cycle time of an assembly process is usually defined as the duration between the production of two products: this sets the time which is available for each assembly station. Typically, high throughput machines reach a volume up to 50000 products/h, which means up to 14 products/s or about 70 ms/operation. The pick and place operation of a component must therefore be achieved in 70 ms. Assuming that the limitation does not come from the performances of the robotic picking head, we had a look at the typical time of the liquid bridge, i.e. the time required by the meniscus to displace and modify its shape, under the action of inertia, viscous and surface tension forces (as described in section 4.3.4).

Figure 6.32 presents a series of 5 snapshots taken every 2 ms showing the formation of a liquid bridge from two wetting droplets (the upper solid is moving rightwards).

Figure 6.33 presents a series of 10 snapshots taken every 2 ms showing the rupture of a liquid bridge into two wetting droplets and their oscillations toward equilibrium (the upper solid is moving leftwards).

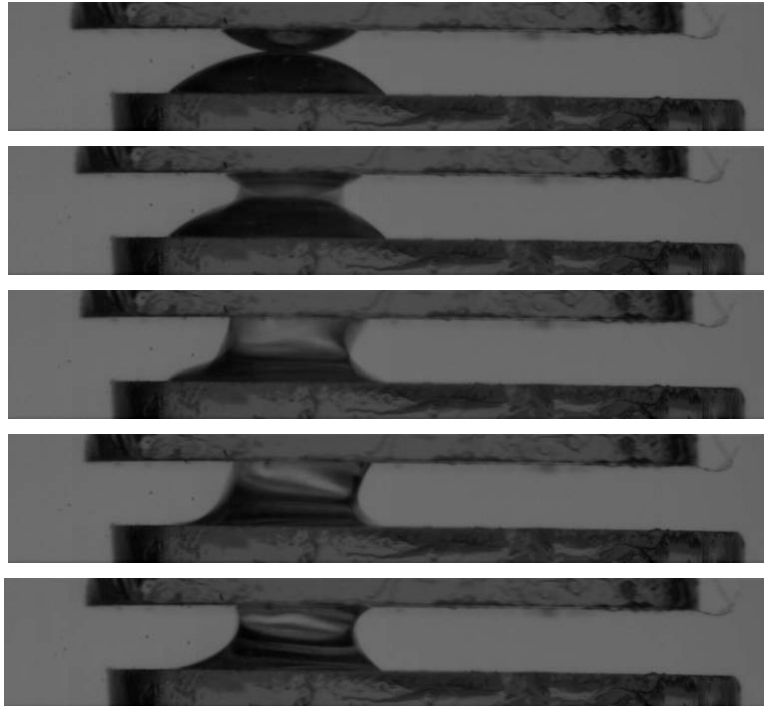


Figure 6.32: Snapshots taken during the rightwards motion of the upper solid (every 2 ms with water, gap=900 μm).

6.6.3 What is the force applied on the component during picking?

The force applied on the component during the approach of the picking head can be computed with the developed models. Let us first explain the problem with figure 6.34. The picking head is approaching the component with a downwards velocity of the order of 1 ms^{-1} . A deceleration of about 100 ms^{-2} is applied in order to stop the picking head at a distance from the component chosen to be $50 \mu\text{m}$, leading to the kinematics shown in figure 6.35. The time step at which the droplet contacts the component is indicated with a red arrow. From the previous section we know that the duration of the liquid bridge is of the order of a few milliseconds. Assuming however the liquid bridge to be shaped instantaneously, we can compute the force it exerts on the component during the end of this kinematics, i.e. until the velocity of the picking head is reduced to zero. Using the equivalent models of section 4.3.4, we can compute the capillary (F_C), viscous (F_V) and inertial (F_I) components of the total force (F_T) applied on the component. The evolution of these components is plotted in figure 6.36

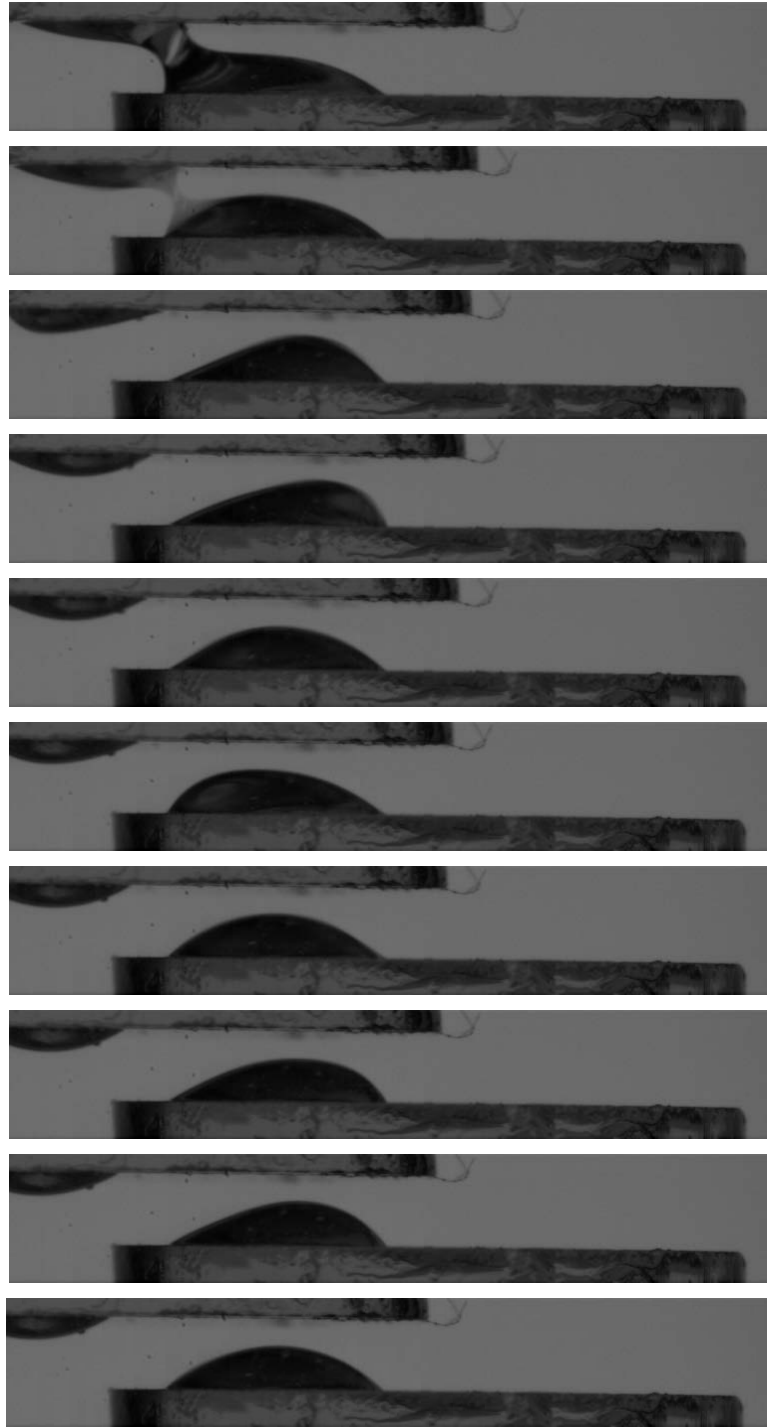


Figure 6.33: Snapshots taken during the leftwards motion of the upper solid (every 2 ms, with water, $gap = 900 \mu\text{m}$).

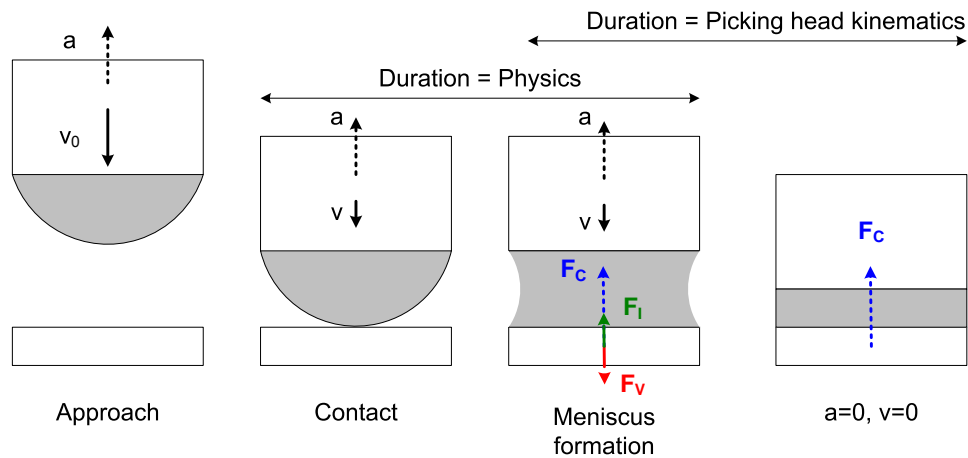


Figure 6.34: Picking phase governed by the deceleration of the picking head: after contact of the hanging droplet, a liquid bridge is formed in a few milliseconds and the force applied on the component depends on capillary (F_c), viscous (F_v) and inertial (F_i) effects. When the picking head is stopped (velocity and acceleration equal to zero), the remaining force exerted on the component is due to surface tension

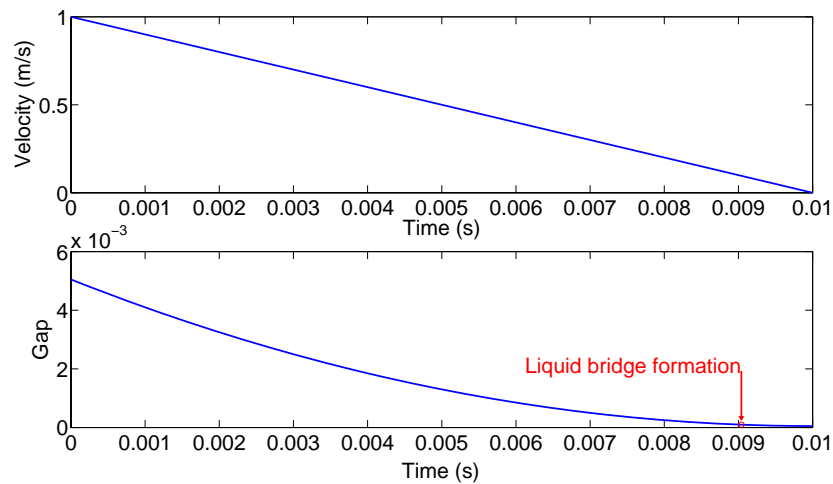


Figure 6.35: Kinematics of the picking head: assuming a constant deceleration, we can see the typical linear velocity profile and the associated position. When the gap between the head and the component is equal to the height of the hanging droplet, the latter is transformed in a liquid bridge with a time scale of a few millisecond.

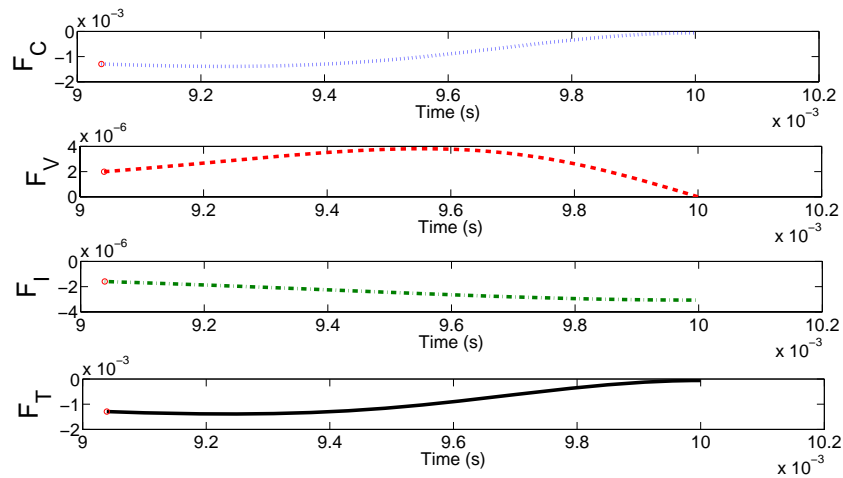


Figure 6.36: During the final phase of the approach, a liquid bridge links the picking head and the component, which exert a force on the latter, according to the capillary (dotted blue line), viscous (dashed red line) and inertial (dash-dotted green line) effects described in section 4.3.4

6.6.4 What liquids are recommended not to pollute the surfaces

It is often thought about water, despite its drawbacks in terms of experimental variability (contact angle hysteresis observed with water are usually quite large - a few tens of degrees). Silicone oil can be used if evaporation is a drawback (for example for experimental measurements), but traces will be left on components after meniscus rupture. Consequently, volatile liquids (isopropanol) are recommended since they evaporate and are often used as cleaning liquids. But the pick and place process must be performed quick enough to avoid the complete evaporation of the liquid bridge.

6.7 Surface tension based robotic platform

We explained in section 4.4.2 the emerging need for introducing compliance in microsystem. We tried to introduce this compliance with surface tension on the one hand and with gas compressibility on the other hand. Combining this in a micro-robotic approach, we currently work on a microrobotic platform with 6 degrees-of-freedom, trying to actively control 3 of them, as explained in the following.

Moreover, due to physics explained in section 4.4.2, we know that the proposed model allow two determine two unknowns among the position of the platform, the force exerted on it, the pressure in the fluidic legs and the number of gas molecules in the legs. If the latter may be known by calibration, this means that the knowledge of the pressure allows to compute the position and the force. The device acts in this case as a force-position sensor.

6.7.1 Kinematics of the microrobotic platform

The platform is carried by three fluidic legs, actuating the translation along the z axis and the tilts θ_x and θ_y (axis defined in figure 6.37).

6.7.2 Current results

The platform has been manufactured and tested. Figure gives a general view of the device: 3 holes (1) can be seen on the substrate (2), which are connected to the inlet tubes (3) which supply the gas. This substrate is immersed in a tank (4) containing silicone oil (5). Once the bubbles have been generated (they cannot be seen on the picture), the platform (6) is roughly positioned above the substrate. Capillary forces provide self-centering. The fluidic legs (7) can be imaged with a camera whose optical axis is vertical (8), thanks to a mirror (9) tilted with 45° .

To benchmark the model proposed in section 4.4.2 and more specifically the results of figure 4.48, we have applied 3 different forces by putting three objects with known weight on the platform. For each loading case, figure 6.38 indicates the value of these weights (red circles \circ), the result of the model using the number of gas molecules n and the gap as inputs (solid blue line) and the value of the force computed from the image of a leg (blue square \square). This kind of image permits to compute the pressure in the meniscus from the curvature of the liquid-gas interface. The large crosses indicate the dispersion of measurements on the value of the force and gap.

6.7.3 Conclusions

A patent is currently pending on these aspects. The fluidic leg can be seen as a natural miniaturization of macroscopic fluidic flexible actuators, in which the gas is confined by an elastic membrane. Here, this membrane is replaced by the liquid-gas interface ruled by surface tension. Our design is therefore intrinsically miniaturized.

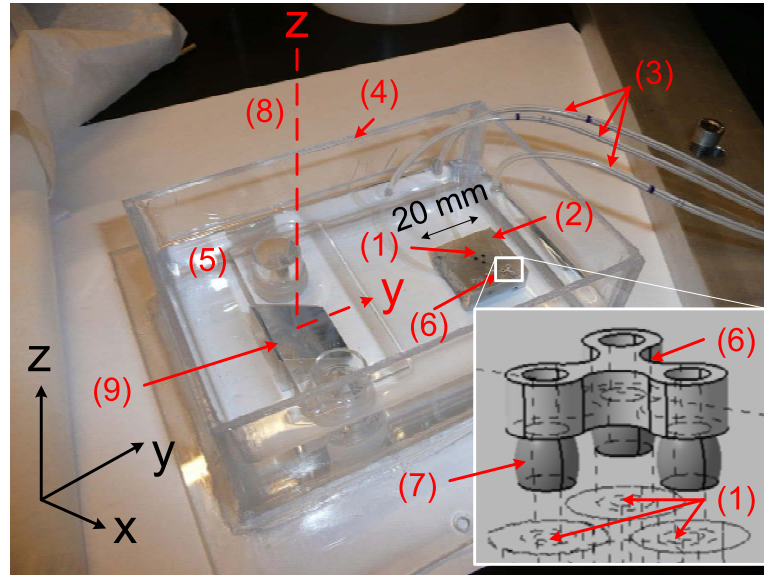


Figure 6.37: General overview of the device: 3 holes (1) can be seen on the substrate (2), which are connected to the inlet tubes (3) which supply the gas. This substrate is immersed in a tank (4) containing silicone oil (5). Once the bubbles have been generated (they cannot be seen on the picture), the platform (6) is roughly positioned above the substrate. The fluidic legs (7) can be imaged with a camera whose optical axis is vertical (8), thanks to a mirror (9) tilted with 45° .

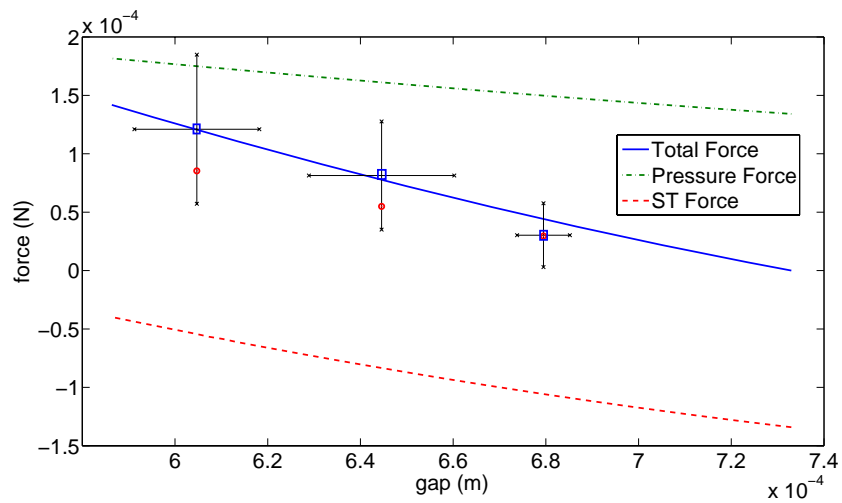


Figure 6.38: Force-displacement behavior of a fluidic leg (Parameters: $V_0 = \frac{nRT}{p_0} = 98.17 \cdot 10^{-9} \text{ m}^3$, $T =$, $\gamma = 72 \text{ mNm}^{-1}$, s , $p_0 =$). The solid blue line is the result of the numerical simulation, the three red circles represent the force applied on the platform and the three squares the value of these forces obtained through an image of the fluidic leg (see the text for further information)

6.8 Soil mechanics

Thanks to a recent collaboration with Fabio Gabrieli (University of Padova, Italy), we could apply our capillary forces models to the adhesion between grains in soil mechanics. This has led to the submission of a paper entitled "Micromechanical modeling of erosion of partially wet granular slope" in the International Journal for Numerical and Analytical Methods in Geomechanics.

6.8.1 Presentation of the problem

It is well-known in soil mechanics that in many circumstances natural slopes of granular material may exceed their specific soil friction angle (Picarelli et al., [150]). This apparently strange behavior is due to the presence of a cohesion among soil grains, that should be caused by several physical and chemical phenomena. A tensile force can be easily experimented also in all partially wet granular soil, especially in the fine-grained ones: this feature is well known for sand as it can be handled to obtain wonderful sand castles (Barabasi et al. [4], Nowak et al. [143]). In this collaboration with Gabrieli, the focus was on dry and funicular states, according to figure 6.39.

Saturation degree	Regime		Principal forces
0%	Dry		Gravity, contact
0-5%	Pendular		Gravity, contact, capillary
5-35%	Funicular		Gravity, contact, capillary
35-90%	Capillary		Gravity, contact, capillary, viscous drag
90-100%	Saturated		Gravity, contact, viscous drag

Figure 6.39: Soil saturation states (adapted and revised from Newitt and Conway-Jones [142]).

6.8.2 Experimental study

Evaporation can be measured by tracking the weight decrease to water evaporation during the process. Figure 6.40 shows the evolution of the slope of the granular material before and after evaporation.

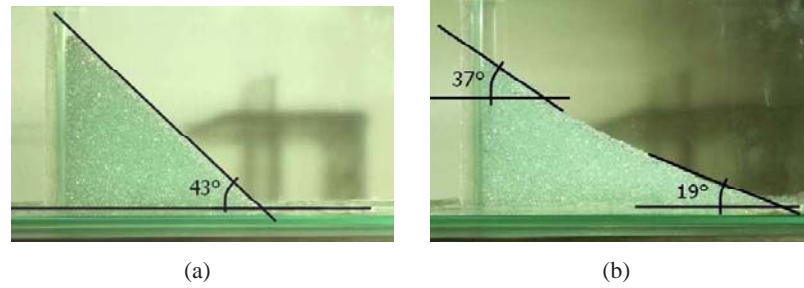


Figure 6.40: Photos of slope profile during evaporation test: (a) initial shape for water content $W = 1.24\%$ and (b) final stage with mean water content $W = 0.7\%$. W is the mass ratio of water over the mass of the grains.

6.8.3 Simulation

Assuming an evaporation rate law, this evolution can be simulated by taking into account the adhesive interactions between each pair of grains. An example of result of such a simulation is given in figure 6.41 where it can be seen that the superficial layer of material has dried and fallen down due the vanishing of the capillary bond by evaporation.

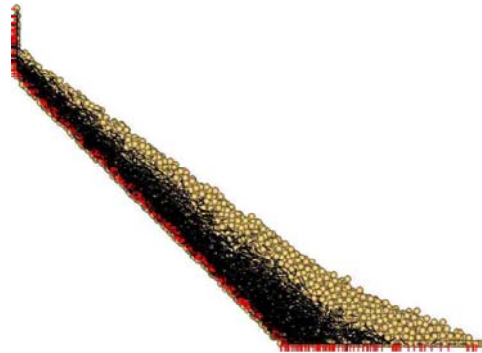


Figure 6.41: Evolution of capillary bridge distribution during the simulation: the black segments represent the capillary bonds between particles in contact and without contact respectively; no segment means loosened particles

The use of Surface Evolver was not suitable in this study due to the large number of capillary force interactions to compute (one for each pair of grains). Therefore, the parabolic and numerical methods presented in chapter 4 have been used. They are compared in figure 6.42 with a powerful empirical law by Soulié [173], who proposed an empirical model based on the fit of numerical simulation results,

leading to a capillary force estimated by:

$$F = \pi\gamma\sqrt{R_1R_2} \left[c + \exp\left(a\frac{h}{R_2} + b\right) \right] \quad (6.13)$$

where:

$$a = -1.1 \left(\frac{V}{R_2^3}\right)^{-0.53}$$

$$b = \left(-0.148 \log\left(\frac{V}{R_2^3}\right) - 0.96\right) \theta^2 - 0.0082 \log\left(\frac{V}{R_2^3}\right) + 0.48$$

$$c = 0.0018 \log\left(\frac{V}{R_2^3}\right) + 0.078$$

with V the volume of liquid (m^3), R_2 the sphere radius (m), θ the contact angle in radian, γ the surface tension (Nm^{-1}).

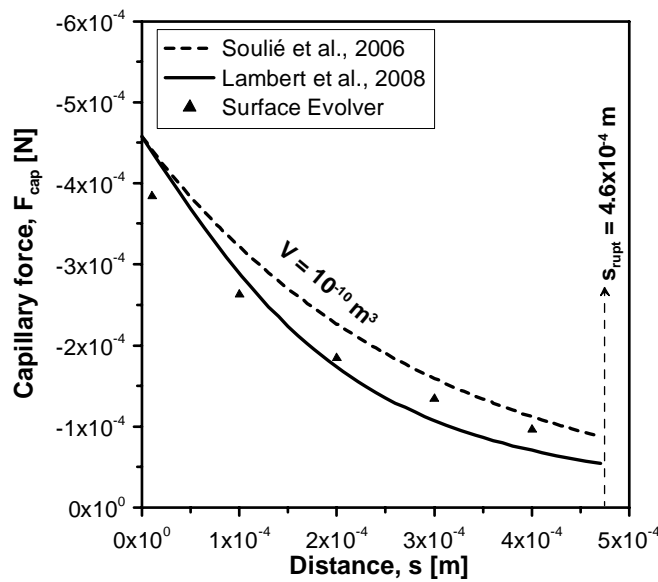


Figure 6.42: Benchmarking Soulié and own models with Surface Evolver ($R = 1 \text{ mm}$, $\theta = 0^\circ$, $V = 10^{-10} \text{ m}^3$, $\gamma = 72 \text{ mm}^{-1}$, $\text{gap}=0$)

6.8.4 Conclusion

This study was an opportunity to apply models to a totally different application field. The main contribution was to benchmark the empirical model of Soulié with our models, so that Gabrieli could use this empirical model in an efficient way in his simulations.

6.9 Capillary rise

6.9.1 Introduction

The capillary rise problem consists in simulating the filling of a capillary tube by a liquid. This knowledge can theoretically be applied to the filling of any fluidic system. More particularly, one of the goals defined at the beginning of this study was to design channels geometries in order to minimize the presence of gas bubbles in the system (this problem is known as the 'priming' of fluidic devices, such as micropumps).

Static capillary rise is described by the so-called Jurin's law:

$$h_{\infty} = \frac{2\gamma \cos \theta_s}{R\rho g} \quad (6.14)$$

where γ is the surface tension, θ_s is the static contact angle, R the tube radius, ρ the liquid density and g the gravity.

Dynamic simulation of capillary rise is much more complex because of the large displacement of the liquid-gas interface during the liquid motion, the dependence of contact angles to the triple line velocity ($\theta \neq \text{constant}$) and the unusual slip boundary condition (to allow the triple line displacement along the inner wall of the tube). The problem is sketched in figure 6.43.

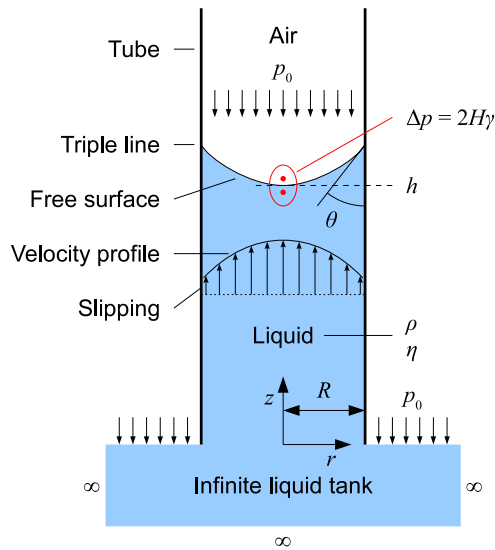


Figure 6.43: Illustration of the capillary rise problem in a tube of radius R . Fluid properties are represented by the density ρ , dynamic viscosity μ , surface tension γ . h is the height of the liquid, θ the contact angle at the triple line. According to the so-called Laplace law, the curvature $2H$ induces a pressure difference across the liquid-gas interface, which drives the liquid into the tube.

6.9.2 Dynamic contact angles

The term contact angle must be detailed carefully:

- equilibrium or static contact angle θ_s is the angle made by a droplet posed on a substrate (this angle is used in surface energy measurement devices);
- advancing θ_{adv} and receding θ_{rec} contact angles are static contact angles observed when the triple line is about to move forward (advancing motion) or backward (receding motion). Advancing contact angles are larger than receding contact angles;
- contact angle hysteresis is the difference between advancing and receding contact angles;
- apparent contact angle is the apparent angle made by the tangent to the solid-gas interface and the tangent to the liquid-gas interface, at macroscopic scale (i.e. what is seen by imaging a meniscus);
- microscopic or real contact angle is the contact angle made by the liquid film under the action of surface tension and disjoining pressure due to van der Waals effects;
- dynamic contact angle θ_d is an advancing contact angle depending on the velocity of the triple line.

The so-called Tanner's law [81] relates the dynamic contact angle to the static contact angle and the capillary number Ca^7 :

$$\theta_d \div Ca^{\frac{1}{3}} \quad (6.15)$$

The comparison made by Jean-Baptiste Valsamis between different other laws from literature is illustrated in figure 6.44.

Own experimental measurements have been done by imaging capillary rises with a high speed camera (for less viscous liquids, characteristic time of liquid rise is of the order of 100 ms). The finite difference of meniscus height indicates the velocity (hence the capillary number Ca) and the angles are measured on each image (see Valsamis's PhD for details concerning the post treatment method). These results are shown in figure 6.45, superimposed with the dynamic contact angles from literature models (Brake, Jiang, Hof-Voi-Tan and Kistler). The static contact angles θ_s indicated in this figure have been computed from the equilibrium height h_∞ given by the Jurin's law (equation 6.14). Note well that these results have been obtained using surface tension as a driver: the liquid is not pushed in the tube by an external pressure, it is pulled by the surface tension effects occurring at the liquid-gas interface. By comparison, in the case study related to assembly machines, the

⁷The capillary number Ca is a non dimensional number balancing the viscous and surface tension effects: $Ca = \frac{\mu V}{\gamma}$

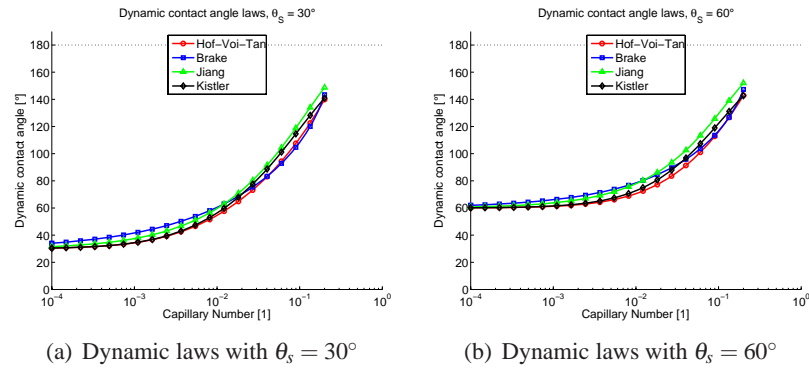


Figure 6.44: These figures show the dependence of the dynamic contact angle on the static contact angle and the capillary number, according to several authors: Hof-Van-Toi, Brake, Jiang [77] and Kistler.

Capillary number is of the order of 10^{-1} , which is larger than the Capillary numbers governing the capillary rise. Since we observe (at larger Capillary numbers) a deviation between the experimental dynamic contact angles and those given by literature models, we conclude that it can be useful to proceed to own dynamic contact angle characterization in such a case study.

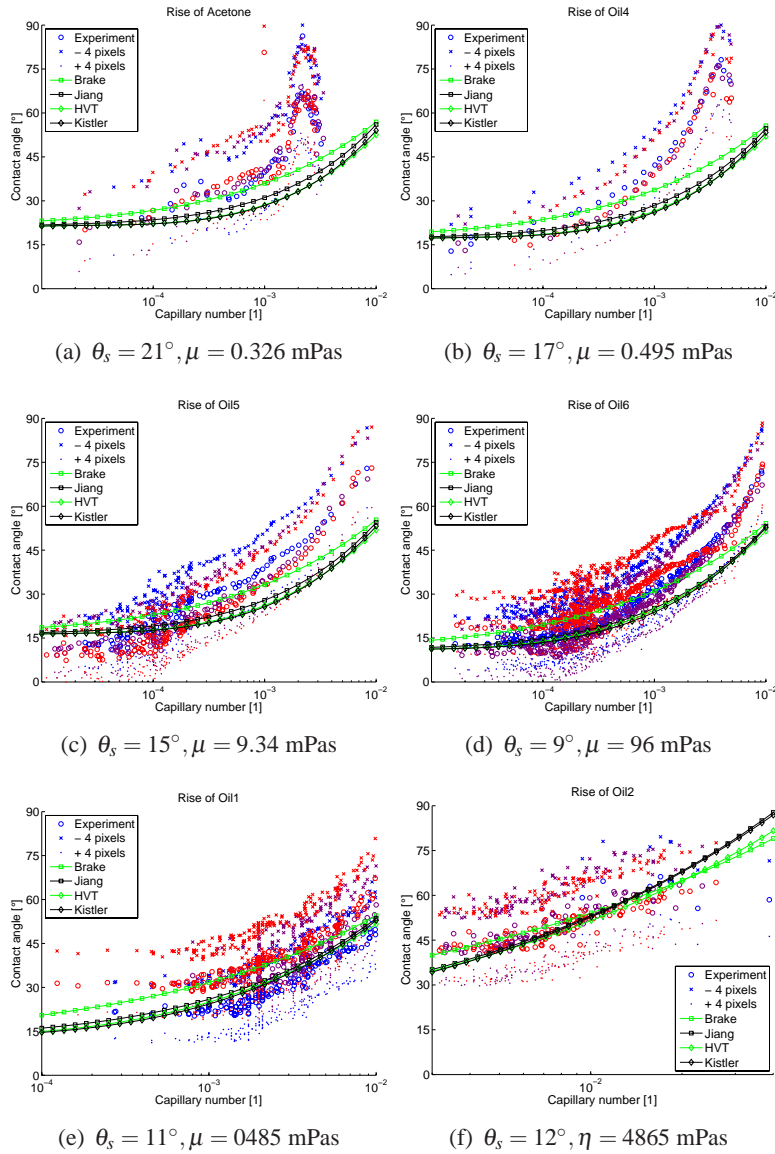


Figure 6.45: Dynamic contact angles measured from experimental capillary rises. The static contact angles θ_s indicated in this figure have been computed from the equilibrium height h_∞ given by the Jurin's law (equation 6.14)

6.9.3 Slip length

The usual no-slip condition used in fluid mechanics is not valid anymore for capillary rise since the triple line of the meniscus is moving. De Gennes [42] proposed a description similar to the "chenilles" kinematics to explain the motion of the triple line, however the phenomena does not seem to be very well understood. Numerical simulations therefore usually introduce the concept of slip length [20, 35, 40, 151],

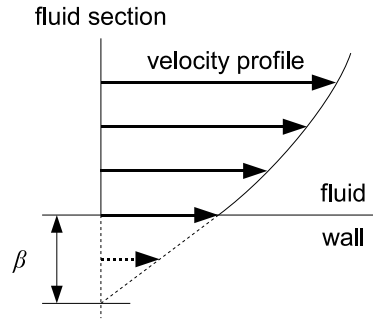


Figure 6.46: Slip length representation: the velocity profile vanishes below the wall, at a depth β

as indicated in figure 6.46: the slip length β is the distance below the surface where the linear extrapolation of the velocity profile u on the wall vanishes. In his work, Jean-Baptiste Valsamis points out open questions:

1. although the slip length concept has been proven by observations, it mainly appears for non-wetting surfaces. Choi et Al. [35] conclude that slipping remains uncertain between water and hydrophilic surfaces;
2. the assumption of constant slip length is also controversial. Choi et Al. observe a linear variation of the slip length, but they underline their own experimental scattering;
3. molecular dynamics has been introduced by [40] to study this phenomenon, but this goes beyond the scope of this study;

Let us add to these conclusions the weak dependence of the results to this slip length in the simulation of capillary rise. The contact angle variation is much more impacting the results.

6.9.4 1D benchmark

Neglecting the study of the liquid-gas interface, the problem becomes 1-dimensional, with the capillary height $h(t)$ as single unknown of the problem, described by the usual Newton's law:

$$\frac{d(m(t)\dot{h}(t))}{dt} = \sum_i F_i(t) \quad (6.16)$$

Schoenfeld [169] develops this equation with the capillary force driving the liquid upward against internal viscous force and weight. This leads to:

$$R^2 \rho (h\ddot{h} + \dot{h}^2) = 2R\gamma \cos \theta - R^2 \rho gh - 8\eta h\dot{h} \quad (6.17)$$

This equation can be analytically solved under various assumptions described by Valsamis, or numerically integrated with an ODE solver. In this case, θ may be depending on the velocity \dot{h} . This will be done for plotting the results of figure 6.47 entitled 'Newton' (the name on the right indicating the dynamic contact model which was used).

6.9.5 Experimental results

Experimental capillary rises have been imaged with a high speed camera: the results are shown in figure 6.47. The comparison with literature models is proposed by Jean-Baptiste Valsamis

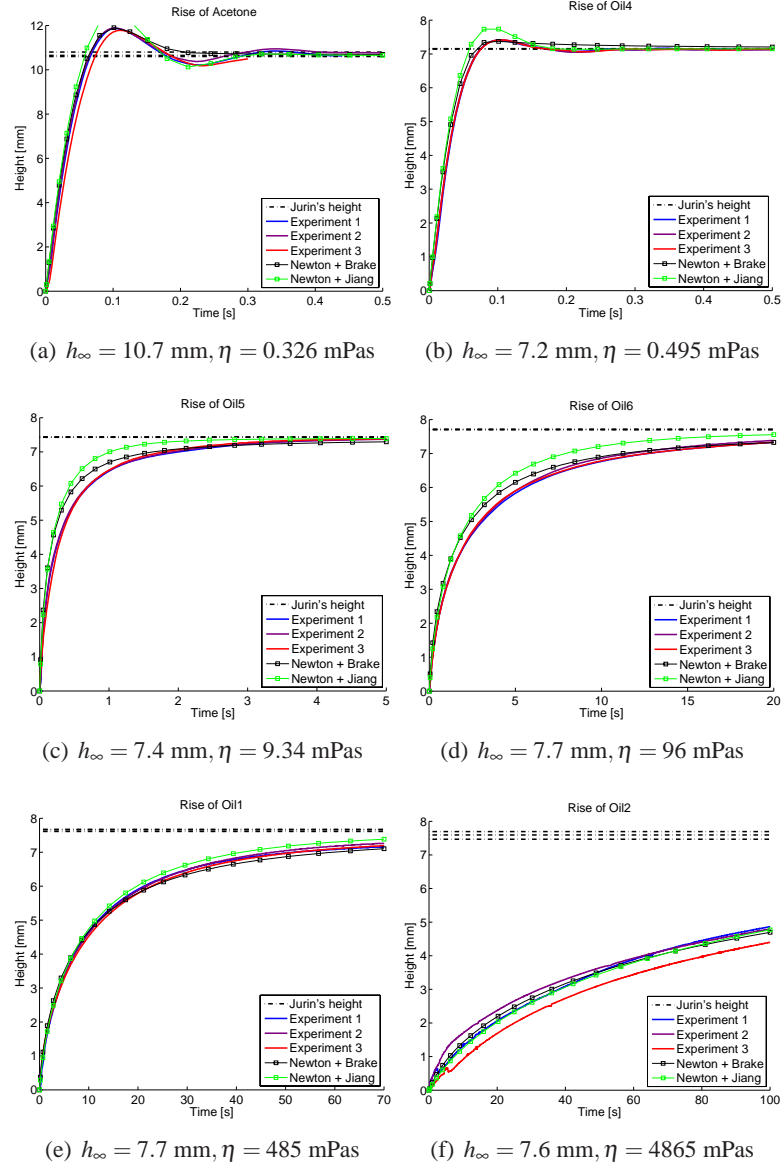


Figure 6.47: Experimental evolution of meniscus height h as a function of the time. Results obtained by the numerical integration of Newton's law are superimposed (see equation 6.17).

6.9.6 Numerical results

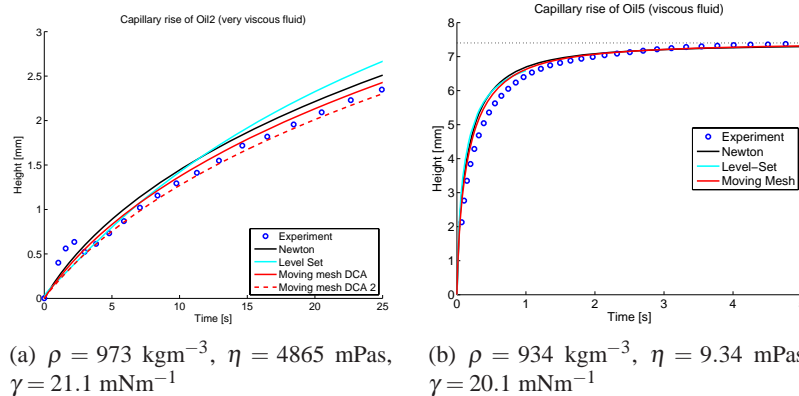


Figure 6.48: Numerical results from [181] for a tube with inner diameter 1.138 mm. These results illustrate the agreement between experiment, an approached 1D numerical simulation and both Comsol results, the first one using the so-called level-set method and the second one the moving mesh approach. The contact angles used in these simulations are the apparent ones, i.e. the angles measured with a high speed camera.

6.9.7 Conclusions

The questions answered by this section are manifold: (1) the apparent dynamic contact angle measured with a high speed camera drives the liquid in capillary rise, since numerical simulation based on the measured angles catch experiment with fair concordance; (2) for our problem, 2D axisymmetric CFD (computer fluid dynamics) does not provide significantly better results than the numerical integration of the approached Newton's equation; (3) the numerical value of the slip length does not significantly modify the results of the numerical simulation.

6.10 Electrospays

6.10.1 Introduction

Electrospays are a way to generate sprays by applying an electrostatic pressure to a droplet coming out of a small needle or out of a nozzle. This creates a specific flow shape around the needle tip known as Taylor cone, whose main property is to generate a cylindrical fillet of liquid which degenerates into a series of droplets due to the well known Rayleigh-Taylor instability. The fact that the fillet diameter is very stable and repeatable leads to a cloud of droplets with a very narrow diameters distribution. Consequently, this physics is of the utmost interest in fuel injection or

drug delivery for example. The latter application framework was supported among the MuNA (Micro Nozzles Arrays) and NEOFOR projects for drug delivery by inhalation⁸.

6.10.2 Literature review: from monosprays to mutisprays

Mastering spray parallelization in multi needles arrays opens a lot of perspectives as various as electrosprays devices for nanoparticles and molecules characterization [166], pulmonary drug delivery [64, 47], transdermal patches, fuel injection...

However, due to the interest of our industrial partner we focused on multiplexed electrosprays (i.e. electrosprays generated through an array of ejectors). We present the literature review on this subject along three axis: (1) overview of published methods of electrosprays; (2) single spray optimization; (3) multi electrosprays.

For example, [62] experimentally shows an increasing droplets diameters and spray focusing with increasing flow rate. He details the working conditions leading to jet instability with bimodal droplets distribution. Another study rests on dimensional and similitude laws. For example, [43] shows the influence of electrical conductivity of polar liquids: the diameter d_j of the fillet coming out of the Taylor cone is given as a function of the flow rate Q and of the characteristic electrical time τ , the latter being defined as the ratio of permittivity ϵ_0 over conductivity k :

$$d_j^3 \div Q\tau \quad (6.18)$$

Additionally, the Rayleigh instability relates the instable jet diameter d_j to the droplets diameter d :

$$d = 1.9d_j \quad (6.19)$$

(This instability is also named after a famous Belgian scientist Joseph Plateau [153]. The sketch of figure is taken from his manuscript).

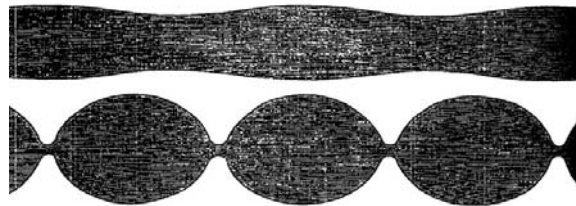


Figure 6.49: Onduloid by Plateau [153]

Other authors used numerical simulation [197, 198, 114] but they results are note easy to exploit. Lastow [114] shows a square dependence between the flow rate and the diameter:

$$d = 1.9d_j \div \sqrt{Q} \quad (6.20)$$

⁸Région wallonne funding, projects NEOFOR (call Biowin) and MuNA (call First Postdoc

Lastow experimentally confirmed the results of Tang [177] according to which diameters of the order of $1.6 \mu\text{m}$ (industrial target) correspond to flow rate of about $2 - 4 \mu\text{Lmin}^{-1}$ (much far away from the industrial target). As this step, we concluded the electro spray technique to be out of scope for our purpose. Nevertheless, design optimization could improve the flow rate, as indicated by the studies of [159] (flow rate up to $8.6 \mu\text{Lmin}^{-1}$) or [38] which reaches flow rate up to $1 \mu\text{Ls}^{-1}$ using Corona effect to discharge the spray.

A second promising track was the multiplication of sprays nozzles, as followed by [84] (figure 6.50).

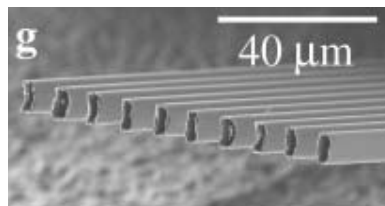


Figure 6.50: Multi nozzles electro spray

[88, 164] seem to gain one order of magnitude on flow rate, but this is parallelization has been discarded by [50], because of a claimed larger dispersion of diameter. The latter author took benefit from spray in multi-jet mode, as demonstrated by [159] for sprays velocities U larger than L/τ where L is a typical length of the system and τ is the electrical time already defined here above. Ragucci proposed a map to drive the electro spray in different modes (see figure 6.51)

6.10.3 Current results

This project is still going on at Université libre de Bruxelles (Marion Sausse-Lhernould and Nicolas Julémont), and recently promising results were obtained by Marion Sausse-Lhernould, as illustrated in figure 6.52

This multiple electro spray has been obtained with a mix water-ethanol (40%-60%). The nozzles have a $150 \mu\text{m}$ diameter, encircled by a groove of $100 \mu\text{m}$ depth. There is 2 mm between two nozzles. These nozzles have been manufactured by excimer laser in a polycarbonate substrate ($750 \mu\text{m}$ thick). The counter electrode (which cannot be seen in the picture) is placed at a distance a bit smaller than 1 mm , and the applied voltage reaches up to 5 kV .

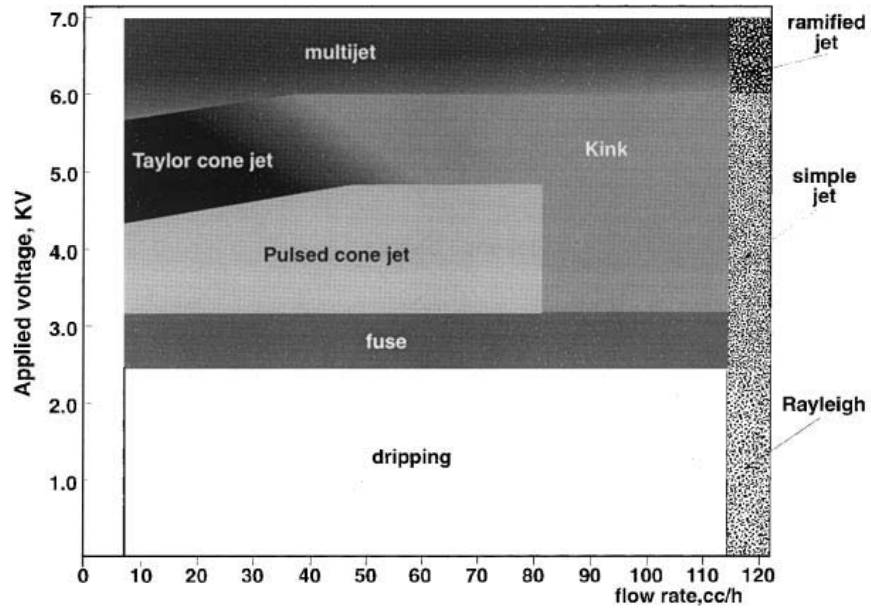


Figure 6.51: Ragucci

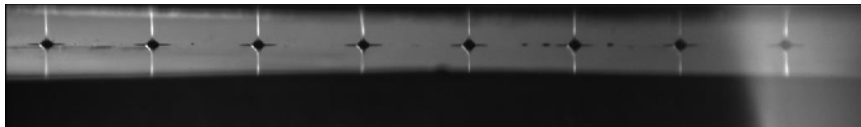


Figure 6.52: Example of multiple electrospay

6.11 Additional contribution: Stick and slip actuator

Inspired from Breguet's work [18], we developed in early research work a stick-slip piezo-actuator [89].

The aim of the research was to propose a simple and cheap system, able to produce a macroscopic (centimetric) travel with a very high (nanometric) resolution. The solution principle described yields a theoretically infinite travel based on the accumulation of successive steps. The travel of the constructed prototype is equal to two centimeters, the size of the steps being about twenty nanometers. The actuation is based on the stick-slip effect: during the first stage of a step, the legs of the actuator slowly translate the carried structure; in the second stage the legs are moved back in their initial position very quickly, so that thanks to their inertia, the structure stays at the same place. Each leg of the system, glued on a main frame, consists in a piezoelectric device working in shear mode, ended by a ruby hemisphere. The structure itself is in steel, to get a sufficiently high inertia. An originality of the proposed translator is that the guiding elements of the structure (guiding grooves) are also used to transmit the motion. The friction force between the legs and the grooves can be tuned thanks to a magnet placed in the main frame allowing to adjust the normal load on the legs. The paper presents the different functional elements of the translator and its electronic command system. It also explains its functioning. The influence of several parameters (supported load, friction, resistive axial load) on the step size and thus on both the resolution and the speed of the system is then studied.

First we validated our design by measuring a few steps of the translator with interferometry (figure 6.53a): during a period of 0.5ms, the slider steps 34 nm forwards, before undergoing a 9 nm backward loss. The difference between this 25 nm measured step and the 46 nm theoretical step can partially be explained by the elastic loss of the leg under the tangential traction of the kinetic friction force. In [18], a contact deformation of 18 nm for a 2 mm diameter sapphire sphere is estimated. Our calculation leads to an elastic deformation of about 16 nm using Hertz theory and Amonton's law [78]. Taking this deformation into account, we get a measured step of 25 nm for a predicted value of 29 nm.

Then, we experimentally found an optimum for the frequency, leading to a maximal displacement velocity, as indicated in figure 6.53b.

Theoretically, the higher the frequency, the smaller the step loss [18], but one should keep in mind the assumptions made: the model is not valid if the mechanical response time can no longer be neglected against the working period T . The model proposed in [199] should be replaced by a flexible modeling of the system. However, the experiment illustrated in figure 6.53b allows us to find the optimal frequency (4 kHz) in order to get quick displacements (almost $110 \mu\text{ms}^{-1}$).

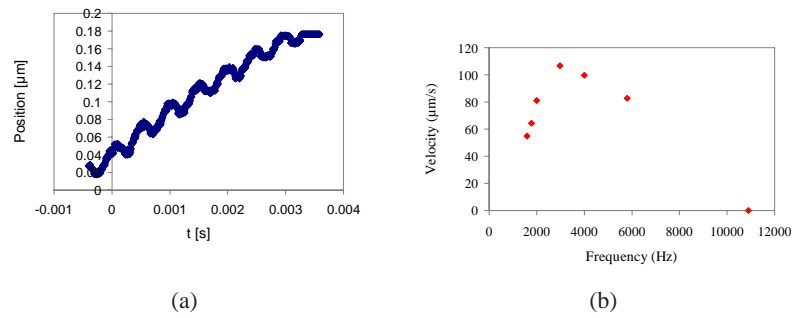


Figure 6.53: (a) Step detail at 2kHz; (b) Mean velocity as a function of the frequency.

6.12 General conclusions

In this chapter, we tried to show our efforts and ability to develop case studies bridging the gap between fundamental models and applicative frameworks. Some developments have led to patent application (surface tension based microrobotic platform) while other ones are led in close collaboration with industry (electrosprays). The interaction between many research works and PhD students under my supervision was very successful to this aim.

Chapter 7

Perspectives

7.1 Microfluidic assembly

During the two years I'm going to spend in the LIMMS¹, I would like to study how to achieve manipulation of micrometric components using droplets as carriers. The motivation for such a study is briefly reported in section 7.1.1. The research objectives are detailed in section 7.1.2: how to encapsulate micrometric components into droplets (section 7.1.3), how to displace these components using droplets as carriers (section 7.1.4) and how to merge two droplets in order to bring two different components close to one another (section 7.1.5). Finally, we briefly present the related state of the art on these aspects (section 7.1.6). These aspects were proposed in a project we applied for in the French research call ANR last January. Funding decision is still pending.

7.1.1 Context and motivation

The research in the field of assembly tends towards both 3D assembly and miniaturization. An historical vision of 3D-assembly has been recently proposed by [10]. This vision encompasses the evolution of assembly progressing from " 0D " assembly (i.e. manual labor) to " 1D assembly " (first conveyor belts), " 2D assembly " (e.g. electronic packaging) or even emerging " 3D assembly ", which is currently mainly beyond range.

The second trend is the miniaturization of the handled component: literature currently refers the handling of individual nanocomponents [196] or biological components [11]. Before the 3D assembly paradigm can be reached thanks to full self-organization principles (" self-assembly "), a robotic approach is often thought to provide the required tools to handle small individual components, assemble them and provide them with intelligent functions such as sensing or actuation.

In this project, this handling is thought to be achieved in liquid environment

¹LIMMS = Laboratory for Integrated Micro-Mechatronic Systems LIMMS/CNRS/IIS UMI 2820, which will welcome me from September 2010 to September 2012

thanks to the tools of microfluidics. The justification for using such microfluidic tools relies on the fact that many efforts have already been done in robotic handling with various gripping techniques, without overcoming a quite tedious serial *modus operandi*. Alternative tracks are for example the hybrid assembly paradigm pursued in the European research project Hydromel - i.e. combine rough robotic positioning with fine but short range self-alignment. Promising self-assembly techniques rely on surface tension effects provided by liquid environments. Additionally, this kind of environment is compatible with biological components and with many manufacturing processes. This project proposes an original approach based on using droplets and microfluidics to perform the feeding operations on a parallel way (Figure 7.2).

Targeting the production and assembly of micrometric components with microfluidics tools would be an actual breakthrough. To our knowledge, there is only few work at the crossing point of the mentioned thematic.

7.1.2 Research objective and methodology

The scientific questions raised in this project can be summarized in figure 7.1 and serve as a basis for the working program. They consist in studying the following aspects, all necessary steps toward a demonstrator of microfluidic assembly:

1. How to immerse a component into a conveying droplet?
2. How to displace the conveying droplets?
3. How to to move the component with a conveying droplet?
4. How to merge two droplets without absorbing liquid from environment?

The methodology will be based on the design, manufacturing and experimental characterization of adequate devices to achieve the functions described here above. Three tasks are to be done: (1) droplets feeding and encapsulation, (2) components displacement and (3) droplets merging.

7.1.3 Droplets feeding and component encapsulation

This task aims at generating separated droplets to be used as conveyors of components, targeting one single component in each droplet (this task is called feeding in assembly). Beyond the state of the art, the targeted LDEP device aims at avoiding parent droplet generation using a micropipette for which droplet extraction from a microfluidic channel is neither used nor (consequently) studied. Our goal here is to automate the extraction of a droplets array, each droplet containing a single component. Therefore, the LDEP device will be composed of a closed and an open environment (figure 7.2). The first one is responsible for the isolation of a single element as well as its positioning before extraction (in a droplet). The second one ensures droplets generation and merging. Indeed, open environment (containing

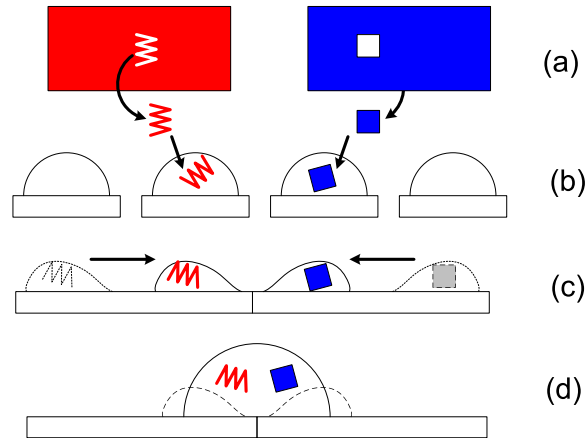


Figure 7.1: a) components manufacturing, (b) components insertion, (c) components displacement, (d) droplets merging

the assembled system in droplets) is accessible to external probing, magnetic or any other actuation/alignment principle to be applied on the components.

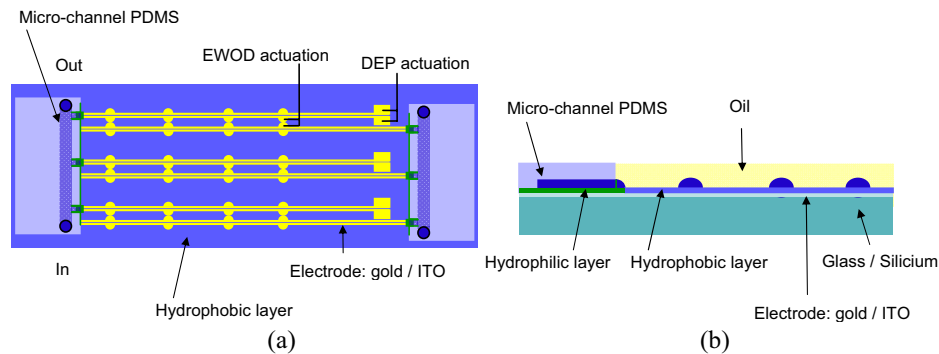


Figure 7.2: (a) Top view of the microfluidic device: the liquid extraction is done using DEP actuation. The droplet fusion can be obtained using EWOD process; (b) Side view of the microfluidic device. The choice for respectively glass / Silicon for the substrate and gold / ITO for the electrodes depends on the needs for transparency microfluidic device

7.1.4 Components displacement

It is necessary to move two droplets to one another in order to merge them and put their two components in contact. LDEP displacement is already partially ensured by the extraction mechanism, since droplets are generated from the hydrodynamic instability of a rivulet placed on an electrode line: this mechanism is here called LDEP displacement. Nevertheless, additional displacement may be required, such

as for example to lead resulting droplet containing two types components to alignment sites which may be required. Consequently, alternative displacements can be considered:

1. Passive displacement: since droplets just have to be moved from their generation (LDEP) point to their merging point, the motion may be irreversible. Therefore, passive actuation is a reasonable option. The conditions of surface texturation have already been defined by [57], but this author focused on the criterion for suspension or collapse of droplets posed on a textured substrate. This criterion is based on the perimeter/area ratio of the protuberances (dashed squares in Figure 3). In our case, the goal is not to know whether the carrying droplet can collapse or not, but to pattern a wettability gradient along the track linking the generation point to the merging point. Details of this patterning are usually within the micron. [170] demonstrated the feasibility of this concept for millimetric droplets, but it will be necessary to investigate the design modification for picoliter droplets in (probably) liquid environment (to avoid evaporation).

The goal of this task is not specifically to study the displacement of droplets - which is already known -, but well to determine the conditions under which a micron sized component can be moved by a conveying droplet. Especially, the incidence of the texturation on the displacement of the components will be studied. If necessary, a chemical functionalization can be considered.

2. Active displacement: in case an active actuation is required, LDEP or EWOD will be implemented, according to the expertise of LIMMS in that domain. LDEP is the research track (10 μm and below) while EWOD is more to be considered as the back up solution, for larger droplets (100 μm).

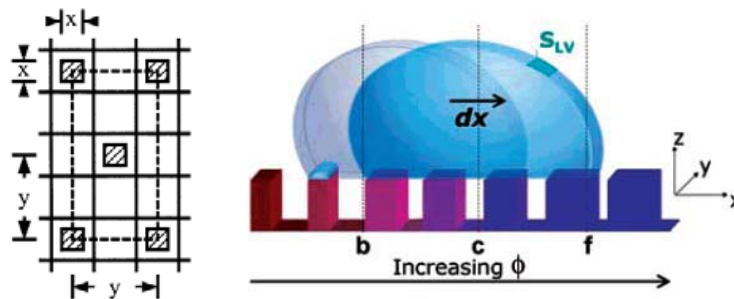


Figure 7.3: Example of surface texturation by [57] (on the left) and surface gradient based mobility by [170] (on the right)

7.1.5 Droplet merging

According to LIMMS expertise [138] LDEP can also be used to merge two droplets. As indicated in figure 7.4, two LDEP lines can be placed parallel and covered by

silicone oil to prevent evaporation. Applying an AC voltage (300 Vrms at 100 kHz), two rivulets can be formed (2), which are split into droplets to the dominance of surface tension once the voltage supply is removed (3). Finally, by applying frequency AC voltage (300 Vrms at 100 Hz) between facing electrodes, the droplets are attracted by the electrostatic forces and merged (4). Spontaneous coalescence can also be used to merge two droplets moving to one another under the effect of surface gradients described previously.

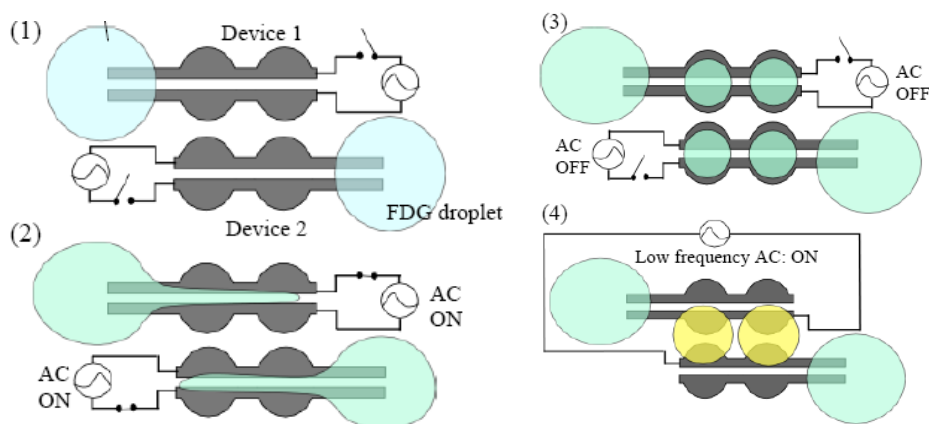


Figure 7.4: : illustration of LIMMS expertise [138] ; (1) two LDEP lines placed parallel and covered by silicone oil to prevent evaporation, (2) rivulets formation by applying an AC voltage (300 Vrms at 100 kHz), (3) droplets generation due to the dominance of surface tension once the voltage supply is removed, (4) applying frequency AC voltage (300 Vrms at 100 Hz) between facing electrodes, the droplets are attracted by the electrostatic forces and merged

7.1.6 Related literature review

Concerning fluidic handling, we don't consider here well-established channel microfluidics and only consider so-called open microfluidics, which consists in handling droplets and bubbles in order to displace, separate or merge them on a patterned substrate.

Droplets motion can be achieved using gravity [63] (not really relevant at micron size), wettability or texturation gradients [170], electrowetting-on-dielectrics (EWOD) and its variant using optical actuation [36]. According to [79], Liquid Di-ElectroPhoresis (LDEP) can apply a force on dielectric liquid, first by collecting in regions where the imposed field magnitude is maximized and then by configuring itself with its free surfaces primarily tangential to the electric field. EWOD² has been the object of an extensive review by [140]. Additionally, LDEP forces are

²EWOD = Electrowetting on dielectric: a thin layer of dielectric is coated on the conductive substrate in order to avoid water electrolysis

larger than EWOD and are consequently preferred. Based on the expertise of the LIMMS laboratory, [138, 193], we propose to apply LDEP and/or EWOD to use droplets as components carriers.

Droplet extraction is in a sense well mastered in ink jet printing. An alternative targeting the micron size and below consists in electro spraying the liquid [39, 48, 44]. The principle is here to pull a liquid out of a small channel or needle, using the electrostatic pressure to overcome surface tension effects. In the so-called cone jet mode, the liquid flows into a thin cylinder, which is subject to Rayleigh instabilities, leading to the formation of droplets. In 2D, this instability principle is achieved by LDEP. Applying an AC voltage on a large parent droplet, [79] demonstrated the extraction of a so-called rivulet which tends to break up according to Rayleigh instability (Figure 3). Patterning bumps periodically along the electrode strip helps getting regular droplets separated by the Rayleigh wavelength (Figure 3). Remaining challenges are ; (1) decrease Joule heating, (2) scaling down the electrodes for sub-nanoliter droplets generation, (3) encapsulate bead inside a droplet using LDEP actuation [31].

Liquid encapsulation using electro sprays is reported by [131]. Additionally, enclosing multiple components into a single capsule without contact is cited by [30, 31]. Nevertheless, the proper encapsulation of one single component into one single droplet is still challenging. The partner LIMMS recently demonstrated the isolation of DNA thanks to LDEP [193].

Moving components inside droplets is also a current track of research, including the concept of railed microfluidics [37], a levitation principle by [187] or a fluidic conveying system [139]. None of these techniques is really satisfactory in our problem. The railed microfluidics consists in accumulating a series of identical components in a channel, using the liquid pressure to push to one another. The levitation principle consists in displacing water droplets containing multiple components, as indicated in Figure 3.

Droplet fusion is also manifold. [59] recently reported on a method for droplet fusion based on a surface energy pattern on the walls of a microfluidic device. [136] reported on mastering droplet coalescence. Fusion techniques generally include the application of localized electric fields, modification of surface properties [59] and the control of microdroplet velocities by variation of the microchannel geometries [19] [73]. If the microdroplet is generated using LDEP device in open environment, droplets merging may also be done with EWOD actuation. That is to say, several droplets are put into contact and the mechanical force overcomes the tensile surface and allows the fusion [34, 138, 56].

All these techniques are expected to overcome robotic tweezers (which operate on a serial way while the matricial device of Figure 8 is expected to work parallel). Separating objects to assemble in confined environments - i.e. the droplets - will increase the efficiency of chemical recognition which are strong at contact but present limited attraction ranges.

7.2 Laser excimer manufacturing

Recently we could use an excimer laser machine³ to manufacture micrometric details in polycarbonate plates. The performances of this machine are briefly mentioned in section 7.2.1. Then, two ongoing case studies are presented: patterning capillary stops (section 7.2.2) for electrospays and microgravity experiments on the one hand and patterning electrodes on piezo-ceramics on the other hand (section 7.2.3).

7.2.1 Machine performances

The machine basically consists in a excimer laser source, the adequate optics and a 4 degrees-of-freedom positioning table allowing to program complex designs (see figure 7.5).

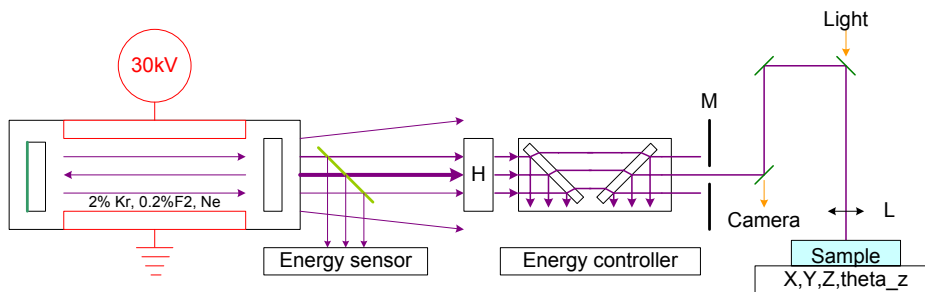


Figure 7.5: The excimer gas is excited by an electric field: the resulting laser beam is homogenized by (H), leading to a homogeneously intense beam. A fraction of this energy can be removed by the energy controller, before the beam passes through a mask (M). The length of the optical path between the mask and the sample can be tuned in order to adjust both the focus and the demagnification of the image formed by the mask. The focus is done manually thanks to visible light.

The laser is pulsed with a lightening period of about 20 ns, leading to cold ablation of the material: it was shown in [141] that the kinetic energy of the ablated particle is roughly equal to the incident optical energy. Therefore, thermal effects are reduced a lot. The working frequency is however much smaller, of the order of 100 Hz (also called repetition rate). Considering the wave length of such lasers (KrF: 248 nm, ArF: 193 nm), polymers manufacturing is very efficient and a single flash can remove a layer of 300 nm, i.e the ablating speed is of the order of $0.3 \mu\text{m} \times 100 \text{ Hz} = 30 \mu\text{ms}^{-1}$. Aspect ratio is about 10:1.

A classical x, y, θ_z table allows to manufacture any 2D pattern. The z -axis is devoted to the focus or to manufacturing non horizontal surfaces. The total precision of the system – including optics resolution – is of the order of a few μm .

³Centre Technifutur, Liège, Belgium (Contact: Frédéric Cambier)

7.2.2 Capillary stops

The principle of capillary stops is to prevent wetting of low energy liquid on relatively high energy substrate, thanks to geometrical discontinuities which increase the apparent contact angle (see figure 7.6).

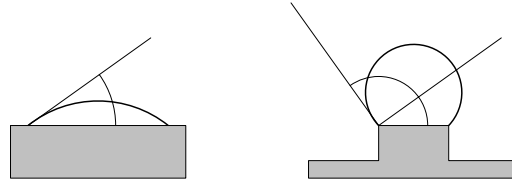


Figure 7.6: Principles

This principle has been applied to avoid mixing of droplets coming out from nozzles close to each other. As shown in figure 7.7, a nozzle of $\text{Ø}100\ \mu\text{m}$ is encircled by a groove of $160\ \mu\text{m}$ width and a mean radius equal to $180\ \mu\text{m}$. The left hand figure indicates the desired design, and the circle called SP8 indicates the path of the laser, along which a number of pulses is defined in order to get the desired ablation depth (here of the order of $50\ \mu\text{m}$). The cross in the middle of this circle indicates a different number of pulses, allowing to drill the $750\ \mu\text{m}$ substrate completely. A sketch of the actual result is shown on the right, indicating the deviation introduced by the conicity of such a laser drilling. In the middle, we can see a picture of the result.

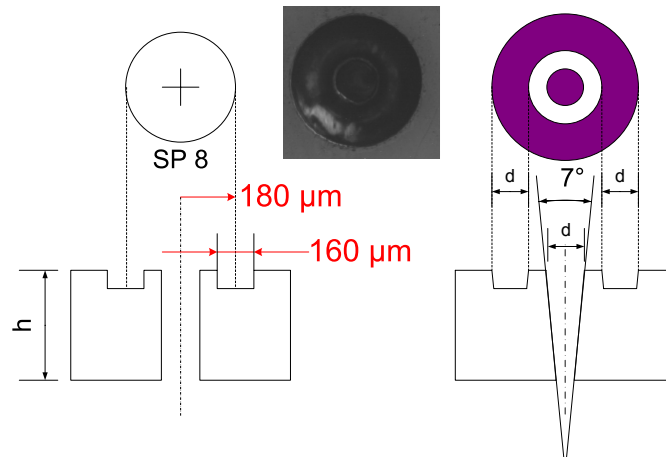


Figure 7.7: Example of capillary stop

Recently, we have tried to miniaturize the platform presented in section 6.7 using the excimer to pattern a groove (figure 7.8, top face) encircling a via linked to a supply channel (bottom face).

The pictures taken from both sides of this sample are shown in figure 7.9.

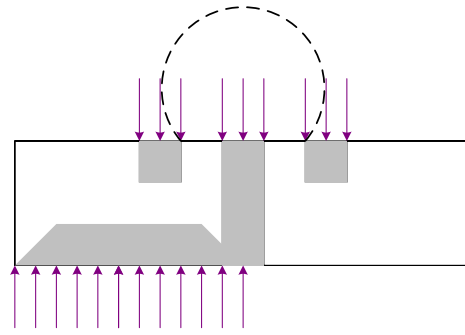


Figure 7.8: Two-side microfluidic circuit, made of a supply channel conducting the liquid from the bottom face to the top face through a via. The emerging droplet is confined with the circular groove.

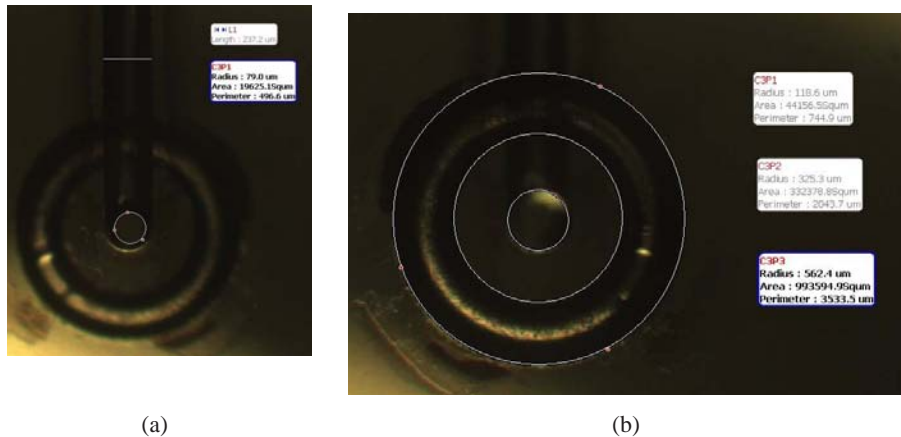


Figure 7.9: (a) bottom view showing the open channel (width: 237 μm) and the via ($\text{Ø}178 \mu\text{m}$); (b) top view showing the via ($\text{Ø}236 \mu\text{m}$) and the inner and outer circular edges of the groove (respectively $\text{Ø}650 \mu\text{m}$ and $\text{Ø}1125 \mu\text{m}$) – we deduce a conicity equal to $\tan^{-1}((236/178)/750) = 4.4^\circ$

A second application of capillary stops is related to microgravity experiments, where fluid is not confined by gravity anymore. Since the targeted experiment⁴ used to require an opening for vision, the liquid tank could not be sealed completely. The idea was to prevent liquid from wetting with such capillary stops, whose efficiency is graphically shown in figure 7.10.

⁴Sam Dehaeck and Pierre Colinet, Université libre de Bruxelles

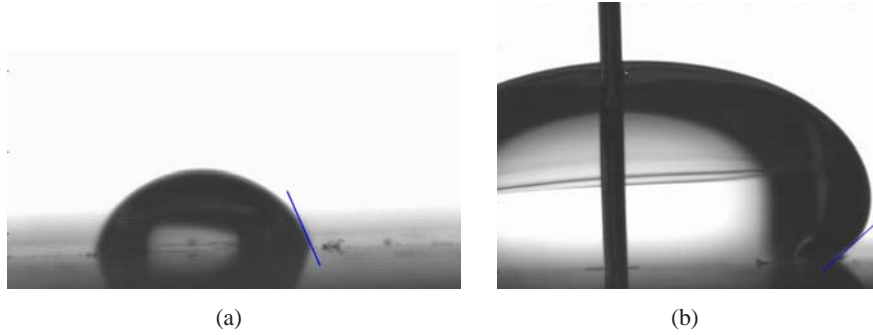


Figure 7.10: Contact angles made by water on a stainless steel substrate: (a) without capillary stop ($\theta = 66^\circ$); (b) with a capillary stop ($\theta = 138^\circ$)

7.2.3 Ceramic micro-electrodes patterning

The excimer laser is normally best suited for polymer ablation [141]. We tried however to pattern PMN-PT ceramic to be used as piezo-actuators. Therefore, it is necessary: (1) to cut a piece of ceramic from a 200 μm thickness sheet and (2) to pattern the electrodes by ablating a 5 μm gold coating. Current results are illustrated in figure 7.11.

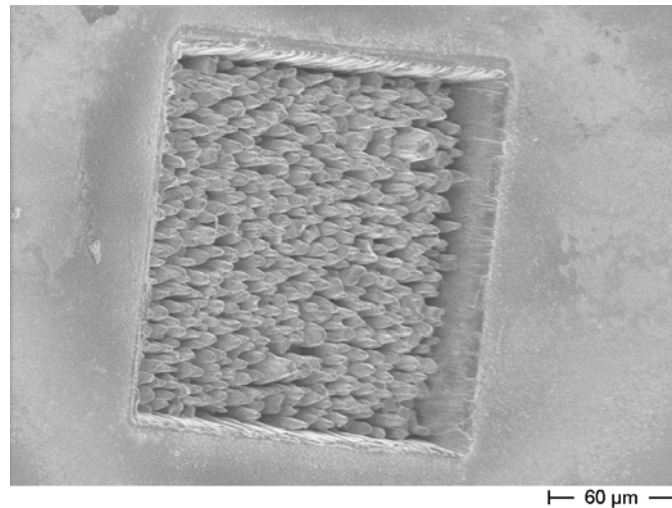


Figure 7.11: Example of PMN-PT ablation (optical axis is tilted by 30° wrt the normal). Parameters: Laser energy 300 mJ, repetition rate 120 Hz, number of pulses 1000, demagnification 14, attenuator 94%, square mask 2.5 mm \times 2.5 mm

From figure 7.11, we can find the ablation rate to be about 50 μm for 1000 pulses, i.e. about 50nm pulse^{-1} .

In figure 7.12a, we measure the edge of the ablated pattern to be about 180 μm (theoretically, the edge is equal to $2500 \mu\text{m}/14 = 178 \mu\text{m}$). In figure 7.12b, we

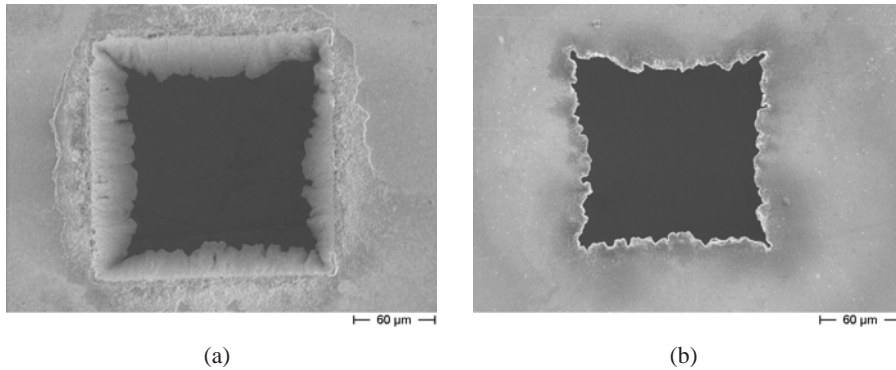


Figure 7.12: Example of PMN-PT ablation (optical axis is tilted by 30° wrt the normal). (a) top view; (b) bottom view. Parameters: Laser energy 300 mJ, repetition rate 60 Hz, number of pulses 17000, demagnification 14, attenuator 94%, square mask $2.5 \text{ mm} \times 2.5 \text{ mm}$

see a significant deviation from the ideal square shape: the edge measured between two adjacent summits is about $148 \mu\text{m}$ while the distance measured between the mid points of two opposite edge is about $128 \mu\text{m}$. Therefore the lateral faces of the ablated pattern are not perpendicular to the top and bottom faces of the sample, but rather inclined with an angle equal to $\tan^{-1}((180 - 138)/(2 \times 100)) = 6^\circ$

Obviously the result is not satisfactory from a geometrical point of view. Nevertheless, we are studying whether this geometry deviation has a significant impact on the function of the final actuator. Related tests are still ongoing, in collaboration with Joël Agnus and Alex Ivan from FEMTO-ST.

7.3 Other perspectives

7.3.1 Applications of spray technologies

The electro-spray technology is very promising as far as a large number of applications is concerned: drug delivery, nanopatterning, microcomponent encapsulation for micro-assembly, glue deposition...

Mastering spray parallelization in multineedles arrays⁵ opens a lot of perspectives as various as electro-sprays devices for nanoparticles and molecules characterization [166], pulmonary drug delivery [64, 47], transdermal patches, fuel injection...

It will also be looked at the possible combination with fluidic technologies which will be studied in my work in the LIMMS.

⁵Work of my postdoc Marion Sausse-Lhernould in Université libre de Bruxelles

7.3.2 Liquid encapsulation

Recently, a promising encapsulation technique based on Gorham process was proposed by Charmet [54, 55] to deposit a 2 μm parylene layer on various liquids: glycerols, silicone oils, adipates and phtalates, water. This so-called SOLID process (SOLid on LIquid Deposition) allows drug and microlenses encapsulation. The parylene film is transparent, biocompatible, atomically flat, and shows good chemical and mechanical properties.

Such a technique is of interest to encapsulate liquid bridges and droplets, avoiding evaporation.

Chapter 8

Conclusions

The switch from assembly toward microassembly was not just a matter of size, but used to require a much deeper insight on physics governing the considered scales. Therefore, it was necessary to get into knowledges which are usually not familiar to mechanical engineers, such as adhesion science. This step is always difficult because we are brought face to face with specialists of other domains. This raises the question to know whether the developed work is not too light compared with the existing knowledge.

The goal was obviously not to compete with these specialist in their own field, but rather develop models which are useful to the micromechanical and micro-robotician communities. In that sense, we hope that we contributed to feed these communities with capillary forces models which can now be applied in various domains: assembly and packaging, microrobotics, soil mechanics, microfluidics... These results rely on theoretical modeling and experimental validation, which is essential in our approach. Sometimes, it was even possible to produce decisive results concerning specialist questions, such as the equivalence between capillary forces modeling presented in section 4.3.2. Fundamental work was also done on capillary forces at the nanoscale (i.e. capillary condensation) and capillary forces dynamics.

Besides, resting on the micro-assembly framework, we developed our research activities on using, reducing, avoiding or overcoming surface tension effects.

Beside handling and micromanipulation, I think now that micro-assembly will require more operational knowledge and technological solutions (microjoining for example).

My natural tropism will probably lead me toward additional modeling, but I'd like to develop more technological based research, in order to be closer to applications. The field of microtechnologies, microproducts and microrobotics is indeed fascinating because of its multidisciplinary background¹. After several years spent at interfaces, I'm quite impatient to get *into* liquid droplets and open microfluidics in Tokyo.

¹From this perspective non specialized engineering education may probably be a very good trump

Appendix A

Analytical approximations of the capillary forces with the energetic method

This appendix aims at detailing the mathematical developments required to calculate the analytical approximations of the capillary forces, based on energetic approach (section 4.2.1).

A.1 Preliminary

1. Definitions

$$\begin{aligned} A(\phi) &\equiv \frac{2\pi}{3} \left(1 - \frac{3}{2} \cos \phi + \frac{1}{2} \cos^3 \phi \right) \\ \frac{dA}{d\phi} &= \pi \sin^3 \phi \end{aligned}$$

2. Properties

$$\begin{aligned}
\cos \phi &= 1 - \frac{\phi^2}{2} + \frac{\phi^4}{24} + O(\phi^6) \\
\cos^2 \phi &= 1 - \phi^2 + \frac{\phi^4}{3} + O(\phi^6) \\
\cos^3 \phi &= 1 - \frac{3}{2}\phi^2 + \frac{7}{8}\phi^4 + O(\phi^6) \\
\sin \phi &= \phi - \frac{\phi^3}{6} + O(\phi^5) \\
\sin^2 \phi &= \phi^2 - \frac{\phi^4}{3} + O(\phi^6) \\
\sin^3 \phi &= \phi^3 + O(\phi^5) \\
A(\phi) &= \frac{\pi}{4}\phi^4 + O(\phi^6) \\
\frac{dA}{d\phi} &= \pi\phi^3 + O(\phi^5) \\
1 - \cos \phi &\approx \frac{\sin \phi^2}{2} \approx \frac{\phi^2}{2}
\end{aligned}$$

A.2 Between a sphere and a plane (Israelachvili approximation)

The force between a sphere and a plane is developed in [74]. The used notations are defined in figure A.1.

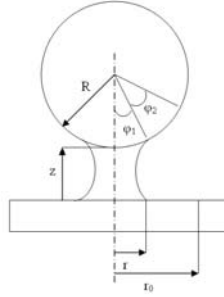


Figure A.1: Studied configuration

In this figure, ϕ_0 and r_0 are arbitrary constants. Their exact value does not play any role because the force will be calculated by derivating the interfacial energy W with respect to the gap z between the sphere and the plane [74]:

$$F = -\frac{dW}{dz} \quad (\text{A.1})$$

Let us write the interfacial energy of the system:

$$\begin{aligned} W(z) &= A_{SL}\gamma_{SL} + A_{SV}\gamma_{SV} + \Sigma\gamma \\ &= \gamma_{SL}\pi r^2 + \gamma_{SV}\pi(r_0^2 - r^2) + \gamma 2\pi r(z + R(1 - \cos\phi)) \\ &\quad + \gamma_{SL}2\pi R^2(1 - \cos\phi) + \gamma_{SV}2\pi R^2((1 - \cos\phi_0) - (1 - \cos\phi)) \end{aligned} \quad (\text{A.2})$$

Since ϕ is assumed to be small, W can be rewritten as:

$$\begin{aligned} W(z) &= \pi r^2(\gamma_{SL} - \gamma_{SV}) + \gamma 2\pi r z + \gamma \pi r R \sin^2\phi + \gamma_{SV}\pi r_0^2 \\ &\quad + \pi R^2 \sin^2\phi(\gamma_{SL} - \gamma_{SV}) + \gamma_{SV}\pi R^2 \sin^2\phi_0 \end{aligned}$$

and, by considering the Young-Dupré equation ($\gamma \cos\theta = -\gamma_L + \gamma_{SV}$):

$$W = -2\pi R^2 \sin^2\phi \gamma \cos\theta + \gamma_{SV}\pi r_0^2 + \gamma 2\pi r z + \gamma \pi R^2 \sin^3\phi + \gamma_{SV}\pi R^2 \sin^2\phi_0 \quad (\text{A.3})$$

Let us now consider the derivative of W :

$$\frac{dW}{dz} = -4\pi R^2 \sin\phi \cos\phi \gamma \cos\theta \frac{d\phi}{dz} + \gamma 2\pi R \sin\phi + \gamma 2\pi z R \cos\phi \frac{d\phi}{dz} + 3\gamma \pi R^2 \sin^2\phi \cos\phi \frac{d\phi}{dz} \quad (\text{A.4})$$

or, by assuming $\sin\phi \approx \phi$ and $\cos\phi \approx 1$:

$$\frac{dW}{dz} = -4\pi R^2 \phi \gamma \cos\theta \frac{d\phi}{dz} + \gamma 2\pi R \phi + \gamma 2\pi R z \frac{d\phi}{dz} + 3\gamma \pi R^2 \phi^2 \frac{d\phi}{dz} \quad (\text{A.5})$$

The value of $\frac{d\phi}{dz}$ must be evaluated in equation A.5. Therefore, the meniscus volume is assumed to be constant, leading to $\frac{dV}{dz} = 0$. Moreover the meniscus will be assumed to be cylindrically shaped so that the volume is the difference between the external liquid cylindre and the volume of the spherical cap inside the external cylindre:

$$V = \pi r^2(z + R(1 - \cos\phi)) - \frac{2\pi R^3}{3} \left(1 - \frac{3}{2}\cos\phi + \frac{\cos^3\phi}{2}\right) \quad (\text{A.6})$$

Once again the assumption of small ϕ is made, leading to the following approximation:

$$\frac{2\pi R^3}{3} \left(1 - \frac{3}{2}\cos\phi + \frac{\cos^3\phi}{2}\right) = A(\phi)R^3 \approx \frac{\pi R^3}{4}\phi^4 \quad (\text{A.7})$$

The final expression for V is now given by:

$$V = \pi r^2 z + \frac{\pi r^2 R}{2} \sin^2\phi - \frac{\pi R^3}{4} \phi^4 \quad (\text{A.8})$$

$$= \pi R^2 \sin^2\phi z + \frac{\pi R^3}{2} \sin^4\phi - \frac{\pi R^3}{4} \phi^4 \quad (\text{A.9})$$

so that:

$$\begin{aligned}
\frac{dV}{dz} &= 2\pi R^2 z \sin \phi \cos \phi \frac{d\phi}{dz} + \pi R^2 \sin \phi + 2\pi R^3 \sin^3 \phi \cos \phi \frac{d\phi}{dz} - \pi R^3 \phi^3 \frac{d\phi}{dz} \\
&= 2\pi R^2 z \phi \frac{d\phi}{dz} + \pi R^2 \phi^2 + \pi R^3 \phi^3 \frac{d\phi}{dz} \\
&= 0 \\
\Rightarrow \frac{d\phi}{dz} &= \frac{-\pi R^2 \phi^2}{2\pi R^2 \phi z + \pi R^3 \phi^3} \\
&= \frac{-1}{\frac{2z}{\phi} + R\phi}
\end{aligned} \tag{A.10}$$

The total capillary force is then given by substituting this latter result into equation A.5:

$$F = -\frac{4\pi R^2 \phi \gamma \cos \theta}{\frac{2z}{\phi} + R\phi} - \gamma 2\pi R\phi + \frac{\gamma 2\pi R z}{\frac{2z}{\phi} + R\phi} + \frac{3\gamma \pi R^2 \phi^2}{\frac{2z}{\phi} + R\phi} \tag{A.11}$$

Since $h = R(1 - \cos \phi) \approx \frac{R}{2} \sin^2 \phi \approx \frac{R}{2} \phi^2$:

$$\begin{aligned}
F &= -\frac{4\pi R \gamma \cos \theta}{\frac{2z}{R\phi^2} + 1} - \gamma 2\pi R\phi + \frac{\gamma 2\pi R z}{\frac{2z}{\phi} + R\phi} + \frac{3\gamma \pi R \phi}{\frac{2z}{R\phi^2} + 1} \\
&= -\frac{4\pi R \gamma \cos \theta}{\frac{z}{h} + 1} - \gamma 2\pi R\phi + \frac{\gamma 2\pi R z}{\frac{2z}{\phi} + R\phi} + \frac{3\gamma \pi R \phi}{\frac{z}{h} + 1}
\end{aligned}$$

The last three terms of equation A.12 represent the contribution of the ‘LV’ interface to the total interfacial energy. Let us assess their relative importance with respect to the first term. Their sum is given by:

$$\frac{\pi R \gamma \phi (R\phi^2 - 2z)}{R\phi^2 + 2z} \tag{A.12}$$

The ratio of the the first term to the sum of the last three ones is equal to:

$$\frac{\frac{4\pi R \gamma \cos \theta}{\frac{z}{h} + 1}}{\frac{\pi R \gamma \phi (R\phi^2 - 2z)}{R\phi^2 + 2z}} = \frac{4 \cos \theta h}{\phi (h - z)} \tag{A.13}$$

If $z = 0$, this ratio tends towards infinity if ϕ tends to zero. Since ϕ cannot be exactly equal to zero, the last three terms can be neglected with the (now) classical assumption $\phi \ll$. This leads to the well-known approximation [74]:

$$F_{max} = -4\pi R \gamma \cos \theta \tag{A.14}$$

If $z \neq 0$ but by neglecting the contribution of lateral area to W , the total capillary force can be rewritten as follows:

$$F = -\frac{4\pi R \gamma \cos \theta}{\frac{z}{h} + 1} \tag{A.15}$$

A.3 Between two spheres

Let us assume two spheres S_1 and S_2 characterized by their radius R_1 and R_2 such as depicted in figure A.2.

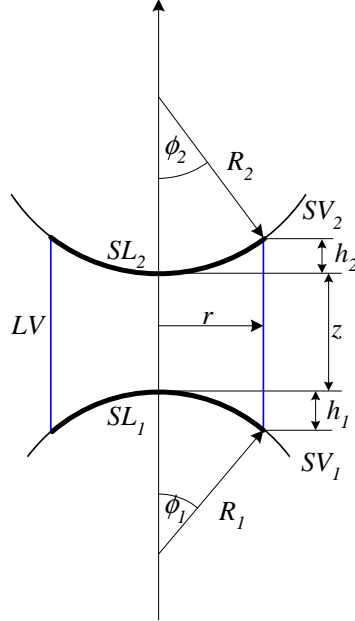


Figure A.2: Notations

A.3.1 Preliminaries

$$\begin{aligned}
 r &\equiv R_1 \sin \phi_1 \equiv R_2 \sin \phi_2 \\
 \frac{dr}{dz} &= R_1 \cos \phi_1 \frac{d\phi_1}{dz} = R_2 \cos \phi_2 \frac{d\phi_2}{dz} \\
 r &\approx R_1 \phi_1 \approx R_2 \phi_2 \\
 \frac{dr}{dz} &\approx R_1 \frac{d\phi_1}{dz} = R_2 \frac{d\phi_2}{dz} \\
 \phi'_i &\equiv \frac{d\phi_i}{dz} \\
 r' &\equiv \frac{dr}{dz} \approx R_1 \phi'_1 \approx R_2 \phi'_2
 \end{aligned}$$

A.3.2 Expression of the interfacial energy

The total interfacial energy W can be expressed as follows:

$$\begin{aligned}
W &= \gamma 2\pi r(z + R_1(1 - \cos \phi_1) + R_2(1 - \cos \phi_2)) + \gamma_{SL_2} 2\pi R_2^2(1 - \cos \phi_2) \\
&\quad + \gamma_{SV_2} 2\pi R_2^2(C - (1 - \cos \phi_2)) + \gamma_{SL_1} 2\pi R_1^2(1 - \cos \phi_1) + \gamma_{SV_1} 2\pi R_1^2(C' - (1 - \cos \phi_1))
\end{aligned} \tag{A.16}$$

where C and C' are arbitrary constants. With the assumptions that:

$$\begin{aligned}
C &= C' = 0 \\
\phi \rightarrow 0 &\Rightarrow \sin^2 \phi \approx 2(1 - \cos \phi) \\
r &= R_1 \sin \phi_1 = R_2 \sin \phi_2 \\
\gamma_{SV_i} &= \gamma_{SL_i} + \gamma \cos \theta_i
\end{aligned}$$

W can be rewritten into:

$$\begin{aligned}
W &= \pi r \gamma (2z + R_1 \sin^2 \phi_1 + R_2 \sin^2 \phi_2) + \pi \gamma_{SL_2} R_2^2 \sin^2 \phi_2 \\
&\quad - \gamma_{SV_2} \pi R_2^2 \sin^2 \phi_2 + \pi \gamma_{SL_1} R_1^2 \sin^2 \phi_1 - \gamma_{SV_1} \pi R_1^2 \sin^2 \phi_1 \\
&= 2\pi r \gamma z + \pi \gamma R_1^2 \sin^3 \phi_1 + \pi \gamma R_2^2 \sin^3 \phi_2 - \pi R_2^2 \sin^2 \phi_2 \gamma \cos \theta_2 - \pi R_1^2 \sin^2 \phi_1 \gamma \cos \theta_1 \\
\Rightarrow \frac{dW}{dz} &= 2\pi \gamma r + 2\pi \gamma z r' + 3\pi \gamma R_1^2 \sin^2 \phi_1 \cos \phi_1 \phi_1' + 3\pi \gamma R_2^2 \sin^2 \phi_2 \cos \phi_2 \phi_2' \\
&\quad - 2\pi \gamma R_2^2 \sin \phi_2 \cos \phi_2 \phi_2' \cos \theta_2 - 2\pi \gamma R_1^2 \sin \phi_1 \cos \phi_1 \phi_1' \cos \theta_1
\end{aligned}$$

As it can still be assumed that $\phi \rightarrow 0$, $\sin \phi \approx \phi$ and $\cos \phi \approx 1$, leading to:

$$\frac{dW}{dz} = 2\pi \gamma r + 2\pi \gamma z r' + 3\pi \gamma R_1^2 \phi_1^2 \phi_1' + 3\pi \gamma R_2^2 \phi_2^2 \phi_2' - 2\pi \gamma R_2^2 \phi_2 \phi_2' \cos \theta_2 - 2\pi \gamma R_1^2 \phi_1 \phi_1' \cos \theta_1 \tag{A.17}$$

It can be emphasized that $r \approx R_1 \phi_1 \approx R_2 \phi_2$ and that consequently, $\phi_2' = \phi_1' \frac{R_1}{R_2}$. ϕ_1' must still be determined, so the conservation of liquid volume is assumed ($\frac{dV}{dz} = 0$). The volume of liquid can be approached by the volume of the cylinder of radius r and height $z + h_1 + h_2$ decreased by the volumes of two spherical of radii R_1 and R_2 , and limited by the angles ϕ_1 and ϕ_2 :

$$V = \pi r^2 (z + R_1(1 - \cos \phi_1) + R_2(1 - \cos \phi_2)) - A_1 R_1^3 - A_2 R_2^3$$

leading to:

$$\begin{aligned}
\frac{dV}{dz} &= 2\pi r r' (z + R_1(1 - \cos \phi_1) + R_2(1 - \cos \phi_2)) + \pi r^2 (1 + R_1 \phi_1 \phi_1' + R_2 \phi_2 \phi_2') \\
&\quad - \pi \phi_1^3 \phi_1' R_1^3 - \pi \phi_2^3 \phi_2' R_2^3 \\
&\equiv 0 \\
\Leftrightarrow R_1 \phi_1' &= -\frac{r^2}{2rz + rR_1 \phi_1^2 + rR_2 \phi_2^2 + r^2 \phi_1 + r^2 \phi_2 - \phi_1^3 R_1^2 - R_2^2 \phi_2^3} \\
&= -\frac{r}{2z + r\phi_1 + r\phi_2} \\
&= -\frac{r}{2z + r^2(\frac{1}{R_1} + \frac{1}{R_2})} \tag{A.18}
\end{aligned}$$

Equation A.17 can now be rewritten into:

$$\frac{dW}{dz} = \frac{\pi \gamma r}{2z + r^2(\frac{1}{R_1} + \frac{1}{R_2})} (2z - R_1 \phi_1^2 - R_2 \phi_2^2 + 2r(\cos \theta_1 + \cos \theta_2))$$

At contact ($z = 0$), the assumption of small ϕ leads to:

$$\frac{dW}{dz} = \frac{\pi \gamma r}{r^2(\frac{1}{R_1} + \frac{1}{R_2})} 2r(\cos \theta_1 + \cos \theta_2)$$

Let us note $2 \cos \theta \equiv \cos \theta_1 + \cos \theta_2$ and $\frac{1}{R} \equiv \frac{1}{R_1} + \frac{1}{R_2}$ so that the last equation finally leads to:

$$F \equiv -\frac{dW}{dz} = -4\pi \gamma R \cos \theta \tag{A.19}$$

It can then be concluded that at contact and with small amounts of liquid ($\phi \ll$), the force between two spheres with radii R_1 and R_2 is equal to that between a plane and a sphere of radius R given by $\frac{1}{R} = \frac{1}{R_1} + \frac{1}{R_2}$.

Appendix B

Equivalence of the energetic and the Laplace equation based methods for capillary forces computation

B.1 Introduction

This appendix will give evidence of the equivalence between the energetic approach and the direct formulation based on the Laplace and the tension term:

$$F = F_L + F_T = -\frac{dW}{dz} \quad (\text{B.1})$$

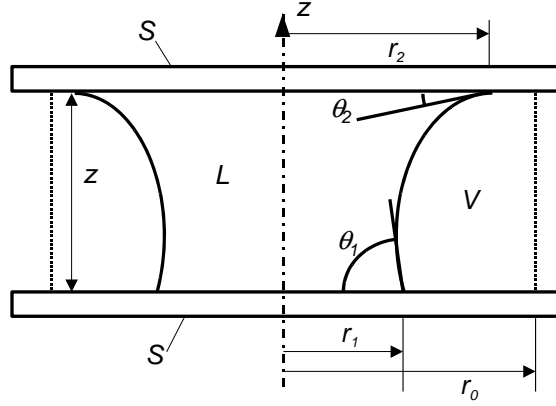
where F_L and F_T are given by equation (4.27). z is the separation distance between both solids.

B.2 Qualitative Arguments

The energetic approach involves both Laplace and tension terms. Let us illustrate this in the case of two parallel plates (see figure 4.3 reprinted in figure B.1) separated by a distance z (for the need of convenience, both contact angles have been chosen equal to θ). Based on the arguments of section 4.2.1, we have shown [92] that:

$$F = -\frac{2\gamma V \cos \theta}{z^2} - \frac{2\gamma\pi^{\frac{1}{2}} V^{\frac{1}{2}}}{z^{\frac{1}{2}}} \quad (\text{B.2})$$

Let us now consider the case $\theta = \frac{\pi}{2}$ in order to compare the force derived from the energy with that one computed from the meniscus geometry. Indeed, in this case, the approximation of the meniscus shape by a cylindrical volume is exact (stripped lateral area in figure B.1) and we can directly compute the mean

Figure B.1: Case of two parallel plates separated by a gap z

curvature of this cylinder. Consequently, we have to compare the force derived from the energy:

$$F = -\gamma\sqrt{\frac{\pi V}{z}} \quad (\text{B.3})$$

and the one established from the mean curvature, which is here given by:

$$2H = \frac{1}{r} + 0 \quad (\text{B.4})$$

leading to a pressure difference:

$$\Delta p = 2H\gamma = \frac{\gamma}{r} \quad (\text{B.5})$$

and henceforth to a ‘Laplace’ term of the force equal to:

$$\begin{aligned} F_L &= \pi r^2 \Delta p \\ &= \pi \gamma r \end{aligned} \quad (\text{B.6})$$

Note that this term is positive, i.e. repulsive, because the meniscus is convex, leading to a positive pressure difference. The ‘tension’ term of the force F_T can be written as:

$$F_T = -2\pi r \gamma \quad (\text{B.7})$$

leading to a total capillary force equal to:

$$F = F_L + F_T = -\gamma \pi r \quad (\text{B.8})$$

Assuming a cylindrical shape for the meniscus ($V = \pi r^2 z$), the latter equation can be rewritten into:

$$F = F_L + F_T = -\gamma\sqrt{\frac{\pi V}{z}} \quad (\text{B.9})$$

Since (B.3) and (B.9) are equal, we conclude that the force derived from the energy exactly represents the both terms of the capillary force (note well that the expression $F = 4\pi\gamma R \cos \theta$ proposed at equation (15.35) of [74] has been derived this way, consequently including both terms).

Another argument is geometric: let us consider the case depicted in figure B.2 where both contact angle are equal to $\frac{\pi}{2}$. The idea behind the following intuitive ar-

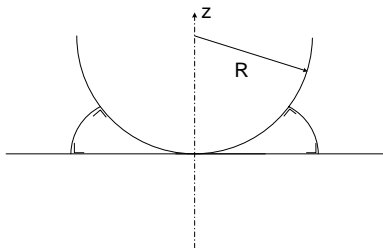


Figure B.2: A sphere (radius R) and a plate separated by a gap z : both contact angles are equal to $\theta = \frac{\pi}{2}$

gumentation is to proof that the energetic method well involves both terms. On the one hand, the case depicted in figure B.2 can be modeled thanks to equation (4.8) where h is set equal to 0: $F = 4\pi R\gamma \cos \theta$. As indicated in appendix A.3, this expression is based on the energetic approach. In the proposed case, this equation leads to $F = 0$. On the other hand, the meniscus is clearly convex, leading to a repulsive ‘Laplace’ force which is here counted strictly positive. Now, if we take the (always) attractive ‘tension’, we see (qualitatively) that we could have a total force equal to zero. This argument also conveys the idea that both approaches are equivalent.

B.3 Analytical Arguments

B.3.1 Definition of the Case Study

We propose to demonstrate the equivalence of the approaches on a prism-plane configuration. The prism is defined by its length in the y direction, L , and its angular aperture ϕ . Its location is defined by the distance¹ D between its apex A and the plane. Let us assume a volume of liquid V wetting the plane with a contact angle θ_1 and the prism with a contact angle θ_2 . Since the curvature of the meniscus in the direction y perpendicular to Oxz is equal to zero, the Laplace equation (4.24) becomes:

$$\frac{x''}{(1+x'^2)^{\frac{3}{2}}} = \frac{\Delta p}{\gamma} \quad (\text{B.10})$$

where $x' = \frac{dx}{dz}$.

¹For the sake of clarity, since z will be used as one of the coordinates, the gap is noted D in this chapter

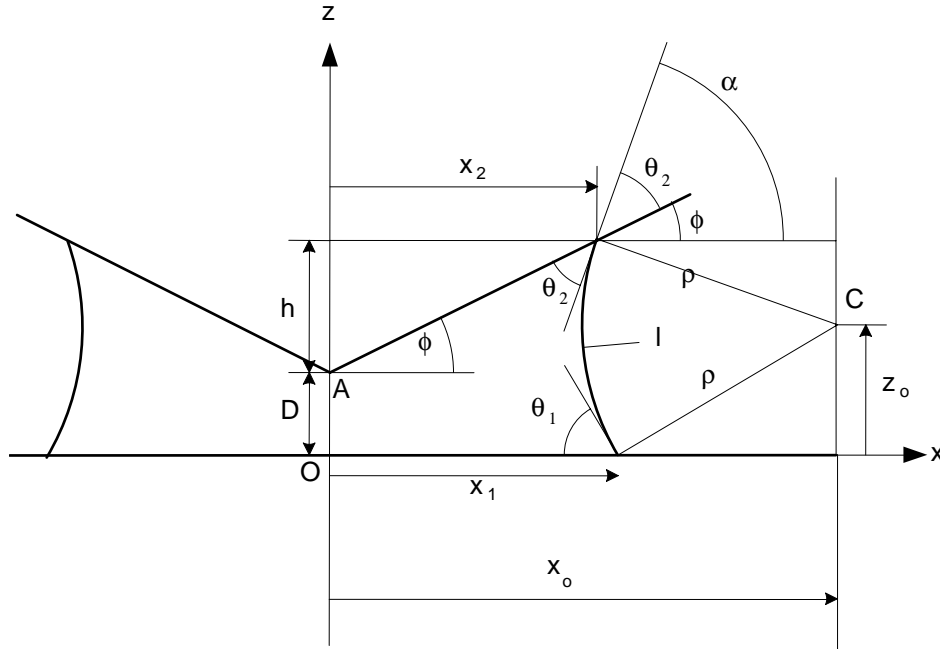


Figure B.3: Prism-plane configuration

Assuming a vanishing Bond number, the hydrostatic pressure inside the meniscus is neglected by comparison to the Laplace pressure difference Δp , which is therefore constant in all the meniscus. Therefore, the second term of (B.10) is constant and this equation can be integrated twice with respect to z , in order to find the relation $x = x(z)$, with two integration constants and the undefined pressure difference Δp . A more straight forward derivation is based on the fact that since one of the curvature radius is infinite and that the total curvature $2H$ is constant, the second curvature radius $\frac{(1+x'^2)^{\frac{3}{2}}}{x''}$ is constant: let us note it ρ . Therefore the meniscus profile is a curve with constant curvature, i.e. a circle given by the following equation:

$$(x - x_0)^2 + (z - z_0)^2 = \rho^2 \quad (\text{B.11})$$

where x_0 and z_0 are the coordinates of the circle center. Once again, three parameters are to be determined: x_0 , z_0 and ρ . This can be done using three boundary conditions: both contact angles θ_1 and θ_2 and the volume of liquid V .

B.3.2 Preliminary Computations

Let us express x_0 , z_0 and ρ as functions of known data $(\phi, D, \theta_1, \theta_2)$ and the immersion height h , which is still unknown at this step, but which will be determined using the condition on the volume of liquid V . Note that x_2 is an intermediary vari-

able and that x_1 will be used later. For sake of convenience, the notation $\alpha = \theta_2 + \phi$ has been adopted in the following equations:

$$x_2 = \frac{h}{\tan \phi} \quad (\text{B.12})$$

$$\rho = \frac{D + h}{\cos \theta_1 + \cos \alpha} \quad (\text{B.13})$$

$$z_0 = \rho \cos \theta_1 \quad (\text{B.14})$$

$$x_0 = x_2 - (z_0 - D - h) \tan \alpha \quad (\text{B.15})$$

$$x_1 = x_0 - z_0 \tan \theta_1 \quad (\text{B.16})$$

Additional useful relations are the meniscus equation:

$$x = x_0 - \sqrt{\rho^2 - (z - z_0)^2} \quad (\text{B.17})$$

the meniscus slope x' :

$$x' = -\frac{z - z_0}{x - x_0} \quad (\text{B.18})$$

and finally, the rewritten Laplace equation linking Δp and ρ :

$$\Delta p = \frac{\gamma}{\rho} \quad (\text{B.19})$$

h is still to be determined using the volume of liquid V (see next step).

B.3.3 Determination of the Immersion Height h

The volume of liquid can be used to determine the value of the immersion height h , starting from the following expression of V as illustrated in figure B.4:

$$V = 2LA \quad (\text{B.20})$$

$$= 2L[x_0(h + D) - A_{\text{I}} - A_{\text{II}} - A_{\text{III}} - A_{\text{IV}}] \quad (\text{B.21})$$

where:

$$A_{\text{I}} = \frac{x_2 h}{2} \quad (\text{B.22})$$

$$A_{\text{II}} = \frac{(x_0 - x_2)(D + h - z_0)}{2} \quad (\text{B.23})$$

$$A_{\text{III}} = \frac{z_0(x_0 - x_1)}{2} \quad (\text{B.24})$$

$$A_{\text{IV}} = \frac{\rho^2(\pi - \alpha - \theta_1)}{2} \quad (\text{B.25})$$

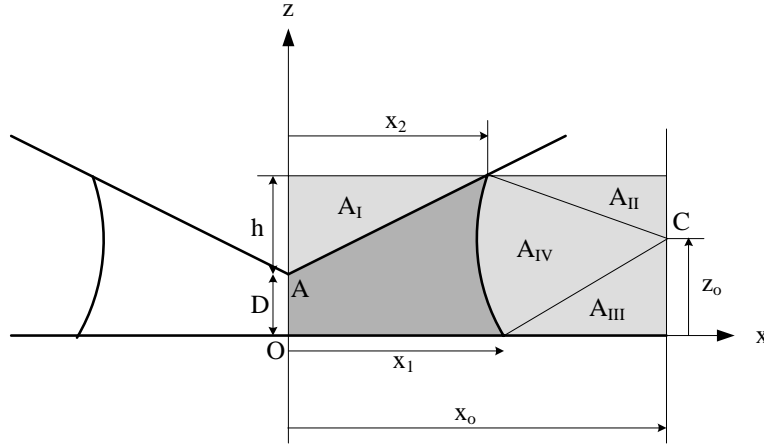


Figure B.4: Determination of the immersion height from the volume of liquid

Therefore, the equation giving the volume V can be rewritten as follows:

$$V = 2L[x_0(D+h) - \frac{x_2 h}{2} \dots \dots - \frac{\rho^2(\pi - \alpha - \theta_1)}{2} - \frac{(x_0 - x_2)(D+h-z_0)}{2} - \frac{z_0(x_0 - x_1)}{2}] \quad (\text{B.26})$$

$$= L[2x_2 D + x_2 h \dots \dots + \rho^2 [\underbrace{\sin \alpha \cos \alpha + 2 \sin \alpha \cos \theta_1 - \pi + \alpha + \theta_1 - \sin \theta_1 \cos \theta_1}_{\equiv \mu(\cos \theta_1 + \cos \alpha)^2}]] \quad (\text{B.27})$$

$$= L[h^2(\frac{1}{\tan \phi} + \mu) + 2hD(\frac{1}{\tan \phi} + \mu) + \mu D^2] \quad (\text{B.28})$$

This latter equation can be rewritten as a second degree equation with respect to the unknown h :

$$h^2 + 2hD + \frac{\mu D^2 - V/L}{\mu + \frac{1}{\tan \phi}} = 0 \quad (\text{B.29})$$

which leads to:

$$h = -D \pm \sqrt{D^2 - \frac{D^2 \mu - V/L}{\mu + \frac{1}{\tan \phi}}} \quad (\text{B.30})$$

The '-' solution makes no physical sense since the immersion height cannot be negative. Consequently:

$$h = -D + \sqrt{D^2 - \frac{D^2 \mu - V/L}{\mu + \frac{1}{\tan \phi}}} \quad (\text{B.31})$$

and the variation of h with respect to a variation of the separation distance D (it

will be used in what follows) is given by:

$$\frac{dh}{dD} = -1 + \frac{D}{D+h} \frac{1}{1 + \mu \tan \phi} \quad (\text{B.32})$$

B.3.4 Laplace Equation Based Formulation of the Capillary Force

As it has previously been explained, the capillary force can be written as the sum of a term depending on the Laplace pressure difference Δp and the so-called tension term:

$$F = 2Lx_1 \Delta p + 2L\gamma \sin \theta_1 \quad (\text{B.33})$$

$$= 2L\gamma \left(\frac{x_1}{\rho} + \sin \theta_1 \right) \quad (\text{B.34})$$

$$= 2L\gamma \frac{x_0}{\rho} \quad (\text{B.35})$$

$$= 2L\gamma \left(\frac{x_2}{\rho} + \frac{D+h-z_0}{\rho} \tan \alpha \right) \quad (\text{B.36})$$

$$= 2L\gamma \left(\frac{h}{D+h} \frac{\cos \theta_1 + \cos \alpha}{\tan \phi} + \sin \alpha \right) \quad (\text{B.37})$$

Using (B.31), the force can be expressed as a function of the volume of liquid V , the separation distance D and the angles of the problem: contact angles θ_1 and θ_2 at the one hand and the prism angle ϕ at the other hand. Let us remind that $\alpha = \theta_2 + \phi$.

B.3.5 Energetic Formulation of the Capillary Force

As previously explained, the energetic or thermodynamic approach is based on the differentiation of the total surface energy W with respect to the separation distance D .

$$W = \gamma(\Sigma - A_1 \cos \theta_1 - A_2 \cos \theta_2) \quad (\text{B.38})$$

where:

$$\Sigma = 2L\ell = 2L\rho(\pi - \alpha - \theta_1) \quad (\text{B.39})$$

$$A_1 = 2Lx_1 \quad (\text{B.40})$$

$$A_2 = 2L \frac{h}{\sin \phi} \quad (\text{B.41})$$

Consequently, the reduced surface energy $W/(2L\gamma)$ can be written as (+ any arbitrary constant):

$$\frac{W}{2L\gamma} = \rho(\pi - \alpha - \theta_1) - \cos \theta_1 \left(\frac{h}{\tan \phi} + \rho \sin \alpha - \rho \sin \theta_1 \right) - h \frac{\cos \theta_2}{\sin \phi} \quad (\text{B.42})$$

$$= (D+h) \underbrace{\frac{\pi - \alpha - \theta_1 - \sin \alpha \cos \theta_1 + \sin \theta_1 \cos \theta_1}{\cos \theta_1 + \cos \alpha}}_{\equiv \beta} \dots$$

$$\dots - h \left(\frac{\cos \theta_1}{\tan \phi} + \frac{\cos \theta_2}{\sin \phi} \right) \quad (\text{B.43})$$

$$= D\beta + h \left(\beta - \frac{\cos \theta_1}{\tan \phi} - \frac{\cos \theta_2}{\sin \phi} \right) \quad (\text{B.44})$$

To compute the force from the energy, the latter equation has to be derived with respect to D using (B.32) (β is constant with respect to D):

$$\frac{dW}{dD} \frac{1}{2L\gamma} = \beta + \left(-1 + \frac{D}{D+h} \frac{1}{1 + \mu \tan \phi} \right) \left(\beta - \frac{\cos \theta_1}{\tan \phi} - \frac{\cos \theta_2}{\sin \phi} \right) \quad (\text{B.45})$$

$$= \frac{\cos \theta_1}{\tan \phi} + \frac{\cos \theta_2}{\sin \phi} \dots$$

$$\dots + \frac{D}{D+h} \frac{1}{1 + \mu \tan \phi} \left(\beta - \frac{\cos \theta_1}{\tan \phi} - \frac{\cos \theta_2}{\sin \phi} \right) \quad (\text{B.46})$$

where μ , h and β have been defined in (B.27), (B.31) and (B.43). All the other parameters are given data. It should be now proofed that (B.37) and (B.46) are equivalent.

B.3.6 Equivalence of Both Formulations

Equation (B.46) can be rewritten as:

$$\frac{dW}{2L\gamma dD} = \frac{\cos \theta_1}{\tan \phi} + \frac{\cos \theta_2}{\sin \phi} + \frac{D}{D+h} \dots$$

$$\dots \left[\frac{\pi - \alpha - \theta_1 - \sin \alpha \cos \theta_1 + \sin \theta_1 \cos \theta_1}{(\cos \theta_1 + \cos \alpha)(1 + \mu \tan \phi)} - \frac{1}{1 + \mu \tan \phi} \left(\frac{\cos \theta_1}{\tan \phi} + \frac{\cos \theta_2}{\sin \phi} \right) \right] \quad (\text{B.47})$$

It can be shown that the expression under brackets in (B.47) is equal to $-(\cos \theta_1 + \cos \alpha)/\tan \phi$. Therefore, (B.47) can be rewritten into:

$$\frac{dW}{dD} \frac{1}{2L\gamma} = \frac{\cos \theta_1}{\tan \phi} + \frac{\cos \theta_2}{\sin \phi} - \frac{D}{D+h} (\cos \theta_1 + \cos \alpha) \frac{\cos \phi}{\sin \phi}$$

$$= \frac{(\cos \theta_1 \cos \phi + \cos \theta_1)(D+h) - D \cos \phi (\cos \theta_1 + \cos \theta_2 \cos \phi - \sin \theta_2 \sin \phi)}{(D+h) \sin \phi} \quad (\text{B.48})$$

In order to let appear the term $\sin \alpha$ present in (B.37), let us add and subtract $\sin \alpha$ simultaneously to the latter equation: after some (tedious) calculations and using

the relation $\alpha = \theta_2 + \phi$, the following expression can be obtained:

$$\begin{aligned} \frac{dW}{dD} \frac{1}{2L\gamma} &= \frac{h \cos \phi (\cos \theta_1 + \cos \theta_2 \cos \phi - \sin \theta_2 \sin \phi)}{(D+h) \sin \phi} + \sin \alpha \\ &= \frac{h}{D+h} \frac{\cos \theta_1 + \cos \alpha}{\tan \phi} + \sin \alpha \end{aligned} \quad (\text{B.49})$$

As a conclusion, the latter equation leads to a force given by:

$$F = -\frac{dW}{dD} = -2L\gamma \left(\frac{h}{D+h} \frac{\cos \theta_1 + \cos \alpha}{\tan \phi} + \sin \alpha \right) \quad (\text{B.50})$$

The negative sign in front of $2L$ indicates that the force is attractive. Consequently, it is concluded that the force computation based on the Laplace equation (equation B.37) and the expression obtained from the energy formulation (B.50) are equal.

B.4 Conclusions

As it is shown that both approaches are equivalent, it means that the energetic approach already involves the tension term and the Laplace term on an implicit way. Consequently, the energetic approach as proposed by Israelachvili (see equation (4.8)) includes both terms, even if, for zero separation distance, the pressure term usually dominates the tension one. For axially symmetric configurations, the method based on the Laplace equation will be preferred because it can be easily numerically solved.

Appendix C

Design rules for capillary grippers

C.1 Introduction

To conclude this part, we propose to summarize the obtained results in terms of picking on the one hand and of releasing on the other hand. Additionally, some rules will be proposed, to be applied to the design of a surface tension based gripper.

C.2 Picking Operations

In terms of picking task, and especially in terms of picking force, the influence of the following parameters can be pointed out:

1. Influence of contact angles: contact angle θ_1 depends on the combination component material-gripping liquid while θ_2 depends on the combination gripping liquid-gripper material. Therefore, if the component is imposed, the gripping liquid must be chosen to cause small θ_1 , in order to increase the force (it has been shown that the force decreases as a function of θ_1 , a little more slowly than the cosine function). Note that for a given component material, a low energy liquid (i.e. with small γ) provokes smaller θ_1 but is less efficient as the force is also proportional to γ . Therefore a compromise must be found.

Additionally, it must be noted that in the case of the conforming gripper used in the watch bearing case study, the force is attractive even for non wetting coating.

2. Influence of volume of liquid: for spherical grippers, the volume of liquid plays almost no role. Consequently the dispensing accuracy or evaporation for example are not parameters of the utmost importance here. On a different way, the force can remain quite steady if the amount of liquid can be kept

constant, which is more or less the case with a foam gripper. Nevertheless, for conical grippers, the larger the volume, the larger the force. At the contrary, in the case of the conforming gripper of the watch bearing case study, the force increases with decreasing volume of liquid, which is of the utmost interest in a high throughput application. Consequently, no general rule can be drawn concerning the influence of the volume of liquid: it depends on the conformation between the component and the gripper geometries. Moreover the amount of liquid also determines the approaching contact distance and the rupture distance.

3. Influence of the gripper's geometry: cylindrical grippers lead to the largest forces. As far as spherical grippers are concerned, the force is proportional to their radius as illustrated by the Israelachvili approximation [74]:

$$F \approx 4\pi R\gamma\cos\theta \quad (\text{C.1})$$

4. Influence of surface tension: the force developed by a liquid bridge is proportional to surface tension. Nevertheless, liquids with a low surface tension better wet solids, leading to smaller contact angles: therefore a compromise has to be found.
5. Influence of the gap: the force decreases with the separation distance so that the maximal force is observed when gripper and component touch each other.
6. As an order of magnitude, forces up to several mN can be reached easily (1mN corresponds to a mass $m = 100$ mg). The rule of thumb is 1 mN for a 1 mm sized component.

In case of picking more than one component at a time, the gripper could be cleaned by dipping it to a liquid tank. Of course, a better solution would be to develop a specific feeder according to the application. This will be considered in the perspectives of this work, at least as far as the watch bearing is concerned.

C.3 Releasing Strategies

In a 'micro' driven design, care should also be taken of the possibilities to release the component. In macromanipulation, indeed, the picking force F_{\max} is replaced by $F_{\min} = 0$ at release while in the case of a surface tension based gripper (or any adhesive principle based gripper), there is always a residual adhesion force $F_{\min} > 0$ that can prevent the component from being released if F_{\min} is larger than its weight W . Consequently, an adhesion or surface tension based gripper can only be designed for a restricted mass range $[m_{\min}, m_{\max}]$ of components as illustrated in table C.1. In order to compare the different release strategies in a quantified way,

Table C.1: Mass range

Mass position	Description
$m > m_{\max}$	Component cannot be picked up
$m_{\max} > m > m_{\min}$	Component can be picked up and released
$m_{\min} > m$	Component can be picked up but cannot be released

the following ‘adhesion’ ratio has been introduced:

$$\phi = \frac{F_{\min}}{F_{\max}} \quad (\text{C.2})$$

ϕ ranges from 0 (no residual adhesion, the releasing task is not a problem) to 1 (residual adhesion force is as large as the picking one, handling cannot be performed). Let us now summarize the different release strategies (sorted by decreasing ϕ):

1. reduce the volume of the liquid bridge: this strategy cannot be used with spherical grippers since the developed force is almost independent from the amount of liquid but can be achieved for conical grippers.
2. tilt the gripper with respect to the component: if the orientation of the gripper is changed from 0 to 5°, the ratio is:

$$\phi \approx \frac{2.4 \text{ mN}}{5.5 \text{ mN}} \approx 0.436 \quad (\text{C.3})$$

and, if the gripper is tilted to 10°:

$$\phi \approx \frac{1.2 \text{ mN}}{5.5 \text{ mN}} \approx 0.218 \quad (\text{C.4})$$

3. move the gripper in the shear direction: in this case, if the component is blocked laterally, the gripper can be moved in the xy plane (i.e. perpendicular to the axial symmetry axis z) and the force to generate depends on the friction between the gripper and the component:

$$F_{\text{shear}} = f_o F \quad (\text{C.5})$$

where f_o is the static friction coefficient (‘static’ because the gripper is moved from rest). In this case, the ratio of the forces to develop is simply given by f_o . This release is sometimes called scrapping release method [49]. This method has been successfully implemented in the watch bearing case study. Note that in order to achieve a reliable release of a spherical component, the gap between the latter and the summit of the cavity should not be larger than a fifth of the ball diameter (figure 6.20).

4. increase the gap (figure 4.16): by increasing the gap, the force can be reduced efficiently. In the example of figure 4.16, it can be seen that a gap $z = 500 \mu\text{m}$ leads to:

$$\phi \approx \frac{0.10 \text{ mN}}{0.95 \text{ mN}} \approx 0.105 \quad (\text{C.6})$$

5. change the gripper geometry: if the angular aperture was increased from 0° to 5° , the force reduction would lead to:

$$\phi \approx \frac{2 \text{ mN}}{20 \text{ mN}} \approx 0.100 \quad (\text{C.7})$$

6. use dynamical effects: let us assume that the picking task of a mass m is achieved with a zero velocity and a force F . Therefore, the limit for m is $\frac{F}{g}$ ($g = 9.81 \text{ m s}^{-1}$). If now an acceleration a is imposed to the gripper, the heaviest acceptable mass is $m' = m \frac{g}{a+g}$. Therefore, the force seems to have been reduced by $\frac{g}{a+g}$. If $a \approx 100 \text{ m s}^{-2}$, the ratio becomes:

$$\phi = \frac{g}{a+g} \approx 0.089 \quad (\text{C.8})$$

Note that this method has to be envisaged carefully because of its low positioning accuracy.

7. use an auxiliary releasing tip: for example, by substituting an auxiliary PTFE tip to a steel cylindrical gripper generating forces about 5mN, the force can be reduced to about 60 μm , leading to:

$$\phi \approx \frac{0.060 \text{ mN}}{5 \text{ mN}} \approx 0.012 \quad (\text{C.9})$$

8. control the contact angle (for example using electrowetting): if the contact angle was controlled and set to $\frac{\pi}{2}$, the residual force could be avoided as it essentially depends on $\cos \theta$. In this case:

$$\phi \approx 0 \quad (\text{C.10})$$

Several strategies can be combined: for example, a gripper tilting achieved with a dynamical release: in this case the total efficiency of the release strategy can be assessed by:

$$\Phi = \prod_{i=1}^n \phi_i \quad (\text{C.11})$$

C.4 Design Aspects

In a given application, the component is imposed, that is its material and its geometry cannot be changed. The freedom of the designer concerns the handling liquid (surface tension, volatility, dynamic viscosity), the gripper (material and coating, geometry) and the releasing strategy.

- *Surface tension:* The larger the surface tension, the larger the capillary force. Nevertheless, a liquid with a lower surface tension will better wet the component, leading to an opposite effect. This issue must be carefully addressed.
- *Volatility:* To achieve experimental measurements, we recommend to use a non volatile liquid, such as for example the silicone oil we have used in this work. Since it does not evaporate, the volume of liquid remains constant during the experiment. Nevertheless, this can be a drawback from the application point of view, since a non volatile liquid will leave residual traces on the component. If the assembly task can be achieved very quickly (less than 1 second to fix the order of magnitude), volatile liquids such as alcohols are suitable: they do not leave traces;
- *Contact Angle Hysteresis:* To achieve experimental measurements, it is of the utmost importance to know whether the advancing or the receding contact angle should be used in the models. Moreover, the larger the hysteresis, the larger the variability of the results. Consequently, water is not recommended. At the contrary, silicone oils or alcohols seem to be better, however it is recommended to first measure the contact angles with the liquid one proposes to use;
- *Dynamic viscosity:* The proposed force models rely on an equilibrium assumption. Therefore, the viscosity does not play any role in these models (i.e. the viscosity does not change the amount of force at equilibrium). Nevertheless, in high throughput machines, the transient effects become dominant. We have proposed an approximation of the characteristic damping time τ by solving the Lucas-Washburn equation:

$$\tau = \frac{1}{\lambda} = \frac{\rho d^2}{6\mu} \quad (\text{C.12})$$

Implementing a dynamical simulation is one of the perspectives of this work;

- *Gripper Material:* A gripper with high energy (metals for example) leads to smaller contact angles θ_2 than a gripper with low energy (polymers for example). Nevertheless, equation 6.1 indicates that a non wetting gripper can also lead to an attractive capillary force. The choice of the material can also be ruled by manufacturing aspects;

- *Gripper Surface:* According to the well-known Wenzel model [194], the roughness amplifies the wetting behavior: angles lower than 90° are decreased by roughness, while the angle increases if it is larger than 90° . This means that the gripping force of a capillary gripper could be increased by using rough gripper tips. The surface impurities increase the contact angle hysteresis. Finally, we have observed that the presence of a coating could be a drawback if it not mechanically resistant to wear (the gripper is subject to many contacts). Of course, a wear resistant coating permits to change the contact angle θ_2 ;
- *Gripper Geometry:* The geometry of the gripper is of the utmost importance. Actually, the important parameter to keep in mind is that near contact, the ‘pressure’ or ‘Laplace’ term of the capillary force dominates the ‘tension’ one (see figure 4.17). To maximize the capillary force, the gripper should maximize the pressure difference $p_{in} - p_{out}$ and also the area on which this pressure difference is acting. The first objective can be done with small θ_1 and θ_2 but also by keeping distance between the gripper and the component as small as possible, i.e. designing a conforming geometry. This also respects the second condition since, for a given volume of liquid, a conforming gripper leads to a larger contact circle radius, henceforth to a larger area. This principle is qualitatively discussed from figure C.1. We see on this picture that for the (hypothetic) depicted gripper, the distance between the gripper and the component is smaller for a volume of liquid corresponding to a meniscus wetting in B than in A . Hence, the pressure difference Δp_B is larger than the pressure difference Δp_A . Moreover, since the meniscus radius r_B is larger than the meniscus radius r_A , the area over which this pressure difference acts is much larger, leading to a larger force ($F_B > F_A$). If the volume of liquid is increased a bit more, the meniscus will wet the component at a distance $r_C > r_B$ from the symmetry axis. Therefore, the area is increased, but the pressure difference is reduced, since the distance between the component and the gripper increases. Both effects fight one another, and qualitatively, the force can increase or decrease, which is shown in the bottom right sketch of figure C.1. We also see on this picture the qualitative evolution of the volume of liquid. It is clear that it will be difficult to master the volume of liquid between V_A and V_B , since the sensitivity of the volume is very low. At the contrary, there is a dramatic increase of the volume of liquid as soon as $r > r_C$. These principles can be applied to optimize the design of a gripper intend to pick flat components. We see in figure C.2a that giving the gripper the shape of a truncated cone, we increase the ‘acting’ area¹ with keeping a small distance between the gripper and the component, leading to a large pressure difference. We let the reader compare this configuration with the spherical or the conical gripper presented in a previous chapter. This has been applied in [168] to pick up square molybdenum dies

¹The area on which the pressure difference acts

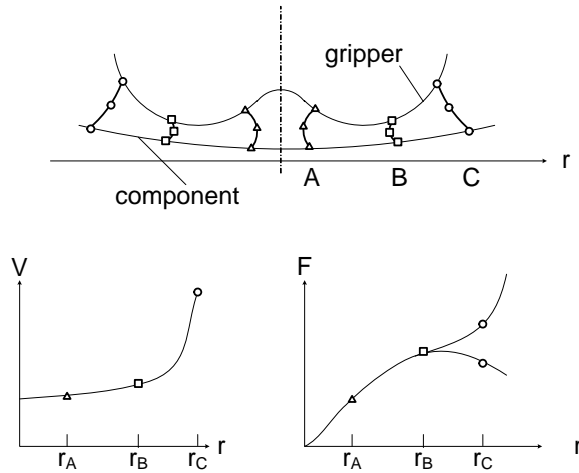


Figure C.1: Design rules

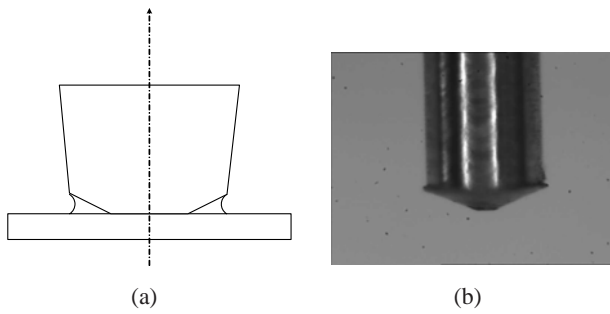


Figure C.2: (a) Example of a truncated conical gripper, which allows a large pressure difference together with a large acting area; (b) Example of the gripper proposed by [168] (Courtesy of D. Schmid, EPFL/STI/IPR/LPM)

($100\ \mu\text{m} \times 100\ \mu\text{m} \times 20\ \mu\text{m}$), simulating optical components. An example of the used gripper is given in figure C.2b.

- *Scaling Law*: the capillary force linearly depends on the system size. Therefore, this principle is of the utmost interest in miniaturization.

Appendix D

Parabola model

The main (empirical¹) assumption is that the meniscus shape can be modeled with a parabola (see figure D.1):

$$r(z) = a_0 + a_1z + a_2z^2 \quad (\text{D.1})$$

where r and z are the axis shown in figure 4.18. Since the parabola passes through the edges of the pad and the component, this gives two conditions to determine the value of a_0 and a_1 as a function of a_2 :

$$a_0 = R - \frac{a_2h^2}{4} \quad (\text{D.2})$$

$$a_1 = 0 \quad (\text{D.3})$$

The parameter a_2 is to be determined to respect the volume of liquid condition (V and R are known and h is an input parameter):

$$\begin{aligned} V &= \int_{-\frac{h}{2}}^{\frac{h}{2}} \pi r^2(z) dz \\ &= \pi \left(hR^2 + \frac{a_2^2h^5}{30} - \frac{a_2Rh^3}{3} \right) \end{aligned} \quad (\text{D.4})$$

From this volume equation, we can determine a_2 and its derivative with respect to h :

$$a_2 = \frac{5R}{h^2} - \sqrt{\frac{30V}{\pi h^5} - \frac{5R^2}{h^4}} \quad (\text{D.5})$$

$$\frac{da_2}{dh} = -\frac{10R}{h^3} - \frac{10R^2/h^5 - 75V/(\pi h^6)}{\sqrt{30V/(\pi h^5) - 5R^2/h^4}} \quad (\text{D.6})$$

¹This assumption does not rely on any physical consideration but corresponds to the meniscus shape observed experimentally

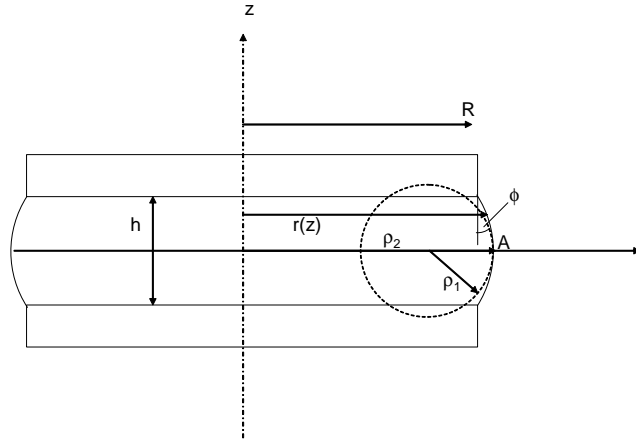


Figure D.1: Parabola model

The force F_z can be determined from its both components:

$$\begin{aligned} F_z &= F_L + F_T \\ &= \pi R^2 dp - 2\pi R \gamma \cos \phi \end{aligned} \quad (\text{D.7})$$

where $\cos \phi$ is given by the geometric condition $\tan \phi = r'(z = h/2) = a_2 h$ leading to:

$$\cos \phi = \frac{1}{\sqrt{1 + a_2^2 h^2}} \quad (\text{D.8})$$

and dp is the pressure difference across the meniscus interface, given by:

$$\begin{aligned} dp &= 2H\gamma \\ &= \left(\frac{1}{\rho_1} + \frac{1}{\rho_2} \right) \gamma \end{aligned} \quad (\text{D.9})$$

where ρ_1 and ρ_2 are the curvature radii shown in figure 4.18:

$$\rho_1 = -\frac{1}{2a_2} \quad (\text{D.10})$$

$$\rho_2 = \frac{1}{a_0} = \frac{1}{R - a_2 h^2 / 4} \quad (\text{D.11})$$

Consequently, the axial force F_z is given by:

$$F_z = \pi R \gamma \left(-2a_2 R + \frac{4R}{4R - a_2 h^2} \right) - \frac{2\pi R \gamma}{\sqrt{1 + a_2^2 h^2}} \quad (\text{D.12})$$

In the particular case of $a_2 = 0$ (corresponding to a cylindrical meniscus), the force is equal to the well-known value $-\pi R\gamma$. The axial stiffness k_z can be computed by derivation ($a'_2 = \frac{da_2}{dh}$):

$$k_z = \frac{dF_z}{dz} \quad (\text{D.13})$$

$$= -2\pi R^2 \gamma a'_2 + \frac{4\pi R^2 \gamma (a'_2 h^2 + 2a_2 h)}{(4R - a_2 h^2)^2} + 2\pi R \gamma \frac{a_2 a'_2 h^2 + a_2^2 h}{(1 + a_2^2 h^2)^{3/2}} \quad (\text{D.14})$$

For a cylindrical meniscus, $a_2 = 0$, and we have $a'_2 = 3R/h^3$, which leads to:

$$k_{z0} = -\pi \gamma \left[6 \left(\frac{R}{h} \right)^3 - \frac{3}{4} \left(\frac{R}{h} \right) \right] \quad (\text{D.15})$$

We see that the stiffness increases when h decrease (i.e. when the volume of liquid V decreases) and when the radius of the pad decreases. It is interesting to note that if the system is downscaled homothetically, i.e. the ratio R/h remains unchanged (in the case of cylindrical meniscii), the stiffness is independent on the size of the system.

Appendix E

Axial dynamics

E.1 Volume of liquid as a function of the contact angle and the gap

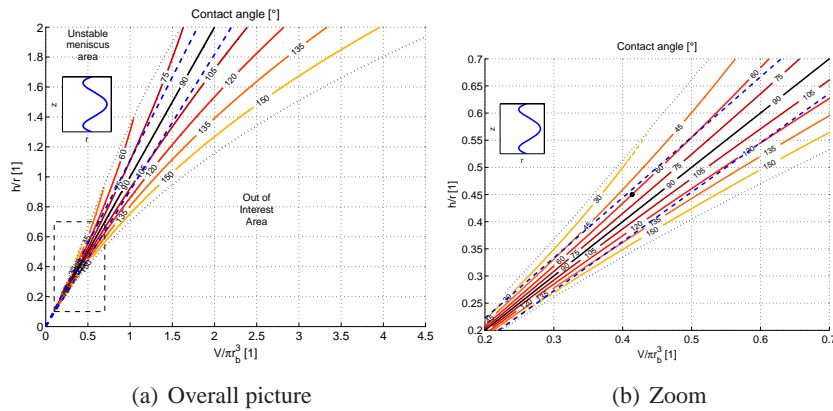


Figure E.1: Contact angle as a function of the reduced volume of liquid and the reduced gap. The black line is the contour at 90° corresponding to a cylindrical configuration. The blue dashed lines delimit the area of 10% of volume variation at constant gap. (Courtesy of J.-B. Valsamis [181])

E.2 Numerical validation

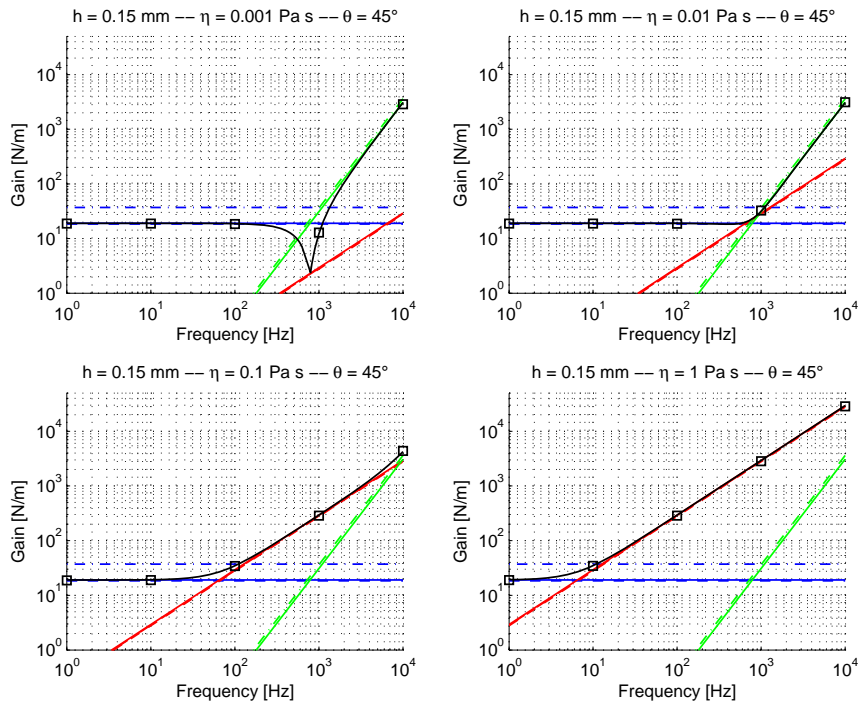
The parameters used for the numerical experiments led by Jean-Baptiste Valsamis are indicated in table E.1.

Parameter	Symbol	Value
Radius	r_b	0.75mm
Gap	h	0.15mm, 0.25mm
Contact angle	θ	45°, 90°, 135°
Viscosity	η	0.001Pas, 0.01Pas, 0.1Pas, 1Pas
Frequency	f	1Hz, 10Hz, 100Hz, 1kHz, 10kHz

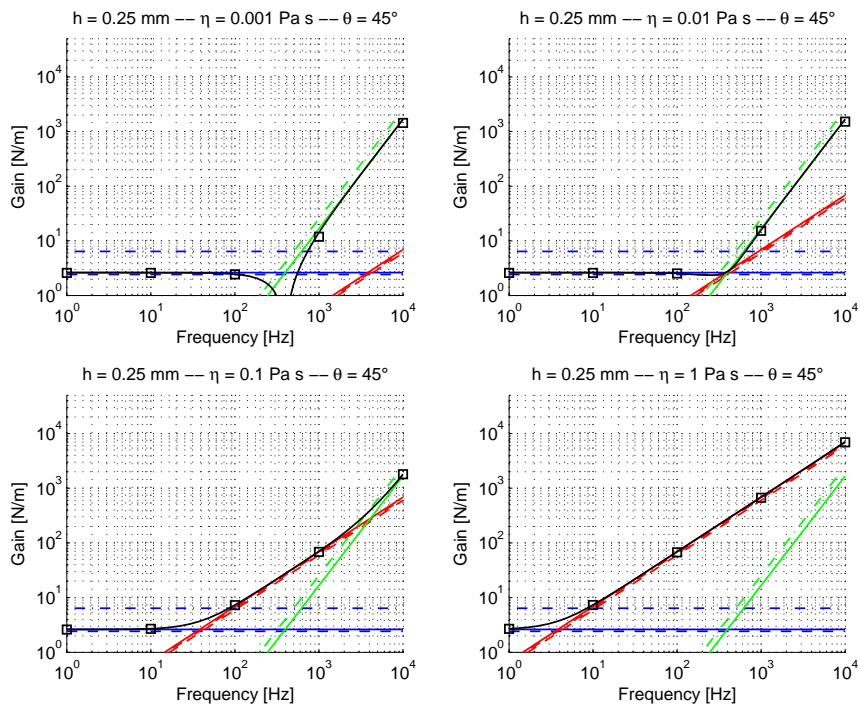
Table E.1: Parameters of the numerical simulations

Line	Signification
— (solid blue)	k by numerical integration
- · - · - (dash-dot blue)	k with the circular model
- - - (dashed blue)	k with the parabolic model
— (solid red)	b , assumption b1
- · - · - (dash-dot red)	b , assumption b2
- - - (dashed red)	b , assumption b3
— (solid green)	m , assumption m1
- · - · - (dash-dot green)	m , assumption m2
— (solid black)	Gain curve with k, b and m
□ (open square)	Numerical experiment

Table E.2: Legend of numerical experiments vs analytical models. The b -coefficient obtained with assumptions b1 (total stress balanced) assumption b2 (total pressure balanced) and assumption b3 (local pressure balanced) tend to each other when the aspect ratio of the meniscus is small ($\eta \gg h$) (see [181] for further details, section 13.2 Damping Coefficient). The m -coefficient obtained with assumption m1 (conservation of the force exerted by the pressure only, i.e. neglecting surface tension and viscous effects) or with assumption m2 (conservation or the kinetic energy conservation) lead to one another when the aspect ratio of the meniscus is small (see [181], section 13.3 Equivalent mass)

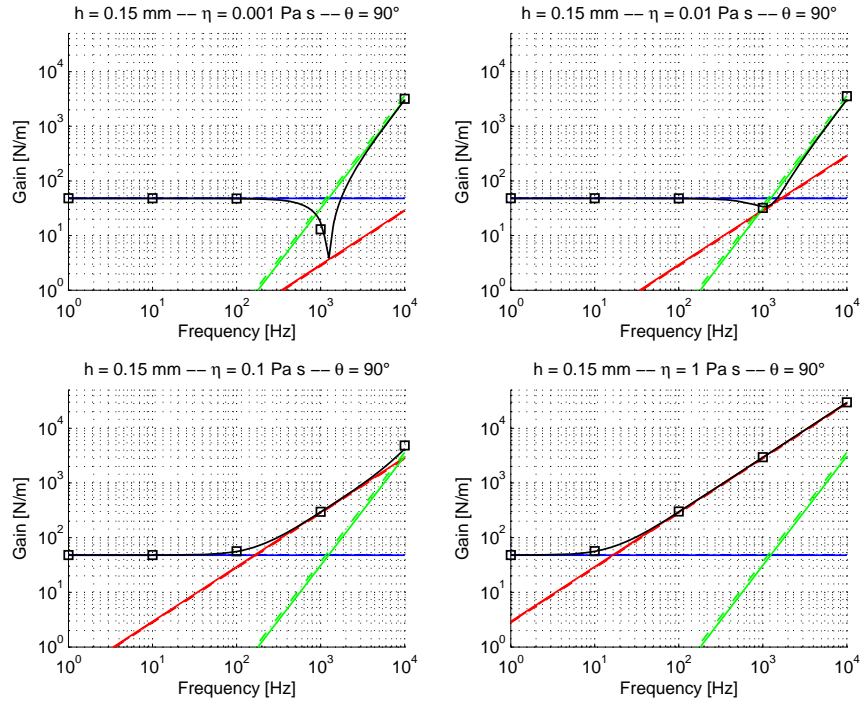


(a)

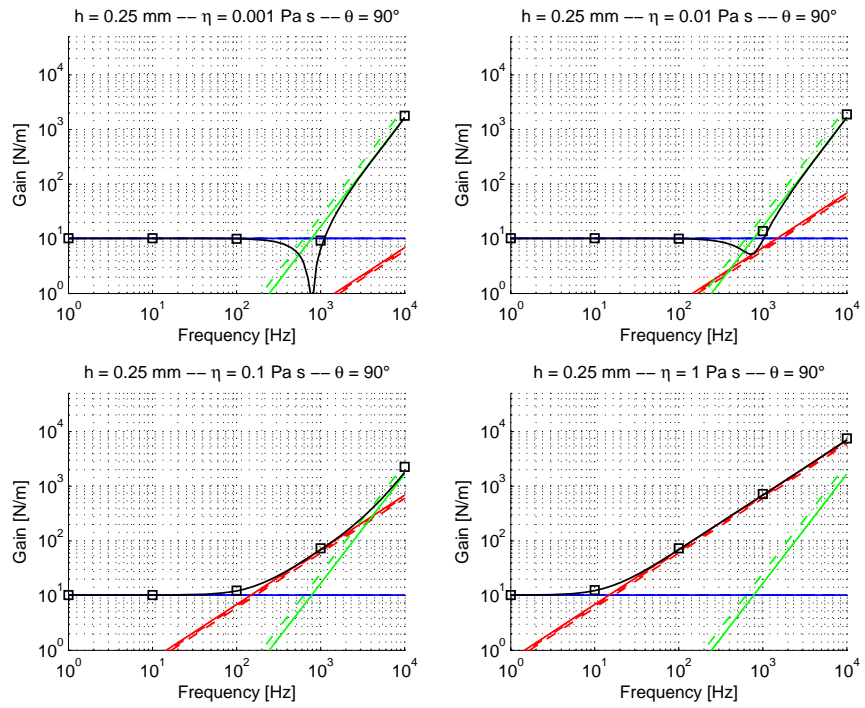


(b)

Figure E.2: Gain curves for $\theta = 45^\circ$

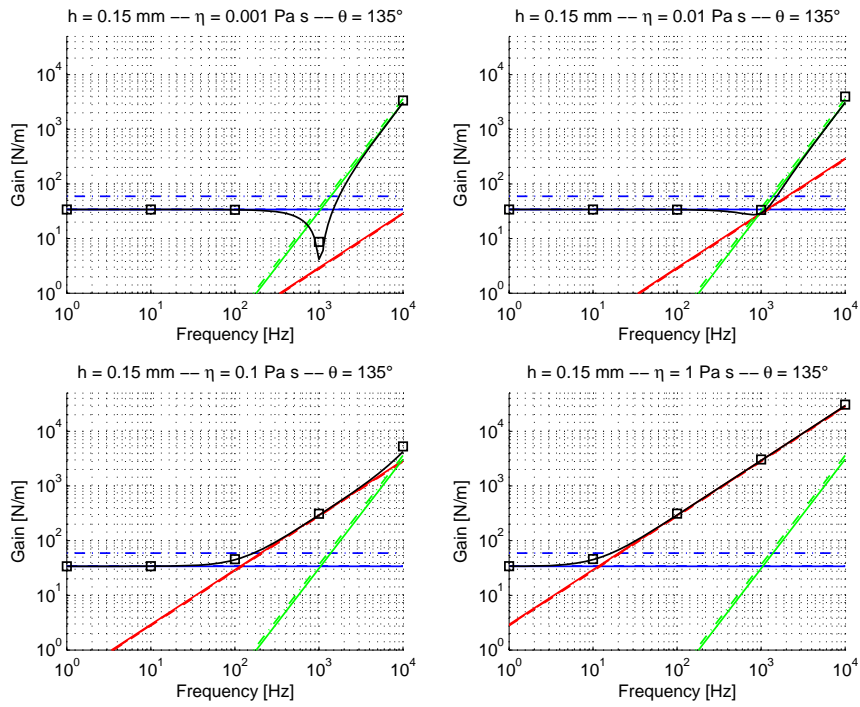


(a)

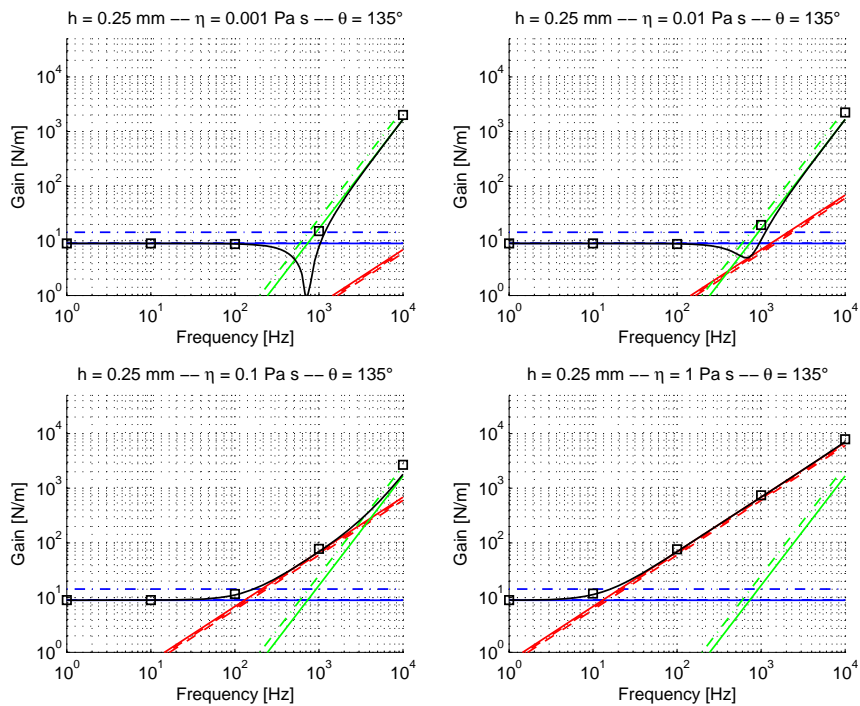


(b)

Figure E.3: Gain curves for $\theta = 90^\circ$



(a)



(b)

Figure E.4: Gain curves for $\theta = 135^\circ$

E.3 Experimental validation

Experiments have been led whose parameters are summarized in table E.3.

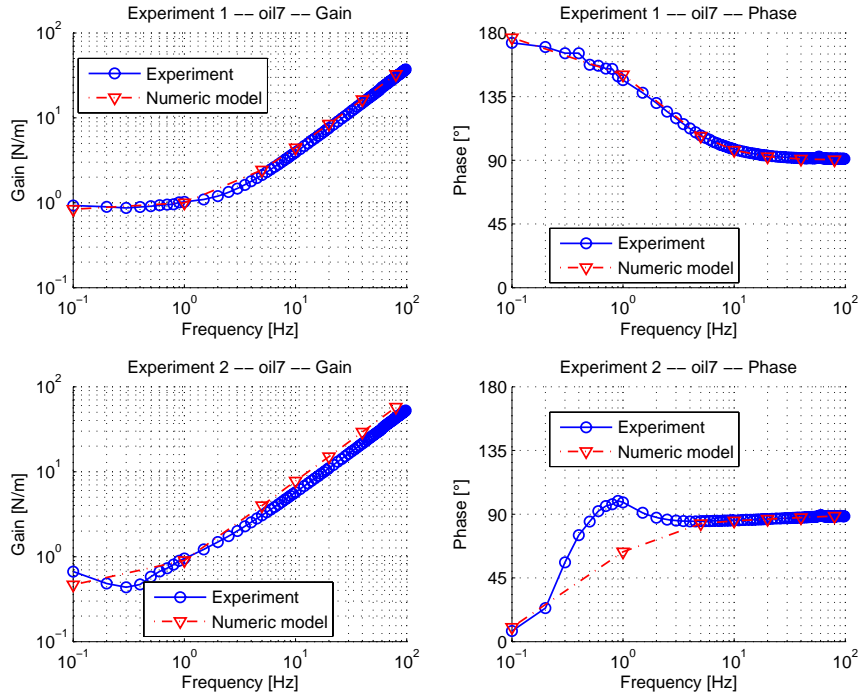
Exp	Liquid	Bot. radius (mm)	Top radius (mm)	Bot. angle (°)	Top angle (°)	Gap (mm)
1	Oil7	0.726	0.713	15.9	20.6	0.282
2	Oil7	0.750	0.736	29.5	35.7	0.231
3	Oil1	0.756	0.747	26.7	29.5	0.320
4	Oil1	0.754	0.746	26.5	37.9	0.279
5	Oil1	0.757	0.751	43.9	46.3	0.249
7	Oil6	0.749	0.747	33.9	35.0	0.159
8	Oil2	0.750	0.746	40.1	40.8	0.565
9	Oil2	0.752	0.749	58.5	59.5	0.483
10	Oil2	0.751	0.752	27.4	27.0	0.266
11	Oil8	0.743	0.750	29.4	27.1	0.296
12	Oil8	0.747	0.760	15.2	11.5	0.339

Table E.3: Parameters of the different experiments (properties of liquids are given page 226 in table E.4)

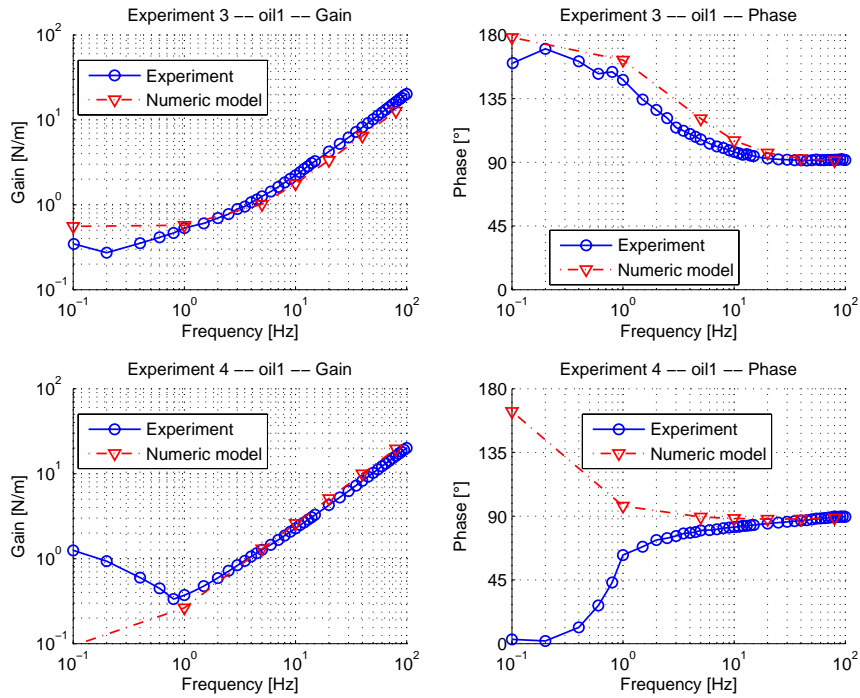
We can see in figures E.5-E.7 a fair concordance between experiments and numerical simulations. Disagreement mainly occur at low frequency (for example on experiments 4 and 7): indeed, in k -regime, the accuracy of the results highly depends on the accuracy of tracking the meniscus profile. Indeed, an error on the approximation of the contour of the liquid bridge has a much higher impact on the curvature and the contact angles, rather than on the

Liquid ID	ρ (kgm^{-3})	η (Pas)	γ (Nm^{-1})	Supplier
1	970	0.485	0.0211	Rhodorsil R47V500
2	973	4.865	0.0211	Rhodorsil R47V5000
6	960	0.096	0.0209	Dow Corning DC200FLUID100
7	971	0.971	0.0212	Dow Corning DC200FLUID1000
8	976	58.56	0.0215	Dow Corning DC200FLUID60000

Table E.4: Liquid properties

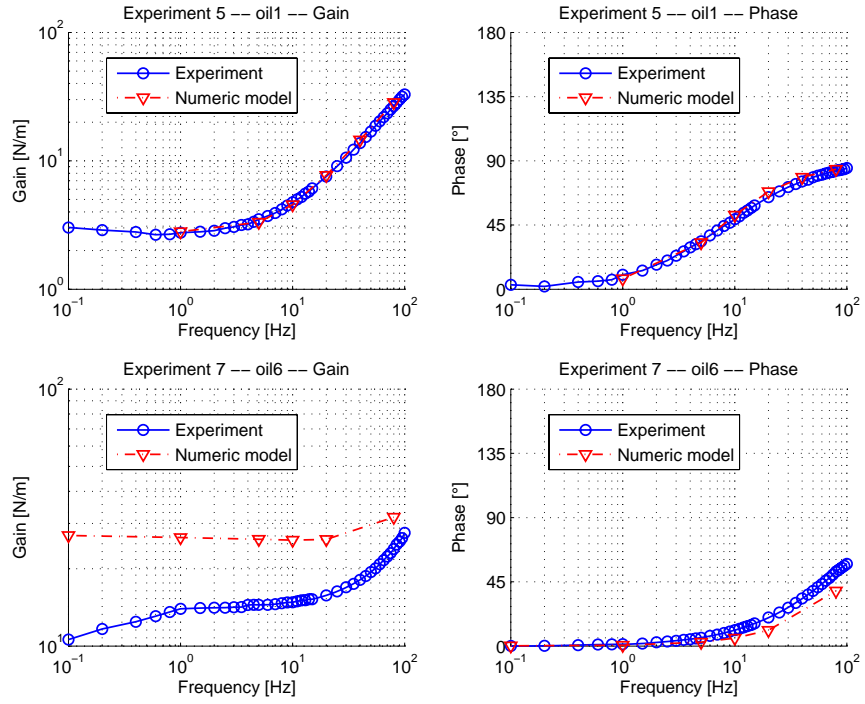


(a)

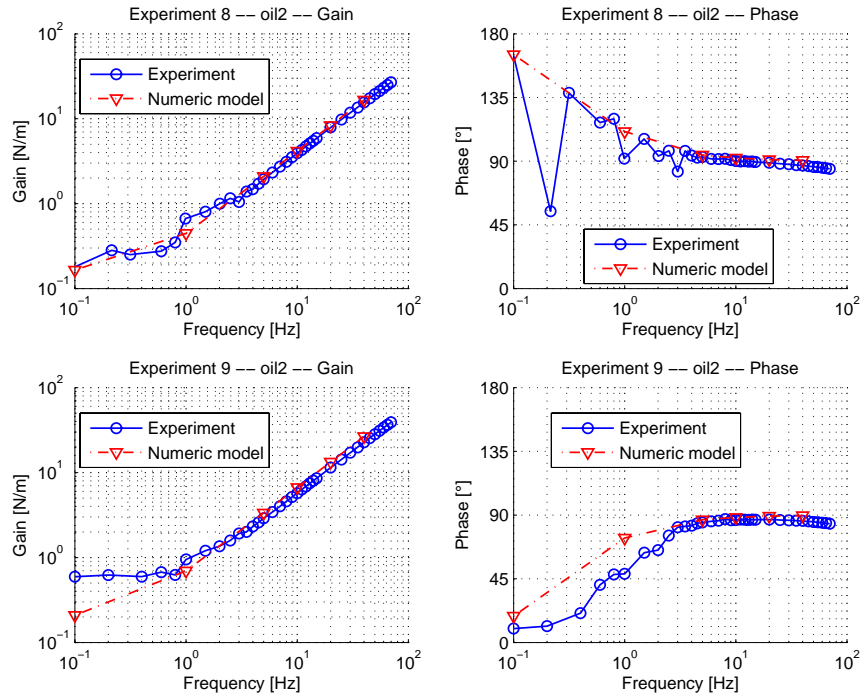


(b)

Figure E.5: Gain and phase curves for experiments 1, 2, 3 and 4



(a)



(b)

Figure E.6: Gain and phase curves for experiments 5, 7, 8 and 9

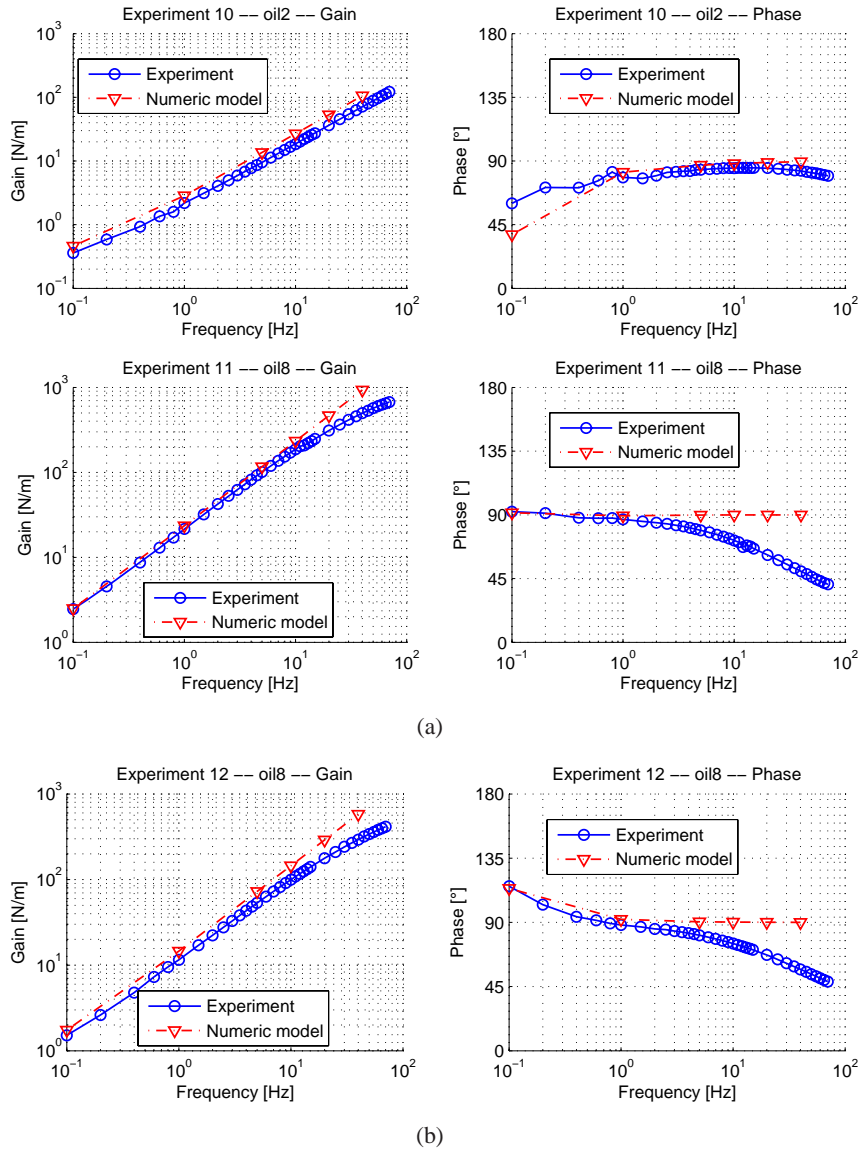


Figure E.7: Gain and phase curves for experiments 10, 11 and 12

Appendix F

Lateral dynamics

As indicated in the main text, the problem described by equations (4.48-4.49) is firstly normalized using characteristic length δ and time τ :

$$x = \delta \tilde{x} \quad (\text{F.1})$$

$$t = \tau \tilde{t} \quad (\text{F.2})$$

$$u = \frac{\delta}{\tau} \tilde{u} \quad (\text{F.3})$$

where δ is the initial position of the chip and $\tau = \sqrt{\frac{m}{k}}$ is a characteristic time of the chip dynamics. The y coordinate ranging from 0 to h is replaced by \tilde{y} ranging from -1 to 1 ($y = (1 + \tilde{y})\frac{h}{2}$). This leads to two non dimensional equations:

$$\ddot{\tilde{x}} = -\tilde{x} - \underbrace{\frac{\rho Sh}{2m}}_{\tilde{m}^{-1}} \underbrace{\frac{4\nu\tau}{h^2}}_{\alpha} \frac{\partial \tilde{u}}{\partial \tilde{y}} \Big|_{\tilde{y}=+1} \quad (\text{F.4})$$

$$\frac{\partial \tilde{u}}{\partial \tilde{t}} = \frac{4\nu\tau}{h^2} \frac{\partial^2 \tilde{u}}{\partial \tilde{y}^2} \quad (\text{F.5})$$

with the following boundary and initial conditions:

$$\tilde{u}(\tilde{y} = -1, \tilde{t}) = 0 \quad (\text{F.6})$$

$$\tilde{u}(\tilde{y} = +1, \tilde{t}) = \dot{\tilde{x}} \quad (\text{F.7})$$

$$\tilde{u}(\tilde{y}, \tilde{t} = 0) = 0 \quad (\text{F.8})$$

$$\tilde{x}(\tilde{t} = 0) = 1 \quad (\text{F.9})$$

$$\dot{\tilde{x}}(\tilde{t} = 0) = 0 \quad (\text{F.10})$$

It can be seen from both non dimensional equations that the problem only depends on two non dimensional parameters: (i) $\alpha = 4\nu\tau/h^2$ the diffusion coefficient and (ii) $\tilde{m} = 2m/(\rho Sh)$ the mass ratio.

In the following the symbol \sim has been dropped everywhere and the superscript ⁽ⁱ⁾ indicates the i th derivative with respect to y . With these conventions, the un-

known velocity field u can be written as a series of Chebyshev polynomials $T_k(y)$:

$$u(y,t) = \sum_{k=0}^N a_k(t) T_k(y) \quad (\text{F.11})$$

where the series has been found in our case to converge towards $u(y,t)$ as soon as the order N is equal to or larger than 11. Indeed, a convergence curve has been computed in figure F.1, showing the maximal relative error between the results obtained with a given N and the results obtained with $N = 25$, for several N and reduced viscosity α . As shown, the convergence is already obtained with $N = 4$ for large α . For smaller viscosities, the error becomes negligible as soon as $N > 11$.

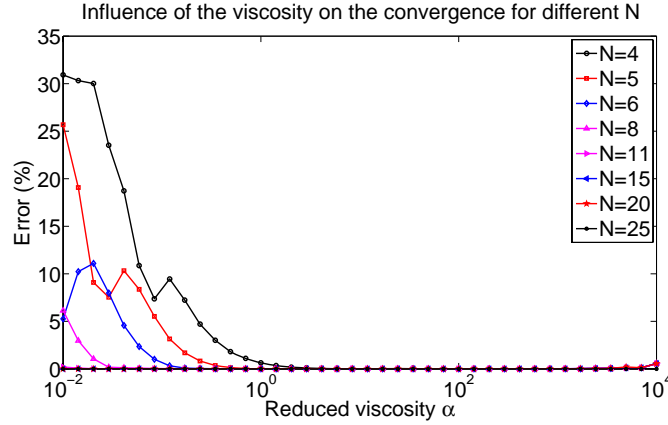


Figure F.1: Influence of the reduced viscosity α on the convergence curve, for different N

Chebyshev polynomials introduced in equation (F.11) are known to show interesting properties [14]:

$$u^{(1)} \equiv \frac{du}{dy} = \frac{d(\sum a_k(t) T_k(y))}{dy} = \sum a_k^{(1)} T_k(y) \quad (\text{F.12})$$

where it can be shown that the $a_k^{(1)}$ coefficients can be expressed as:

$$a_i^{(1)} = \sum D_{ik}^{(1)} a_k \quad (\text{F.13})$$

where the $D^{(1)}$ matrix is given by:

$$D_{ij}^{(1)} = \begin{cases} j & \text{if } i = 0 \text{ and } j = 1, 3, 5 \dots \\ 2j & \text{if } i = 1, 2, \dots, N-1 \text{ and } j = i+1, i+3, i+5 \dots \\ 0 & \text{in the other cases} \end{cases} \quad (\text{F.14})$$

It is also known that the second derivative of the u can be expressed on a similar way as:

$$u^{(2)}(x) = \sum_{k=0}^{N-2} a_k^{(2)} T_k(x) \quad (\text{F.15})$$

where the $a_k^{(2)}$ coefficients can be computed with:

$$a_k^{(2)} = \sum D_{ki}^{(2)} a_i \quad (\text{F.16})$$

where the matrix $D^{(2)} = D^{(1)}D^{(1)}$.

Consequently, the diffusion equation (F.5) leads to:

$$\dot{u} = \sum_{k=0}^N \dot{a}_k(t) T_k(y) \stackrel{(F.5)}{=} \alpha \sum a_k^{(2)} T_k \quad (\text{F.17})$$

whose identification leads to $k = 0..N - 2$ equations:

$$\dot{a}_k = \alpha \sum_{j=0}^N D_{kj}^{(2)} a_j \quad (\text{F.18})$$

The boundary condition (F.7) allows to write \dot{x} as a function of u :

$$\dot{x} = u(y = 1) = \sum_{k=0}^N a_k \underbrace{T_k(1)}_{\equiv 1} = \sum_{k=0}^N a_k \quad (\text{F.19})$$

which is now used to rewrite the Newton law (F.4) as:

$$\begin{aligned} \ddot{x} &\stackrel{(F.19)}{=} \sum_{k=0}^N \dot{a}_k \stackrel{(F.4)}{=} -x - \frac{\alpha}{\tilde{m}} u^{(1)}(y = 1) \\ &= -x - \frac{\alpha}{\tilde{m}} \sum_{k=0}^n a_k^{(1)} \underbrace{T_k(1)}_{\equiv 1} \\ &= -x - \frac{\alpha}{\tilde{m}} \sum_{k=0}^n \sum_{j=0}^n D_{kj}^{(1)} a_j \\ &= -x - \frac{\alpha}{\tilde{m}} \sum_{j=0}^n \left(\underbrace{\sum_{k=0}^n D_{kj}^{(1)}}_{\equiv f_j} \right) a_j \end{aligned} \quad (\text{F.20})$$

Finally, the boundary condition (F.6) can be expressed as:

$$u(y = -1) = 0 = \sum a_k T_k(-1) = \sum_{k=0}^N a_k (-1)^k \quad (\text{F.21})$$

and obviously $\dot{u}(y = -1)$ is also equal to zero, leading to:

$$\begin{aligned} \dot{u}(y = -1) &= 0 \\ &= \sum \dot{a}_k T_k(-1) \\ &= \sum \dot{a}_k (-1)^k + \underbrace{0}_{(F.21)} \\ &= \sum \dot{a}_k (-1)^k + \sum a_k (-1)^k \end{aligned} \quad (\text{F.22})$$

Table F.1: M matrix

1					0	0	0
	1				0	0	0
		..			0	0	0
			[Size = $N - 1 \times N - 1$]		0	0	0
				..	0	0	0
					0	0	0
				1	0	0	0
1	-1	..	$(-1)^j$	$(-1)^N$	0
1	1	..	1	1	0
0	0	..	0	0	1

Table F.2: A matrix

$\alpha D_{00}^{(2)}$	$\alpha D_{0(N-2)}^{(2)}$	$\alpha D_{0(N-1)}^{(2)}$	$\alpha D_{0N}^{(2)}$	0
$\alpha D_{10}^{(2)}$	0
..	0
..	$\alpha D_{ij}^{(2)}$	0
..	0
$\alpha D_{(N-2)0}^{(2)}$	$\alpha D_{(N-2)(N-2)}^{(2)}$	$\alpha D_{(N-2)(N-1)}^{(2)}$	$\alpha D_{(N-2)N}^{(2)}$	0
-1	1	..	$-(-1)^j$	$-(-1)^N$	0
..	$-\frac{\alpha}{\bar{m}} f_j$	-1
1	1	1	1	1	1	1	1	0

This latter condition is rather arbitrary, but it allows to write the algebraic condition of equation F.21 into a first order differential equation which adds an equation to the system described by equation (F.24). It can be shown that it adds an eigen value equal to -1 and an associated amplitude $w_j = 0$ as used in equation (F.26).

Posing the unknown vector X with $N + 2$ unknowns defined as:

$$X = (a_0 \ a_1 \ .. \ a_i \ .. \ a_N \ x)^T \quad (\text{F.23})$$

it can be shown that the $N - 1$ ($k = 0..N - 2$) equations (F.18), equation (F.19), equation (F.20) and equation (F.22) constitute a $N + 2$ differential equations system, which can be written as:

$$M\dot{X} = AX \quad (\text{F.24})$$

with the following initial condition:

$$X(t = 0) = X_0 = (\underbrace{0 \ .. \ 0}_{1 \times N+1} \ 1)^T \quad (\text{F.25})$$

M and A matrices are detailed in Tables F.1 and F.2. This constant coefficient system of ODEs (F.24) is easily solved analytically:

$$X_i = \sum_{j=1}^{N+2} r_{ij} w_j e^{\lambda_j t} \quad (\text{F.26})$$

where λ_j is the j th eigen value, r_{ij} the i th component of the j th eigenvector associated with λ_j and w_j the j th component of the vector \mathbf{w} given by $\mathbf{w} = V^{-1}X_0$, and V is the matrix whose columns are the eigenvectors r_j .

Appendix G

Surface tension transducer

G.1 Parabolic model of the meniscus

G.1.1 Equations

In this preliminary note, we focus only on a simplified model, based on the assumption that the meniscus profile $r(z)$ can be written as a parabola:

$$r(z) = a_0 + a_2 z^2 \quad (\text{G.1})$$

The equations of the model are:

1. a geometrical condition:

$$r = a_0 + \frac{a_2 h^2}{4} \quad (\text{G.2})$$

2. the expression of the curvature $2H$ [92]:

$$2H = -2a_2 + \frac{1}{a_0} \quad (\text{G.3})$$

3. the Laplace law:

$$dp = 2H\gamma \quad (\text{G.4})$$

4. the capillary force expression:

$$F = -2a_2 \gamma \pi a_0^2 - \pi \gamma a_0 \quad (\text{G.5})$$

5. the volume of liquid in the meniscus v_{cap} :

$$v_{\text{cap}} = \pi \int_{-h/2}^{h/2} r^2(z) dz = \pi \left(\frac{a_2^2 h^5}{80} + \frac{a_0 a_2 h^3}{6} + a_0^2 h \right) \quad (\text{G.6})$$

G.1.2 Numerical scheme

The problem is solved as follows, for a range of possible gaps h between $r/2$ and r (this range can be enlarged if necessary):

1. assuming a known value of h and using equation (G.5) to get a_2 , we can rewrite equation (G.2) into:

$$a_0^3(\pi\gamma) - a_0^2(8\pi\gamma h) - a_0(\pi\gamma h^2) - h^2 f = 0 \quad (\text{G.7})$$

2. after solving numerically the latter equation, we get a_0 , and subsequently a_2 with equation (G.2);
3. we can now compute the curvature $2H$ (equation (G.3)), the pressure difference dp (equation (G.4)) and the volume of the meniscus (equation (G.6))
4. using the control variable u and the piston section A , the total volume of gas is given by:

$$V = v_{\text{cap}} + uA \quad (\text{G.8})$$

5. the final step is to compute the indicator I and find the value of h for which $I = 1$:

$$I = \frac{(p + dp)(v_{\text{cap}} + uA)}{nRT} \quad (\text{G.9})$$

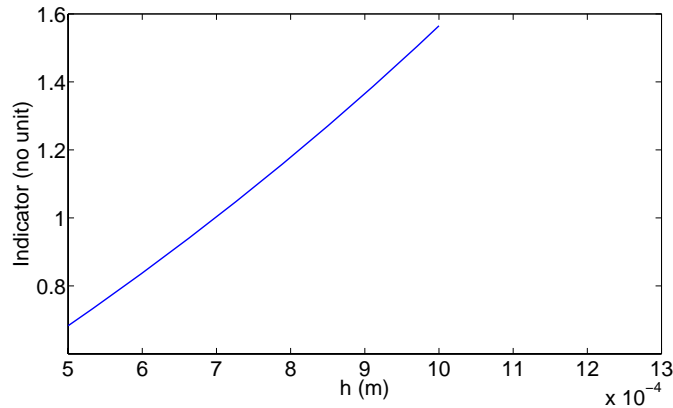


Figure G.1: Indicator as a function of h

The correct value of h is one of the output, and the output pressure difference dp is also known from this numerical scheme.

Appendix H

Symbols

Table H.1: Greek symbols

Symbol	Description	Units
α	Angular beam deflection	$^{\circ}$
β	Filling angle	$^{\circ}$
δ	Beam deflection	m
δ_e	Beam deflection at calibration	m
Δp	Pressure difference across the LV interface = $p_m - p_{out}$	Pa
ε	Misalignment	m, $^{\circ}$
ϕ	Residual adhesion ratio	—
γ	Surface tension of a liquid	Nm ⁻¹
	Energy of the interface Liquid-Vapor	Jm ⁻²
γ_{SL}	Energy of the interface Solid-Liquid	Jm ⁻²
γ_{SV}	Energy of the interface Solid-Vapor	Jm ⁻²
μ	Dynamic viscosity	Pas
ρ	Principal curvature radius of the meniscus (usually < 0)	m
ρ'	Principal curvature radius of the meniscus (usually > 0)	m
	Density	kgm ⁻³
Σ	Lateral area of the liquid bridge	m ²
θ	Contact angle	rad
θ_A	Advancing contact angle	rad
θ_R	Receding contact angle	rad
θ_1	Contact angle at the component side	rad
θ_2	Contact angle at the gripper side	rad

Table H.2: Latin symbols

Symbol	Description	Units
a	Acceleration	m s^{-2}
b	Beam width	m
B_o	Bond number	–
C	Capacity of the SL interface in electrowetting	F
C_a	Capillary number (non dimensional)	–
d	Characteristic size of the meniscus in non dimensional analysis	m
D	Diameter of a droplet posed on the substrate Gap in chapter??	m
$dpinc$	Pressure increment in θ_1 search	Pa
$dpstart$	Initial pressure difference in θ_1 search	Pa
E	Young modulus	GPa
	Differential operator to compute H	
F	Differential operator to compute H	
F_L	Laplace term of the capillary force	N
F_T	Interfacial tension term of the capillary force	N
g	Earth gravity	9.81ms^{-2}
G	Differential operator to compute H	
k	Stiffness of the cantilevered beam	Nm^{-1}
K	Interaction constant depending on materials (VDW)	Jm^6
h	Beam thickness	m
	Height of a droplet posed on the substrate	m
	Immersion height	m
	Capillary rise	m
H	Mean curvature	m^{-1}
I	Inertia moment of the beam section	m^4
L	Length of the cantilevered beam	m
	Differential operator to compute H	
L_C	Capillary length	m
m_0	Standardized mass(es) used for calibration	kg
M	Differential operator to compute H	
N	Differential operator to compute H	
p	Gripper parameter (radius or angular aperture)	m or $^\circ$
p_1, p_2	Permanent dipoles (VDW)	
p_{in}	Pressure in the liquid phase	Pa
p_{out}	Pressure in the vapor phase	Pa
r_1	Radius of the liquid bridge at the component side	m
r_2	Radius of the liquid bridge at the gripper side	m
r_{neck}	Radius of the liquid bridge at the neck height	m
R	Radius of a droplet posed on the substrate	m
	Radius of spherical grippers	m
	Molar gas constant (8.314)	$\text{JK}^{-1}\text{mol}^{-1}$
S	Area of a spherical cap	m^2
U	Total interfacial energy of the droplets (S-V, L-V, S-L)	J
U_{LV}	Partial interfacial energy of the droplets (L-V)	J
v	Molar volume	$\text{m}^3\text{mol}^{-1}$
V	Volume of liquid, usually between 0.1 and $1\mu\text{L}$	m^3

Table H.3: Latin symbols (Continued)

Symbol	Description	Units
W	Component weight	N
	Total interfacial energy of the meniscus (S-V, L-V, S-L)	J
W_{LV}	Partial interfacial energy of the meniscus (L-V)	J
z	Separation distance between the gripper and the object	m
z_A	Approaching contact distance before the droplet hung to the gripper contacts the object	m
z^*	Distance at which the meniscus breaks and is replaced by two droplets	m

Table H.4: Abbreviations

Abb.	Description
AFM	Atomic force microscope
BEAMS	Bio-, Electro- And Mechanical Systems
CSEM	Swiss Centre for Electronics and Microtechnology
DIN	German norms
DMT	Derjagin–Muller–Toporov
EAP	Electro-active polymer
EDM	Electro-discharge machining
FSRM	Fondation Suisse pour la Recherche en Microtechnique
ISIR	Institut des Systèmes Intelligents et Robotiques
JKR	Johnson–Kendall–Roberts model
LAB	Automation Laboratory of Besançon
LIGA	Lithographie-Galvanoformung-Abformung
LPM	Microtechnology Production Laboratory (EPFL)
LRP	Robotics laboratory of Paris (Paris VI)
MEL	Mechanical Engineering Laboratory
MEMS	Micro Electro Mechanical System
MOC	Microrobot on chip
RH	Relative humidity
SEM	Scanning electron microscope
SFA	Surface force apparatus
SMA	Shape Memory Alloy
SMD	Surface mount device
VDW	van der Waals

Bibliography

- [1] Arthur W. Adamson and Alice P. Gast. *Physical Chemistry of Surfaces*. John Wiley and Sons, 6th edition, 1997.
- [2] Joël Agnus, Nicolas Chaillet, Pierre Lambert, and Stéphane Régnier. *La microrobotique: applications à la micromanipulation*. Hermès Science (Lavoisier), 2008.
- [3] Sébastien Alvo, Pierre Lambert, Michaël Gauthier, and Stéphane Régnier. A van der waals force based adhesion model for micromanipulation. *J. Adhes. Sci. Technol.*, Accepted, 2009.
- [4] A.L. Barabási, R. Albert, and P. Schiffer. The physics of sand castles: maximum angle of stability in wet and dry granular media. *Physica A*, 266(1-4):366–371, 1999.
- [5] C. Bark and T. Binnenboese. Gripping with low viscosity fluids. In *Proc. of IEEE Int. Workshop on MEMS*, pages 301–305, Heidelberg, 1998.
- [6] K.-B. Bark. *Adhäsives Greifen von kleinen Teilen mittels niedrigviskoser Flüssigkeiten*. Springer, 1999.
- [7] Nicolas Bastin, Alexandre Chau, Alain Delchambre, and Pierre Lambert. Effects of relative humidity on capillary force and applicability of these effects in micromanipulation. In *a Poster at the Proc. of the IEEE/RSJ 2008 International Conference on Intelligent Robots and Systems*, Nice, September 22-26 2008.
- [8] Bharat Bhushan. *Modern Tribology Handbook, Two Volume Set*. CRC Press, December 2000.
- [9] Fabio Biganzoli, Irene Fassi, and Claudia Pagano. Development of a gripping system based on capillary force. In *Proceedings of ISATP05*, pages 36–40, Montreal, Canada, 19-21 July 2005.
- [10] Karl F. Bohringer. Heterogeneous system integration by self-assembly. Hybrid and Self-Assembly Workshop, Brussels, March 12th 2009, March 12th 2009.

- [11] M. Boukallel, M. Girot, and S. Régnier. Characterization of cellular mechanical behavior at the microscale level by a hybrid force sensing device. *Journal of the mechanical behavior of biomedical materials*, 2:297–304, 2009.
- [12] Fabien Bourgeois. *Vers la maîtrise de la qualité des assemblages de précision*. PhD thesis, Ecole Polytechnique Fédérale de Lausanne, 2007.
- [13] George E.P. Box, J. Stuart Hunter, and William G. Hunter. *Statistics for experimenters (Design, innovation and discovery)*. New Jersey and Canada, 2005.
- [14] John P. Boyd. *Chebyshev and Fourier Spectral Methods*. Dover Publications, Inc, 31 East 2nd Street Mineola, New-York 11501, 2001.
- [15] M. Bracke, F. De Voeght, and P. Joos. *The kinetics of wetting: the dynamic contact angle*, volume 79.
- [16] Ken Brakke. The surface evolver. *Exp. Math.*, 1(2):141–65, 1992.
- [17] J. M. Breguet, S. Henein, R. Mericio, and R. Clavel. Monolithic piezoceramic flexible structures for micromanipulation. In *Proc. 9th Int. Precision Engineering Seminar; 4th Int. Conf on Ultraprecision in Manufacturing Engineering*, volume 2, pages 397–400, Braunschweig, Germany, 1997.
- [18] J.M. Breguet. *Actionneurs Stick-Slip pour micro-manipulateurs*. PhD thesis, EPFL, 1998.
- [19] N. Bremond, A. R. Thiam, and J. Bibette. Decompressing emulsion droplets favors coalescence. *Phys. Rev. Lett.*, 100:024501, 2008.
- [20] Henrik Bruus. *Theoretical Microfluidics*. Oxford University Press, 2008.
- [21] B. Capella and G. Dietler. Force-distance curves by atomic force microscopy. *Surf. Sci. Rep.*, 34:1–104, 1999.
- [22] Alexandre Chau. *Theoretical and experimental study of capillary condensation and of its possible use in micro-assembly - Etude théorique et expérimentale des forces dues à la condensation capillaire*. PhD thesis, Université libre de Bruxelles, 2007.
- [23] Alexandre Chau, Alain Delchambre, Stéphane Régnier, and Pierre Lambert. Towards a general three dimensional model for capillary nanobridges and capillary forces. In *Proc. of the 5th International Workshop on Microfactories (IWMF)*, Besançon, France, October 2006.
- [24] Alexandre Chau, Pierre Lambert, Philippe Bouillard, and Alain Delchambre. Behaviour of flexure hinges for use as articulations in high precision

- mechanisms. In *MicroNano Integration*, pages 287–288, Potsdam, Germany, December 2003. Springer.
- [25] Alexandre Chau, Pierre Lambert, and Alain Delchambre. A general 3d model to compute capillary force. In *Proc. Of MicroMechanics Europe 2005*, pages 156–9, Göteborg, Sweden, 4-6 september 2005.
- [26] Alexandre Chau, Pierre Lambert, and Alain Delchambre. Modélisation de la condensation capillaire pour le micro-assemblage. In *Actes de la première journée sur la modélisation et l'analyse dimensionnelle*, Lausanne, Suisse, 2005. EPFL.
- [27] Alexandre Chau, Stéphane Régnier, Alain Delchambre, and Pierre Lambert. Influence of geometrical parameters on capillary forces. In *Proceedings of IEEE International Symposium on Assembly and Manufacturing*, pages 215–220, 2007.
- [28] Alexandre Chau, Stéphane Régnier, Alain Delchambre, and Pierre Lambert. Three dimensional model for capillary nanobridges an capillary forces. *Model. Simul. Mater. Sci. Eng.*, 15:305–317, 2007.
- [29] Alexandre Chau, Stéphane Régnier, Alain Delchambre, and Pierre Lambert. Theoretical and experimental study of the influence of afm tip geometry and orientation on capillary force. *J. Adhes. Sci. Technol.*, Accepted, 2009.
- [30] H. Chen, Y. Zhao, Y. Song, and L. Jiang. One-step multicomponent encapsulation by compound-fluidic electro spray. *J. Am. Chem. Soc.*, 130:7800–7801, 2008.
- [31] HongYan Chen, Yong Zhao, and Lei Jiang. Compound-fluidic electro spray: An efficient method for the fabrication of microcapsules with multicompartement structure. *Chinese Sci Bull*, 54:3147–3153, 2009.
- [32] Xucui Chen and Robert E. Apfel. Radiation force on a spherical object in an axisymmetric wave field and its application to the calibration of high-frequency transducers. *J. Acoust. Soc. Am.*, 99(2):713–724, 1996.
- [33] David Cheneler, Michael C.L. Ward, Michael J. Adams, and Zhibing Zhang. Measurement of dynamic properties of small volumes of fluid using mems. *Sensors and Actuators B*, 130(2):701–706, 2008.
- [34] S.K. Cho and CJ Kim. Particle separation and concentration control for digital microfluidics systems, 2003.
- [35] Chang-Hwan Choi, K. Johan A. Westin, and Kenneth S. Breuer. Apparent slip flows in hydrophilic and hydrophobic microchannels. *Phys. Fluids*, 15(10):2897–2902, 2003.

- [36] Han-Sheng Chuang, Alope Kumar, and Steven T. Wereley. Open optoelectrowetting droplet actuation. *Appl. Phys. Lett.*, 93:064104, 2006.
- [37] S.E. Chung, W. Park, S. Shin, S.A. Lee, and S. Kwon. Guided and fluidic self-assembly of microstructures using railed microfluidic channels. *Nature Materials*, 7:581, 2008.
- [38] M Cloupeau. Recipes for use of ehd spraying in cone-jet mode and notes on corona discharge effects. *J. Aerosol Sci.*, 25:1143–1157, 1993.
- [39] M. Cloupeau and B. Prunet-Foch. Electrostatic spraying of liquids in cone-jet mode. *J. Electrostat.*, 22:135–159, 1989.
- [40] Cécile Cottin-Bizonne, Jean-Louis Barrat, Lydéric Bocquet, and Elisabeth Charlaix. Low-friction flows of liquid at nanopatterned interfaces. *Nature Materials*, 2(4):237–240, April 2003.
- [41] R. G. Cox. Inertial and viscous effects on dynamic contact angles. *J. Fluid Mech.*, 357:249–278, 1998.
- [42] Pierre-Gilles de Gennes, Françoise Brochart-Wyart, and David Quéré. *Gouttes, bulles, perles et ondes*. Belin, 2002.
- [43] J. Fernandez de la Mora. On the outcome of the coulombic fission of a charged isolated drop. *J. Colloid Interface Sci.*, 78:209–218, 1996.
- [44] Juan Fernandez de la Mora. The fluid dynamics of taylor cones. *Annu. Rev. Fluid Mech.*, 39:217–243, 2007.
- [45] Pierre-Simon de Laplace. Sur l’action capillaire. In *Mécanique Céleste - Supplément au Livre X*, pages 349–498. Courcier, Paris, 1805.
- [46] A. de Lazzer, M. Dreyer, and H. J. Rath. Particle-surface capillary forces. *Langmuir*, 15(13):4551–9, 1999.
- [47] W. Deng, J. K. Klemic, X. Li, M. A. Reed, and A. Gomez. Increase of electro-spray throughput using multiplexed microfabricated sources for the scalable generation of monodisperse droplets. *J. Aerosol Sci.*, 37:696–714, 2005.
- [48] W. Deng, J.F. Klemic, X. Li, M.A. Reed, and A. Gomez. Liquid fuel micro-combustor using microfabricated multiplexed electro-spray sources. In *Proceedings of the Combustion Institute*, volume 31, pages 2239–2246, 2007.
- [49] W. Driesen, T. Varibel, S. Régnier, and J-M. Breguet. Micro manipulation by adhesion with tow collaborating mobile micro robots. Microfactory, 4th International Workshop on Microfactories, October 15-17, 2004, Shanghai, China., 2004.

- [50] M.-H. Duby, W. Deng, K. Kim, T. Gomez, and A. Gomez. Stabilization of monodisperse electrosprays in the multi-jet mode via electric field enhancement. *J. Aerosol Sci.*, 37(5):306–322, 2006.
- [51] H.E. Edgerton, E.A. Hauser, and W.B. Tucker. Studies in drop formation as revealed by the high-speed motion camera. *J. Phys. Chem.*, 41:1017–1028, 1937.
- [52] T. F. W. Embleton. Mean force on a sphere in a spherical sound field II (experimental). *J. Acoust. Soc. Am.*, 26(1):46–50, 1954.
- [53] Jan Engmann, Colin Servais, and Adam S. Burbidge. Squeeze flow theory and applications to rheometry: A review. *J. Non-Newtonian Fluid Mech.*, 132(1-3):1–27, 2005.
- [54] Jérôme Charmet et Al. Liquid as template for next generation micro devices. *Journal of physics: Conference Series*, 182:012021, 2009.
- [55] Jérôme Charmet et Al. Solid on liquid deposition. *TSF*, 2010.
- [56] Dipankar Chugh et Karan V. I. S. Kaler. Integrated liquid and droplet dielectrophoresis for biochemical assays. *Microfluid Nanofluid*, 8(4), 2010.
- [57] C.W. Extrand. Model for contact angles and hysteresis on rough and ultraphobic surfaces. *Langmuir*, 18:7991–7999, 2002.
- [58] R. S. Fearing. Survey of sticking effects for micro parts handling. In *Proc. of IEEE/RSJ Conf. on Intelligent Robots and Systems*, pages 212–217, 5-9 August 1995.
- [59] Luis M. Fidalgo, Chris Abell, and Wilhelm T. S. Huck. Surface-induced droplet fusion in microfluidic devices. *LAB CHIP*, 7:984–986, 2007.
- [60] L. R. Fisher and J. N. Israelachvili. Direct measurement of the effect of meniscus forces on adhesion: A study of the applicability of macroscopic thermodynamics to microscopic liquid interfaces. *Colloids Surf.*, 3:303–19, 1981.
- [61] Maxime Frennet, Pierre Lambert, and Alain Delchambre. Catching and releasing of small parts using capillary forces. In *Proceedings of the Mechatronics and Robotics 2004 Conference (6 pages)*, Aachen, Germany, 2004.
- [62] T. Funakawa. New electron injection technique for generating electro spray. *Science Link Japan*, 13:185–190, 2004.
- [63] T. Gilet, D. Terwagne, and N. Vandewalle. Digital microfluidics on a wire. *Appl. Phys. Lett.*, 95:014106, 2009.

- [64] A. Gomez. The electrospray and its application to targeted drug inhalation. *Respiratory Care*, 47(12):1419–1431, 2002.
- [65] Aline De Greef, Pierre Lambert, and Alain Delchambre. A minimally invasive surgery actuator based on a flexible and inflatable structure. In *Proceedings of the First Annual symposium of the IEEE/EMBS Benelux Chapter, 7-8 December 2006, Brussels, Belgium, 7-8 December 2006*.
- [66] Aline De Greef, Pierre Lambert, and Alain Delchambre. Flexible fluidic actuators: Determining force and position without force or position sensors. In *Proceedings of the IEEE ISAM2009 conference (Suwon, Korea - 17-20 November 2009)*, page 6, 2009.
- [67] Aline De Greef, Pierre Lambert, and Alain Delchambre. Towards flexible medical instruments: Review of flexible fluidic actuators. *Precis. Eng.*, 33:311–321, October 2009.
- [68] H. Grutzeck and L. Kiesewetter. Downscaling of grippers for micro assembly. *Microsyst. Technol.*, 8:27–31, 2002.
- [69] D. Sinan Haliyo. *Les forces d'adhésion et les effets dynamiques pour la micro-manipulation*. PhD thesis, Université Pierre et Marie Curie, 2002.
- [70] Takahi Hasegawa. Acoustic radiation force on a sphere in a quasistationary wave field - experiment. *J. Acoust. Soc. Am.*, 65(1):41–44, 1979.
- [71] Simon Henein. *Conception des guidages flexibles*. Presses Polytechniques et universitaires romandes, 2001.
- [72] J. Höppner. *Verfahren zur berührungslosen Handhabung mittels leistungsstarker Schallwandler*. PhD thesis, Technische Universität München, 2002.
- [73] Lung-Hsin Hung, Kyung M. Choi, Wei-Yu Tseng, Yung-Chieh Tan, Kenneth J. Shea, and Abraham Phillip Lee. Alternating droplet generation and controlled dynamic droplet fusion in in microfluidic device for cds nanoparticle synthesis. *LAB CHIP*, 6:174–178, 2006.
- [74] J. N. Israelachvili. *Intermolecular and Surface Forces*. Academic Press, 2nd edition, 1992.
- [75] J. N. Israelachvili, Y Min, M. Akbulut, A. Alig, G. Carver, W. Greene, K. Kristiansen, E. Meyer, N. Pesika, K. Rosenberg, and H. Zeng. Recent advances in the surface forces apparatus (sfa) technique. *Rep. Prog. Phys.*, 73:036601, 2010.
- [76] Joonkyung Jang, M. A. Ratner, and George C. Schatz. Atomic-scale roughness effect on capillary force in atomic force microscopy. *J. Phys. Chem. B*, 110:659–62, 2005.

- [77] Tsung-Shann Jiang, O. H. Soo-Gun, and John C. Slattery. Correlation for dynamic contact angle. *J. Colloid Interface Sci.*, 69(1):74–77, 1979.
- [78] K.L. Johnson. *Contact Mechanics*. Cambridge University Press, London, 1985.
- [79] TB Jones. Microfluidic schemes using electrical and capillary forces. *Electrostatics*, 142:012054, 2008.
- [80] James Jurin. An account of some experiments shown before the royal society: With an enquiry into the cause of ascent and suspension of water in capillary tubes. *Phil. Trans. Roy. Soc.*, 30:739–747, 1718.
- [81] Serafim Kalliadasis and Hsueh-Chia Chang. Apparent dynamic contact angle of an advancing gas-liquid meniscus. *Phys. Fluids*, 6(1):12–23, 1994.
- [82] M. Kaneda, M. Yamamoto, K. Nakaso, T. Yamamoto, and J. Fukai. Oscillation of a tilted circular pad on a droplet for the self-alignment process. *Precis. Eng.*, 31:177–184, 2007.
- [83] J.M. Kim, Y.E. Shin, and K. Fujimoto. Dynamic modeling for resin self-alignment mechanism. *Microelectronics reliability*, 44:983–992, 2004.
- [84] K. Kim and J.-B. Lee. High aspect ratio tapered hollow metallic microneedles arrays with microfluidic interconnector. *Microsyst. Technol.*, 13:231–235, 2007.
- [85] Mika M. Kohonen and Hugo K. Christenson. Capillary condensation of water between rinsed mica surfaces. *Langmuir*, 16:7285–8, 2000.
- [86] T. Kondo, S. Juodkazis, and H. Misawa. Reduction of capillary force for high-aspect ratio nanofabrication. *Appl. Phys. A*, 81(8):1583–1586, 2005.
- [87] S. Konishi, F. Kawai, and P. Cusin. Thin flexible end-effector using pneumatic balloon actuator. *Sensors and Actuators A*, 89:28–35, 2001.
- [88] D.C. Kyritsis. Optimization of a catalytic combustor using electrosprayed liquid hydrocarbons for mesoscale power generation. *Combust. Flame*, 139:77–89, 2004.
- [89] Pierre Lambert. DEA : Simulation dynamique d’une tâche de micromanipulation utilisant les forces de surface. Master’s thesis, Université libre de Bruxelles, Brussels, Belgium, 2003.
- [90] Pierre Lambert. Mécanique appliquée. Presses Universitaires de Bruxelles, 2003.
- [91] Pierre Lambert. *A Contribution to Microassembly: a Study of Capillary Forces as a gripping Principle*. PhD thesis, Université libre de Bruxelles, Belgium, 2004.

- [92] Pierre Lambert. *Capillary Forces in Microassembly: Modeling, Simulation, Experiments, and Case Study*. Microtechnology and MEMS. Springer, October 2007.
- [93] Pierre Lambert. Fluidic assembly and capillary forces: modeling, experiments and case studies. In *Proc. of the Smart Systems Integration Conference*, Brussels, March 2009.
- [94] Pierre Lambert, Nicolas Chaillet, and Stéphane Régnier. Microassembly: application to liquid environment. In *Workshop on microrobotics held during the Robotics: Science and Systems (2 pages)*, Philadelphia, USA, 16-19 August 2006.
- [95] Pierre Lambert, Ludovic Charvier, Lucas Raggi, and Jacques Jacot. Etude des antichocs. Technical report, Ecole Polytechnique Fédérale de Lausanne, 2008.
- [96] Pierre Lambert, Alexandre Chau, Alain Delchambre, and Stéphane Régnier. Comparison between two capillary forces models. *Langmuir*, 24(7):3157, 2008.
- [97] Pierre Lambert and Alain Delchambre. Forces acting on microparts: towards a numerical approach for gripper design and manipulation strategies in micro-assembly. In Svetan Ratchev and Alain Delchambre, editors, *Proc. of the 1st Int. Precision Assembly Seminar (IPAS)*, pages 79–84, Bad Hofgastein, Austria, 2003.
- [98] Pierre Lambert and Alain Delchambre. Capillary forces: Use and modelling in micro-assembly. In *Proceedings of the International Conference on Intelligent Manipulation and Grasping, Genoa, Italy, July 1-2 2004*, pages 29–30, 2004.
- [99] Pierre Lambert and Alain Delchambre. Design rules for a capillary gripper in microassembly. In *Proceedings of the 6th IEEE ISATP'05*, pages 67–73, Montreal, Canada, 19-21 July 2005.
- [100] Pierre Lambert and Alain Delchambre. Parameters ruling capillary forces at the submillimetric scale. *Langmuir*, 21:9537–9543, 2005.
- [101] Pierre Lambert and Alain Delchambre. A study of capillary forces as a gripping principle. *Assembly Automation*, 25(4):275–283, 2005.
- [102] Pierre Lambert and Jacques Jacot. Introduction à l'analyse dimensionnelle. In *Actes de la première journée sur la modélisation et l'analyse dimensionnelle*, pages 1–9. EPFL, June 15th 2005.
- [103] Pierre Lambert, Benoit Lagrange, Arianna Valentini, Pierre G. De Lit, Consuelo Marsico, and Alain Delchambre. Design and performances of a

- piezoelectric stick-slip nanoactuator. In *Proceedings of the 12th International Conference on Flexible Automation and Intelligent Manufacturing (FAIM2002)*, pages 582–591, Dresden, Germany, July 15-17 2002. Oldenburg Verlag.
- [104] Pierre Lambert, Pierre Letier, and Alain Delchambre. Capillary and surface tension forces in the manipulation of small parts. In *Proc. of Int. Symposium on Assembly and Tasks Planning (ISATP)*, pages 54–59, 2003.
- [105] Pierre Lambert, Marion Sausse Lhernould, Alexandre Chau, Vincent Vandaele, Jean-Baptiste Valsamis, and Alain Delchambre. Surface forces modelling: Application to microassembly. In *Proc. of IARP*, Paris, 23-24 October 2006.
- [106] Pierre Lambert, Massimo Mastrangeli, Jean-Baptiste Valsamis, and G. Degrez. Spectral analysis and experimental study of lateral capillary dynamics (for flip-chip applications). *Microfluid Nanofluid*, Published online, 2010.
- [107] Pierre Lambert and Stéphane Régnier. Surface and contact forces models within the framework of microassembly. *Journal of Micromechatronics*, 3(2):123–157, 2006.
- [108] Pierre Lambert, Frank Seigneur, Sandra Koelemeijer, and Jacques Jacot. A case study of surface tension gripping: the watch bearing. *J. Micromech. Microeng.*, 16(7):1267–1276, 2006.
- [109] Pierre Lambert, Frank Seigneur, Sandra Koelemeijer, and Jacques Jacot. Design of a capillary gripper for a submillimetric application. In Svetan Ratchev, editor, *Precision Assembly Technologies for Mini and Micro Products*, pages 3–10, Bad Hofgastein, February 19-22 2006. Springer.
- [110] Pierre Lambert, Frank Seigneur, Sandra Koelemeijer, Jacques Jacot, and Alain Delchambre. Use of surface tension in micromanipulation. In *Proc. of the 7th NCTAM Congres (8 pages)*, Mons (Belgium), 29-30 May 2006.
- [111] Pierre Lambert, Arianna Valentini, Benoit Lagrange, Pierre G. De Lit, and Alain Delchambre. Design and performances of a one-degree-of-freedom guided nano-actuator. *RCIM*, 19(1):89–98, 2003.
- [112] Pierre Lambert, Jean-Baptiste Valsamis, Frank Seigneur, Sandra Koelemeijer, Alain Delchambre, and Jacques Jacot. Surface tension gripping applied to mesoscopic case study. In *Proc. of the 1st CIRP - International Seminar on Assembly Systems*, pages 153–158, Stuttgart, Germany, 15-17 November 2006.
- [113] Pierre Lambert, Vincent Vandaele, and Alain Delchambre. Non-contact handling in micro-assembly: State of the art. In Svetan Ratchev and Alain

- Delchambre, editors, *Proc. of Int. Precision Assembly Seminar (IPAS)*, pages 67–76, Bad Hofgastein, Austria, 12-13 February 2004.
- [114] O. Lastow and W. Balachandran. Novel low voltage ehd spray nozzle for atomization of water in the cone jet mode. *J. Electrostat.*, 65:490–499, 2007.
- [115] Cyrille Lenders. DEA: Study of valves used in microfluidics. Master’s thesis, Université libre de Bruxelles, Brussels, Belgium, 2006.
- [116] Cyrille Lenders. *Temporary title: Fluid-Structure Interaction in Micromechanics*. PhD thesis, Université libre de Bruxelles, 2010.
- [117] Cyrille Lenders, Michaël Gauthier, and Pierre Lambert. Microbubble generation using a syringe pump. In *Proceedings of the 2009 IEEE International Conference on Intelligent Robots and Systems*, Saint-Louis (Missouri), October 11-15 2009.
- [118] Cyrille Lenders, Jean-Baptiste Valsamis, Maxime Desaedeleer, Alain Delchambre, and Pierre Lambert. Assembly of a micro ball-bearing using a capillary gripper and a microcomponent feeder. In *Micro-Assembly Technologies and Applications*. International Precision Assembly Seminar (IPAS), Springer, 2008.
- [119] David Lengacher. Capteur de forces pour antichoc horloger. Master’s thesis, Ecole Polytechnique Fédérale de Lausanne, 2008.
- [120] E. Leung, N. Jacobi, and T. Wang. Acoustic radiation force on a rigid sphere in a resonance chamber. *J. Acoust. Soc. Am.*, 70(6):1762–1767, 1981.
- [121] Marion Sausse Lhernould. *Theoretical and experimental study of electrostatic forces applied to micromanipulation: influence of surface topography*. PhD thesis, Université libre de Bruxelles, 2008.
- [122] Marion Sausse Lhernould, Peter Berke, Thierry J. Massart, Stéphane Régnier, and Pierre Lambert. Variation of the adhesive electrostatic forces on a rough surface due to the deformation of roughness asperities during micromanipulation of a spherical rigid body. *J. Adhes. Sci. Technol.*, 23(9):1303–1325, 2009.
- [123] Marion Sausse Lhernould, Alain Delchambre, Stéphane Régnier, and Pierre Lambert. Displacement of an object placed in an electric field: application to micro-assembly. In *Proceedings of the EUSPEN 7th International Conference, Bremen, Germany*, 2007.
- [124] Marion Sausse Lhernould, Alain Delchambre, Stéphane Régnier, and Pierre Lambert. Electrostatic forces and micromanipulator design: on the importance of surface topography parameters. In *Proceeding of the 2007 IEEE/ASME International Conference on Advanced Intelligent Mechatronics*, 2007.

- [125] Marion Sausse Lhernould, Alain Delchambre, Stéphane Régnier, and Pierre Lambert. Electrostatic forces in micromanipulations: Review of analytical models and simulations including roughness. *Appl. Surf. Sci.*, 253:6203–6210, 2007.
- [126] Marion Sausse Lhernould, Pierre Lambert, and Alain Delchambre. Modelling of electrostatic forces for microassembly. In *Actes de la première journée sur la modélisation et l'analyse dimensionnelle (6 pages)*. EPFL, 2005.
- [127] Marion Sausse Lhernould, Pierre Lambert, Alain Delchambre, and Stéphane Régnier. Influence of surface topography in electrostatic forces simulations for microassembly. In *Proc. of the 5th International Workshop on Microfactories, Besançon, France*, 2006.
- [128] Marion Sausse Lhernould, Michel Pierobon, and Pierre Lambert. Determination of ehd generated droplet size: Review of models and experimental tools. In *Proceedings of the European Aerosol Conference, Karlsruhe*, 2009.
- [129] Cheng Lin, Fangang Tsen, Heng CHuan Kan, and CHing-Chang CHIeng. Numerical studies on micropart self-alignment using surface tension forces. *Microfluid Nanofluid*, 2008.
- [130] Wei Lin, Susan K. Patra, and Y. C. Lee. Design of solder joints for self-aligned optoelectronic assemblies. *IEEE Transactions on Advanced Packaging*, 18(3):543–551, 1995.
- [131] I. G. Loscertales. Micro/nano encapsulation via electrified coaxial liquid jets. *Science*, 295:1695, 2002.
- [132] H. Lu and C. Bailey. Dynamic analysis of flip-chip self alignment. *IEEE Transactions on Advanced Packaging*, 28(3):475–480, 2005.
- [133] M. Mastrangeli, W. Ruythooren, C. Van Hoof, and J.-P. Celis. Conformal dip-coating of patterned surfaces for capillary die-to-substrate self-assembly. *Journal of Micromechanics and Microengineering*, 19(4):12, April 2009.
- [134] Massimo Mastrangeli, Jean-Baptiste Valsamis, C Van Hoof, J.-P. Celis, and Pierre Lambert. Lateral capillary forces of cylindrical fluid menisci: an experimental, analytical and numerical study. *J. Micromech. Microeng.*, ? :Accepted, 2010.
- [135] C. H. Mastrangelo. Mechanical stability and adhesion of microstructures under capillary forces - part i: Basic theory. *J. Microelectromechanical Syst.*, 2(1):33–43, 1993.

- [136] Linas Mazutis, Ali Fallah Araghi, Oliver J. Miller, Jean-Christophe Baret, Lucas Frenz, Agnes Janoshazi, Valérie Taly, Benjamin J. Miller, J. Brian Hutchison, Darren Link, Andrew D. Griffiths, and Michael Ryckelynck. Droplet-based microfluidic systems for high-throughput single dna molecule isothermal amplification and analysis. *Anal. Chem.*, 81:4813–4821, 2009.
- [137] Marie-Hélène Meurisse and Michel Querry. Squeeze effects in a flat liquid bridge between parallel solid surfaces. *J. Tribology*, 128(3):575–584, 2006.
- [138] M.Kumemura, D. Collard, and H. Fujita. Droplet formation and fusion for enzyme activity measurement by liquid dielectrophoresis. In *Proc. of Solid State Sensors, Actuators and Microsystems Conference*, pages 813–816, 21–25 June 2009.
- [139] Ilju Moon and Joonwon Kim. Using ewod (electrowetting-on-dielectric) actuation in a micro conveyor system. *Sensors and Actuators A*, 130:537–544, 2006.
- [140] F. Mugele and J.C. Baret. Electrowetting: from basics to applications. *J. Phys.: Condens. Matter*, 17:R705–75, 2005.
- [141] K. Naessens. *Eximer laser ablation of microstructures in polymers for photonic applications*. PhD thesis, Universiteit Gent, 2004.
- [142] D.M. Newitt and Conway-Jones. A contribution to the theory and practice of granulation. *Trans. Inst. Chem. Engrs.*, 36(422-442), 1958.
- [143] S. Nowak, A. Samadani, and A. Kudrolli. Maximum angle of stability of a wet granular pile. *Nature Physics*, 1:50–52, 2005.
- [144] F. M. Orr, L. E. Scriven, and A. P. Rivas. Pendular rings between solids: meniscus properties and capillary force. *J. Fluid Mech.*, 67:723–42, 1975.
- [145] D. E. Packham. Surface energy, surface topography and adhesion. *Int. J. Adhes. Adhes.*, 23(6):437–48, 2003.
- [146] J. F. Padday, G. Pétré, C. G. Rusu, J. Gamero, and G. Wozniak. The shape, stability and breakage of pendant liquid bridges. *J. Fluid Mech.*, 352:177–204, 1997.
- [147] C. Pagano, L. Zanoni, I. Fassi, and F. Jovane. Micro-assembly: design and analysis of a gripper based on capillary force. In *Proc. of the 1st CIRP - International Seminar on Assembly Systems*, pages 165–170, Stuttgart, Germany, 15-17 November 2006.
- [148] N.W. Pascarella and D.F. Baldwin. Compression flow modeling of underfill encapsulants for low cost flip chip assembly. In *Proc. of 1998 International*

Symposium of Underfill Encapsulants for Low Cost Flip Chip Assembly, page 33, 1998.

- [149] Xavier Pepin, Damiano Rossetti, Simon M. Iveson, and Stefaan J. R. Simons. Modeling the evolution and rupture of pendular liquid bridges in the presence of large wetting hysteresis. *J. Colloid Interface Sci.*, 232:289–97, 2000.
- [150] L. Picarelli, L. Olivares, L. Comegna, and E. Damiano. Mechanical aspects of flow-like movements in granular and fine grained soils. *Rock Mech. Rock Enging.*, 41(1):179–197, 2008.
- [151] R. Pit, H. Hervet, and L. Léger. Direct experimental evidence of slip in hexadecane: solid interfaces. *Phys. Rev. Lett.*, 85(5):980–983, 2000.
- [152] Olivier Pitois, Pascal Moucheront, and Xavier Chateau. Liquid bridge between two moving spheres: An experimental study of viscosity effects. *J. Colloid Interface Sci.*, 231(1):26–31, 2000.
- [153] Joseph Antoine Ferdinand Plateau. *Statique expérimentale et théorique des liquides soumis aux seules forces moléculaires*. Gauthier-Villars, Paris, 1873.
- [154] Yu. Plevachuk, V. Sklyarchuk, S. Eckert, and G. Gerbeth. Some physical data of the near eutectic liquid lead-bismuth. *Journal of Nuclear Materials*, 373:335–342, 2008.
- [155] Yu. Plevachuk, V. Sklyarchuk, A. Yakymovych, B. Willers, and S. Eckert. Electronic properties and viscosity of liquid pb-sn alloys. *Journal of Alloys and Compounds*, 394:63–68, 2005.
- [156] L.C. Prasad and A. Mikula. Role of surface properties on the wettability of sn-pb-bi solder alloys. *Journal of Alloys and Compounds*, 282:279–285, 1999.
- [157] Y. I. Rabinovich, J. J. Adler, M. S. Esayanur, A. Ata, R. K. Singh, and B. M. Mougdil. Capillary forces between surfaces with nanoscale roughness. *Adv. Colloid Interface Sci.*, 96:213–30, 2002.
- [158] Yakov I. Rabinovich, Madhavan S. Esayanur, and Brij M. Mougdil. Capillary forces between two spheres with a fixed volume liquid bridge: Theory and experiment. *Langmuir*, 21:10992–7, 2005.
- [159] R. Ragucci, F. Fabiani, A. Cavaliere, P. Muscetta, and C. Noviello. Characterization of stability regimes of electrohydrodynamically enhanced atomization. *Experimental Thermal And Fluid Science*, 21:156–161, 2000.
- [160] Vincent Raman and Pierre Lambert. *Recueil d'exercices pour le cours de mécanique rationnelle (ba1)*. Presses Universitaires de Bruxelles, 2009.

- [161] Frédéric Restagno, Lydéric Bocquet, and Thierry Biben. Metastability and nucleation in capillary condensation. *Phys. Rev. Lett.*, 84(11):2433–6, 2000.
- [162] Frédéric Robert, Valérie Duchateau, Vincent Raman, Cédric Boey, Nadine Postiaux, and Pierre Lambert. Détecter les préconceptions pour corriger les représentations erronées des étudiants: application à la mécanique et à l'électronique. Congrès AIPU (Association Internationale de Pédagogie Universitaire), mai 2007, Montréal (Canada), 2007.
- [163] Isadore Rudnick. Measurements of the acoustic radiation pressure on a sphere in a standing wave field. *J. Acoust. Soc. Am.*, 62(1):20–22, 1977.
- [164] A.J. Rulison and R.C. Flagan. Scale-up of electrospray atomization using linear arrays of taylor cones. *Rev. Sci. Instrum.*, 64(3):683–686, 1993.
- [165] S. Saito, T. Motokado, K.J. Obata, and K. Takahashi. Capillary force with a concave probe-tip for micromanipulation. *Appl. Phys. Lett.*, 87, 2005.
- [166] O.V. Salata. Tools of nanotechnology: Electrospray. *Current Nanoscience*, 1:25–33, 2005.
- [167] V. Sariola, Q. Zhou, R. Laass, and H.N. Koivo. Experimental study on droplet based hybrid microhandling using high speed camera. In *Proc. of the 2008 IEEE/RSJ International Conference on Intelligent Robots and Systems*, pages 919–924, Nice, September 22-26 2008.
- [168] David Schmid, Sandra Koelemeijer, Jacques Jacot, and Pierre Lambert. Microchip assembly with capillary gripper. In *Proc. of the 5th International Workshop on Microfactories (4 pages)*, 25-27 October 2006.
- [169] F. Schoenfeld and K.S. Drese. *Modelling and Simulation of Micro Fluidic Systems*. FSRM Course, 2005.
- [170] A. Shastry, M.J. Case, and K.F. Bohringer. Directing droplets using microstructured surfaces. *Langmuir*, 22:6161–6167, 2006.
- [171] K.F. Bohringer Sheng-Hsiung Liang, X. Xiong. Towards optimal designs for self-alignment in surface tension driven self-assembly. In *Proceedings the 17th IEEE International Conference on MEMS*, pages 9–12. IEEE, 2004.
- [172] Lucel Sirghi, Robert Szoszkiewicz, and Elisa Riedo. Volume of a nanoscale water bridge. *Langmuir*, 22:1093–8, 2005.
- [173] F. Soulié, F. Cherblanc, M.S. El Youssoufi, and C. Saix. Influence of liquid bridges on the mechanical behaviour of polydisperse granular materials. *Int. J. Numer. Anal. Meth. Geomech.*, 30:213–228, 2006.

- [174] T. Stifter, O. Marti, and B. Bhushan. Theoretical investigation of the distance dependence of capillary and van der Waals forces in scanning force microscopy. *Phys. Rev. B*, 62(20):13667–73, 2000.
- [175] Atsushi Takei, Kiyoshi Matsumoto, and Isao Shimoyama. Capillary torque caused by a liquid droplet sandwiched between two plates. *Langmuir*, 26(4):2497–2504, 2009.
- [176] Enrico Tam, Marion Sausse Lhernould, Pierre Lambert, Alain Delchambre, and Marie-Paule Delplancke. Electrostatic forces in micromanipulation: Experimental characterization and simulation including roughness. *Appl. Surf. Sci.*, 255(18):7898–7904, 2009.
- [177] K. Tang and A. Gomez. Generation of a monodisperse water droplets from electrosprays in a corona-assisted cone-jet mode. *J. Colloid Interface Sci.*, 175:326–332, 1995.
- [178] L. H. Tanner. The spreading of silicone oil drops on horizontal surfaces. *J. Phys. D*, 12(9):1473–1484, 1979.
- [179] Marcel Tichem, Fabien Bourgeois, Pierre Lambert, Vincent Vandaele, and Defeng Lang. Capturing micro-assembly process windows on process data sheets. In *Proc. of the IEEE Int. Symposium on Assembly and Task Planning (ISATP05)*, Montréal, Canada, 19-21 July 2005.
- [180] C.G. Tsai, C.M. Hsieh, and J.A. Yeh. Self-alignment of microchips using surface tension and solid edge. *Sensors and Actuators A*, 139:343–349, 2007.
- [181] Jean-Baptiste Valsamis. *A Study of Liquid Bridges Dynamics: an Application to micro-Assembly*. PhD thesis, Université libre de Bruxelles.
- [182] Jean-Baptiste Valsamis, Alain Delchambre, and Pierre Lambert. An experimental study of prehension parameters during manipulation task. In *Proc. of the 5th International Workshop on Microfactories*, 25-27 October 2006.
- [183] N. van Veen. Analytical derivation of the self-alignment motion of flip chip soldered components. *Journal of Electronic Packaging*, 121:116–121, 1999.
- [184] Vincent Vandaele. *Contactless handling for micro-assembly: acoustic levitation*. PhD thesis, Université libre de Bruxelles, Brussels, Belgium, 2008.
- [185] Vincent Vandaele, Pierre Lambert, and Alain Delchambre. Non-contact handling in microassembly: acoustical levitation. *Precis. Eng.*, 29(4):491–505, 2005.
- [186] Vincent Vandaele, Pierre Lambert, Alain Delchambre, and Philippe Bouillard. Design and implementation of a flexible guiding system in translation.

- In H. Knobloch and Y. Kaminorz, editors, *Proc. of Int. Forum on Micro-Nano Integration - From Science to Application*, pages 293–295, Potsdam, Germany, December 2003. Springer.
- [187] O.D. Velev, B.G. Prevo, and K.H. Bhatt. On-chip manipulation of free droplets. *Nature*, 426:515, 2003.
- [188] Julien Vitard, Pierre Lambert, Alexandre Chau, and Stéphane Régnier. Capillary forces models for the interaction between a cylinder and a plane. In *Proc. of the 5th International Workshop on Microfactories (4 pages)*, Besançon, 25-27 October 2006.
- [189] Julien Vitard, Pierre Lambert, and Stéphane Régnier. Study of cylinder/plan capillary force near millimeter scale and experimental validation. In *Proceedings of IEEE International Symposium on Assembly and Manufacturing, 2007*.
- [190] O.V. Voinov. Hydrodynamics of wetting. *Fluid Dynamics*, 11(5):714–721, 1976.
- [191] Š. Šikalo, H.D. Wilhelm, I.V. Roisman, S. Jakirlić, and C. Tropea. Dynamic contact angle of spreading droplets: Experiments and simulations. *Phys. Fluids*, 17(6):1–13, 2005.
- [192] E.W. Washburn. The dynamics of capillary flow. *Phys. Rev.*, 17(3):273–283, 1921.
- [193] B. Wee, M. Kumemura, D. COLLARD, and H. Fujita. Isolation of single dna molecule in a picolitre-sized droplet formed by liquid dielectrophoresis. In *Proc. of the 12th International Conference on Miniaturized Systems for Life Sciences*, October 12-16 2008.
- [194] R. N. Wenzel. cited by [145]. *Ind. Eng. Chem.*, 28:988, 1936.
- [195] Dongmin Wu, Nicholas Fang, Cheng Sun, and Xiang Zhang. Stiction problems in releasing of 3d microstructures and its solution. *Sensors and Actuators A*, 128:109–15, 2006.
- [196] H. Xie, S. Haliyo, and S. Régnier. A versatile atomic force microscope for 3d nanomanipulation and nanoassembly. *Nanotechnology*, 20:215301, 2009.
- [197] F. Yan, B. Farouk, and F. Ko. Numerical modeling of an electrostatically driven liquid meniscus in the cone-jet mode. *J. Aerosol Sci.*, 34:99–116, 2002.
- [198] J. Zeng, D. Sobek, and T. Korsmeyer. Electro-hydrodynamic modeling of electrospray ionization: Cad for a μ fluidic device - mass spectrometer interface. Technical report, Coventor, 2003.

- [199] W. Zesch, M. Brunner, and A. Weber. Vacuum tool for handling microobjects with a nanorobot. In *Proc. of Int. Conf. on Robotics and Automation*, pages 1761–1766, 1997.
- [200] Wolfgang Zesch. *Multi-Degree-of-Freedom Micropositioning Using Stepping Principles*. PhD thesis, ETHZ, Zürich, 1997.